

eISSN 2300-262X (online)



POLISH ACADEMY OF SCIENCES
INSTITUTE OF FUNDAMENTAL TECHNOLOGICAL RESEARCH
COMMITTEE ON ACOUSTICS

ARCHIVES of ACOUSTICS

QUARTERLY

Vol. 48, No. 4, 2023

WARSAW



ARCHIVES of ACOUSTICS

QUARTERLY, Vol. 48, No. 4, 2023

In Memoriam

Professor Janusz Wójcik 463

Research Papers

J. Du, Z. Peng, L. Ge, S. Lyu, F. Zhou, Y. Liu, *Modulation mechanism of acoustic scattering in underwater corner reflectors with acoustic metasurfaces*..... 465

B. Li, F.-L. Zhou, J. Fan, B. Wang, L.-W. Tan, *Research on the performance optimization of turbulent self-noise suppression and sound transmission of acoustic windows made from functionally graded material*..... 475

G. Szczepański, M. Podleśna, L. Morzyński, A. Włodarczyk, *Investigation of the acoustic properties of a meta-material with a multi-ring structure* 497

C.-I. Wu, G.-P. Too, B.-H. Wu, *Impulse excitation in a watertight steel circular cylindrical shell and influence of structural configuration on underwater radiated noise*..... 509

P. Kowalski, A. Alikowski, *Laboratory tests and numerical simulations of two anti-vibration structures made by 3D printing – comparative research*..... 523

J. Chu, X. Liang, Z. Yang, H. Liang, T. Chen, L. Su, Z. Zhou, *A multi-layer micro-perforated panel structure based on curled space for broadband sound absorption at low frequencies* 529

V. Morkun, N. Morkun, V. Tron, O. Serdiuk, A. Haponenko, *Evaluation of the sedimentation process in the thickener by using the parameters of longitudinal ultrasonic oscillations and Lamb waves*..... 539

P. Karwat, *Algorithm for computationally efficient imaging of sound speed in conventional ultrasound sonography* 549

J. Tasinkiewicz, *3D synthetic aperture imaging method in spectrum domain for low-cost portable ultrasound systems* 559

A. Ozga, J. Wierzbicki, D. Mleczko, *A proposal concerning assessment of alternative cityscape designs with audiovisual comfort and health of inhabitants*..... 573

P. Falkowski-Gilski, G. Debita, *Quality evaluation of speech transmission via two-way BPL-PLC voice communication system in an underground mine*..... 585

M. Huang, S. Jin, G. Nie, X. Wang, Q. Zhang, Y. An, Z. Qu, W. Yin, *Removal of fouling from steel plate surfaces based on multi-frequency eco-friendly ultrasonic guided wave technology*..... 593

Chronicle

LXIX Open Seminar on Acoustics 603

Editorial Board

Editor-in-Chief: NOWICKI Andrzej (Institute of Fundamental Technological Research PAS, Poland)

Deputy Editor-in-Chief: WÓJCIK Janusz (Institute of Fundamental Technological Research PAS, Poland)
GAMBIN Barbara (Institute of Fundamental Technological Research PAS, Poland)

Associate Editors

General linear acoustics and physical acoustics

RDZANEK Wojciech P. (University of Rzeszów, Poland)
SNAKOWSKA Anna (AGH University of Krakow, Poland)

Architectural acoustics

KAMISIŃSKI Tadeusz (AGH University of Krakow, Poland)
MEISSNER Mirosław (Institute of Fundamental Technological Research PAS, Poland)

Musical acoustics and psychological acoustics

MIŚKIEWICZ Andrzej (The Fryderyk Chopin University of Music, Poland)
PREIS Anna (Adam Mickiewicz University, Poland)

Underwater acoustics and nonlinear acoustics

GRELOWSKA Grażyna (Gdańsk University of Technology, Poland)
MARSZAL Jacek (Gdańsk University of Technology, Poland)

Speech, computational acoustics, and signal processing

KOCIŃSKI Jędrzej (Adam Mickiewicz University, Poland)

Ultrasonics, transducers, and instrumentation

GAMBIN Barbara (Institute of Fundamental Technological Research PAS, Poland)
OPIELIŃSKI Krzysztof (Wrocław University of Science and Technology, Poland)

WÓJCIK Janusz (Institute of Fundamental Technological Research PAS, Poland)

Sonochemistry

DZIDA Marzena (University of Silesia in Katowice, Poland)

Electroacoustics

ŻERA Jan (Warsaw University of Technology, Poland)

Vibroacoustics, noise control and environmental acoustics

ADAMCZYK Jan Andrzej (Central Institute for Labor Protection – National Research Institute, Poland)
KLEKOT Grzegorz (Warsaw University of Technology, Poland)
KOMPALA Janusz (Central Mining Institute, Poland)
LENIOWSKA Lucyna (University of Rzeszów, Poland)
PIECHOWICZ Janusz (AGH University of Krakow, Poland)
PLEBAN Dariusz (Central Institute for Labor Protection – National Research Institute, Poland)

Journal Managing Editor: JEZIERSKA Eliza (Institute of Fundamental Technological Research PAS, Poland)

Advisory Editorial Board

Chairman: WESOŁOWSKI Zbigniew (Polish Academy of Science, Poland)

BATKO Wojciech (AGH University of Krakow, Poland)
BLAUERT Jens (Ruhr University, Germany)
BRADLEY David (The Pennsylvania State University, USA)
CROCKER Malcolm J. (Auburn University, USA)
DOBRUCKI Andrzej (Wrocław University of Science and Technology, Poland)
HANSEN Colin (University of Adelaide, Australia)
HESS Wolfgang (University of Bonn, Germany)
KOZACZKA Eugeniusz (Gdańsk University of Technology, Poland)
LEIGHTON Tim G. (University of Southampton, UK)
LEWIN Peter A. (Drexel University, USA)
MAFFEI Luigi (Second University of Naples SUN, Italy)
PUSTELNY Tadeusz (Silesian University of Technology, Poland)
SEREBRYANY Andrey (P.P. Shirshov Institute of Oceanology, Russia)
SUNDBERG Johan (Royal Institute of Technology, Sweden)
ŚLIWIŃSKI Antoni (University of Gdańsk, Poland)
TITTMANN Bernhard R. (The Pennsylvania State University, USA)
TORTOLI Piero (University of Florence, Italy)
VORLÄNDER Michael (Institute of Technical Acoustics, RWTH Aachen, Germany)

Polish Academy of Sciences
Institute of Fundamental Technological Research PAS
Committee on Acoustics PAS

Editorial Board Office

Pawińskiego 5B, 02-106 Warsaw, Poland
phone (48) 22 826 12 81 ext. 206
e-mail: akustyka@ippt.pan.pl <https://acoustics.ippt.pan.pl>

Indexed in BazTech, Science Citation Index-Expanded (Web of Science Core Collection),
ICI Journal Master List, Scopus, PBN – Polska Bibliografia Naukowa,
Directory of Open Access Journals (DOAJ)

Recognised by The International Institute of Acoustics and Vibration (IIAV)

Edition co-sponsored by the Ministry of Science and Higher Education

PUBLISHED IN POLAND

Typesetting in L^AT_EX: JEZIERSKA Katarzyna (Institute of Fundamental Technological Research PAS, Poland)

In Memoriam

Janusz Wójcik Professor of the IPPT PAN



1957–2023

Janusz Wójcik was born in the heart of Poland near Czarnolas in August 1957. He obtained an M.Sc. Eng. degree at the Warsaw University of Technology in 1983. From 1984 until the last days of his life, he worked at the Institute of Fundamental Technological Research Polish Academy of Sciences in Warsaw. He received his doctoral degree on the basis of the dissertation “Non-linear Envelope Waves in The Vlasov-Maxwell Plasma” in 1990. In 2004, he was given a permanent position of IPPT PAN professor and a year later he was appointed Head of the Ultrasound Introscopy Laboratory at the Department of Ultrasound.

From the beginning of his work his scientific activity was focused on the thermodynamics of ultrasonic waves in tissues modeled as fluids. The theoretical description of thermal effects occurring under the influence of ultrasonic waves on tissues is of fundamental importance not only in planning thermal therapies (hyperthermia) used in medicine but also in the elucidation of attenuation phenomena to improve the quality of medical ultrasonography.

Among the many issues addressed by Professor Janusz Wójcik, one included, e.g., the quantitative determination of the transient temperature increase in lithotripsy (1991), the temperature increase in focused Gaussian ultrasonic beams at various insonation times (1993), the temperature increase for three-layer and

four-layer two-layer model of obstetric tissue in cases of non-linear and linear ultrasonic propagation (1999). He computed also possible temperature effects for acoustic microscopy used for living cells (2004), analyzed the phenomena related to the nonlinear reflection and transmission of plane acoustic waves (2001), and solved theoretically and numerically the aspects of nonlinear reflection–transmission phenomena in acoustics (2018).

The most important scientific achievement of Professor Janusz Wójcik was the introduction, for the first time in the world, of non-local equations for a liquid lossy medium, published in the article “Conservation of energy and absorption in acoustic fields for linear and nonlinear propagation”, *JASA*, 1998.

In 2000, he completed his habilitation thesis “Energy Transport in the Field of Ultrasonic Waves”, which summarized the above results.

In the following years, Professor Wójcik studied the scattering of scalar waves in complex media, modeled systems processing scalar waves in stochastic media, and built a numerical solver for such calculations. He developed a numerical environment for modeling stochastic tissue structures and determining echoes of scattered scalar ultrasonic waves in tissues to search and study the correlation of structure features with the statistical characteristics of echoes. These studies

were focused on improving diagnostic tools for pathological changes in the structure of spongy bone and in arterial walls, and heart tissue dynamics.

Professor Janusz Wójcik was the author and co-author of nearly 100 scientific papers published in the best acoustics journals and several dozen papers presented at international conferences. His works constitute an important contribution to the foundations of understanding the phenomena of nonlinear fluid dynamics; in particular, they allowed the study of the influence of nonlinearity on the thermal effects of sonication and ultrasonic streaming phenomena in fluids.

The center of Janusz Wójcik's interests has always been the fundamentals of physics and mathematics in applied acoustics. He was passionate about them until the end of his life, even in poor health, he was discovering new paths and scientific truths, his two recent publications are the best proof of this. The first of these publications, "Analytical Solution of the Nonlinear Equations of Acoustic in the Form of Gaussian Beam" (2022) makes a significant contribution to applied mathematics by proposing an analytical form of solving nonlinear acoustic equations in the form of a Gaussian beam, and the second publication, "Derivation of Acoustical Streaming Equations for Nonlinear and Dispersive Fluids" (2023) constitutes a theoretical basis for explaining and modeling the physical phe-

nomenon of the so-called acoustic streaming. In the second paper, he obtained formulas that generalize the known descriptions of the form of forces driving streaming and extend their application to the case of nonlinear propagation.

It should be emphasized that Professor Janusz Wójcik was able to cooperate with other scientists, he was always full of enthusiasm and willing to help in solving problems. He passed on his knowledge and made his numerical software available to both his colleagues and younger science students, for whom he lectured during their doctoral studies at IPPT PAN.

Professor Janusz Wójcik was the Deputy Editor-in-Chief of *Archives of Acoustics*.

His scientific contribution to the nonlinear acoustic allows us to remember the Horatian *non omnis moriar*.

We will remember Janusz Wójcik not only as a great scientist, but as a man with a big heart, cheerful, kind to everyone, and, above all, incredibly heroic in the last months of his serious illness, working until the last days of his life.

Janusz Wójcik passed away on September 4, 2023.

We have lost a dear colleague and sincere friend.

Barbara Gambin, Andrzej Nowicki,
and the Editorial Board of *Archives of Acoustics*

Research Paper

**Modulation Mechanism of Acoustic Scattering
in Underwater Corner Reflectors with Acoustic Metasurfaces**Jiaman DU⁽¹⁾, Zilong PENG^{(1)*}, Lili GE⁽¹⁾, Shijin LYU^{(1),(2)}, Fulin ZHOU⁽³⁾, Yan LIU⁽⁴⁾

⁽¹⁾ *School of Energy and Power Engineering
Jiangsu University of Science and Technology
Zhenjiang, China*

⁽²⁾ *National Key Laboratory on Ship Vibration and Noise
China Ship Science Research Center
Wuxi, China; e-mail: lsj5341@163.com*

⁽³⁾ *School of Naval Architecture, Ocean and Civil Engineering
Shanghai Jiao Tong University
Shanghai, China; e-mail: zhoufulin@sjtu.edu.cn*

⁽⁴⁾ *Shanghai Research Institute of Materials
Shanghai, China; e-mail: 13930661775@163.com*

*Corresponding Author e-mail: zlp_just@sina.com

(received November 30, 2022; accepted May 15, 2023)

Using the underwater corner reflector (CR) to simulate the acoustic scattering characteristics of the military target is a new technology to counter active sonar detection. Existing underwater CRs only have the ability to interfere with the acoustic field, but have limitations in acoustic wave modulation. Therefore, acoustic metasurfaces applied on CRs to enhance the ability of acoustic wave modulation has a great application prospect. A fast prediction method based on the Kirchhoff approximation (KA) and the ray tracing theory is proposed to calculate the acoustic scattering characteristics of CR with acoustic metasurfaces in grooves array type. The accuracy of the method is verified by the finite element method (FEM) simulation. The modulation effect of CR with grooves array in different gradient combinations on the structural scattering acoustic field is analyzed. The research shows that the CR with different combinations of the acoustic metasurface has an obvious modulation effect on the amplitude of the acoustic waves and the deflection of acoustic field. In particular, the grooves array in combination with positive and negative gradients has an obvious deflection impact on the scattering acoustic field.

Keywords: acoustic scattering; metasurface; ray tracing; corner reflector; virtual source method.



Copyright © 2023 The Author(s).
This work is licensed under the Creative Commons Attribution 4.0 International CC BY 4.0
(<https://creativecommons.org/licenses/by/4.0/>).

1. Introduction

The radar corner reflector (CR) is an effective passive jamming device to counter radar detection, which can be used to blanket the genuine target signal to protect valuable facilities. The radar CR generally consists of three rigid plates, which are welded together vertically. The CR with a special geometric structure can cause an incident electromagnetic wave to be scattered in it, multiplied and then reflected back to the original

direction. Therefore, CR has a strong backward radar cross section (RCS), which can cause obvious jamming and deception impacts on radar-guided weapon systems (HUANG, 1993; XIONG, 2008); and CR has advantages such as low cost, wide frequency bandwidth, long operating time, and obvious interference that make it widely used in protection of important facilities.

Considering excellent performance in countering radar detection, CRs have shown promising prospects in underwater applications. The detection and iden-

tification of low noise level targets in water is based on an active sonar, and the receive-respond approach is used as the traditional method to counter the active sonar by receiving, processing, and transmitting back the active sonar detection signal (CHEN, ZHAO, 2014; XU *et al.*, 2017; LU, 2009). The prospects for engineering applications are limited by the complexity of the method, and the difficulty in the simulation of a real echo of the target. Therefore, the passive jamming devices, especially CRs, have recently attracted a lot of attention from researchers. It was discovered that elasticity or rigidity has no influence on strong scattering capacity of underwater CRs (CHEN *et al.*, 2018; CHEN, LUO, 2019). Moreover, the structural characteristics indicate that multiple scattering of acoustic waves must be taken into account in calculation. Therefore, the “shooting and bouncing acoustic beams” method based on the planar element method (PEM) is proposed to calculate the scattering sound field of an underwater CR (CHEN, 2012; CHEN, SUN, 2013). However, this is only an approximate numerical calculation, problems such as non-convergence of calculation results and idealistic analysis conditions still exist. MÖLLER and TRUMBORE (1997) proposed a fast algorithm to judge whether a ray passes through a particular triangle, which makes it possible to introduce the virtual source method into PEM to calculate the multiple scattering acoustic field.

The existing underwater CRs only have the ability to interfere with the sound field, limitations still exist in modulation of sound waves, which can be compensated by utilization of acoustic metasurfaces. Such structures are theoretically based on the generalized Snell law and acoustic wave modulation can be realized through surface phase changes (LI *et al.*, 2013; ZHAO *et al.*, 2013; 2018; TIAN *et al.*, 2020). With reference to optical metasurfaces, acoustic metasurfaces was first proposed in 2013, in which a structure with a phase abrupt change was used to make incident waves conform to the generalized Snell law, thus achieving an anomalous refraction and reflection on the interface of different mediums (YANG *et al.*, 2022; YUAN *et al.*, 2020; ZHAO *et al.*, 2020). CHRISTENSEN *et al.* (2007) proposed a grooves array structure and used the coupling of the surface acoustic wave (ASW) to achieve the acoustic field control. Since then, the ability to modulate acoustic waves of acoustic metasurface has attracted widespread attention.

The dihedral CR is one of reflectors with strong multiple scattering ability (LU *et al.*, 2020). In this paper, a dihedral CR embedded with acoustic metasurface is designed based on the generalized Snell law, and the metasurface itself is grooves array whose depth varies in gradient. An improved PEM combining the Kirchhoff approximation (KA) and ray tracing is proposed to calculate the scattering acoustic field of CR with acoustic metasurface. Furthermore, the influence

of different combination of an acoustic metasurface on the dihedral CRs scattering acoustic field is discussed.

2. Relevant theories and models

2.1. Acoustic metasurface

Different from the traditional Snell law, the modulation effect of phase variation on the acoustic wave was first proposed in the generalized Snell law, the modulating mechanism of which is expressed as:

$$\sin \theta_r - \sin \theta_i = \frac{\lambda_0}{2\pi} \frac{d\Phi(x)}{dx}, \quad (1)$$

where θ_r and θ_i are the reflection and incident angles, $d\Phi(x)/dx$ is the surface phase gradient, and λ_0 is the wavelength.

The dihedral CR with an acoustic metasurface was designed based on the generalized Snell law. In order to realize the phase change of the surface acoustic wave, a group of grooves whose depth varies in gradient are constructed on the surface, as shown in Fig. 1. The surface whose thickness usually less than the wavelength is called acoustic metasurface (YU *et al.*, 2021). The relationship between the reflection and incident angles of an acoustic wave scattered by a metasurface can be written as:

$$\theta_r = \arcsin(\sin \theta_i + 2g), \quad (2)$$

where θ_r is the reflection angle, g is the gradient of grooves array (ZHU, 2018). The dihedral CR with an acoustic metasurface was designed based on the generalized Snell law (Fig. 1). The gradient of grooves is $g = dh_i/dx = 0.1$. When the frequency of the incident acoustic wave f_0 is 10 kHz, the acoustic phase variation ranges of the grooves array according to Eq. (1) is $0 \sim 2\pi$, and the step size is $\pi/5$.

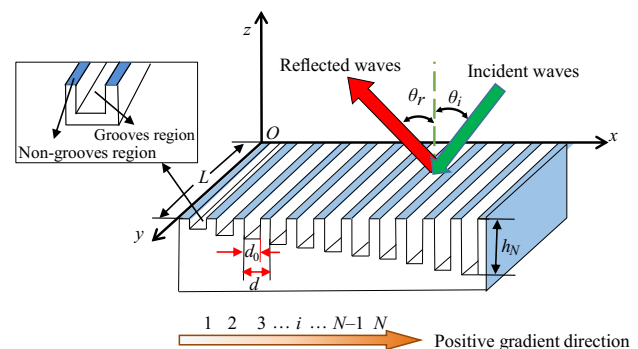


Fig. 1. Calculation model on scattering acoustic field of acoustic metasurface unit.

In this paper, an improved PEM is proposed using the Snell law combined with the virtual source method and the ray tracing method to calculate the directional modulation effect of CR with acoustic metasurfaces.

2.2. Improved planar element method

PEM mainly uses the KA theory, which is called the physical acoustic method (FAN *et al.*, 2012). This approximation method has two basic assumptions:

- 1) the scattering surface can be divided into illuminated areas that has contribution to acoustic scattering and shadow areas that has no contribution to acoustic scattering;
- 2) each part of illuminated area can be treated as a plane and the reflected wave conforms to reflection rule.

As shown in Fig. 2, S is the entire outer surface of scattering object; \mathbf{r}_1 and \mathbf{r}_2 are the vectors from the unit surface dS to the incident point M_1 and receiving point M_2 ; θ_1 and θ_2 are the angles between the surface normal vector \mathbf{n} and \mathbf{r}_1 , \mathbf{r}_2 , respectively.

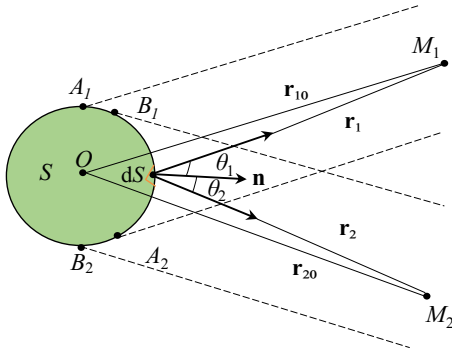


Fig. 2. Kirchhoff approximation theoretical model.

Assuming that the incident acoustic potential is ϕ_S , the scattering acoustic potential satisfies the following Helmholtz integral equation, which is expressed as:

$$\phi_S(\mathbf{r}_2) = \frac{1}{4\pi} \int_S \left[\phi_i \frac{\partial}{\partial n} \left(\frac{e^{jk\mathbf{r}_2}}{r_2} \right) - \frac{\partial \phi_i}{\partial n} \frac{e^{jk\mathbf{r}_2}}{r_2} \right] dS. \quad (3)$$

Considering the scattering object as a rigid surface, the expression of scattering acoustic pressure is

$$\phi_S(\mathbf{r}_2) = -\frac{jk}{4\pi} \iint_S \frac{e^{jk(\mathbf{r}_1+\mathbf{r}_2)}}{\mathbf{r}_1\mathbf{r}_2} (\cos \theta_1 + \cos \theta_2) dS. \quad (4)$$

In the monostatic case, $|\mathbf{r}_1| = |\mathbf{r}_2| = |\mathbf{r}|$, $|\mathbf{r}_{10}| = |\mathbf{r}_{20}| = |\mathbf{r}_0|$, $\Delta r_1 = \Delta r_2 = \Delta r$, and $\theta_1 = \theta_2$. Equation (4) becomes

$$\phi_S(\mathbf{r}) = -\frac{jk}{2\pi} \frac{e^{jk2\mathbf{r}_0}}{\mathbf{r}_0^2} \iint_S e^{jk2\Delta r} \cos \theta_1 dS. \quad (5)$$

The phase variation caused by the grooves array can be expressed as:

$$\varphi = 2kh_i = \begin{cases} \varphi_i & (i \in \text{the grooved region}), \\ 0 & (i \in \text{the non-grooves region}), \end{cases} \quad (6)$$

where h_i is the depth of the i -th groove.

When calculating the scattering sound pressure of the acoustic metasurface, the corresponding phase variation should be considered. Therefore, the scattering acoustic wave potential function at the i -th groove is:

$$\phi'_{S,i} = \phi_{S,i} \cdot e^{j\varphi_i}. \quad (7)$$

The target strength (TS) is calculated by summing the scattered acoustic wave potential functions, which is expressed as:

$$\text{TS} = 20 \log_{10} \left(\left| \sum_{i=1}^M \phi'_{S,i} \right| r^2 \right), \quad (8)$$

where r is the distance from the incidence point to the center point of the plate.

2.3. Dihedral CR with acoustic metasurface

The double acoustic scattering phenomenon in the dihedral CRs makes the solution of the scattering acoustic field more complicated. It can be simplified as the double scattering problem between two discrete rigid plates, as shown in Fig. 3. In the monostatic case, where T is the incidence and receiving point, T' is the geometric symmetric point of T with respect to plate 1, M and P are the centers of plates 1 and 2; \mathbf{n}_1 and \mathbf{n}_2 are the outer normal vectors of plate 1 and plate 2, respectively; \mathbf{r}_1 is the vector from the incident point T to M , \mathbf{r}_2 is the vector from the incident point T to any point Q on plate 2, and \mathbf{r}_{12} is the vector from the center of plate 1 to arbitrary point Q on plate 2.

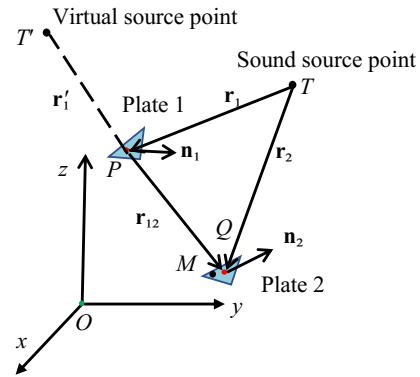


Fig. 3. Schematic of double scattering diagram between discrete plates.

In the monostatic case, the acoustic wave from the incidence point T is scattered by the plate 1 to plate 2, then reflected by plate 2 and finally comes back to the receiving point T . The process can be equivalent to the situation that an acoustic wave comes from the virtual source point T' to the plate 2, and then is scattered to the receiving point T . Furthermore, the multiple scattering acoustic field between plates can be calculated by combining PEM with the virtual source

method, and the double scattering potential function can be expressed as:

$$\phi_S(\mathbf{r}_2) = -\frac{jk}{4\pi} \iint_S \frac{e^{jk(\mathbf{r}'_1 + \mathbf{r}_{12} + \mathbf{r}_2)}}{(\mathbf{r}'_1 + \mathbf{r}_{12})\mathbf{r}_2} (\cos\theta_1 + \cos\theta_2) dS. \quad (9)$$

The dihedral CR with an acoustic metasurface can be achieved by the grooves array, and the single scattering acoustic field is shown in Fig. 4a. Where θ_{i1} , θ_{i2} , θ_{r1} , and θ_{r2} are the incident angles and reflection angles of the acoustic wave of face I and face II, respectively. This paper only considers the monostatic case, thus the incident angle of the single reflection and the reflection angle are on the same side of the normal vector. The single scattering acoustic field consists of two parts, which is the acoustic pressure reflected by grooves regions and non-grooves regions, respectively.

The double scattering acoustic field includes the scattering acoustic wave from face I to II and face II to I. As shown in Fig. 4b, for symmetry of geometry and an angle of incidence, only the scattering acoustic field from face I to II is described.

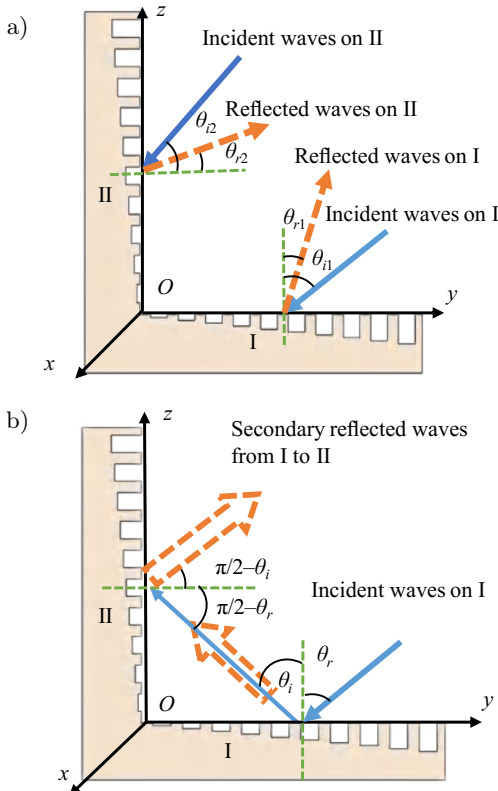


Fig. 4. Reflection of a dihedral reflector: a) single; b) double.

When the acoustic wave is incident on the surface I and scattered on the surface II, the acoustic pressure at the grooves is modified by multiplying phase factors according on Subsec. 2.2, and the double scattering acoustic field of the dihedral CR is acquired by utilizing the improved PEM algorithm combined with

the virtual source method and the ray tracing method, which can be expressed as:

$$\phi_S^{I-II} = -\frac{jk}{4\pi} \left(\sum_{i=1}^M P_i e^{2jk(h_{1,i} + h_{2,i})} \right) \quad (10)$$

where M is the number of planar elements in face I from which an acoustic wave can be scattered to face II, ϕ_S^{I-II} is the corresponding potential function. Assuming that the acoustic wave incident to the planar 1 in the face I and then is scattered to planar 2 in face II, h_1 is the depth of the corresponding groove if planar 1 is in the grooves' region, $h_1 = 0$ if planar 1 is in the non-grooves' region. The determination of h_2 follows the similar process by considering situation in face II. P_i can be expressed as:

$$P_i = \frac{e^{jk(\mathbf{r}'_{q,i} + \mathbf{r}_{m,i})}}{|\mathbf{r}'_{q,i}| |\mathbf{r}_{m,i}|} [\mathbf{n}_2 \cdot (\mathbf{r}'_{q,i} + \mathbf{r}_{m,i})] I_{S,i}^{I-II}, \quad (11)$$

where $\mathbf{r}'_{q,i}$ is the local coordinates of a virtual source point of the incident point about planar 1, $\mathbf{r}_{m,i}$ is the local coordinates of receiving point, \mathbf{n}_2 is the normal vector of planar 2, the scattering contribution $I_{S,i}^{I-II}$ is written as:

$$I_{S,i}^{I-II} = \iint_{S^{I-II}} e^{-jk\mathbf{R} \cdot [\mathbf{r}'_{q0,i} + \mathbf{r}_{m0,i}]} dS, \quad (12)$$

where $\mathbf{r}'_{q0,i}$ and $\mathbf{r}_{m0,i}$ are the unit vectors of $\mathbf{r}'_{q,i}$ and $\mathbf{r}_{m,i}$, respectively.

A similar process can be used to obtain ϕ_S^{II-I} . The total scattering acoustic field is the summation of the potential function of single reflection and double reflection:

$$\phi = \phi_S^I + \phi_S^{II} + \phi_S^{I-II} + \phi_S^{II-I}, \quad (13)$$

where ϕ_S^I and ϕ_S^{II} are the potential function of single reflection from face I and II, respectively; ϕ_S^{I-II} and ϕ_S^{II-I} are the potential functions of double reflection from face I to II and II to I, respectively.

3. Simulation

The acoustic scattering characteristics of the dihedral CR with an acoustic metasurface are studied to verify the control effectiveness on the scattering acoustic field of the structure, and the accuracy of the improved PEM. The schematic of the dihedral CR with and without acoustic metasurface is shown in Figs. 5a and 5b. Calculation results of TS of the dihedral CR with an acoustic metasurface and CR itself using the finite element method (FEM) is shown in Fig. 5c. Comparison of dihedral CRs with acoustic metasurfaces calculated with FEM and improved PEM proposed in Sec. 2 is shown in Fig. 5d. All the calculation is under monostatic situation, as a result,

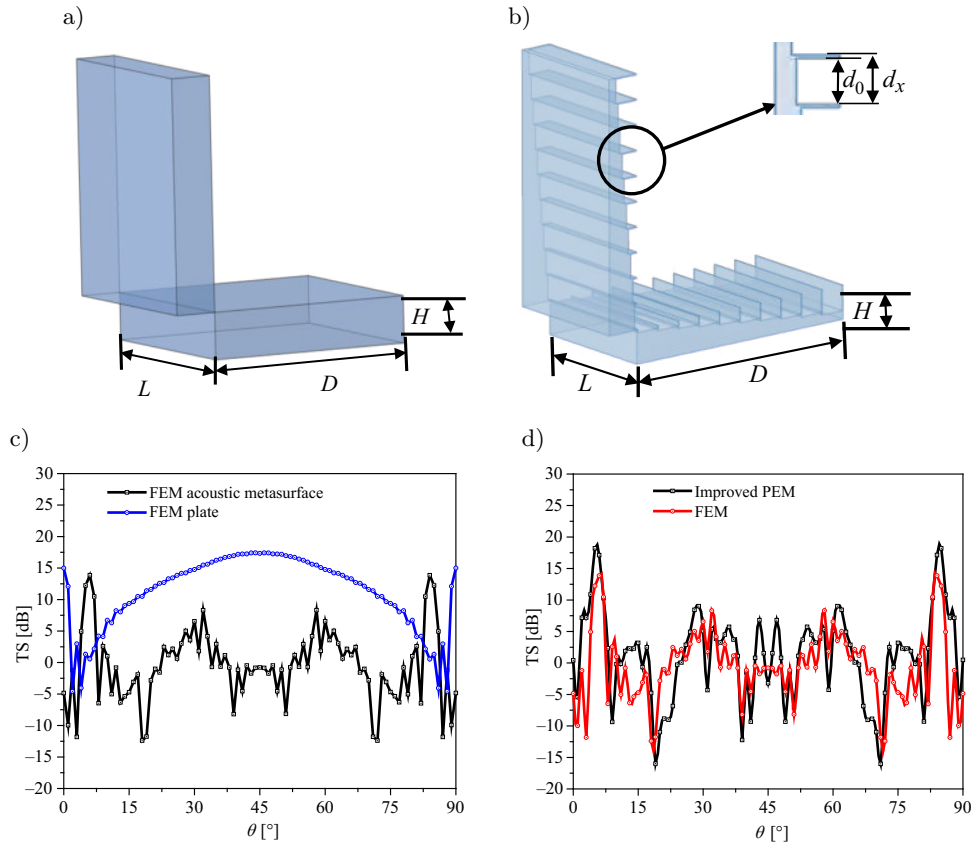


Fig. 5. a) Model of dihedral CR; b) model of dihedral CR with acoustic metasurface; c) calculation results of TS of dihedral CR with acoustic metasurface and CR itself using FEM; d) comparison of dihedral CRs with acoustic metasurfaces calculated with FEM and improved PEM proposed in this article.

θ in Figs. 5c and 5d is both an incident angle and a reflection angle. The effect of different structural combinations and periodic arrangements on the scattering acoustic field is studied in Subsecs. 3.1 and 3.2.

When frequency is 25 kHz and θ is $0^\circ \sim 90^\circ$, the scattering acoustic field of the dihedral CR (Fig. 5a) and the dihedral CR with the acoustic metasurface (Fig. 5b) were analyzed using FEM, respectively, as shown in Fig. 5c. The TS of the dihedral CR reaches the peaks values of 14.98, 17.33, and 14.98 dB at $\theta = 0^\circ$, $\theta = 45^\circ$, and $\theta = 90^\circ$. The TS of the dihedral CR with an acoustic metasurface reaches peak values of 13.86 dB at $\theta = 6^\circ$ and $\theta = 84^\circ$. The dihedral CR with an acoustic metasurface has significantly decreased the TS amplitude θ ranges from 7.5° to 83.5° . The results show that the dihedral CR applying an acoustic metasurface can significantly decrease their TS in most incident angle ranges and change the directivity.

Figure 5d shows that the TS of the acoustic metasurface dihedral CR calculated by the improved PEM and the FEM fits well, which verifies the accuracy of the improved PEM, but there are still some errors. The main reason is that the improved PEM calculation merely considers the effects of acoustic metasurface as phase changing, while the multiple reflections between the bottom and the side walls of the grooves are

not considered, which is taken into account by FEM. Therefore, that is the reason why two methods have errors under certain incident angles.

3.1. Grooves array in single-period gradient

Based on the generalized Snell law, the acoustic reflection angle is not only related to the acoustic incident frequency, but also to the gradient of the metasurface groove array. When the frequency of the incident acoustic wave is $f = 10$ kHz and the angle of incidence ranges $\theta_i = 0^\circ \sim 90^\circ$, the effect of the gradient magnitude and direction of the grooves array gradient on the scattering acoustic field of the dihedral CR is discussed and analyzed in this section.

3.1.1. Gradient magnitude

The reflection angle of acoustic waves can be adjusted by changing the magnitude of the grooves array based on the generalized Snell law, thus the grooves array gradient can be used to modulate the reflection direction of an acoustic wave. The designed gradients of the grooves array are $g = 0.1, 0.2, 0.3$, respectively. Figures 6a–6c show the dihedral CR models and TS results of the grooves array in different gradients. As shown in Figs. 6d–6f, the dihedral CR with different

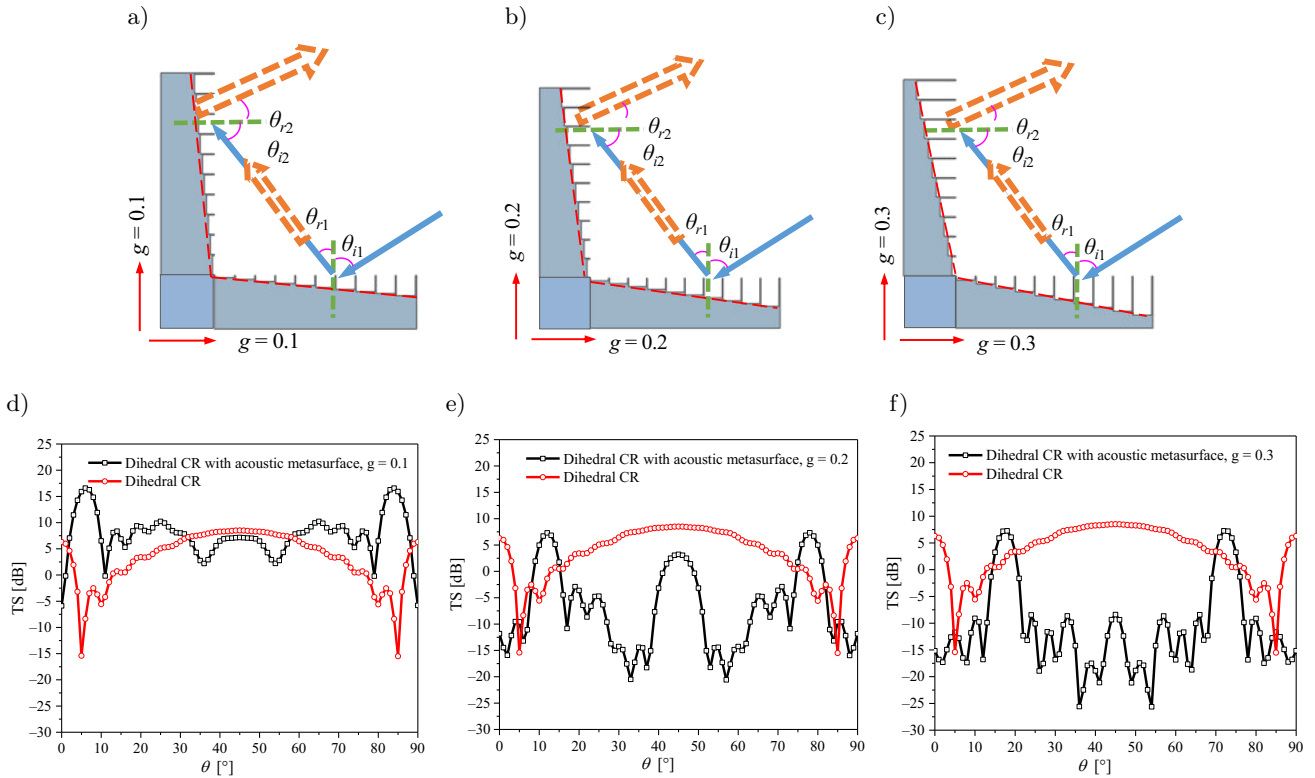


Fig. 6. Models and TS calculation results of grooves array in different gradient magnitude: a) $g = 0.1$; b) $g = 0.2$; c) $g = 0.3$; d)–f) are calculation results for model a)–c), respectively.

gradients of grooves array has different modulation effects on the scattering acoustic field of the target. The TS amplitude is modulated at most incident angles, and increases or decreases with an incident angle. By comparing dihedral CR with acoustic metasurface and dihedral CR itself, the results show that the corresponding angles of peaks change significantly.

As shown in Figs. 6d–f, when $g = 0.1$, the TS of the dihedral CR with acoustic metasurface is significantly higher than CR itself at the angle range of $3^\circ \sim 30^\circ$ and $60^\circ \sim 87^\circ$, and has peak values near the incident angles of 5° and 85° . When $g = 0.2$, the TS of the dihedral CR with acoustic metasurface is significantly higher than CR itself at the angle range of $8^\circ \sim 15^\circ$ and $75^\circ \sim 82^\circ$, and has peak values at 12° and 78° . When $g = 0.3$, the TS of the dihedral CR with acoustic metasurface is significantly higher than CR itself at the angle range of $14^\circ \sim 20^\circ$ and $70^\circ \sim 76^\circ$, and has peak values at 17.5° and 72.5° .

Comparing the calculation results in Figs. 6d–6f, the corresponding angle of the peak varies with the magnitude of the gradient of the grooves array, which indicates that magnitude of gradients can change the main direction of an acoustic scattering field. It can also be seen that the TS amplitude is reduced most effectively when $g = 0.3$. Therefore, it is possible to realize enhancing or reducing the TS of the underwater simulator within a large range of incident angles.

3.1.2. Gradient direction

Without changing the gradient magnitude of the grooves array (gradient magnitudes are $g = 0.1$), the TS of the dihedral CR of the grooves array with different gradient direction combinations is calculated and analyzed. Figure 7 shows schematic of a calculation model and comparison of calculation results between the dihedral CRs and dihedral CRs with an acoustic metasurface in different combinations of the gradient direction. It can be seen that TS of all the dihedral CRs with an acoustic metasurface in different gradient combinations have been significantly reduced in a certain range of angles, which proves that all the three structures are effective in modulation of the scattering acoustic field.

As shown in Fig. 7d, the whole TS curve of the structure in a positive-negative gradient has a tendency to approach to $\theta = 0^\circ$, which means that the phase change has occurred in the process of wave propagation of the structure, and the main reflection direction of acoustic scattering is significantly changed. Figure 7e shows that the TS amplitude of the structure in the negative-negative gradient has decreased obviously in most angles, with valley values of 35.4 dB at $\theta = 35^\circ$ and $\theta = 55^\circ$, respectively. Figure 7f shows the structure of combination of positive-positive gradient has enhanced TS amplitudes at $\theta = 5^\circ \sim 35^\circ$ and $\theta = 55^\circ \sim 85^\circ$, and the peak values appear at $\theta = 6^\circ$ and $\theta = 84^\circ$.

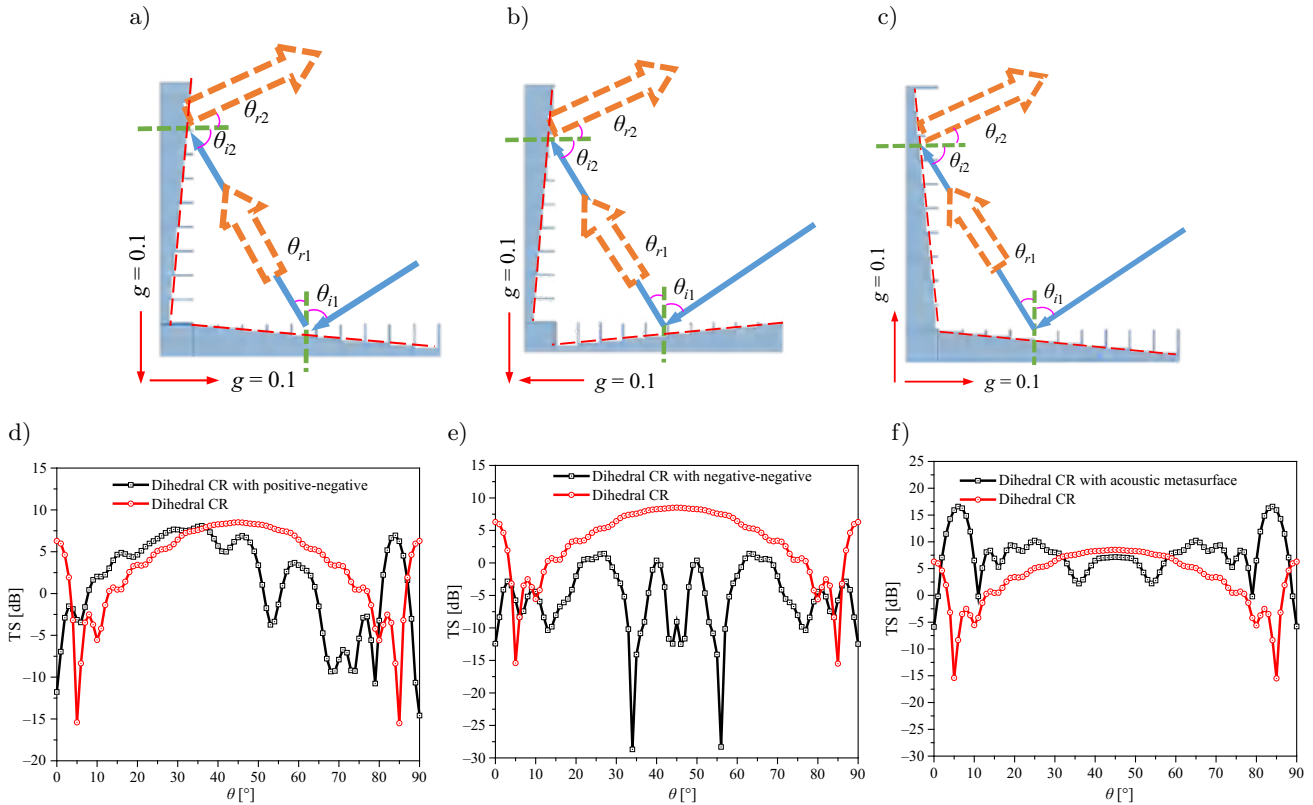


Fig. 7. Models and calculation results of grooves array with different gradient combinations: a) positive-negative gradient model; b) negative-negative gradient model; c) positive-positive gradient model; d)–f) are calculation results for model a)–c), respectively.

From the above results, it is shown that all three structures have different effects on modulation of acoustic scattering. The structure in positive-negative gradient has a more obvious modulation effect on the directivity of an acoustic wave. And the model of negative-negative gradient has a more apparent modulation effect on the TS reduction of the target. Therefore, the application of dihedral with an acoustic metasurface is of great value in modulation of the scattering acoustic field.

3.2. Grooves array in double-period gradient

The dihedral CR with the double-period gradient acoustic metasurface is composed of the acoustic metasurface whose gradient is $g = 0.1$ as the unit, as shown in Figs. 8a–8c. The acoustic scattering characteristics with different combinations are studied, and the results are shown in Figs. 8d–8f.

As shown in Fig. 8d, the TS directivity curve has a tendency to approach to $\theta = 0^\circ$, and the TS amplitude decreases significantly at $\theta = 9^\circ \sim 81^\circ$, while increases significantly at $\theta = 82^\circ \sim 87^\circ$. The modulation of the main reflection direction and the TS amplitude of an acoustic scattering wave is more obvious compared with Fig. 7d. Figure 8e shows that the TS amplitude of the dihedral CR with the double-period

negative-negative gradient is obviously decreased at all incidence angles, and the decrease effect is more obvious comparing with Fig. 7e. The TS amplitude of the double-period positive-positive gradient combination of dihedral CR decreases between 8° and 82° , while increases significantly at the incidence angle of $3^\circ \sim 7^\circ$ and $83^\circ \sim 87^\circ$, as shown in Fig. 8f. Moreover, the range of angles at which the TS decreases is larger compared to the single-period (Fig. 7f).

The results show that the TS amplitude of these three double-period combinations is significantly reduced in most of the incident angle ranges and increases in a small angle range. Compared with the single period, the dihedral CR with double-period combination has more complex TS directivity curve and more peaks, and the modulation effect of acoustic scattering characteristic is more obvious. Therefore, increasing of the periodicity of the grooves array has a positive effect in reduction of the TS amplitude and enhancing of the main direction of acoustic scattering. The modulating effect of the grooves array on the dihedral CR acoustic field is the reason of the reduction effect of TS amplitude. On the one hand, as the grooves increase the propagation distance of acoustic wave compared to the flat plate, which causes a decrease in the sound pressure amplitude. On the other hand, the phase change caused by the acoustic wave in the groove

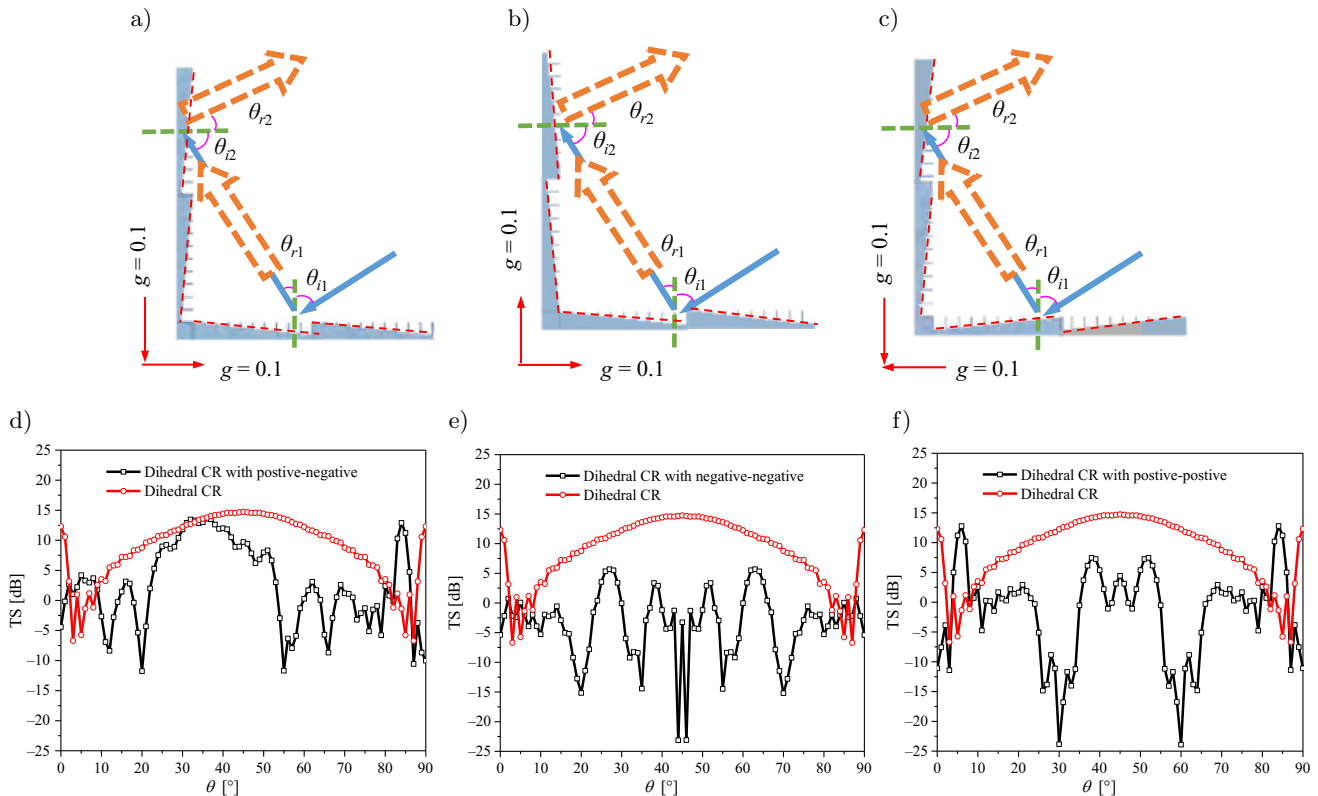


Fig. 8. Models of grooves array in different double-period gradient combinations and its calculation results: a) double-period positive-negative gradient; b) double-period negative-negative gradient; c) double-period positive-positive gradient, d)–f) are calculation results for model a)–c), respectively.

leads to an abnormal relationship between the incident and reflected angles, creating a change in the acoustic field.

4. Conclusion

A dihedral CR with an acoustic metasurface is designed by the generalized Snell law, to realize modulation of the underwater scattering acoustic field. An improved PEM method, taking into account the phase variation caused by grooves, is proposed to calculate the TS of the structure. By comparing the simulation results and PEM results, the effectiveness of the calculation method is verified. The scattering acoustic field and the modulation effects of dihedral CR with an acoustic metasurface in different combinations of the gradient and period is calculated and discussed. The results show that single-period and double-period grooves array can be applied to dihedral reflectors to modulate the amplitude and the main direction of acoustic scattering. In particular, the combination of positive-negative gradient grooves array is more effective in modulating the main direction of acoustic scattering, and the combination of negative-negative gradient grooves array is effective in reducing the TS amplitude of the target. Increasing the periodicity can further reduce the TS amplitude and enhance the modu-

lation effect of the main direction of an acoustic field. As the dihedral CR is the structural basis of underwater CRs, it is important to study the modulation mechanism of the scattering acoustic field from the dihedral CR, which establishes the foundation of the innovative design of underwater passive acoustic decoys.

Acknowledgments

We acknowledge the support of the National Natural Science Foundation of China (the grant no. 52201397), the Natural Science Foundation of the Jiangsu Higher Education Institutions of China (the grant no. BK2020 0995) and the Postgraduate Research & Practice Innovation Program of Jiangsu Province (the grant no. KYCX22_3851).

References

1. CHEN J.Q., ZHAO J.J. (2014), Fidelity analysis of a scale target simulation [in Chinese], *Torpedo Technology*, **22**(6): 442–446, <https://kns.cnki.net/kcms/detail/detail.aspx?FileName=YLJS201406007&DbName=CJFQ2014>.
2. CHEN W.J. (2012) *Research on the Backscattering Characteristics of Underwater Corner Reflector Acoustic Markers*, Ph.D. Thesis, Harbin Engineering

- University, <https://kns.cnki.net/KCMS/detail/detail.aspx?dbname=CDFD1214&filename=1012518440.nh>.
3. CHEN W.J., SUN H. (2013), Beam bouncing method for calculating the scattered sound field of underwater concave targets [in Chinese], *Acta Acoustic*, **38**(02): 147–152, doi: [10.15949/j.cnki.0371-0025.2013.02.018](https://doi.org/10.15949/j.cnki.0371-0025.2013.02.018).
 4. CHEN X. *et al.* (2018), Sound scattering characteristics of underwater elastic corner reflector [in Chinese], *Acta Armamentarii*, **39**(11): 2236–2242.
 5. CHEN X., LUO Y. (2019), Scattering characteristics of underwater rigid corner reflectors [in Chinese], *Technical Acoustics*, **38**(03): 278–283, doi: [10.16300/j.cnki.1000-3630.2019.03.007](https://doi.org/10.16300/j.cnki.1000-3630.2019.03.007).
 6. CHRISTENSEN J., FERNANDEZ-DOMINGUES A.I., DE LEON-PEREZ F., MARTIN-MORENO L., GARCIA-VIDAL F.J. (2007), Collimation of sound assisted by acoustic surface waves, *Nature Physics*, **3**(12): 851–852, doi: [10.1038/nphys774](https://doi.org/10.1038/nphys774).
 7. FAN J., WANG W.L., ZHOU L.K. (2012), Planar elements method for predicting echo characteristics of sonar targets, *Journal of Ship Mechanics*, **16**(1–2): 171–180, doi: [10.3969/j.issn.1007-7294.2012.01.020](https://doi.org/10.3969/j.issn.1007-7294.2012.01.020).
 8. HUANG P.K. (1993), *Radar Target Characteristic Signal*, Beijing: China Astronautic Publishing House Press.
 9. LI Y., LIANG B., GU Z., ZOU X., CHENG J. (2013), Reflected wavefront manipulation based on ultrathin planar acoustic metasurfaces, *Scientific Reports*, **3**(1): 2546, doi: [10.1038/srep02546](https://doi.org/10.1038/srep02546).
 10. LU G. (2009), Discussion on the technology of attracting and sweeping active attack mines, *Mine Warfare and Ship Self-Defence*, **17**(04): 1–6+29, <https://kns.cnki.net/kcms/detail/detail.aspx?FileName=SLZH200904003&DbName=CJFQ2009>.
 11. LU T., WANG Y., YANG H., HUANG X., ZHOU Y., WU J. (2020), Absorbing properties of metamaterial dihedral corner reflector, *Materials Research Express*, **7**(2): 025802, doi: [10.1088/2053-1591/ab7567](https://doi.org/10.1088/2053-1591/ab7567).
 12. MÖLLER T., TRUMBORE B. (1997), Fast, minimum storage ray-triangle intersection, *Journal of Graphics Tools*, **2**(1): 21–28, doi: [10.1080/10867651.1997.10487468](https://doi.org/10.1080/10867651.1997.10487468).
 13. TIAN H.W., SHEN H.Y., ZHANG X.G., LI W., JIANG W.X., CUI T.J. (2020), Terahertz metasurfaces: Toward multifunctional and programmable wave manipulation, *Frontiers in Physics*, **8**: 584077, doi: [10.3389/fphy.2020.584077](https://doi.org/10.3389/fphy.2020.584077).
 14. XIONG Q.L. (2008), *Integrated Electronic Warfare: The Killer Tool of Information Warfare* [in Chinese], 2nd ed., National Defense Industry Press.
 15. XU H.-Z., YUAN Y.-Y., LIU X.-H., YU Y. (2017), On performance analysis of linear array decoy in confronting smart torpedo [in Chinese], *Ship Science and Technology*, **39**(5): 135–138, <http://html.rhzh.net/jckxjsgw/html/51967.htm>.
 16. YANG H., FENG K., LI R., YAN J. (2022), Lamb wave propagation control based on modified GSL, *Frontiers in Physics*, **10**: 909318, doi: [10.3389/fphy.2022.909318](https://doi.org/10.3389/fphy.2022.909318).
 17. YU M. *et al.* (2021), Strength analysis of scattering targets based on acoustic metasurfaces, [in:] *Proceedings of the 18th Symposium on Ship Underwater Noise*, pp. 1031–1037.
 18. YUAN S.M., CHEN A.-L., WANG Y.S. (2020), Switchable multifunctional fish-bone elastic metasurface for transmitted plate wave modulation, *Journal of Sound and Vibration*, **470**: 115168, doi: [10.1016/j.jsv.2019.115168](https://doi.org/10.1016/j.jsv.2019.115168).
 19. ZHAO J., LI B., CHEN Z.N., QUI C.-W. (2013), Redirection of sound waves using acoustic metasurface, *Applied Physics Letters*, **103**(15): 151604, doi: [10.1063/1.4824758](https://doi.org/10.1063/1.4824758).
 20. ZHAO S.D., CHEN A.-L., WANG Y.-S., ZHANG C. (2018), Continuously tunable acoustic metasurface for transmitted wavefront modulation, *Physical Review Applied*, **10**(5): 054016, doi: [10.1103/PhysRevApplied.10.054066](https://doi.org/10.1103/PhysRevApplied.10.054066).
 21. ZHU Y.F. (2018), *Sound Manipulation by Acoustic Metasurfaces and Its Applications*, Ph.D. Thesis, Nanjing University, <https://kns.cnki.net/KCMS/detail/detail.aspx?dbname=CDFDLAST2018&filename=1018170719.nh.0>.

Research Paper

Research on the Performance Optimization of Turbulent Self-Noise Suppression and Sound Transmission of Acoustic Windows Made from Functionally Graded Material

Bing LI, Fu-Lin ZHOU*, Jun FAN, Bin WANG, Li-Wen TAN

*Key Laboratory of Marine Intelligent Equipment and System, Ministry of Education
P.R. China*

*Corresponding Author e-mail: zhoufulin@sjtu.edu.cn

(received September 29, 2022; accepted April 14, 2023)

For a simplified sonar dome model, an optimization method for internal gradients of functionally graded material (FGM) acoustic windows is proposed in this paper. This method can be used to design optimized FGM acoustic windows with better turbulent self-noise suppression and sound transmission performances. A theoretical model of FGM acoustic windows to evaluate the reduction of self-noise caused by the turbulent boundary layer (TBL) pulsating pressure and the sound transmission loss (STL) is derived through the double Fourier transform and the wavenumber frequency spectrum analysis, respectively, based on the transfer matrix idea and the classical elastic theory. The accuracy of the theory is verified by the finite element results of COMSOL Multiphysics. Utilizing the genetic algorithm (GA) and taking the monotonic gradient as the constraint condition, the internal gradient optimization method of FGM acoustic windows obtains the optimization variables in the Bernstein polynomial when the optimization objective is minimized by iterating the optimization variables in the deviation function represented by the Bernstein polynomial that is introduced in the gradient function. The STL, the turbulent self-noise reduction or a weighting function of the STL and turbulent self-noise reduction of FGM acoustic windows is chosen as the optimization objective. The optimization calculation of the sound transmission or turbulent self-noise suppression performances is carried out for the FRP-rubber FGM (FGM with fiber reinforced plastic (FRP) as the substrate material and rubber as the top material) acoustic window. The optimized results show that both the sound transmission and turbulent self-noise suppression performance are effectively improved, which verifies the effectiveness of the optimization method. Finally, the mechanism of the sound transmission and self-noise suppression characteristics before and after optimization are explained and analyzed based on the equivalent model of graded materials. The research results of this paper provide a reference value for the future design of FGM acoustic windows for sonar domes.

Keywords: functionally graded material; acoustic window; turbulent self-noise; sound transmission loss; optimization.



Copyright © 2023 The Author(s).
This work is licensed under the Creative Commons Attribution 4.0 International CC BY 4.0
(<https://creativecommons.org/licenses/by/4.0/>).

1. Introduction

When underwater vehicles operate, a sound permeable enclosure, which is known as the sonar dome, is usually configured outside the sonar array to avoid the impact of water flow on the array and prevent direct interference from exposure to turbulent self-noise (LAVENDER, 1994; SRIVASTAVA, 1998). The suitable design of a sonar dome ensures sufficient strength and a favorable linear shape but requires good sound

transmission and turbulent self-noise suppression performance; in particular, the sound transmission loss (STL) of the external acoustic signal or the transmitting signal of the internal matrix should be reduced as much as possible. The turbulent self-noise suppression characteristics require that the acoustic window can suppress “pseudo-sound”, that is, filter out the structural vibration noise caused by external turbulence. Early designs of acoustic windows used stainless steel, but the turbulent self-noise suppression char-

acteristics were poor. In the 1970s and 1980s, the subsequent use of rubber material improved the turbulent self-noise reduction, but the stiffness was not sufficient. Currently, fiber reinforced plastic (FRP) is mostly used as an acoustic window material with good sound transmission performance and strong stiffness; however, its turbulent self-noise reduction needs to be improved (HOFFMANN, 1998; BURTON, 1998). Scholars have found that the effect of multilayer composite plates is better than that of single-layer structures in terms of both sound transmission and turbulent self-noise suppression performance. Compared with a single material, a composite plate can benefit from the advantages of different materials (CREMER *et al.*, 2005; HAM *et al.*, 2018; LEE *et al.*, 2010; YU *et al.*, 2005) and thus, can provide more performance improvements. However, the impedance discontinuities at the interfaces of different materials have a certain influence on the acoustic-vibration characteristics of simple sandwich composite plates.

The functionally graded materials (FGMs) (MORTENSEN, SURESH, 1995; POMPE *et al.*, 2003; LIU *et al.*, 2004; PRAKASH, GANAPATH, 2006), which are widely used in the fields of aviation, optics, and energy, have smooth and continuous material properties along the thickness direction, can achieve continuous impedance transitions and impedance connection matching, and can potentially be applied in acoustics (LANE, 1981). There have been few studies on the sound transmission characteristics and turbulent self-noise suppression characteristics of FGMs; and most studies have focused on structural acoustic radiation (GEORGE *et al.*, 2016; HOSSEINI-HASHEMI *et al.*, 2010; ZHAO *et al.*, 2009; IQBAL *et al.*, 2009; KUMAR *et al.*, 2009). SHANG (1965) studied the acoustic reflection performance of a gradual absorption layer in 1965, deduced a general expression for acoustic reflection of a gradual absorption layer, and concluded that an absorption layer with a linear gradual change in material parameters provided good acoustic absorption performance. CHANDRA *et al.* (2014; 2015) used a simple first-order shear deformation theory to investigate the displacement, velocity, acceleration, radiated sound level, radiated sound pressure level and radiated efficiency of FGM plates with power-law exponential changes. The acoustic transmission loss of FGMs with different incident angles and power-law exponents was studied in detail. The simulation results showed that the transmitted sound power level increased monotonically with an increasing power index in the low frequency range of 0–500 Hz, with a difference of more than 10 dB(A). RABBANI *et al.* (2019) established a thick-walled FGM cylindrical shell theory model to solve the deformation and stress in cylindrical shells by using the state space method based on the three-dimensional elastic theory and the piezoelectric elastic theory and calculated the acoustic trans-

mission loss caused by the piezoelectric effect of thick-walled piezoelectric composite cylindrical shells under plane wave excitation. The results were verified through COMSOL. In the area of turbulent self-noise suppression, ZHOU *et al.* (2020) used FGM to carry out research on sonar self-noise reduction. The Corcos model, which considered the excitation source of the sonar structure, was adopted to establish a hydrodynamic noise prediction model of a uniformly coated layer and conduct research on turbulent self-noise reductions. The effect of FGM on the turbulent self-noise suppression performance was analyzed for four typical distribution characteristics: linear, parabolic, power-law, and exponential functions. According to the literature results, FGMs have good research prospects in both sound transmission and turbulent self-noise suppression. However, these characteristics have not previously been considered simultaneously in previous FGM research.

In this paper, the turbulent self-noise suppression and sound transmission characteristics of acoustic windows made from FGM are studied simultaneously for the sonar dome. Through the internal gradient optimization design, optimized FGM acoustic windows with better turbulent self-noise suppression and sound transmission performance are obtained. The main sections are arranged as follows. In Sec. 2, based on the classical elastic theory and the transfer matrix, a theoretical model on FGM acoustic windows to evaluate the turbulent self-noise caused by external turbulent boundary layer (TBL) pulsating pressure and STL towards an incident plane wave is derived utilizing the double Fourier transform and the wavenumber-frequency analysis, and the accuracy is verified by the finite element results of COMSOL Multiphysics. In Sec. 3, specific internal changes in the gradient optimization method for FGM acoustic windows are proposed based on the twin consideration of the turbulent self-noise suppression and sound transmission performance, which enables design of an optimized FGM acoustic window with higher turbulent self-noise reduction and lower STL. In the optimization method, a monotonic gradient is taken as the constraint condition. Upon combining a genetic algorithm (GA), five optimization variables in the Bernstein polynomial, when the optimization objective is minimized, are obtained by iterating optimization variables in the deviation function represented by the Bernstein polynomial introduced in the gradient function. The optimization objective is expressed as the STL, the turbulent self-noise reduction or a twin weighting function of the STL and turbulent self-noise reduction of FGM acoustic windows. In Sec. 4, optimization calculations of the sound transmission or turbulent self-noise suppression performances are carried out for an FRP-rubber FGM based on the proposed gradient optimization method. In Sec. 5, the mechanism of the sound transmission

and turbulent self-noise suppression characteristics of the FRP-rubber FGM acoustic window before and after optimization are explained based on the spectral method and a thin-plate model, using the equivalent model of graded materials. In Sec. 6, the conclusion is provided.

2. Theory model of turbulent self-noise and STL for a simplified sonar dome with FGM acoustic windows

The sonar dome structurally consists of an acoustic window, a cavity in the dome and a sonar array surface; a simplified two-dimensional sonar dome model (YU *et al.*, 2005; MAIDANIK, 1968; CRIGHTON *et al.*, 1992) composed of flat plates and parallel cavities can be adopted. In this model, the acoustic window is a flat plate made from FGM. Because the material properties of FGM change with thickness, the most efficient method to calculate the vibro-acoustic performance is to use discrete N -layer approximation materials. Each layer is an infinitely homogeneous and isotropic medium. The cavity between the sonar array and the acoustic window is idealized as a liquid layer. The sonar array surface is idealized as a plane with a surface acoustic reflection coefficient of R . Outside the sonar dome is a semi-infinite acoustic medium, which is affected by a stationary random TBL pulsating pressure and an incident plane wave. The theoretical analysis model and the x - z coordinate system of the sonar dome are shown in Fig. 1. The thickness of the acoustic window is H , the total number of layers is N , and the index is numbered from the outer surface ($z = 0$) to the inner surface ($z = H$) of the dome. The 1st layer, i.e., the upper interface, is called the top layer (symbol t). The N -th layer, i.e., the lower interface, is called the base (symbol b). The external water layer is the 0 layer. The sonar cavity water layer is the $N+1$ layer with height L . The time factor is $e^{-i\omega t}$.

Here, p_{in} is the incident plane wave with an incident angle θ_i ; p_r within a reflection angle θ_r and p_t with a refraction angle θ_t are the reflected wave and the sonar cavity acoustic field caused by the incident plane wave, respectively; and p_0 and p_{N+1} are the external acoustic field and the sonar cavity acoustic field caused by the TBL pulsating pressure F , respectively. According to the principle of linear superposition, the self-noise caused by the TBL pulsating pressure F and the transmission acoustic field caused by the external sound source can be calculated separately.

2.1. Theoretical model of the wavenumber-frequency response function of the turbulent self-noise excited by TBL pulsating pressure

Although the TBL pulsating pressure F is random in time and space, it is stable and fixed in the wavenumber-frequency space after statistical analysis. Therefore, the sonar self-noise caused by the TBL pulsating pressure F is calculated as the vibration-acoustic radiation in the wavenumber-frequency space. The double Fourier transform of the TBL pulsating pressure F on the acoustic window is:

$$F(x, z, t) = \frac{1}{(2\pi)^2} \iint_{-\infty}^{\infty} \tilde{F}(k, \omega, z) e^{i(kx - \omega t)} dk d\omega, \quad (1)$$

where \tilde{F} is the excitation force amplitude in the wavenumber space, k is the wavenumber in the x -direction, and ω is the angle frequency. For the medium from 0 to $N+1$, the velocity potential function must satisfy the scalar or vector wave equation:

$$\begin{aligned} \frac{\partial^2 \phi}{\partial x^2} + \frac{\partial^2 \phi}{\partial z^2} &= \frac{1}{c_L^2} \frac{\partial^2 \phi}{\partial t^2}, \\ \frac{\partial^2 \psi}{\partial x^2} + \frac{\partial^2 \psi}{\partial z^2} &= \frac{1}{c_T^2} \frac{\partial^2 \psi}{\partial t^2}, \end{aligned} \quad (2)$$

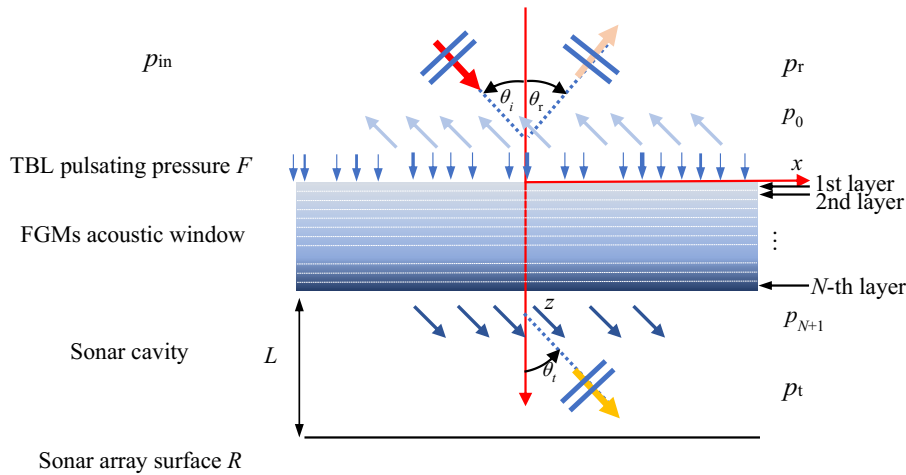


Fig. 1. Theoretical analysis model of the simplified two-dimensional sonar dome.

where c_L and c_T are the p -wave and s -wave velocities of the medium, respectively. The 0 layer and the $N+1$ layer satisfy only the scalar wave equation, and any layer of a FGM acoustic window must satisfy the scalar and vector wave equation. A double Fourier transform is applied to Eq. (2) to obtain the general solution form of the velocity potential of each layer in the wavenumber-frequency space:

$$\begin{cases} \tilde{\phi}_l(k, \omega, z) = A_l e^{-i\sqrt{k_{Ll}^2 - k^2}z} + B_l e^{i\sqrt{k_{Ll}^2 - k^2}z}, \\ \tilde{\psi}_l(k, \omega, z) = C_l e^{-i\sqrt{k_{Tl}^2 - k^2}z} + D_l e^{i\sqrt{k_{Tl}^2 - k^2}z}, \end{cases} \quad (3)$$

where l is any intermediate layer of an FGM acoustic window, k_{Ll} and k_{Tl} are the wavenumbers of the corresponding longitudinal wave and shear wave, respectively; A_l , B_l , C_l , and D_l are the general solution coefficients. Then, the general solution in layer 0 is $\tilde{\phi}_0(k, \omega, z) = A_0 e^{-i\sqrt{k_{L0}^2 - k^2}z}$. The general solution in layer $N+1$ needs to satisfy the reflection coefficient of the sonar array surface:

$$R = \frac{A_{N+1} e^{-i\sqrt{k_{LN+1}^2 - k^2}L}}{B_{N+1} e^{i\sqrt{k_{LN+1}^2 - k^2}L}}, \quad (4)$$

then

$$\begin{aligned} \tilde{\phi}_{N+1}(k, z) = & A_{N+1} \left(e^{i\sqrt{k_{LN+1}^2 - k^2}(z-h)} \right. \\ & \left. + \text{Re}^{2i\sqrt{k_{LN+1}^2 - k^2}L} e^{-i\sqrt{k_{LN+1}^2 - k^2}(z-h)} \right) \end{aligned}$$

is the general solution in layer $N+1$.

Here, k_{L0} and k_{LN+1} represent the wavenumbers of the longitudinal wave in layer 0 and layer $N+1$, respectively. According to the transfer matrix idea (SKELTON, JAMES, 1997; BREKHOVSKIKH, 2012), for any intermediate layer l :

$$\begin{bmatrix} \tilde{V}_x^l \\ \tilde{V}_z^l \\ \sigma_{zz}^l \\ \sigma_{zx}^l \end{bmatrix} = \mathbf{I} |z = z_{lT} \begin{bmatrix} A_l + B_l \\ A_l - B_l \\ C_l - D_l \\ C_l + D_l \end{bmatrix}, \quad (5)$$

$$\begin{bmatrix} \tilde{V}_x^{l-1} \\ \tilde{V}_z^{l-1} \\ \sigma_{zz}^{l-1} \\ \sigma_{zx}^{l-1} \end{bmatrix} = \mathbf{I} |z = z_{lB} \begin{bmatrix} A_l + B_l \\ A_l - B_l \\ C_l - D_l \\ C_l + D_l \end{bmatrix},$$

where \tilde{V}_x^l , \tilde{V}_z^l , σ_{zz}^l , σ_{zx}^l and \tilde{V}_x^{l-1} , \tilde{V}_z^{l-1} , σ_{zz}^{l-1} , σ_{zx}^{l-1} are the results of the double Fourier transforms of the velocity and stress components of the upper interface ($z = z_{lT}$) and the lower interface ($z = z_{lB}$) of the l layer, respectively. The appendix describes the construction of matrix \mathbf{I} . The boundary region of the elastic medium satisfies the continuous conditions of the

velocity and stress. Then, the relationship between the physical quantity of the lower interface of the N -th layer ($z = z_N$) and the upper interface of the first layer ($z = 0$) is as follows:

$$\begin{bmatrix} \tilde{V}_x^N \\ \tilde{V}_z^N \\ \sigma_{zz}^N \\ \sigma_{zx}^N \end{bmatrix} = T_N T_{N-1} \dots T_1 \begin{bmatrix} \tilde{V}_x^0 \\ \tilde{V}_z^0 \\ \sigma_{zz}^0 \\ \sigma_{zx}^0 \end{bmatrix} = F \begin{bmatrix} \tilde{V}_x^0 \\ \tilde{V}_z^0 \\ \sigma_{zz}^0 \\ \sigma_{zx}^0 \end{bmatrix}, \quad (6)$$

where $T_l = \mathbf{I} |z = z_{lT} \mathbf{I}^{-1} |z = z_{lB}$ and $F = T_N T_{N-1} \dots T_1$.

The conditions of the velocity and stress continuity are satisfied on the inner and outer boundaries of the acoustic window. After performing the double Fourier transform, the following conditions are satisfied:

$$\begin{cases} z = 0: & -i\rho_0\omega\tilde{\phi}_0 + \tilde{F}(k, \omega, z) = \tilde{\sigma}_{zz}^0, \\ & -\frac{\partial\tilde{\phi}_0}{\partial z} \Big|_{z=0} = \tilde{V}_z^0, \quad \tilde{\sigma}_{zx}^0 = 0, \\ z = h: & -i\rho_{N+1}\omega\tilde{\phi}_{N+1} = \tilde{\sigma}_{zz}^N, \\ & -\frac{\partial\tilde{\phi}_{N+1}}{\partial z} \Big|_{z=h} = \tilde{V}_z^N, \quad \tilde{\sigma}_{zx}^N = 0. \end{cases} \quad (7)$$

Through the six continuous conditions of Eq. (7) and transfer matrix Eq. (6), the unknown coefficients A_0 and A_{N+1} of the acoustic field inside and outside the acoustic window are obtained. The acoustic field outside and inside the acoustic window can be expressed as:

$$\begin{cases} \tilde{p}_0 = -i\rho_0\omega\tilde{\phi}_0 = -i\rho_0\omega A_0 e^{-i\sqrt{k_0^2 - k^2}z}, \\ \tilde{p}_{N+1} = -i\rho_{N+1}\omega\tilde{\phi}_{N+1} \\ = -iA_{N+1}\rho_{N+1}\omega e^{i\sqrt{k_{N+1}^2 - k^2}(z-h)} \\ \cdot \left(1 + \text{Re}^{2i\sqrt{k_{N+1}^2 - k^2}[L-2(z-h)]} \right), \end{cases} \quad (8)$$

where $k_0 = \frac{\omega}{c_0}$, $k_{N+1} = \frac{\omega}{c_{N+1}}$ and ρ_0 , c_0 , ρ_{N+1} , and c_{N+1} are the density and acoustic velocity of the 0-th and $(N+1)$ -th layers, respectively. Then, A_0 and A_{N+1} are:

$$\begin{aligned} A_0 = & i \frac{(C_{23} - PC_{33})\tilde{F}(k, \omega, z)}{\sqrt{k_0^2 - k^2}(C_{22} - PC_{32}) + \rho_0\omega(C_{23} - PC_{33})}, \\ A_{N+1} = & \frac{\sqrt{k_0^2 - k^2}C_{32}A_0 + C_{33}(\rho_0\omega A_0 - i\tilde{F}(k, \omega, z))}{\rho_{N+1}\omega \left(1 + \text{Re}^{2i\sqrt{k_{N+1}^2 - k^2}L} \right)}, \end{aligned} \quad (9)$$

where

$$\begin{cases} P = -\frac{\sqrt{k_{N+1}^2 - k^2} \left(1 - \text{Re}^{2i\sqrt{k_{N+1}^2 - k^2}L} \right)}{\rho_{N+1}\omega \left(1 + \text{Re}^{2i\sqrt{k_{N+1}^2 - k^2}L} \right)}, \\ C_{ij} = F_{ij} - \frac{F_{4j}F_{i1}}{F_{41}}. \end{cases} \quad (10)$$

According to Eq. (5), the acoustic pressure on the surface of the sonar array can be obtained at $z = h + L$. Then, the spatial filter function of the acoustic window $G(k, \omega)$ can be expressed as:

$$G(k, \omega) = -i\rho_{N+1}\omega\tilde{\phi}_{N+1}|_{z=h+L}. \quad (11)$$

Furthermore, the wavenumber-frequency spectrum of the TBL pulsating pressure needs to be obtained as the excitation source for evaluating the vibration-acoustic response of the structure. The Corcos model (CAIAZZO, DESMET, 2016; TANG *et al.*, 2020), the earliest and most widely used model of the TBL pulsating pressure, is adopted in this paper. The model reflects the migration characteristics of the TBL pulsating pressure. The cross-spectrum density can be obtained by integrating the Fourier transform:

$$\Phi_{ff}(k, \omega) = \frac{\Phi_{ff}(\omega)}{\pi^2} \frac{\alpha_1 \alpha_3 \omega^2}{U_c^2} \cdot \frac{1}{\left(\left(k_1 - \frac{\omega}{U_c} \right)^2 + \left(\alpha_1 \frac{\omega}{U_c} \right)^2 \right) \left(k_3^2 + \left(\alpha_3 \frac{\omega}{U_c} \right)^2 \right)}, \quad (12)$$

where $\alpha_1 = 0.09$, $\alpha_3 = 7\alpha_1$, and $U_c = 0.6U$.

Therefore, the wavenumber-frequency spectrum density function of the sonar array surface under the TBL pulsating pressure excitation can be obtained as:

$$\Phi_{pp}(\omega) = \int_{-\infty}^{\infty} \Phi_{ff}(k, \omega) |G(k, \omega)|^2 dk, \quad (13)$$

where $\Phi_{ff}(k, \omega)$ is the wavenumber-frequency spectrum of the TBL pulsating pressure and $G(k, \omega)$ is the spatial filter function of the sonar dome.

The frequency spectrum density function of the TBL pulsating pressure in the absence of an acoustic window is:

$$\Phi_{pp}^0(\omega) = \int_{-\infty}^{\infty} \Phi_{ff}(k, \omega) dk. \quad (14)$$

The turbulent self-noise reduction of an acoustic window can be defined as:

$$\text{NR} = 10 \log \frac{\Phi_{pp}(\omega)}{\Phi_{pp}^0(\omega)}. \quad (15)$$

The turbulent self-noise suppression effect of two kinds of acoustic windows is defined as the difference in the turbulent self-noise reduction:

$$\text{NR}' = \text{NR}_1 - \text{NR}_2. \quad (16)$$

2.2. Theoretical model of the STL for the sonar dome under plane wave excitation

With the plane wave as the excitation source, the sound field outside the FGM acoustic window is

the sum of the incident velocity potential function ϕ_i and the reflection potential function ϕ_r . The sound field outside the acoustic window obtained by the double Fourier transform is:

$$\begin{aligned} \tilde{\phi}_0(k, \omega, z) &= \tilde{\phi}_i(k, \omega, z) + \tilde{\phi}_r(k, \omega, z) \\ &= e^{i\sqrt{k_0^2 - k^2}z} + a_0 e^{-i\sqrt{k_0^2 - k^2}z}, \end{aligned} \quad (17)$$

where $k_0 = \frac{\omega}{c_0}$ and $k = k_0 \sin \theta$ with incident angle θ . The acoustic field inside the sonar cavity excited by the incident plane wave is similar to:

$$\begin{aligned} \tilde{\phi}_{n+1}(k, \omega, z) &= a_{N+1} \left(e^{i\sqrt{k_{N+1}^2 - k^2}(z-h)} \right. \\ &\quad \left. + \text{Re}^{2i\sqrt{k_{N+1}^2 - k^2}L} e^{-i\sqrt{k_{N+1}^2 - k^2}(z-h)} \right). \end{aligned} \quad (18)$$

The general solutions of the scalar potential function and vector potential function of the intermediate elastic gradient material are consistent with Eq. (3), similar to the matrix transfer relation. Combined with boundary conditions, the following is obtained:

$$\left\{ \begin{array}{l} z = 0: \quad -i\rho_0\omega\tilde{\phi}_0 = \tilde{\sigma}_{zz}^0, \\ \quad \quad \quad -\frac{\partial\tilde{\phi}_0}{\partial z}\Big|_{z=0} = \tilde{V}_z^0, \quad \tilde{\sigma}_{zx}^0 = 0, \\ z = h: \quad -i\rho_0\omega\tilde{\phi}_{n+1} = \tilde{\sigma}_{zz}^n, \\ \quad \quad \quad -\frac{\partial\tilde{\phi}_{n+1}}{\partial z}\Big|_{z=h} = \tilde{V}_z^n, \quad \tilde{\sigma}_{zx}^n = 0. \end{array} \right. \quad (19)$$

With the redundant components eliminated, the acoustic field inside and outside the acoustic window can be expressed as:

$$\left\{ \begin{array}{l} \tilde{p}_0 = -i\rho_0\omega\tilde{\phi}_0 = -i\rho_0\omega \left(e^{i\sqrt{k_0^2 - k^2}z} + a_0 e^{-i\sqrt{k_0^2 - k^2}z} \right), \\ \tilde{p}_{n+1} = -i\rho_{N+1}\omega\tilde{\phi}_{n+1} \\ \quad = -ia_{N+1}\rho_0\omega \left(e^{i\sqrt{k_{N+1}^2 - k^2}(z-h)} \right. \\ \quad \quad \left. + \text{Re}^{2i\sqrt{k_{N+1}^2 - k^2}L} e^{-i\sqrt{k_{N+1}^2 - k^2}(z-h)} \right), \end{array} \right. \quad (20)$$

where a_0 and a_{N+1} are given as:

$$\begin{aligned} a_0 &= \frac{\sqrt{k_0^2 - k^2} (C_{22} - pC_{32}) - \rho_0\omega (C_{23} - pC_{33})}{\sqrt{k_0^2 - k^2} (C_{22} - pC_{32}) + \rho_0\omega (C_{23} - pC_{33})}, \\ a_{N+1} &= \frac{\sqrt{k_0^2 - k^2} C_{32} (1 - a_0) + \rho_0\omega C_{33} (1 + a_0)}{\rho_{n+1}\omega \left(1 + \text{Re}^{2i\sqrt{k_{N+1}^2 - k^2}L} \right)}. \end{aligned} \quad (21)$$

The matrix \mathbf{C} is consistent with Eq. (10), and

$$p = -\frac{\sqrt{k_{N+1}^2 - k^2} \left(1 - \text{Re}^{2i\sqrt{k_{N+1}^2 - k^2}L} \right)}{\rho_{n+1}\omega \left(1 + \text{Re}^{2i\sqrt{k_{N+1}^2 - k^2}L} \right)}. \quad (22)$$

To evaluate the sound transmission performance of FGM acoustic windows, the STL (insertion loss) should be calculated. When acoustic windows do not exist, the acoustic pressure at the $z = h$ position should be:

$$\tilde{p}'_{N+1} = -i\omega\rho_0 \left(e^{i\sqrt{k_{N+1}^2 - k^2}h} + \text{Re} e^{i\sqrt{k_{N+1}^2 - k^2}(h+2L)} \right). \quad (23)$$

The STL is:

$$\text{STL} = -20 \log \left(\left| \frac{\tilde{p}_{N+1}}{\tilde{p}'_{N+1}} \right| \right). \quad (24)$$

2.3. Verification of the theoretical model of the wave-frequency response function of the turbulent self-noise and STL for FGM acoustic windows

The turbulent self-noise caused by the TBL pulsating pressure can be simplified to the acoustic field in the sonar cavity with the acoustic window excited by a point force. The STL of the acoustic window under the plane wave excitation is calculated in the usual way. A linear FRP-rubber FGM acoustic window with $N = 50$ is selected to verify the theoretical results. The material properties setting of every layer are shown in Eq. (28). The material parameters of the FRP and rubber are shown in Table 2.

In Fig. 2, the depth of the sonar cavity is 0.5 m, and the reflection coefficient of the sonar array surface is 0.3. The thickness of the perfectly matched layer (PML) is 0.1 m, and H_1 , H_2 , L_1 , and L_2 are 0.5, 0.3, 100, and 0.5 m, respectively. The theoretical and simulation results of the STL of the linear FRP-rubber FGM acoustic window are shown in Fig. 3.

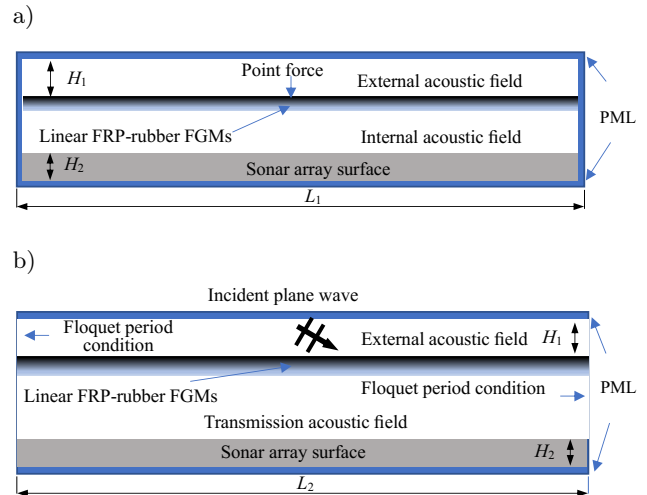


Fig. 2. Calculation setting of the linear FRP-rubber FGM acoustic window in COMSOL Multiphysics software: a) wave-frequency response function; b) STL.

For the acoustic field in the sonar cavity with the linear FRP-rubber FGM acoustic window excited by a point force, the wavenumber-frequency spectrum results of the acoustic pressure on the sonar array surface are selected for comparison, which is shown in Fig. 4.

The results in Figs. 3 and 4 show that the simulation and theoretical results are in complete agreement, both in the calculation results of the STL and in the wavenumber-frequency spectrum results of the acoustic field in the sonar cavity for the linear FRP-rubber FGM acoustic window. Therefore, the accuracy of the theoretical model of the wavenumber frequency response function of the turbulent self-noise and STL are verified for the sonar dome.

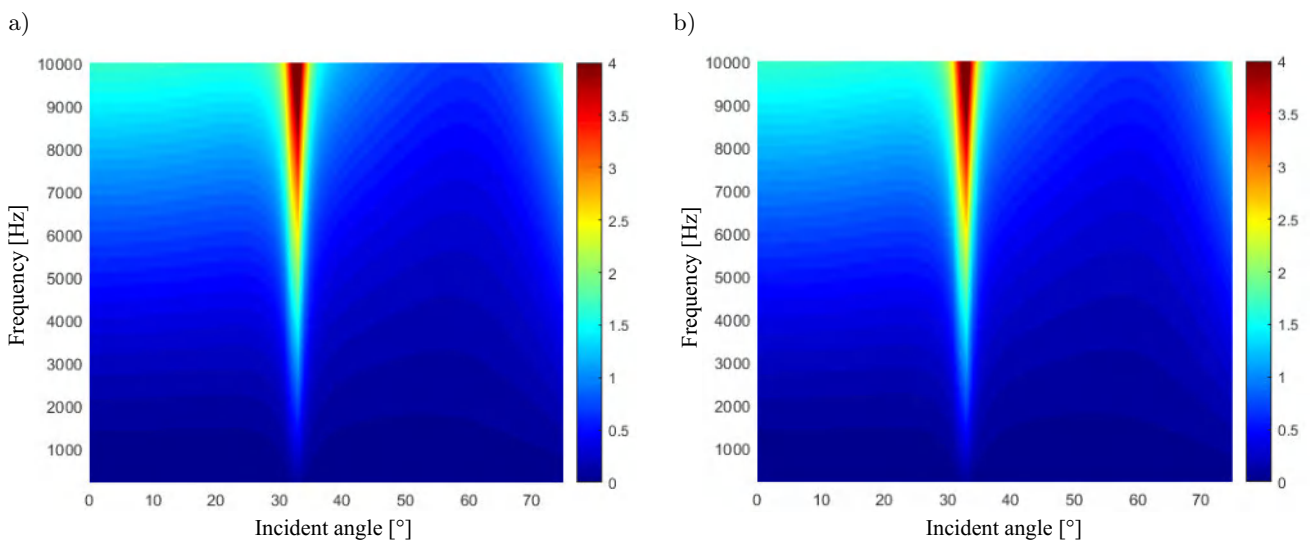


Fig. 3. Comparison results of the STL of the linear FRP-rubber FGM acoustic window: a) theoretical result; b) simulation result.

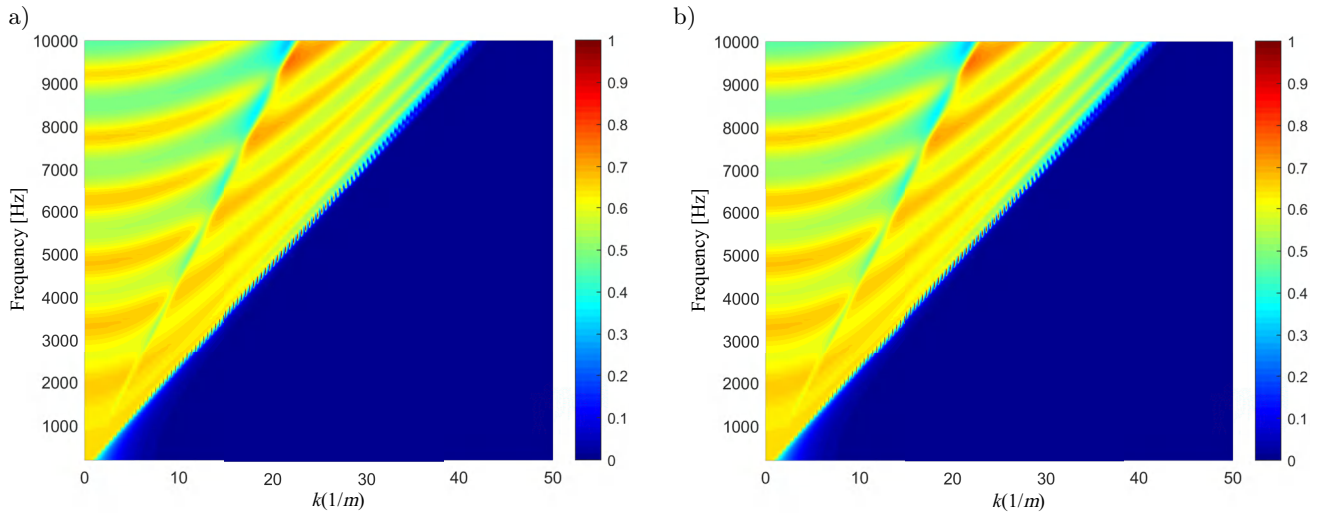


Fig. 4. Comparison results of the wavenumber-frequency spectrum of the acoustic pressure on the sonar array surface in the sonar cavity: a) theoretical result; b) simulation result.

3. Internal gradient optimization design for FGM acoustic windows based on turbulent self-noise suppression and the sound transmission performance

The material properties of FGM are mainly determined by the substrate, top material and an internal gradient form. Different forms of the internal gradi-

ents result in different material properties. Therefore, by studying the internal gradient of the FGM, an optimization method of internal gradients that can design an optimized FGM acoustic window with better turbulent self-noise suppression and sound transmission performance is proposed in this paper (Fig. 5). The existing gradient design mainly includes parabolic functions, power-law functions and exponential functions, but none of them offer a favorable

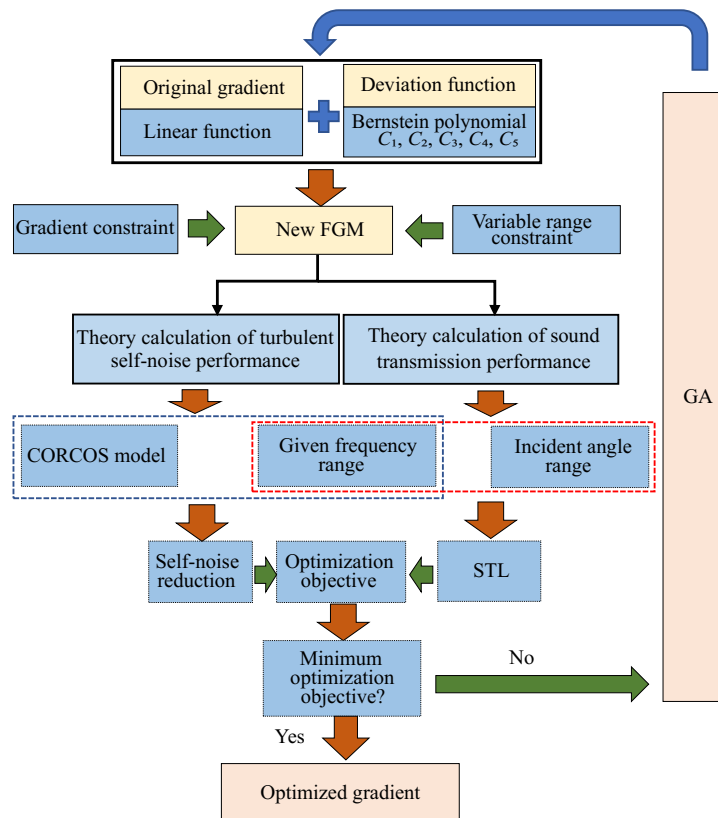


Fig. 5. Overall flow chart of the gradient optimization design method.

function change space. Therefore, in the optimization method, the space layout of the gradient change is readjusted by introducing a deviation function term expressed by the Bernstein polynomial on the basis of the original linear gradient. In addition, upon combining the GA and taking the monotonic gradient as the constraint condition, the results of five optimization variables carried by the Bernstein polynomial when the optimization objective is minimized are obtained in the optimization method by iterating the gradient function. The optimization objective is expressed as the STL, the turbulent self-noise reduction or a weighting function of the STL and turbulent self-noise reduction of FGM acoustic windows.

3.1. Internal gradient function design of FGM acoustic windows

The existing internal gradient change functions of FGMs mainly include parabolic, power-law and exponential functions. These functions have a small adjustment range for the gradient change space, and only convex or concave functions can be selected, which limits the gradient change. Therefore, a deviation function expressed by the Bernstein polynomial is introduced on the basis of the original linear gradient function. By adjusting different parameters in the Bernstein polynomials, the overall coverage of the space range of the optimized gradient is achieved to seek the overall optimal solution (Fig. 6).

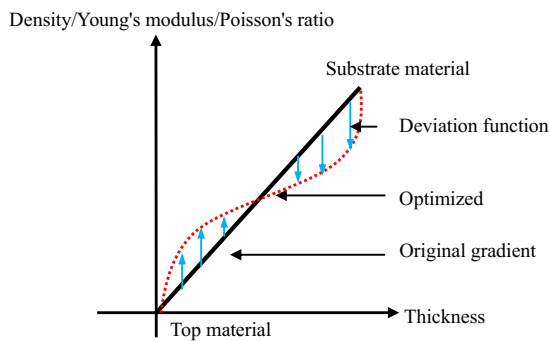


Fig. 6. Optimization gradient design schematic.

The deviation function expressed by the Bernstein polynomial is shown in Eq. (25):

$$\Delta z = \sum_{i=0}^M C_i s^i * (1 - s)^{(M-i)}. \tag{25}$$

The optimization results often depend on the order of the Bernstein polynomials. The more orders that are selected, the finer and better the results that may be obtained. However, the time required for the optimization calculation increases exponentially. Moreover, unsatisfactory optimization results become more likely. Therefore, $M = 5$ is selected to obtain better optimization results. The boundary of $i = 0$ is omitted,

ensuring that the properties of the substrate material and the top material remain unchanged in the optimization process. The deviation function is shown in Eq. (26):

$$\Delta E = (E_t - E_b) \sum_{i=1}^5 C_i \left(\frac{h}{H}\right)^i \left(1 - \frac{h}{H}\right)^{(5-i)}. \tag{26}$$

The gradient function is shown as:

$$E = \frac{E_t - E_b}{H} h + E_b + \Delta E. \tag{27}$$

The specific gradient functions of the density, Young's modulus and Poisson's ratio are:

$$\left\{ \begin{aligned} \rho &= \frac{\rho_t - \rho_b}{H} h + \rho_b \\ &+ (\rho_t - \rho_b) \sum_{i=1}^5 C_i \left(\frac{h}{H}\right)^i \left(1 - \frac{h}{H}\right)^{(5-i)}, \\ E &= \frac{E_t - E_b}{H} h + E_b \\ &+ (E_t - E_b) \sum_{i=1}^5 C_i \left(\frac{h}{H}\right)^i \left(1 - \frac{h}{H}\right)^{(5-i)}, \\ \sigma &= \frac{\sigma_t - \sigma_b}{H} h + \sigma_b \\ &+ (\sigma_t - \sigma_b) \sum_{i=1}^5 C_i \left(\frac{h}{H}\right)^i \left(1 - \frac{h}{H}\right)^{(5-i)}. \end{aligned} \right. \tag{28}$$

3.2. Optimization algorithm, constraints and variable range

To obtain the global optimal solution, a GA is used in this paper. The GA is a kind of stochastic global search and optimization method that simulates the natural selection and genetic mechanism of Darwin evolution. The GA is essentially an efficient, parallel, and global searching method, that can automatically acquire and accumulate information about the search space and adaptive control of the search process to obtain the best solution (Fig. 7). When enough initial random samples are satisfied, the globally unique optimal solution can be obtained.

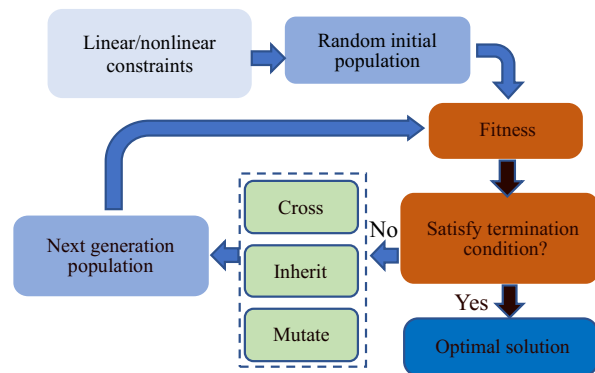


Fig. 7. Optimization flow of the GA.

The termination conditions include population genetic algebra and tolerance. Most of the existing FGMs meet the monotonic variation trend. Therefore, a non-linear gradient constraint is applied to the GA:

$$\frac{dE}{dh} \geq 0. \tag{29}$$

According to Eq. (28), the gradient function in the optimization process is regulated by five optimization variables. Table 1 shows the initial value and variation range of each optimization variable.

Table 1. Range setting of the optimization variables in the gradient function.

| Optimization variables | Initial value | Minimum value | Maximum value |
|------------------------|---------------|---------------|---------------|
| C_1 | 0 | -25 | 25 |
| C_2 | 0 | -25 | 25 |
| C_3 | 0 | -25 | 25 |
| C_4 | 0 | -25 | 25 |
| C_5 | 0 | -25 | 25 |

3.3. Optimization objective function

The design of FGM acoustic windows should not only consider the effect of turbulent self-noise suppression in sonar cavities but also meet the requirement of sound transmission performance. Therefore, the optimization objective function should be designed considering turbulent self-noise reduction and STL at the same time. In the engineering design of sonar acoustic windows, the STL in the incident angle range of 0–75° should be as small as possible, and the turbulent self-noise reduction should be as high as possible. Therefore, the objective function of optimization is shown as:

$$\left\{ \begin{array}{l} F_1 = 10 \log \left(\sum_{\theta=\theta_i}^{\theta_j} \sum_{f=f_i}^{f_j} 10^{\text{TL}(f,\theta)} \right), \\ \sum_{f=f_i}^{f_j} (\text{NR}(f)) = C, \\ F_2 = \sum_{f=f_i}^{f_j} (\text{NR}(f)), \\ 10 \log \left(\sum_{\theta=\theta_i}^{\theta_j} \sum_{f=f_i}^{f_j} 10^{\text{TL}(f,\theta)} \right) = C, \\ F_3 = \frac{10 \log \left(\sum_{\theta=\theta_i}^{\theta_j} \sum_{f=f_i}^{f_j} 10^{\text{TL}(f,\theta)} \right)}{\sum_{f=f_i}^{f_j} (\text{NR}(f))}, \end{array} \right. \tag{30}$$

where f_i is the initial frequency, f_j is the termination frequency, θ_i is the initial optimization angle, θ_j is the end angle, and C is a constant; TL is the transmission loss in the optimal frequency range ($f_i - f_j$) and angle range ($\theta_i - \theta_j$); F_i ($i = 1, 2, 3$) is the objective function of the optimization. F_1 and F_2 can achieve the optimal sound transmission performance or turbulent self-noise suppression performance for FGM acoustic windows, respectively, when the turbulent self-noise suppression performance or sound transmission performance remains unchanged. The minimum optimization objective function F_3 can achieve the effect of the maximum turbulent self-noise reduction and minimum the STL for FGM acoustic windows.

4. Optimization results of the internal gradient of FGM acoustic windows

According to the designed internal gradient optimization method of FGM acoustic windows, the existing FRP-rubber FGM acoustic window is optimized. The materials and properties involved are shown in Table 2.

Here, the optimization results of the internal gradient design for the FRP-rubber FGM acoustic window are presented with $H = 3$ cm, $L = 0.5$ m, and $R = 0.3$.

Moreover, the theoretical model of the turbulent self-noise suppression and sound transmission characteristics of the sonar dome proposed in this paper is solved by discretizing the continuous medium into a layered medium of the acoustic window. Differences in layering affect the calculation accuracy of the theoretical results. Figure 8 shows the layered N convergence calculation results with respect to the turbulent self-noise reduction and STL of the linear FRP-rubber FGM. With increasing N , these parameters gradually converge. To ensure the calculation efficiency and accuracy, the ratio of the corresponding wavelength to the thickness of a single layer is selected to be above 250, corresponding to $N = 50$ at $f = 10$ kHz.

4.1. Optimization of sound transmission performance with turbulent self-noise suppression performance unchanged

According to the optimization method proposed in this paper, the STL of the FRP-rubber FGM acoustic window is taken as the optimization objective function to carry out the calculation when the turbulent self-noise reduction remains unchanged, as shown

Table 2. Materials and properties.

| Material | Density [kg/m ³] | Young's modulus [N/m ²] | Poisson's ratio | Longitudinal wave velocity [m/s] | Shear wave velocity [m/s] | Loss factor |
|----------|------------------------------|-------------------------------------|-----------------|----------------------------------|---------------------------|-------------|
| FRP | 1620 | 1.74e10 | 0.2 | 3455 | 2116 | 0.03 |
| Rubber | 1030 | 1.67e9 | 0.33 | 1550 | 781 | 0.3 |

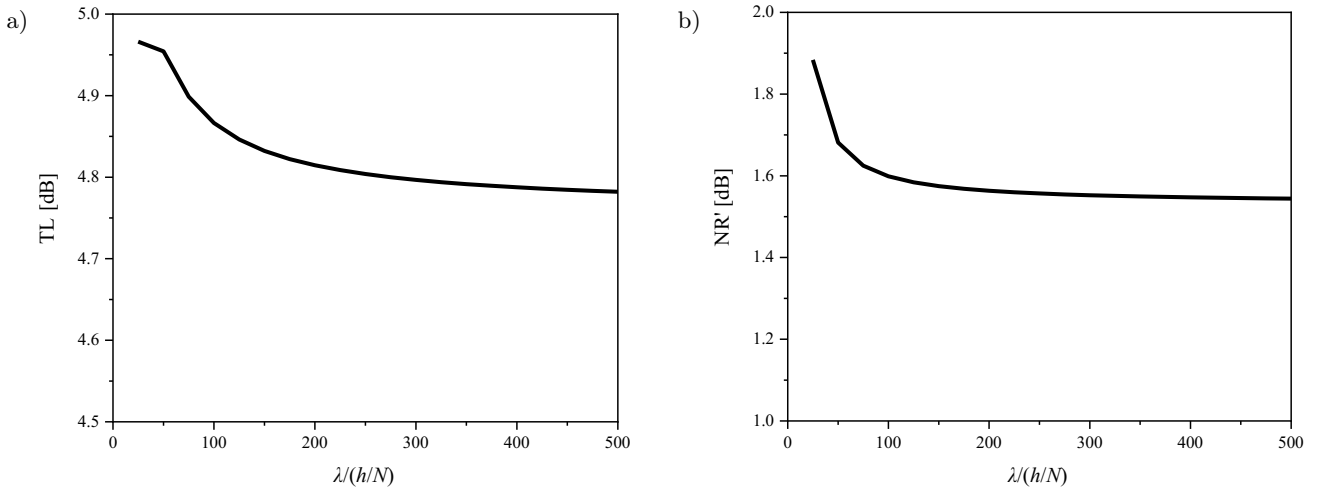


Fig. 8. Convergence relationship with the wavelength to monolayer thickness ratio: a) STL; b) turbulent self-noise reduction.

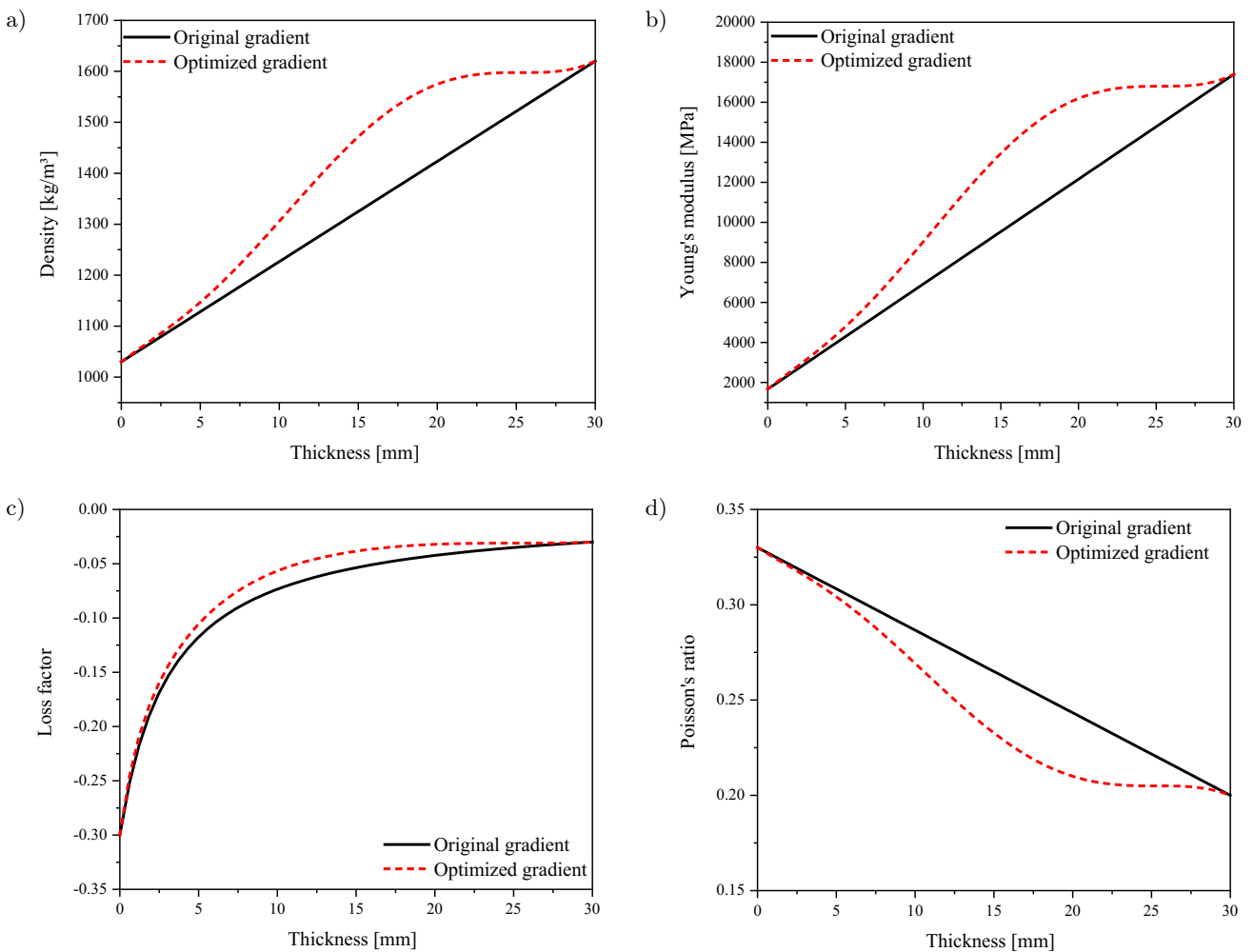


Fig. 9. Comparison results of the FRP-rubber FGM acoustic window before and after the sound transmission performance optimization: a) density; b) Young's modulus; c) loss factor; d) Poisson's ratio.

in Eq. (30)₁. The incident angle range of the STL optimization is selected to be 0–75° with a step size of 1°. The optimization frequency range of the STL and

turbulent self-noise is selected to be 0.2–10 kHz with a step of 0.1 kHz. The main frequency of the calculation computer is 4.5 GHz, the memory is 64 GB,

and the total optimization computing time is 3.45 days. The optimized parameters are shown in Table 3.

Table 3. Calculation results of the gradient optimization variables of the FRP-rubber FGM acoustic window with sound transmission performance optimization.

| Optimization variables | C_1 | C_2 | C_3 | C_4 | C_5 |
|------------------------|--------|--------|--------|---------|--------|
| Optimization results | 0.2345 | 6.4928 | 9.8355 | -0.8583 | 0.1961 |

The comparison results of the density, Young’s modulus, the loss factor, and Poisson’s ratio of the FRP-rubber FGM acoustic window before and after the sound transmission performance optimization are shown in Fig. 9.

The comparison results of the self-noise suppression and the sound transmission performance of the FRP-rubber FGM acoustic window before and after

the sound transmission performance optimization are shown in Fig. 10.

Figure 10 shows that the optimized FGM acoustic window is superior to the initial linear FGM acoustic window in the sound transmission performance when the turbulent self-noise suppression performance remains unchanged. From Fig. 10b, the peak of the STL of the optimized FGM acoustic window compared to that of the initial linear FGM acoustic window decreases by approximately 0.8 dB at $f = 10$ kHz, which corresponds to an 17% increase in the sound transmission performance. Moreover, the optimized effect is not ideal at lower incident angles because the optimization objective function F_1 is the total STL of the optimization angle range without considering every angle optimization effect separately. The value and position changes of the STL peak before and after optimization, and whether it is benefit for the sound transmission performance are explained in Sec. 5.

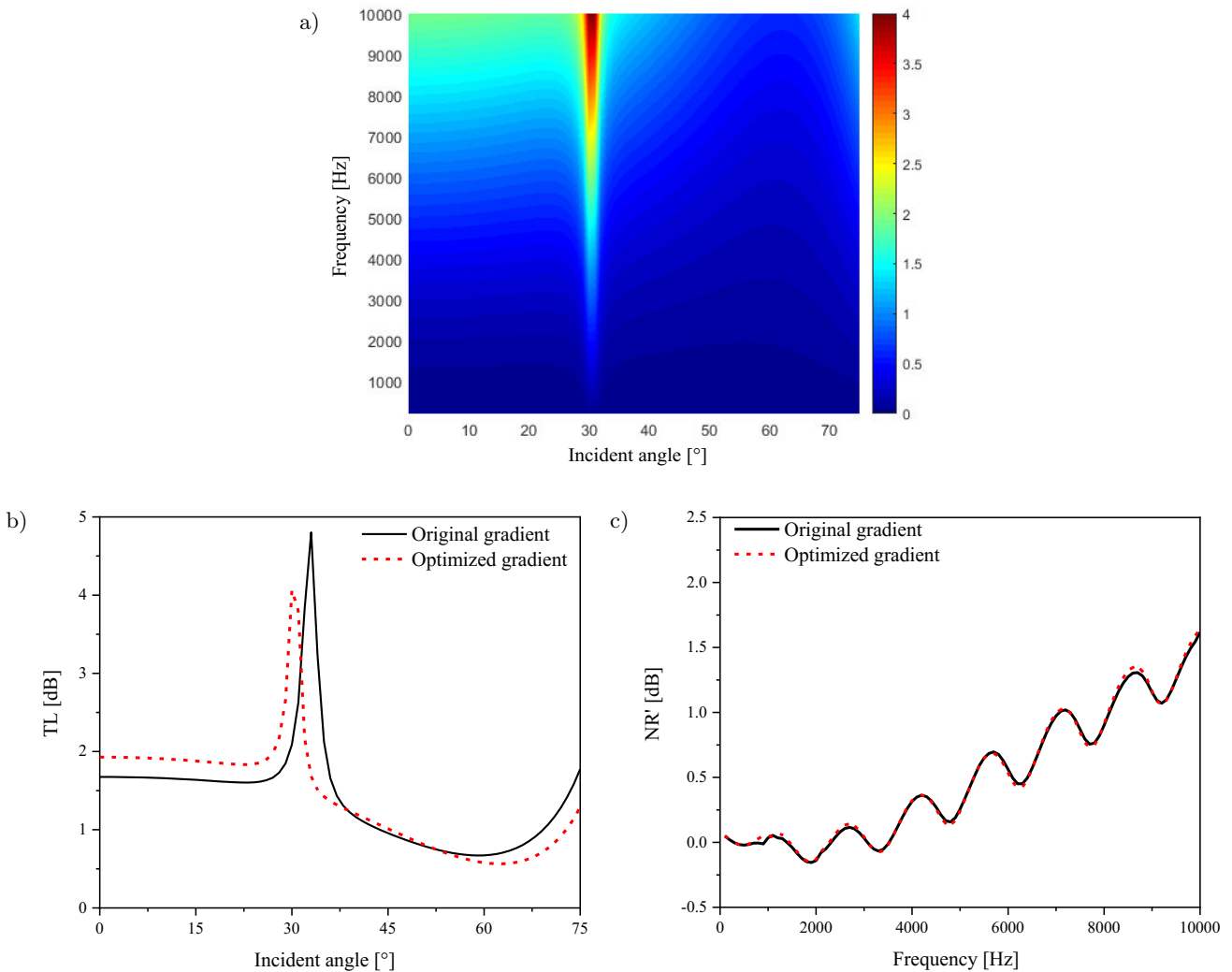


Fig. 10. Comparison results of the turbulent self-noise reduction and STL of the FRP-rubber FGM acoustic window before and after the sound transmission performance optimization: a) STL of the optimized FGM; b) STL at $f = 10$ kHz; c) comparison of the turbulent self-noise reduction.

4.2. Optimization of the turbulent self-noise suppression performance while maintaining the sound transmission performance

According to the optimization method proposed in this paper, the turbulent self-noise reduction of the FRP-rubber FGM acoustic window is taken as the optimization objective function to carry out the calculation when the STL remains unchanged, as shown in Eq. (30)₂. The angle and frequency range of the sound transmission performance optimization and the frequency range of the turbulent self-noise suppression optimization are consistent with the above. The computer parameters are consistent with those above, and the total optimization computing time is 3.95 days. The optimized parameters are shown in Table 4.

The comparison results of the density, Young's modulus, the loss factor and Poisson's ratio of the FRP-rubber FGM acoustic window before and after the turbulent self-noise suppression performance optimization are shown in Fig. 11.

The comparison results of the turbulent self-noise suppression and sound transmission performance of

Table 4. Calculation results of the gradient optimization variables of the FRP-rubber FGM acoustic window for turbulent self-noise suppression performance optimization.

| Optimization variables | C_1 | C_2 | C_3 | C_4 | C_5 |
|------------------------|--------|--------|--------|---------|---------|
| Optimization results | 0.9679 | 4.4406 | 0.9231 | -5.1370 | -0.9862 |

the FRP-rubber FGM acoustic window before and after the turbulent self-noise suppression performance optimization are shown in Fig. 12.

Figure 12 shows that the optimized FGM acoustic window is superior to the initial linear FGM acoustic window in turbulent self-noise suppression performance when the sound transmission performance remains unchanged. From Fig. 12c, the turbulent self-noise reduction of the optimized FGM acoustic window is significantly higher than that of the initial FGM acoustic window. Moreover, the self-noise reduction gradually increases with increasing frequency, and the highest self-noise reduction is approximately 0.4 dB at $f = 10$ kHz, which corresponds to a 25% improvement in the turbulent self-noise suppression performance.

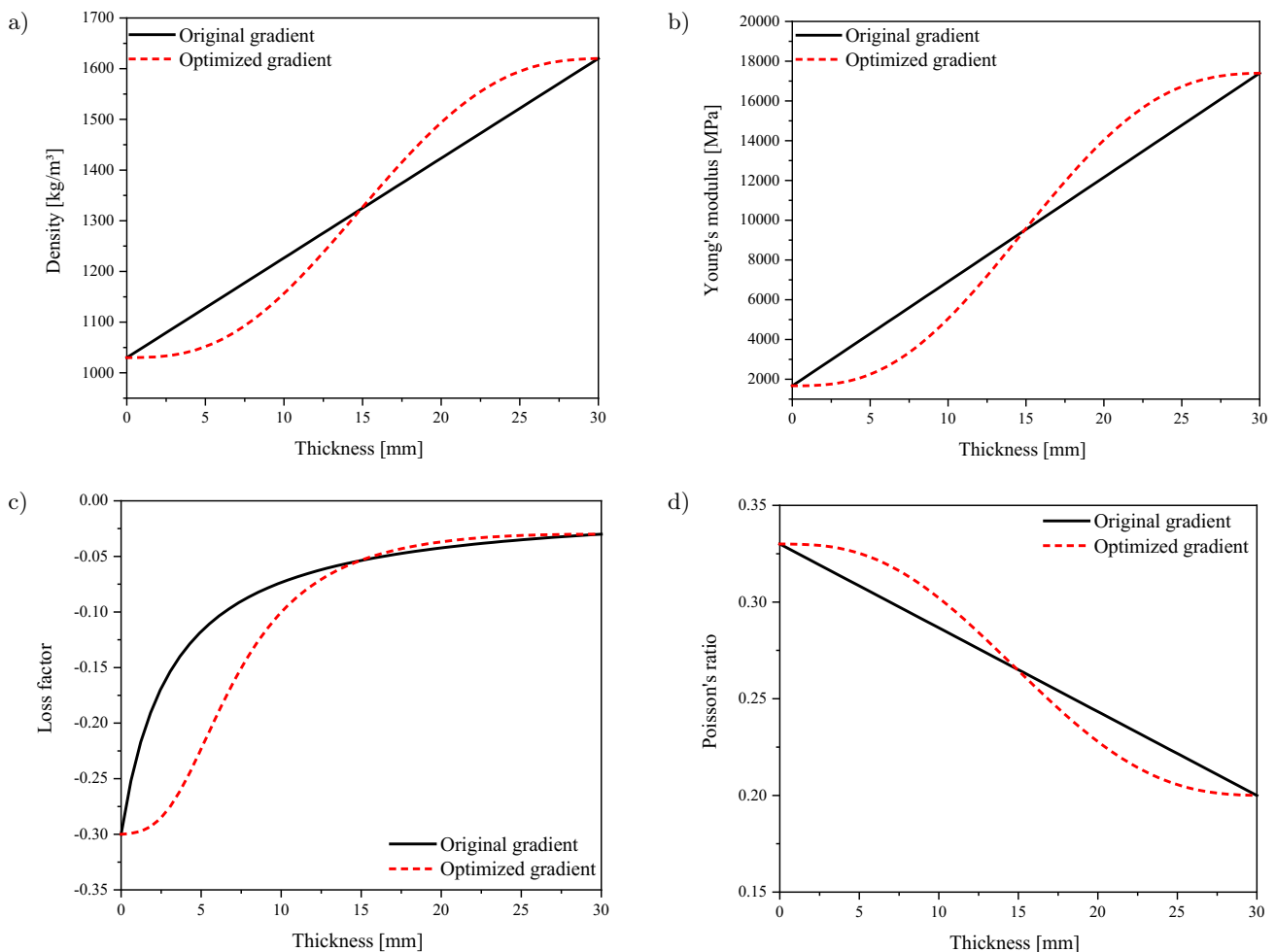


Fig. 11. Comparison results of the FRP-rubber FGM acoustic window before and after the turbulent self-noise suppression performance optimization: a) density; b) Young's modulus; c) loss factor; d) Poisson's ratio.

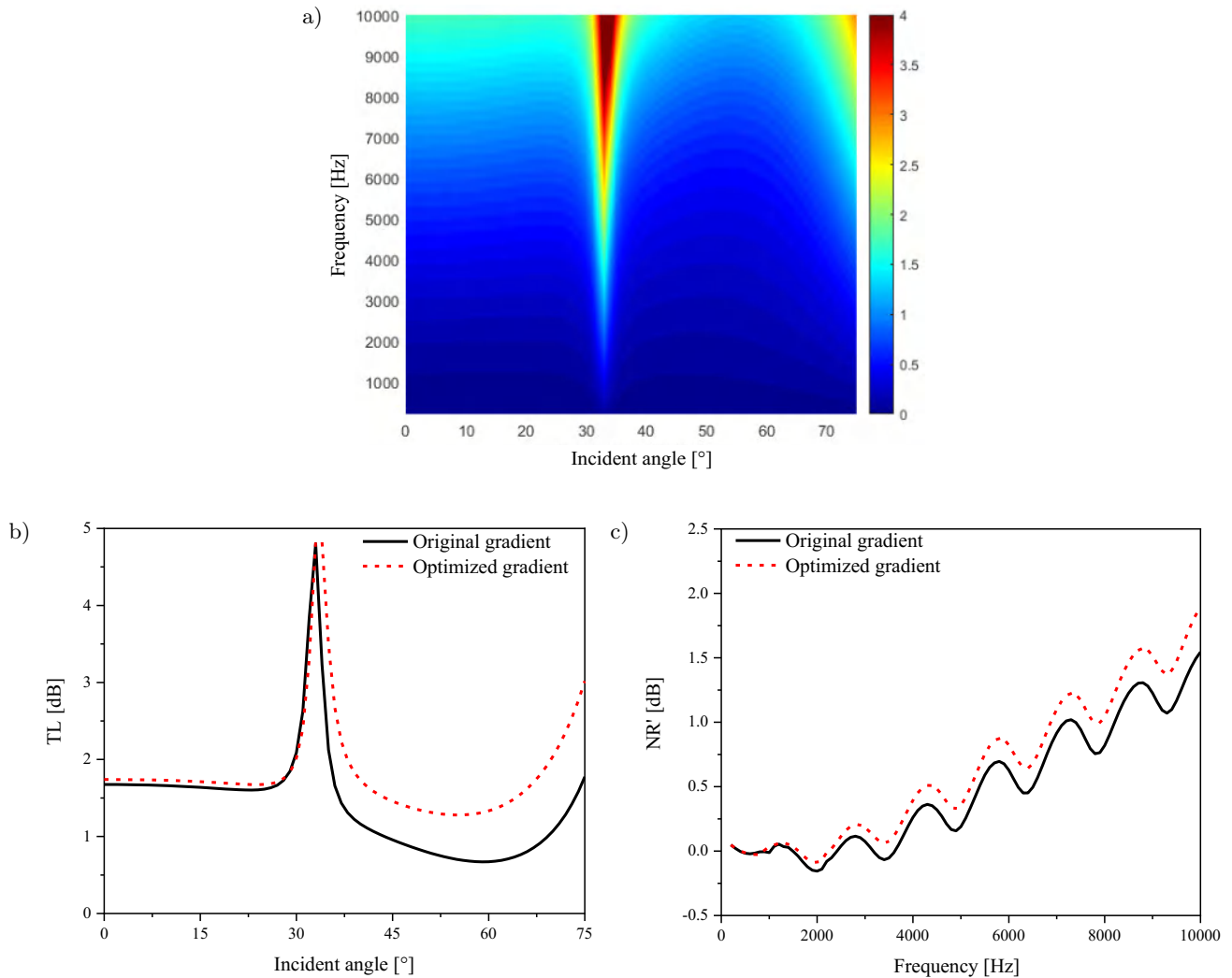


Fig. 12. Comparison results of the turbulent self-noise reduction and STL of the FRP-rubber FGM acoustic window before and after the turbulent self-noise suppression performance optimization: a) STL of the optimized FGM; b) STL at $f = 10$ kHz; c) comparison of the turbulent self-noise reduction.

In addition, it can also be seen that there is a certain difference for the STL in the higher incident angle range before and after optimization. The reason is that only the total TL is considered in the optimization objective function F_2 , which is basically unchanged before and after optimization. The STL at higher incident angles is so small that it makes little contribution to the total STL, which is ignored by the optimization method.

4.3. Optimization of turbulent self-noise suppression and sound transmission performance

According to the optimization method proposed in this paper, the turbulent self-noise reduction and STL of the FRP-rubber FGM acoustic window are taken as the optimization objective function to carry out the calculation, as shown in Eq. (30)₃. The angle and frequency range of the sound transmission performance

optimization and the frequency range of the turbulent self-noise suppression optimization are consistent with the above. The computer parameters are consistent with those above, and the total optimization computing time is 6.75 days. The optimized parameters are shown in Table 5.

Table 5. Calculation results of the gradient optimization variables of the FRP-rubber FGM acoustic window with turbulent self-noise suppression and sound transmission performance.

| Optimization variables | C_1 | C_2 | C_3 | C_4 | C_5 |
|------------------------|--------|--------|---------|--------|---------|
| Optimization results | 0.8339 | 5.0562 | 12.2603 | 0.4194 | -1.0000 |

The comparison results of the density, Young's modulus, the loss factor and Poisson's ratio of the FRP-rubber FGM acoustic window before and after optimization are shown in Fig. 13.

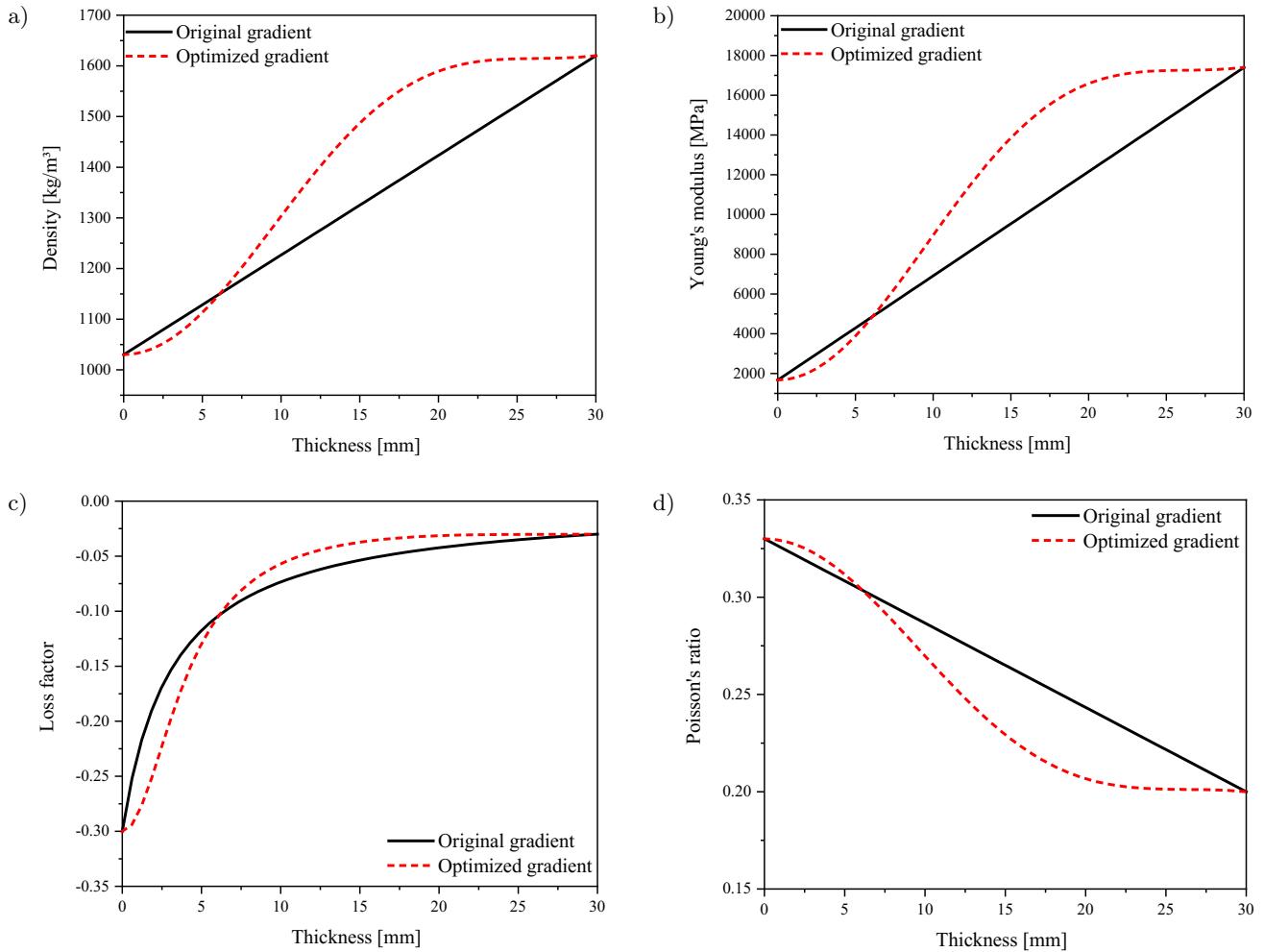


Fig. 13. Comparison results of the FRP-rubber FGM acoustic window before and after the turbulent self-noise suppression and sound transmission performance optimization: a) density; b) Young's modulus; c) loss factor; d) Poisson's ratio.

The comparison results of the self-noise suppression and sound transmission performance of the FRP-rubber FGM acoustic window before and after optimization are shown in Fig. 14.

Figure 14 shows that the optimized FGM acoustic window is superior to the initial linear FGM acoustic window in both turbulent self-noise suppression and sound transmission performance. From Fig. 14b, the peak value of the STL of the optimized FGM acoustic window compared to that of the initial linear FGM acoustic window decreases by approximately 0.6 dB at $f = 10$ kHz, which corresponds to a 12% increase in the sound transmission performance. Figure 14c shows that the turbulent self-noise reduction of the optimized FGM acoustic window is significantly higher than that of the initial FGM acoustic window. Moreover, the self-noise reduction gradually increases with increasing frequency, and the highest self-noise reduction is approximately 0.2 dB at $f = 10$ kHz, which corresponds to a 13% improvement in the turbulent self-noise suppression performance.

5. Analysis of the sound transmission and turbulent self-noise suppression characteristics of FGM acoustic windows before and after optimization

Section 4 indicates that the sound transmission and self-noise suppression performances of the optimized FGM acoustic window is improved. To analyze the reasons, mechanism studies of the sound transmission and turbulent self-noise suppression characteristics of the FRP-rubber FGM acoustic window are carried out.

5.1. Sound transmission analysis of FGM acoustic windows before and after optimization

To analyze the sound transmission mechanism of FGM acoustic windows, the dispersion curve of FRP is calculated based on the spectral method (KARPFINGER *et al.*, 2008; 2010). The critical angles of various elastic waves under Snell's law are calculated based on

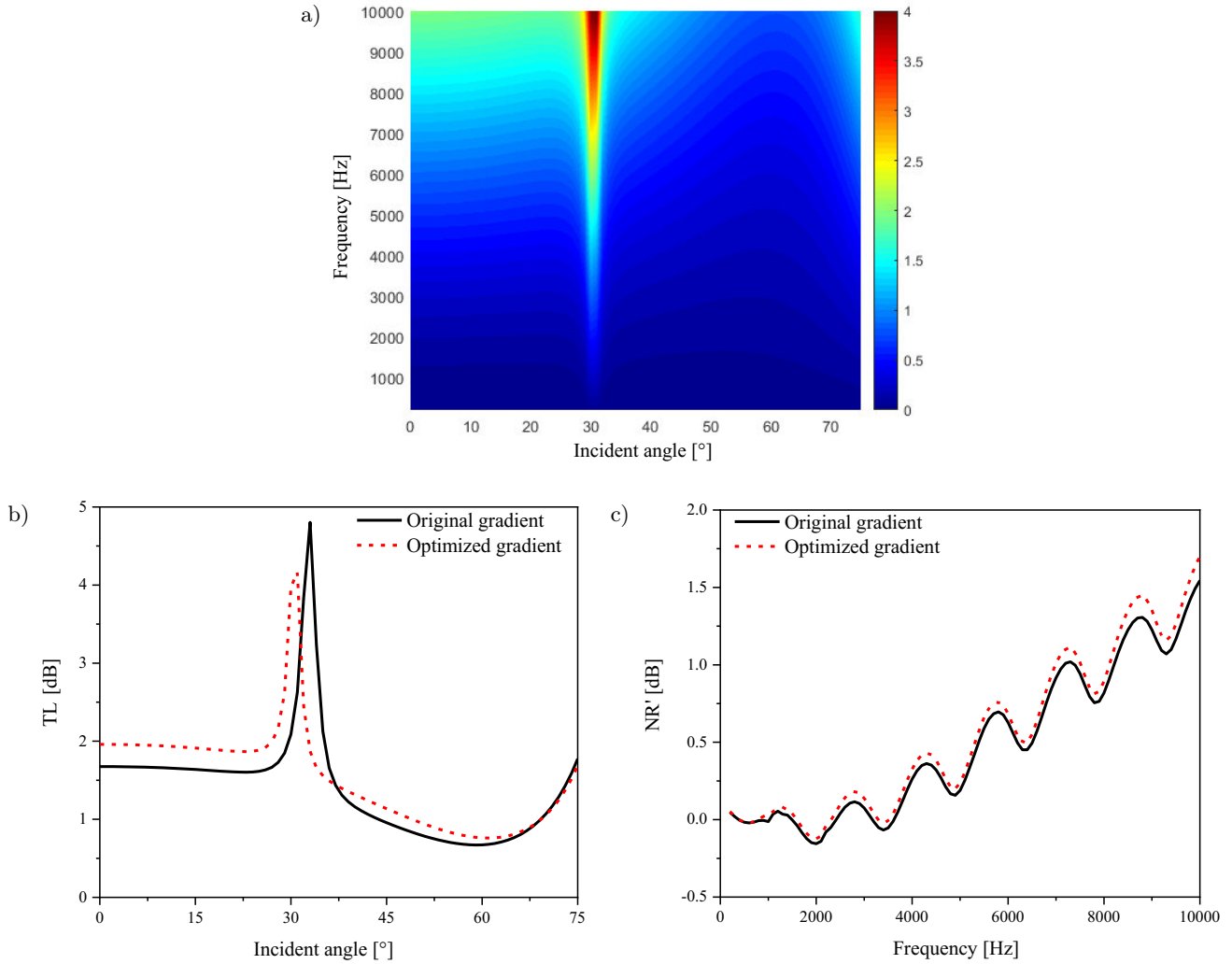


Fig. 14. Comparison results of the turbulent self-noise reduction and STL of the FRP-rubber FGM acoustic window before and after the turbulent self-noise suppression and sound transmission performance optimization: a) STL of the optimized FGM; b) STL at $f = 10$ kHz; c) comparison of the turbulent self-noise reduction.

the obtained phase velocity dispersion curve, as shown in Fig. 15.

The vertical narrow fringe with a strong STL appears near the critical angle (28°) of the total internal reflection of the longitudinal wave in the FRP. The longitudinal wave formed by the refraction of the incident wave propagates along the surface of the plate, and the critical angle corresponds to the velocity of the longitudinal wave. The curved fringe on the left of the critical angle is caused by the high-order Lamb surface wave in the elastic plate, of which the trajectory can be predicted according to the phase velocity of the high-order elastic wave. The internal material properties of the functional gradient materials gradually change along the plate thickness. The internal material properties of the functional gradient materials can be approximated as a single material by gradual changes along the plate thickness direction (BREKHOVSKIKH, 2012). The equivalent Young's modulus E_e is:

$$E_e = \sum_{i=1}^N E_i h/H. \quad (31)$$

The other equivalent acoustic parameters are also calculated based on Eq. (31). Then, according to Eq. (31) and Snell's law, the equivalent longitudinal wave velocity $c_{Le}^2 = \frac{E_e}{(1-\sigma_e^2)\rho_e}$ and the estimated critical angle $\theta = \arcsin\left(\frac{c}{c_{Le}}\right)$ of the FGM acoustic windows before and after the optimization are shown in Table 6.

As shown in Table 6, the critical angle predicted by the equivalent longitudinal wave velocity is basically consistent with the actual critical angle, indicating that the peak value position of STL is derived from the critical angle of the equivalent longitudinal wave, which can be predicted precisely. To analyze the peak values of the STL of the FGM acoustic windows before and after optimization, thin-plate theory ignoring secondary factors is selected for analysis (BREKHOVSKIKH, 2012). When the acoustic wave is

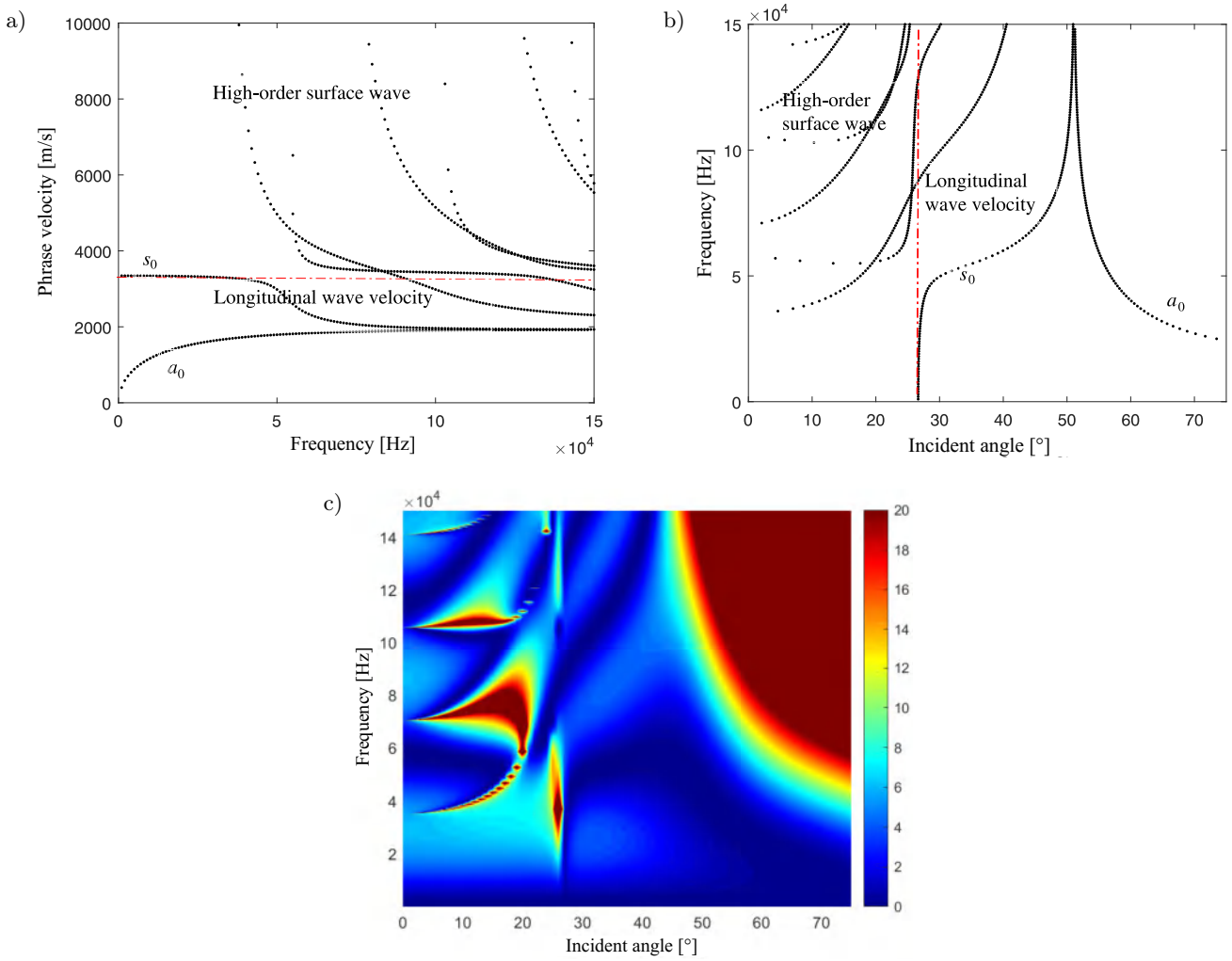


Fig. 15. Dispersion characteristics and STL results of the FRP: a) dispersion curve; b) critical angle of elastic waves; c) angle-frequency spectrum of STL.

Table 6. Equivalent longitudinal wave velocity and the estimated critical angle of the FGM acoustic windows before and after optimization.

| | Equivalent longitudinal wave velocity c_{Le} [m/s] | Estimated critical angle θ [°] | Actual critical angle [°] |
|---|--|---------------------------------------|---------------------------|
| Origin | 2782 | 32.6 | 32.7 |
| Sound transmission performance optimization | 2969 | 30.3 | 30.2 |
| Self-noise reduction performance optimization | 2781 | 32.6 | 32.9 |
| Sound transmission and self-noise suppression | 2971 | 30.2 | 30.7 |

incident at the critical angle of the longitudinal wave, the mechanical impedance of the longitudinal wave is $Z_s = 0$, and the transmission coefficient is:

$$\frac{1}{|W|^2} = \left| \frac{Z}{Z_a} + 1 \right|^2, \quad (32)$$

where Z_a is the mechanical impedance of the shear wave, which is approximately $-i\omega m/2$ at the critical angle of the longitudinal wave; $Z = \rho c / \cos\theta$, where

ρ and c are the density and acoustic velocity, respectively, and θ is the critical incident angle. Then, the STL is satisfied as:

$$\text{STL} \propto 1 + \left(\frac{2\rho c}{\omega m \cos\theta} \right)^2. \quad (33)$$

Combined with the results in Figs. 9 and 13, the optimized FGMs have a larger equivalent mass m and a lower equivalent Poisson’s ratio compared with the initial FGMs but also have a higher equivalent Young’s

modulus. Compared with the magnitude difference of the equivalent Young's modulus, the density and Poisson's ratio changes are both minuscule. As a result, the equivalent longitudinal wave velocity increases, while the critical angle θ of the longitudinal wave decreases. Combined with Eq. (32), the peak value of the STL under the longitudinal wave critical angle will decrease.

The change in the STL before and after optimization at lower incident angles can be explained using the thin-plate theory (MORSE, INGARD, 1986), as shown in Eq. (34):

$$TL = 20 \log \left| \frac{i\gamma}{\rho_{N+1}} \left(D \frac{k^4}{\omega^2} - m \right) + 2 \right|, \quad (34)$$

where

$$\gamma = \sqrt{k_{N+1}^2 - k^2},$$

the bending stiffness is

$$D = \frac{E_e h^3}{12(1 - \sigma_e^2)},$$

and m is the mass per unit length. By combining Eqs. (32) and (34), although the equivalent mass m is improved after optimization, the bending stiffness D is proportional to the equivalent Young's modulus and has the order of the fourth power of the wavenumber k . Therefore, the higher equivalent Young's modulus of the optimized FGM acoustic windows leads to an increase of the STL at lower incident angles. So, when the composition of the FRP in the FRP-rubber FGM acoustic window is increased, the corresponding equivalent Young's modulus is higher, which induces a decrease in the peak value of STL because Young's modulus of rubber is smaller than that of the FRP. A higher equivalent Young's modulus induces an STL decrease at the critical angle, a shift of the critical angle towards lower incident angles, and an increase in the STL at lower incident angles, but the total STL decreases, corresponding to better sound transmission performance.

5.2. Turbulent self-noise suppression characteristics of FGM acoustic windows before and after optimization

To analyze the reasons for the increase in the turbulent self-noise reduction of FGMs before and after optimization, the wavenumber-frequency spectrum results of the spatial filtering function are calculated at $R = 0.3$ and $L = 0.5$ m. Figure 16 shows the calculation results of FRP with $H = 3$ cm.

Three characteristic identification lines are clearly seen in Fig. 16. A relatively clear dividing line is formed between the lower left corner and the upper right corner of the figure, which corresponds to the acoustic wavenumber k_0 in water at each frequency. This is called the dividing line of the acoustic wavenumber,

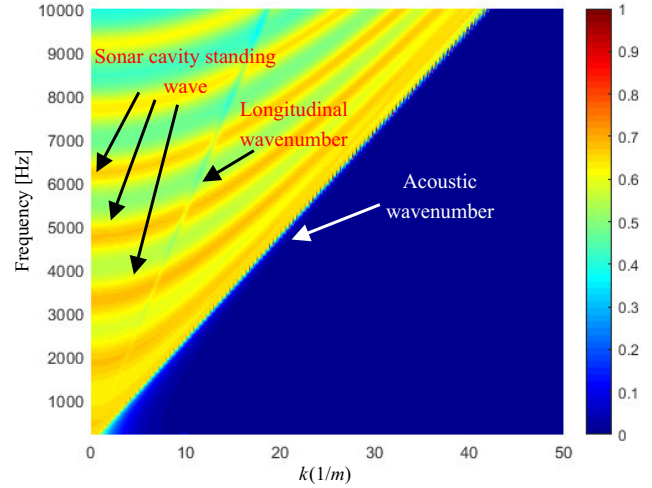


Fig. 16. Wavenumber-frequency spectrum results of the spatial filter function of FRP.

indicating that the spatial filter composed of the acoustic window and sonar cavity has the characteristics of a low-wavenumber passband and a high-wavenumber stopband. There is a lighter stripe from the lower left corner to the upper right corner, which corresponds to the longitudinal wavenumber of FRP. In addition, there are prominent periodic ripple lines in the figure, which are derived from the standing wave field formed in the sonar cavity by self-noise, and this feature is also the reason for the periodic fluctuation in the turbulent self-noise reduction. Figure 17 shows the wavenumber-frequency spectrum results of the spatial filtering function of the FGMs acoustic window before and after turbulent self-noise suppression and sound transmission performance optimization (STL and NR optimization).

As shown in Fig. 17, the corresponding equivalent longitudinal wave velocities of the FRP-rubber FGM acoustic windows before and after optimization are different according to Eq. (30), which results in different slopes of the characteristic lines of the longitudinal wavenumber. For the original FRP-rubber FGM, the reason for the small slope is that a small longitudinal wave velocity corresponds to a large wavenumber. Before and after optimization, the periodic fringe remains consistent because the acoustic medium and the height inside the sonar cavity remain unchanged. The resonance period of the standing wave field formed inside the sonar cavity meets the following requirements:

$$f = \frac{nc_{N+1}}{2L}, \quad (35)$$

where n is the number of fringe periods. Figures 12d and 14d show that an increase in the turbulent self-noise reduction of the FRP-rubber FGM acoustic window before and after optimization is positively correlated with the frequency. To analyze the reason for the increase in self-noise reduction, Fig. 18 shows the spa-

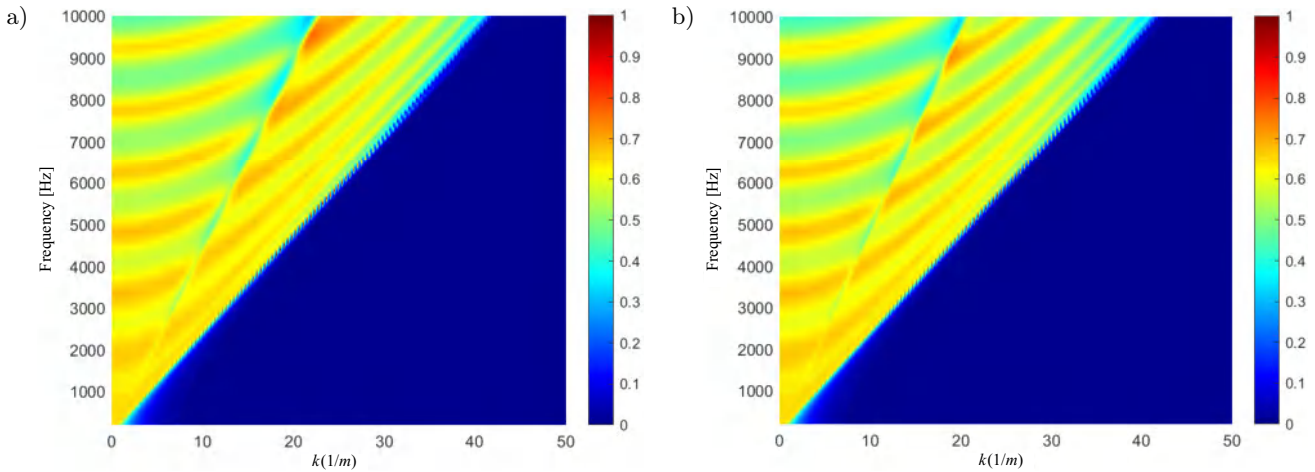


Fig. 17. Wavenumber-frequency spectrum of the spatial filtering function of the FRP-rubber FGM acoustic windows before and after optimization: a) original FGM; b) optimized FGM for STL and NR' optimization.

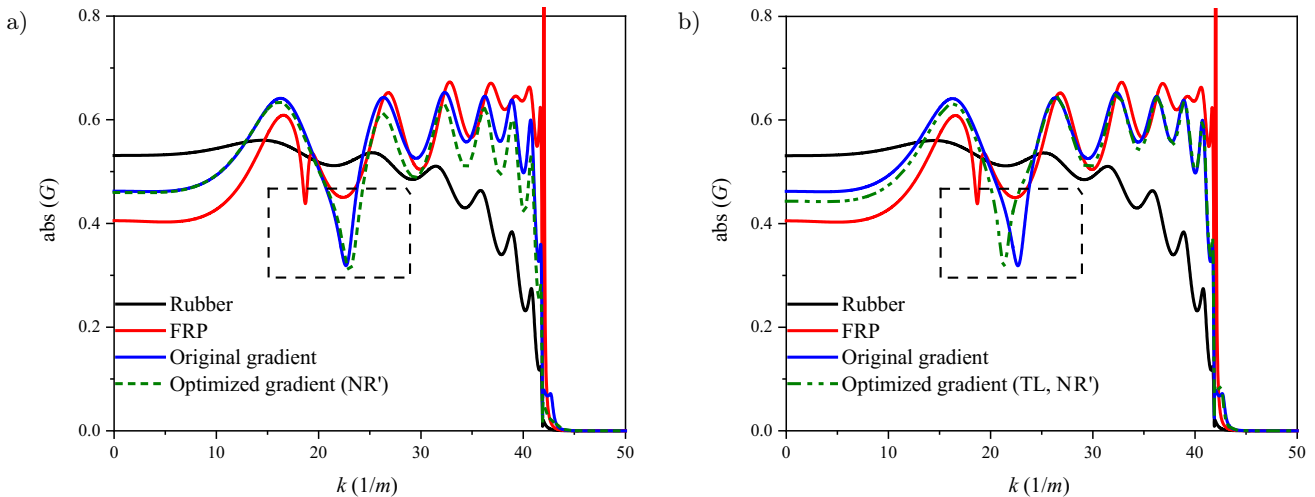


Fig. 18. Comparison of the spatial filtering functions of various acoustic windows at $f = 10$ kHz: a) FRP, rubber and FRP-rubber FGM acoustic window before and after the turbulent self-noise performance optimization (NR'); b) FRP, rubber and FRP-rubber FGM acoustic window before and after the turbulent self-noise and sound transmission performance optimization (TL, NR').

tial filtering function of the FRP-rubber FGM acoustic window before and after optimization at $f = 10$ kHz.

As shown in Fig. 18, the characteristic valley value is caused by the equivalent longitudinal wave of the various acoustic windows made from the FRP, rubber and FRP-rubber FGM before and after optimization. The original FRP-rubber FGM acoustic has a small equivalent longitudinal wave velocity corresponding to a large wavenumber of the characteristic value. For the optimized FRP-rubber FGM acoustic window, the equivalent longitudinal wave velocity is high, corresponding to a small wavenumber of the characteristic value. In addition, as shown in Figs. 18a and 18b, the rubber composition is beneficial for improving the filtering performance of higher wavenumbers, and the composition of FRP is beneficial for improving the filtering performance of lower wavenumbers in the region smaller than the acoustic wavenumber. The opti-

mized specific ratio of rubber and FRP components brings about an FGM acoustic window with better filtering properties in the higher wavenumber region (Fig. 18b) and with better filtering properties in the lower wavenumber region (Fig. 18a), which can effectively suppress and shield the self-noise caused by the TBL pulsating pressure.

6. Conclusions

Considering the sonar self-noise suppression excited by the TBL pulsating pressure and sound transmission performance excited by the incident acoustic source for FGM acoustic windows, an internal gradient optimization method for FGMs is proposed in this paper, which can be used to design optimized FGM acoustic windows with better turbulent self-noise suppression abil-

ity and sound transmission performance. The theoretical modeling for FGM acoustic windows to evaluate the turbulent self-noise reduction and STL is completed in the proposed optimization method, in which the accuracy is verified by the finite element results of COMSOL Multiphysics. Using the optimization method proposed in this paper, the optimization calculations of the sound transmission performance, and the turbulent self-noise suppression performance, the sound transmission and turbulent self-noise suppression performance for the FRP-rubber FGM acoustic window are completed, and the results of the five optimization variables in the gradient function are separately obtained using the Bernstein polynomial as the deviation function. Finally, the mechanism of the sound transmission and turbulent self-noise suppression performance before and after optimization is explained based on the gradient material equivalent model and thin-plate model, respectively. The main conclusions are as follows.

The optimization results of the sound transmission performance, the self-noise suppression performance, and the sound transmission and self-noise suppression performance for the FRP-rubber FGM acoustic window show that the sound transmission or self-noise suppression performance of the optimized FGM acoustic window is effectively improved, indicating the effectiveness of the optimization method.

The peak position of the STL originates from the S_0 wave, which corresponds to the longitudinal wave velocity at the low frequency. The peak STL value and position and the STL at lower incident angles are mainly determined by the equivalent Young's modulus. Appropriately increasing the composition of the FRP can improve the equivalent Young's modulus, which is beneficial to improve the sound transmission performance of the FRP-rubber FGM acoustic window.

The periodicity of the turbulent self-noise reduction with frequency arises from the standing wave resonance inside the sonar cavity; the slope identification feature of the spatial filter function arises from the equivalent longitudinal wavenumber and the acoustic wavenumber.

A spatial filter consisting of an acoustic window and sonar cavity has the characteristics of a low wavenumber passband and a high wavenumber stopband. The spatial filtering performance of the sonar cover can be improved by optimizing the internal gradient form. In the lower wavenumber passband (less than the acoustic wavenumber), rubber enhances higher wavenumber filtering, while FRP is good for lower wavenumber filtering. The optimization results show that reasonable adjustment of the ratio of FRP and rubber can improve not only the sound transmission performance, but also the overall filtering performance, corresponding to improving the turbulent self-noise suppression performance.

The research results of this paper provide a reference value for the future design of FGM acoustic windows for sonar hoods.

Appendix

The matrix \mathbf{I} is:

$$\begin{bmatrix} I_{11} & I_{12} & I_{13} & I_{14} \\ I_{21} & I_{22} & I_{23} & I_{24} \\ I_{31} & I_{32} & I_{33} & I_{34} \\ I_{41} & I_{42} & I_{43} & I_{44} \end{bmatrix}.$$

The elements in the matrix \mathbf{I} in the layer l are:

$$I_{11} = ik \cos\left(\sqrt{k_{Ll}^2 - k^2}z\right),$$

$$I_{12} = k \sin\left(\sqrt{k_{Ll}^2 - k^2}z\right),$$

$$I_{13} = i\sqrt{k_{Tl}^2 - k^2} \cos\left(\sqrt{k_{Tl}^2 - k^2}z\right),$$

$$I_{14} = \sqrt{k_{Tl}^2 - k^2} \sin\left(\sqrt{k_{Tl}^2 - k^2}z\right),$$

$$I_{21} = -\sqrt{k_{Ll}^2 - k^2} \sin\left(\sqrt{k_{Ll}^2 - k^2}z\right),$$

$$I_{22} = -i\sqrt{k_{Ll}^2 - k^2} \cos\left(\sqrt{k_{Ll}^2 - k^2}z\right),$$

$$I_{23} = k \sin\left(\sqrt{k_{Tl}^2 - k^2}z\right),$$

$$I_{24} = ik \cos\left(\sqrt{k_{Tl}^2 - k^2}z\right),$$

$$I_{31} = -(\lambda_l k_{Ll}^2 + 2\mu_l (k_{Ll}^2 - k^2)) \cos\left(\sqrt{k_{Ll}^2 - k^2}z\right) i/\omega,$$

$$I_{32} = i(\lambda_l k_{Ll}^2 + 2\mu_l (k_{Ll}^2 - k^2)) \sin\left(\sqrt{k_{Ll}^2 - k^2}z\right) i/\omega,$$

$$I_{33} = 2\mu_l k \sqrt{k_{Tl}^2 - k^2} \cos\left(\sqrt{k_{Tl}^2 - k^2}z\right) i/\omega,$$

$$I_{34} = -2i\mu_l k \sqrt{k_{Tl}^2 - k^2} \sin\left(\sqrt{k_{Tl}^2 - k^2}z\right) i/\omega,$$

$$I_{41} = -2i\mu_l k \sqrt{k_{Ll}^2 - k^2} \sin\left(\sqrt{k_{Ll}^2 - k^2}z\right) i/\omega,$$

$$I_{42} = 2\mu_l k \sqrt{k_{Ll}^2 - k^2} \cos\left(\sqrt{k_{Ll}^2 - k^2}z\right) i/\omega,$$

$$I_{43} = -i\mu_l (k_{Tl}^2 - 2k^2) \sin\left(\sqrt{k_{Tl}^2 - k^2}z\right) i/\omega,$$

$$I_{44} = \mu_l (k_{Tl}^2 - 2k^2) \cos\left(\sqrt{k_{Tl}^2 - k^2}z\right) i/\omega,$$

where λ_l and μ_l represent the lame constant in the layer l .

Acknowledgments

This work was supported by the National Natural Science Foundation of China (the grant no. 11774229).

References

- BREKHOVSKIKH L. (2012), *Waves in Layered Media*, Elsevier.
- BURTON S.A. (1998), A cost effective solution for noise free GRP sonar domes in dynamic conditions, [in:] *UDT 1998 Conference Proceedings*, pp. 277–281.
- CAIAZZO A, DESMET W.A. (2016), A generalized Corcos model for modelling turbulent boundary layer wall pressure fluctuations, *Journal of Sound and Vibration*, **372**: 192–210, doi: [10.1016/j.jsv.2016.02.036](https://doi.org/10.1016/j.jsv.2016.02.036).
- CHANDRA N., RAJA S., GOPAL K.V.N. (2014), Vibro-acoustic response and sound transmission loss analysis of functionally graded plates, *Journal of Sound & Vibration*, **333**(22): 5786–5802, doi: [10.1016/j.jsv.2014.06.031](https://doi.org/10.1016/j.jsv.2014.06.031).
- CHANDRA N., RAJA S., GOPAL K.V.N. (2015), A comprehensive analysis on the structural–acoustic aspects of various functionally graded plates, *International Journal of Applied Mechanics*, **7**(5): 1550072, doi: [10.1142/S1758825115500726](https://doi.org/10.1142/S1758825115500726).
- CREMER L., HECKL M., PETERSSON B. (2005), *Structure-borne Sound: Structural Vibration and Sound Radiation at Audio Frequencies*, Springer-Verlag.
- CRIGHTON D.G., DOWLING A.P., WILLIAMS J.E., HECKL M., LEPPINGTON F.G. (1992), *Modern Methods in Analytical Acoustics*, Springer-Verlag, pp. 452–509.
- GEORGE N., PITCHAIMANI J., MURIGENDRAPPA S., LENIN BABU MC. (2016), Vibro-acoustic behavior of functionally graded carbon nanotube reinforced polymer nanocomposite plates, [in:] *Proceedings of the Institution of Mechanical Engineers, Part L: Journal of Materials: Design and Applications*, **232**(7): 566–581, doi: [10.1177/1464420716640301](https://doi.org/10.1177/1464420716640301).
- HAM Y., KIM J., CHANG H. (2018), A study on the improvement of adhesive mixing ratio about acoustic window for enhancing sonar performance of submarine, *Journal of the Korea Institute of Military Science and Technology*, **21**(4): 481–488, doi: [10.9766/KIMST.2018.21.4.481](https://doi.org/10.9766/KIMST.2018.21.4.481).
- HOFFMANN C. (1998), Integrated design approach for sonar domes, [in:] *UDT 1998 Conference Proceedings*, pp. 83–86.
- HOSSEINI-HASHEMI S., ZARE M., FADAAE S.R. (2010), A new exact analytical approach for free vibration of Reissner–Mindlin functionally graded rectangular plates, *International Journal of Mechanical Sciences*, **53**(1): 11–12, doi: [10.1016/j.ijmecsci.2010.10.002](https://doi.org/10.1016/j.ijmecsci.2010.10.002).
- IQBAL Z., NAEEM M.N., SULTA N. (2009), Vibration characteristics of FGM circular cylindrical shells using wave propagation approach, *Applied Mathematics and Mechanics*, **208**: 237–248, doi: [10.1007/s00707-009-0141-z](https://doi.org/10.1007/s00707-009-0141-z).
- KARPFINGER F., GUREVICH B., BAKULIN A. (2008), Modeling of wave dispersion along cylindrical structures using the spectral method, *The Journal of the Acoustical Society of America*, **124**(2): 859–865, doi: [10.1121/1.2940577](https://doi.org/10.1121/1.2940577).
- KARPFINGER F., VALERO H.-P., GUREVICH B., BAKULIN A., SINHA B. (2010), Spectral-method algorithm for modeling dispersion of acoustic modes in elastic cylindrical structures, *Geophysics*, **75**(3): H19–H27, doi: [10.1190/1.3380590](https://doi.org/10.1190/1.3380590).
- KUMAR B.R., GANESAN N., SETHURAMAN R. (2009), Vibro-acoustic analysis of functionally graded elliptic disc under thermal environment, *Mechanics of Advanced Material & Structures*, **16**(2): 160–172, doi: [10.1080/15376490802625506](https://doi.org/10.1080/15376490802625506).
- LANE R. (1981), Absorption mechanisms for waterborne sound in Alberich Anechoic layers, *Ultrasonics*, **19**(1): 28–30, doi: [10.1016/0041-624X\(81\)90029-9](https://doi.org/10.1016/0041-624X(81)90029-9).
- LAVENDER M.A. (1994), The application of multi-layer modeling to dome design and hull treatments, [in:] *UDT 1994 Conference Proceedings*, pp. 296–299.
- LEE J.-H., KIM B.-N., SHIN K.-K., YOON S.W. (2010), Insertion loss of sound waves through composite acoustic window materials, *Current Applied Physics*, **10**(1): 138–144, doi: [10.1016/j.cap.2009.05.017](https://doi.org/10.1016/j.cap.2009.05.017).
- LIU Y., COMPSON C., LIU M. (2004), Nanostructured and functionally graded cathodes for intermediate temperature solid oxide fuel cells, *Journal of Power Sources*, **138**(1–2): 194–198, doi: [10.1016/j.jpowsour.2004.06.035](https://doi.org/10.1016/j.jpowsour.2004.06.035).
- MAIDANIK G. (1968), Domed sonar system, *The Journal of the Acoustical Society of America*, **44**(1): 113–124, doi: [10.1121/1.1911045](https://doi.org/10.1121/1.1911045).
- MORSE P.M., INGARD K.U. (1986), *Theoretical Acoustics*, Princeton University Press.
- MORTENSEN A., SURESH S. (1995), Functionally graded metals and metal-ceramic composites: Part 1 processing, *International Materials Reviews*, **40**(6): 239–265, doi: [10.1179/imr.1995.40.6.239](https://doi.org/10.1179/imr.1995.40.6.239).
- POMPE W. *et al.* (2003), Functionally graded materials for biomedical applications, *Materials Science and Engineering: A*, **362**(1–2): 40–60, doi: [10.1016/S0921-5093\(03\)00580-X](https://doi.org/10.1016/S0921-5093(03)00580-X).
- PRAKASH T., GANAPATH M. (2006), Asymmetric flexural vibration and thermoelastic stability of FGM circular plates using finite element method, *Composites Part B: Engineering*, **37**(7–8): 642–649, doi: [10.1016/j.compositesb.2006.03.005](https://doi.org/10.1016/j.compositesb.2006.03.005).

25. RABBANI V., HODAEI M., DEND X., LU H., HUI D., WU N. (2019), Sound transmission through a thick-walled FGM piezo-laminated cylindrical shell filled with and submerged in compressible fluids, *Engineering Structures*, **197**: 109323, doi: [10.1016/j.engstruct.2019.109323](https://doi.org/10.1016/j.engstruct.2019.109323).
26. SHANG E.C. (1965), An approximate formula for the wave reflection from gradual-transition absorbers [in Chinese], *ACTA Acustica*, pp. 192–197.
27. SKELTON E.A., JAMES J.H. (1997), *Theoretical Acoustics of Underwater Structures*, World Scientific.
28. SRIVASTAVA S.K. (1998), Ocean engineering aspects of submarine sonar dome, [in:] *UDT 1998 Conference Proceedings*, pp. 325–329.
29. TANG W.L., YU M.S., WANG B. (2020), *Hydrodynamic Noise Theory* [in Chinese], Science Press.
30. YU M.S., LI D.S., GONG L., XU J. (2005), Design of sandwich acoustic window for sonar dome [in Chinese], *Chinese Journal of Acoustics*, **30**(5): 427–434, doi: [10.15949/j.cnki.0371-0025.2005.05.007](https://doi.org/10.15949/j.cnki.0371-0025.2005.05.007).
31. ZHAO X., LEE Y.Y., LIEW K.M. (2009), Mechanical and thermal buckling analysis of functionally graded plates, *Composite Structures*, **90**(2): 161–171, doi: [10.1016/j.compstruct.2009.03.005](https://doi.org/10.1016/j.compstruct.2009.03.005).
32. ZHOU L., LIU J.S., HU H.H. (2020), Study on acoustic transmission performance of functionally gradient materials under turbulent excitation, [in:] *Noise and Vibration Control*, **40**(5): 71–75+88.

Research Paper

Investigation of the Acoustic Properties of a Metamaterial with a Multi-Ring Structure

Grzegorz SZCZEPAŃSKI*^{}, Marlena PODLEŚNA^{},
Leszek MORZYŃSKI^{}, Anna WŁUDARCZYK^{}

Central Institute For Labour Protection – National Research Institute
Warsaw, Poland

*Corresponding Author e-mail: grszc@ciop.pl

(received December 13, 2022; accepted May 30, 2023)

In this article, the authors present the geometry and measurements of the properties of an acoustic metamaterial with a structure composed of multiple concentric rings. CAD models of the structure were developed and subsequently used in numerical studies, which included the study of resonant frequencies using the Lanczos method and an analysis of sound pressure level distribution under plane wave excitation using the finite element method. Subsequently, experimental tests were carried out on models with the same geometry produced with three different materials (PLA, PET-G, and FLEX) using a fused deposition modeling 3D printing technique. These tests included: determining insertion loss for a single model based on tests using the measurement window of a reverberation chamber and determining transmission loss through tests in a semi-anechoic chamber. Sound wave resonance was obtained for frequencies ranging from 1700 to 6000 Hz. Notably, the experimental studies were carried out for the same structure for which numerical tests were conducted. The physical models of a metamaterial were manufactured using three different readily available 3D printing materials. The results of laboratory tests confirm that the created acoustic metamaterial consisting of multi-ring structures reduces noise in medium and high frequencies.

Keywords: acoustic metamaterials; numerical research; experimental research; finite element method; multi-ring structures.



Copyright © 2023 The Author(s).
This work is licensed under the Creative Commons Attribution 4.0 International CC BY 4.0
(<https://creativecommons.org/licenses/by/4.0/>).

1. Introduction

Noise is the most common hazard in the work environment, accounting for 55.1% of all identified hazards related to the work environment in Poland (GUS, 2019). One of the commonly used protections designed to reduce noise emitted by machines in industrial conditions are sound-insulating enclosures and barriers, which are referred to as passive noise protection (ENGEL *et al.*, 2009). The use of this type of protection is a solution, where the threat of noise is eliminated by preventing its propagation thus preventing further signal transmission. Noise transmission can also be reduced using active methods (WRONA, PAWEŁCZYK, 2019; MORZYŃSKI, SZCZEPAŃSKI, 2018; MAZUR *et al.*, 2018).

The common practice in the case of passive methods was the use of solid materials with sound insula-

tion or sound absorption properties. The effectiveness of a given solution depends on the thickness of the layer and the type of material used (SIKORA, 2011). However, sometimes such solutions are not recommended or possible to implement, due to, e.g., costs, issues with heat dissipation or weight. Acoustic metamaterials offer a solution to such challenges, as their sound attenuation properties mainly depend on their internal structure rather than the material's type or properties (NAKAYAMA *et al.*, 2021; IANNACE *et al.*, 2021; LIU *et al.*, 2020; SZYTŁER, STRUMIŁŁO, 2022; ZHANG *et al.*, 2020). A metamaterial can take the form, for example, a flat or spatial structure made from a non-sound-absorbing material, e.g., one produced using the 3D printing technique (ZIELIŃSKI *et al.*, 2020). Acoustic metamaterial is constructed to absorb sound in a specific frequency band. In the most frequently studied and developed metamaterials containing resonant

structures, these properties are observed notably in narrow frequency bands, closely aligned with the resonance frequencies of the structures used in their construction. For example, acoustic metamaterials based on Helmholtz resonators ensure high sound absorption with a small structure thickness compared to the acoustic wavelength (DUAN *et al.*, 2021; MAHESH, MINI, 2019).

Another type of a metamaterial is a metamaterial with a maze structure, composed of multiple acoustic channels with twisted, meandering paths. A metamaterial can also be made of a porous material in which resonators are placed, allowing to broaden the sound absorption band in the medium and low frequency spectrums (GAO *et al.*, 2022). Structures related to acoustic metamaterials are sonic crystals. They consist of periodically arranged structures, often in the form of elongated rings arranged on a grid, dispersing acoustic waves. Similar to acoustic metamaterials, sonic crystals exhibit sound attenuation properties in a narrow frequency band. Adjusting the crystal's attenuation band is often addressed in research works (RADOSZ, 2019). Efforts are frequently made to manipulate the geometry of sonic crystals, for example, by changing the thickness and the material of the crystal filling (PENNEC *et al.*, 2004). So far, single-ring structures used in metamaterial construction have been extensively studied and discussed in the literature. However, the results obtained up to this point indicate that such structures may exhibit sound attenuation properties across multiple frequency bands, in contrast to single-ring structures (CHEN *et al.*, 2018). Studies on polycyclic-like structures indicate that such structures are capable of attenuating sounds of lower frequencies, which is difficult to achieve in the case of metamaterials (WANG *et al.*, 2012).

In the present article, a barrier model of an acoustic metamaterial consisting of a multi-ring structure is described and subsequently investigated numerically and experimentally.

2. Investigated metamaterial model

Many workstations are separated from each other by safety barriers composed of wire mesh applied to aluminum profiles. Replacing this mesh with an acoustic metamaterial featuring an appropriate structural pattern can reduce noise at adjacent workstations. The main objective in developing the metamaterial cell is to obtain a relatively large number of resonant frequencies in the frequency range of 1 to 6.3 kHz. It was assumed that there might be a noise reduction effect near the resonant frequencies. The metamaterial cell should be as small as possible and allow to obtain multi-format barriers by creating a structure based on a large number of cells. Consequently, it was established that the cell pattern should conform to a shape of a square

with a side of 25 mm (considering the width of the aluminum profiles often used in the construction of workstation partitions).

The cell of such a size can be used, for example, in constructing acoustically beneficial thin workstation partitions or as a sliding industrial curtain. Since the goal of the study is to create a structure with multiple resonant frequencies, it is hypothesized that a structure with multiple chambers (particularly ring-shaped ones) could achieve this goal, and consequently a ring-based structure is proposed as the base shape for the cell. The developed structure consisted of three thin-walled concentrically placed rings connected to a small cylinder, also placed concentrically inside the smallest ring. These rings were connected to each other and to the side walls via arch-shaped walls with openings. The rings have cutouts in several places to allow for airflow. The analyzed model is composed of six structures (metamaterial cells) arranged in a sequence that is 150 mm tall and 140 mm wide, and with a thickness of 25 mm. The geometric model of the developed solid model of a single multi-ring cell and the structure consisting of several multi-ring cells in cross-section is shown in Fig. 1.

The model designed in CAD software was used as the basis for both numerical analysis and constructing three physical models. These physical metamaterial models were created using 3D printing in fusion deposition modeling (FDM) technology, using three types of materials: PLA (a biodegradable polymer), PETG (a transparent polymer with glycol addition), and FLEX (a rubber-like material with a hardness of 40D). A nozzle with a diameter of 0.4 mm was used to create the models. The only places where the use of filling was required (given that the model is thin-walled) were the cylinders located at the center of the rings filled in 100%. The models created for laboratory experiments are shown in Fig. 2.

3. Method

Three types of studies were conducted with the proposed structure: numerical analyses were carried out on the CAD model, and insertion loss and transmission loss studies were implemented using physical models. In numerical analysis, resonant frequencies were first examined, and then they were used for the analysis in frequency domain analysis to assess the distribution of the sound pressure level behind the tested model. In the numerical study, the model was positioned in such a way that the cutouts in the front of the model (Fig. 1, side A) faced the excitation source.

In the experimental studies, measurements were made for two configurations of the metamaterial model: one with the cutouts facing the excitation source and the other with the model's back (Fig. 1, side B) facing the excitation source. The study focused

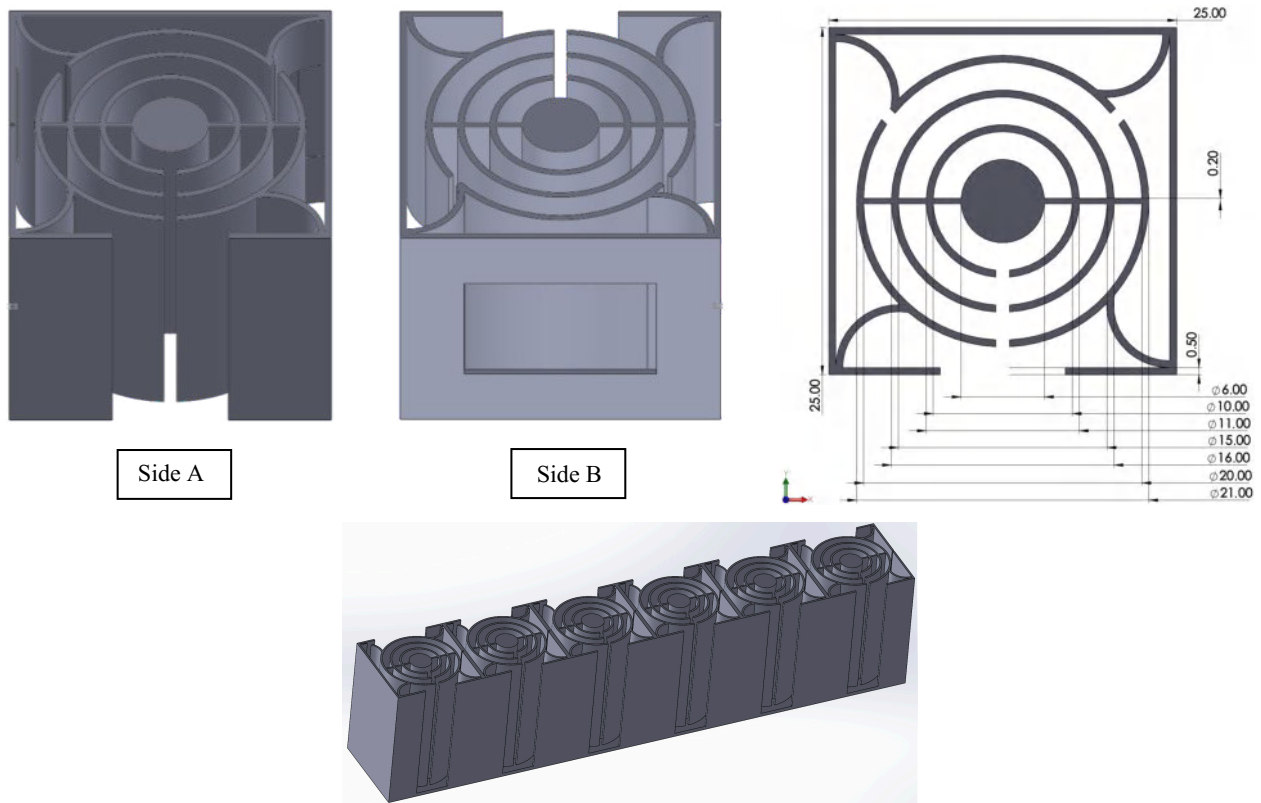


Fig. 1. View of a single metamaterial cell (top) and a structure composed of several cells (bottom).



Fig. 2. Created models of an acoustic metamaterial with a multi-ring structure made out of three different materials (from the left): PLA, FLEX, and PETG.

on determining the transmission loss to check whether the properties of the material used to create the metamaterial influenced its insulating properties. Transmission loss and insertion loss were measured in different sound fields (free and diffuse) to simulate different industrial conditions. Where the replacement of the wire mesh with an acoustic metamaterial (which does not attenuate noise) is considered, the results of the insertion loss study may be. Conversely, in the case of replacing existing barriers, the results of the transmission loss study are more appropriate.

3.1. Numerical analysis

Two types of numerical analyses were performed on the developed CAD models. These studies were conducted using the Siemens Simcenter 3D environment

with solvers SOL103 and SOL108. The first numerical test was aimed to determine the resonant frequencies for a single cell of an acoustic metamaterial as well as for a 6-cell structure using the Lanczos method. The second study was conducted in the frequency domain using the finite element method involving a plane wave excitation with a sound pressure of 2 Pa. The inlet, outlet and side walls of the CAD model were defined as acoustic absorbers. Restraints (permanent constraints) were established for the tunnel's extremities. The FEMAO adaptive technique was used in the calculations.

The performed numerical analyses were of the two-way coupled type (the interaction of the structure and fluid domains). Global connection parameters between the fluid domain and the solid domain were adopted using the default (recommended) coupling method. Be-

fore starting the tests, the quality of the computational mesh was checked, which showed no errors. The excitation tests were performed in the frequency domain in the range from 100 to 6500 Hz in $1/12$ octave bands. The recommended criterion regarding the width of the computational grid (HOWARD, CAZZOLATO, 2017) (dimension smaller than $1/6$ of the wavelength) was met in the tests.

3.2. Sound insertion loss study

The insertion loss studies for the physical model of the acoustic metamaterial barrier made from PLA were carried out using a measurement window in a reverberation chamber. The measurement window took the form of a rectangle measuring 14 cm by 15 cm and was created by two walls (14 and 26 cm thick) separated by an air gap (3 cm thick). The dimensions of the samples were adjusted to match the frame so that no additional mounting elements were needed to attach them. The model was pressed into the mounting frame attached to the outer wall of the chamber. The space between the mounting frame and the chamber wall was sealed with sealing material. The diagram of the measurement stand is shown in Fig. 3.

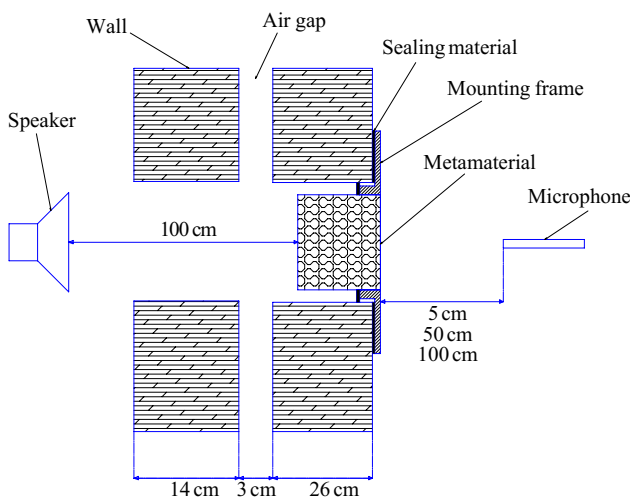


Fig. 3. Diagram of the stand for measuring the insertion loss in the measurement window of the reverberation acoustic chamber.

The reverberant acoustic chamber was treated as a transmission room and a sound source in the form of a loudspeaker was placed in it at a distance of 1 m from the first opening in the wall. The loudspeaker's membrane was facing the central part of the model. The receiving room was designated as the laboratory room. Sound pressure level measurements were conducted using the PULSE B&K system (a 3052-A-030 cassette and a $1/2$ inch TEDS 4191 microphone). In order to avoid obtaining measurement results for a point that may be a local attenuation/amplification (especially close to the structure) the measurements were

performed at three measurement points. The microphone was placed on the side of the receiving room at distances of 5, 50, and 100 cm from the model being measured, perpendicular to its surface, and aligned coaxially with the point of intersection of the diagonals of the model's surface. Pink noise was used as the excitation signal. The duration of the measurement was 30 s for each measurement point in the study of each model and 1 min for the background noise level measurements.

The measurements were carried out in the range from 100 to 6500 Hz. After the measurements, the insertion loss was determined as the difference in sound pressure level of the noise emitted by the loudspeaker with and without the use of a metamaterial model for each of the measurement points.

3.3. Sound transmission loss

The impulse response method (the Dirac delta function method) was used as the research method for determining the transmission loss. The measurements were carried out in a semi-anechoic chamber. A loudspeaker positioned in front of the tested model was used as the sound source. The models were mounted on an arm in the form of a pipe, aligned with the axis of symmetry of the loudspeaker membrane, 2 m from the loudspeaker, and at the same height as the loudspeaker. The measurement stand scheme is shown in Fig. 4.

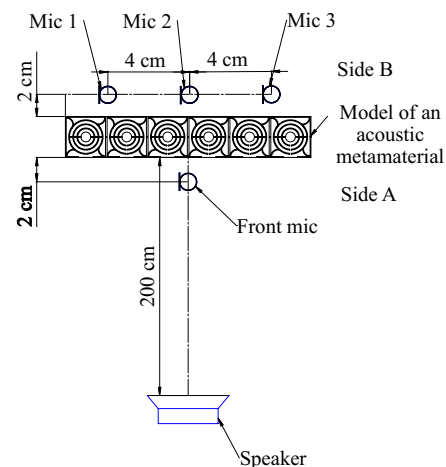


Fig. 4. Measurement stand scheme in the semi-anechoic acoustic chamber.

An e-sweep signal (an exponential sweep, where the frequency increases exponentially over time) was used as the stimulus signal. In order to minimize the impact of the microphone on the sound field distribution, a $1/8$ inch TEDS 4138-A-015 microphone was used. Two measurements were conducted at the same time – in front of and behind the model (both microphones of the same type). The microphones were connected to the NEXUS Bruel & Kjaer signal conditioner, through which the signal was sent via the RME sound card to a computer with Dirac (Bruel & Kjaer) version 5 software. Due to the small size of the model, three measurement points were placed (one opposite the center of the metamaterial and the two at points 3 cm apart from the edges of the sides of the metamaterial) about 2 cm behind the model, i.e., in the acoustic near field area. Because of the unusual geometry of the model, which could result in a highly heterogeneous distribution of acoustic field parameters, especially in close proximity to the structure, the measurements were conducted at three points. The measurements of the sound pressure level in the range from 100 Hz to 6.5 kHz in $1/12$ octave bands were carried out, and the examined parameter was transmission loss – defined as the difference between the sound pressure level of noise emitted by the loudspeaker at a point located 2 cm in front of the applied metamaterial model and the sound pressure level at a point located 2 cm behind the model.

4. Results

4.1. Numerical study

As part of the conducted research on resonant frequencies, the occurrence of such frequencies was found, especially in the medium and high frequency range. Table 1 presents the values of resonant frequencies determined from numerical tests for a single multi-ring

Table 1. Values of resonant frequencies for the multi-ring cell models.

| Model | Resonant frequencies [Hz] |
|--|--|
| The single multi-ring cell | 1718, 2950, 3529, 3912, 3965, 5374, 6385 |
| The structure consisting of six multi-ring cells | 1824, 2129, 2217, 2252, 2369, 2435, 2789, 2820, 2850, 2858, 2877, 2948, 3397, 3430, 3471, 3554, 3558, 3580, 3736, 3976, 4075, 4932, 4987, 5033, 5060, 5342, 5404, 5548, 5563, 5618 |

cell and structure consisting of six multi-ring cells. For computing resonant frequencies the Lanczos method was used.

For a single cell, 8 different resonant frequencies were obtained, and for a structure consisting of 6 cells 30 resonant frequencies were obtained. Examples of resonant frequencies for a single cell and the structure with six cells are shown in Figs. 5 and 6.

The presented figures indicate that resonance of sound wave for particular frequencies occurs at different areas of the structure. These frequencies were then compared with the frequencies at which the most significant reduction was noticed in sound pressure levels behind the barrier in the numerical study with excitation. Exemplar visualizations for selected frequency bands (with and without the resonant frequency component) are shown in Fig. 7.

The presented visualizations show the influence of the metamaterial with a multi-ring structure on sound pressure level behind the structure in a simplified case. As part of the visualization of sound pressure level distribution for the band with a center frequency of 218 Hz, a very small effect of the structure (less than 5 dB) is observed. At the center frequency of the $1/12$ octave band equal to 1830 Hz, there is an increase in the sound pressure level in front of the structure, affecting at the same time the values of the achieved

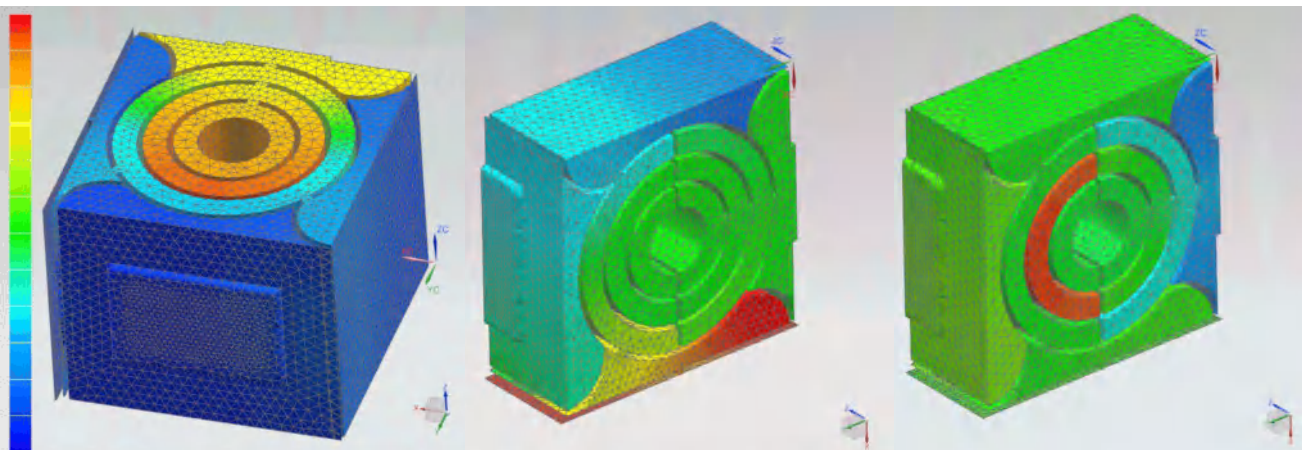


Fig. 5. Pressure distribution in the area of a single cell for the following resonant frequency (from the left): 1718, 2950, and 3529 Hz; areas of increased pressure are marked in red, and areas of ambient pressure are shown in blue.

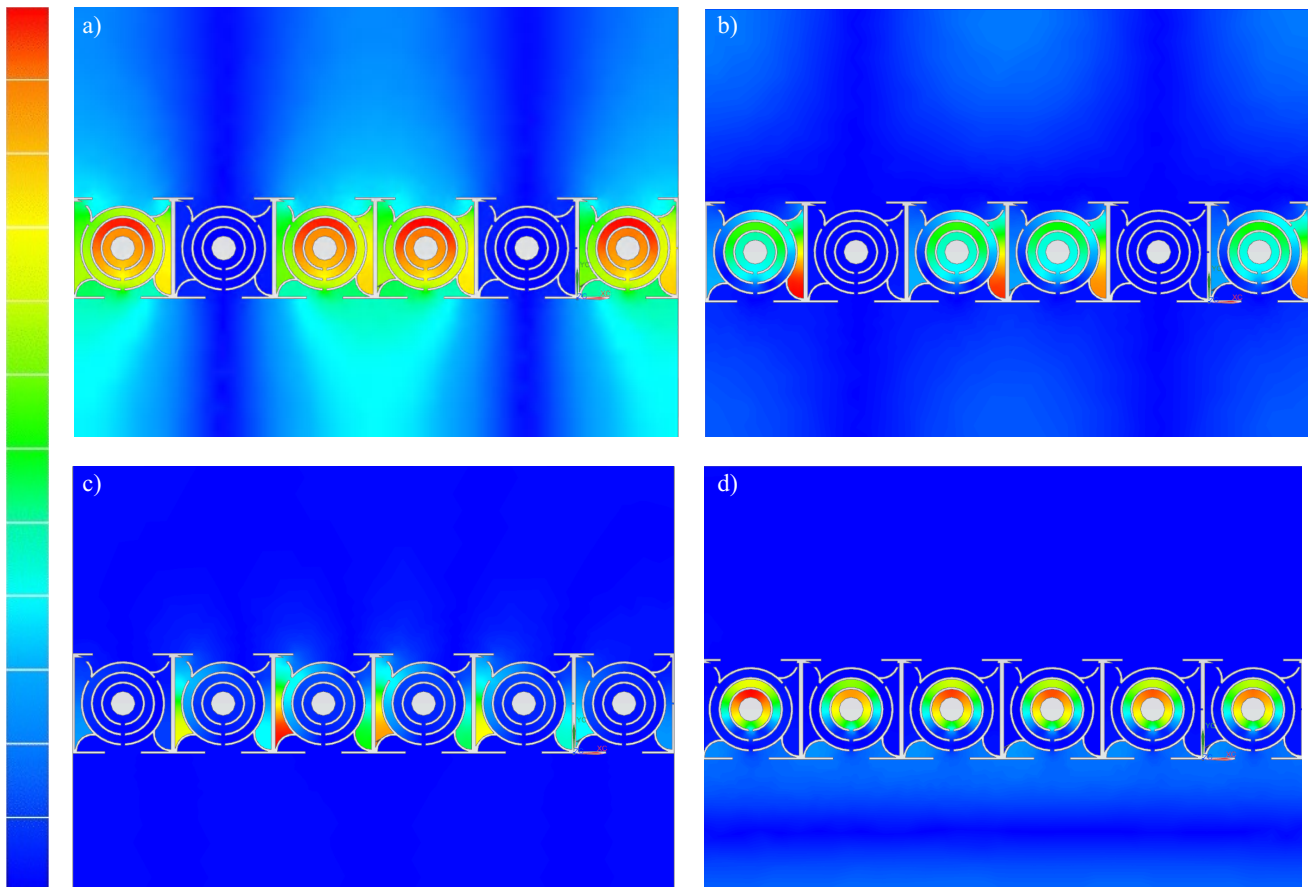


Fig. 6. Pressure distribution in the area of the six-cell structure for the following resonant frequency: a) 1824 Hz; b) 2948 Hz; c) 3580 Hz; d) 5033 Hz; areas of increased pressure are shown in red, and areas of ambient pressure in blue.

insertion loss (the insertion loss is around 10 dB). The positive influence of the structure becomes apparent at higher resonant frequencies, e.g., 3070, 3250, 3650 or 4100 Hz. The lowest values of the sound pressure level behind the acoustic metamaterial are obtained for the $1/12$ octave-band's center frequency equal to 3250 Hz. The most promising results were obtained for the following center frequency bands: 3070, 3250, 3450, 3870, 4100, 4340, 4600, 4870, and 6100 Hz. It can be concluded that the presented structure most effectively impacts mid-frequency and high-frequency range.

4.2. Sound insertion loss study

The insertion loss was determined for an A-weighted sound pressure level. The research began with back-

ground noise measurements. The A-weighted sound pressure level measured was 27.3 dB. Subsequently, measurements of the noise emitted by the loudspeaker were conducted without the model for the excitation signal in the form of pink noise placed in the measurement window. The results are presented in Table 2.

The sound pressure level emitted by the loudspeaker exceeds the sound pressure level of the background noise by more than 40 dB at each measurement point. The insertion loss calculation results range from 7.5 dB (worst case) to 12.6 dB (best case). No disparity was observed between the insertion loss values for both sides of the model. The results of measurements in the form of insertion loss are presented for the $1/12$ octave-band's center frequency from 103 Hz (component is below 15 dB) to 6500 Hz in Fig. 8.

Table 2. A-weighted sound pressure level for a given measurement point, without the model placed, and with the model placed on both sides.

| Measurement point | A-weighted sound pressure level [dB] | | |
|-------------------------|--------------------------------------|-------------------------------|---|
| | Without the model | Side A facing the loudspeaker | Backside of the model side B facing the loudspeaker |
| 5 cm behind the model | 85.9 | 78.4 | 76.4 |
| 50 cm behind the model | 74.9 | 64.1 | 64.8 |
| 100 cm behind the model | 69.8 | 58.9 | 57.2 |

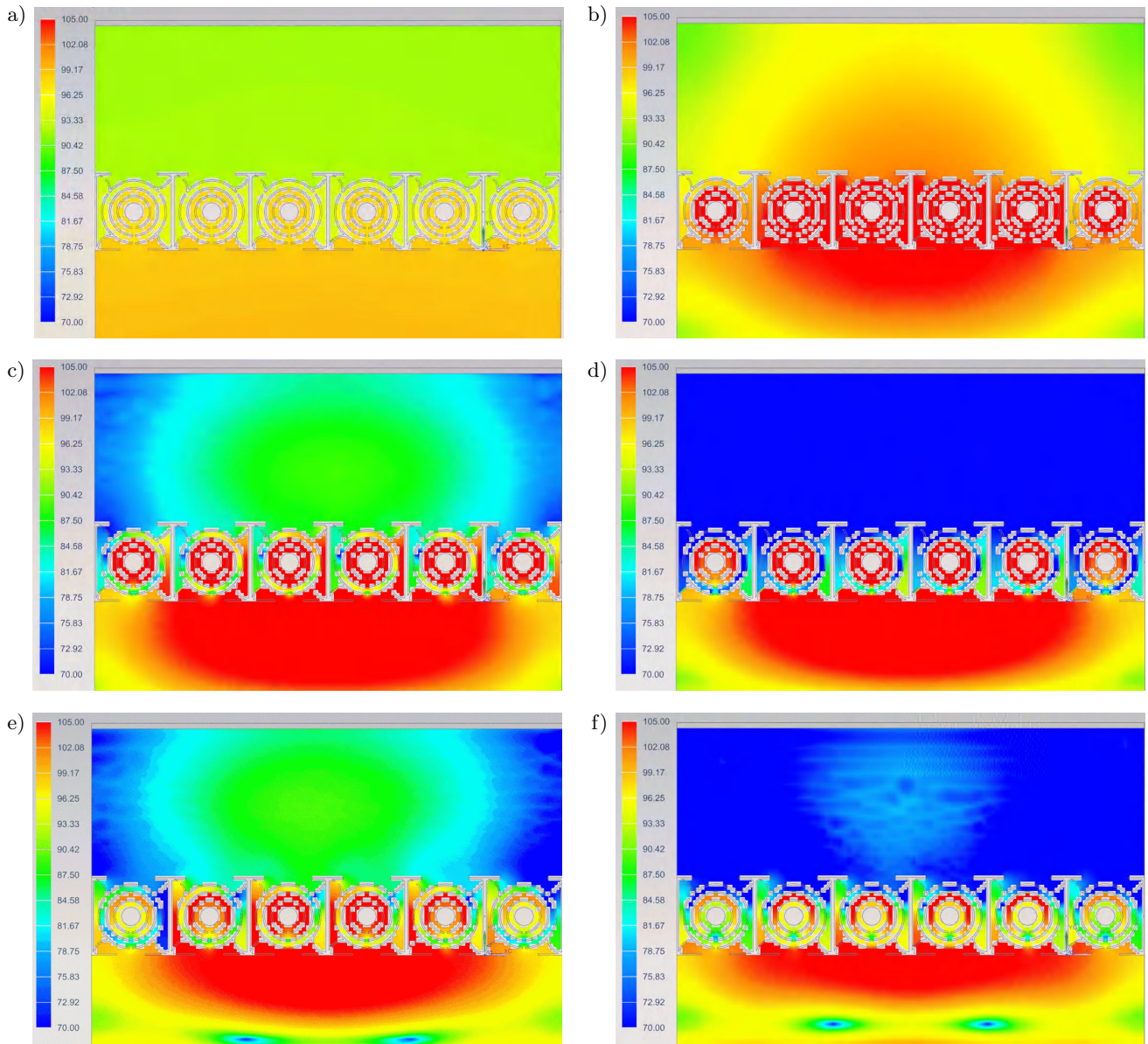


Fig. 7. Distribution of the sound pressure level obtained in a numerical test with excitation for the band with the middle $1/12$ octave: a) 218 Hz; b) 1830 Hz; c) 3070 Hz; d) 3250 Hz; e) 3650 Hz; f) 4100 Hz.

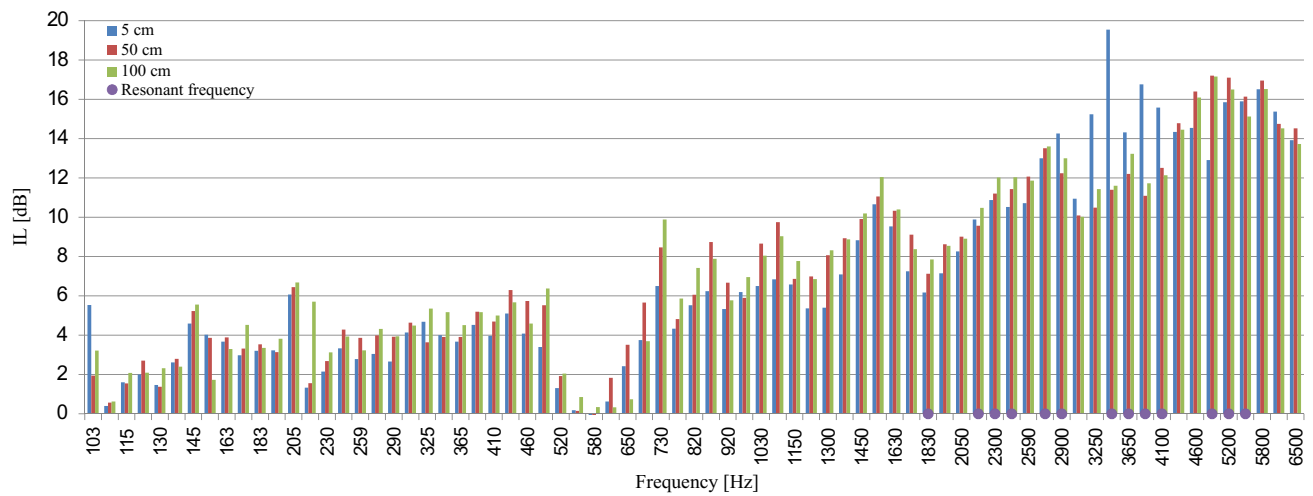


Fig. 8. Insertion loss for a distance of 100 cm behind the metamaterial with a multi-ring structure.

Figure 8 shows relatively large differences between the insertion loss values for the measurement point located 5 cm from the model and the measurement points located 50 cm and 100 cm from the model. These differences are discernable for frequency bands with center frequencies of 3250, 3450, 3650, 4100 Hz. The measurement results for the point located 5 cm away from the model indicate that the reduction takes on larger values locally, that would not be representative to properly evaluate the model. Therefore, the other two measurement points can be considered more representative for insertion loss results. In Fig. 8, the purple dots on the x -axis represent the bands in which the resonance frequencies in the numerical study were determined. Resonance frequencies in most cases occur in bands for which insertion loss was higher than 10 dB. However, the obtained results of insertion loss do not indicate a narrow-band noise reduction effect for the structure within the resonance frequencies themselves, but have a broadband character. This may be influenced by the diffusive character of the acoustic field. Notably, the highest attenuation values occur in the mid-frequency and high-frequency range.

4.3. Sound transmission loss

The measured acoustic background noise in the chamber did not exceed 20 dB. Transmission loss was determined for the A-weighted sound pressure level. Measurements behind the structure were carried out with microphones placed very close to the structure.

Due to the geometry, the distribution of the acoustic field parameters behind the metamaterial structure could be very heterogeneous. Therefore, tests were performed at three measurement points. The aforementioned terminology was adopted for individual measurement points:

- Mic 1: a point located 2 cm behind the tested model on its left side (shifted by 4 cm relative to its center (the axis intersecting its center));
- Mic 2: a point located 2 cm behind the tested model, coaxially with the center of the model;
- Mic 3: a point located 2 cm behind the tested model on its right side (shifted by 4 cm relative to its center (the axis intersecting its center)).

The results of the transmission loss for the $1/12$ octave-band frequencies are shown for an example measurement point (Mic 3), for models made from all three types of materials (for a single side) in Fig. 9.

The presented results show the influence of the metamaterial on the medium-frequency and high-frequency ranges. The highest transmission loss was obtained for the bands 4600, 4870, 5200, 5500, and 1830 Hz (with resonance frequencies obtained for four out of these five of bands). For bands with center frequencies of 3070, 3250, 3450, and 3650 Hz unexpected slight amplifications of the sound pressure level were observed at the Mic 3 measuring point. This is probably due to the measurements being conducted in the near-field region or it can be a constructive (amplifying) resonance effect. A similar situation was observed

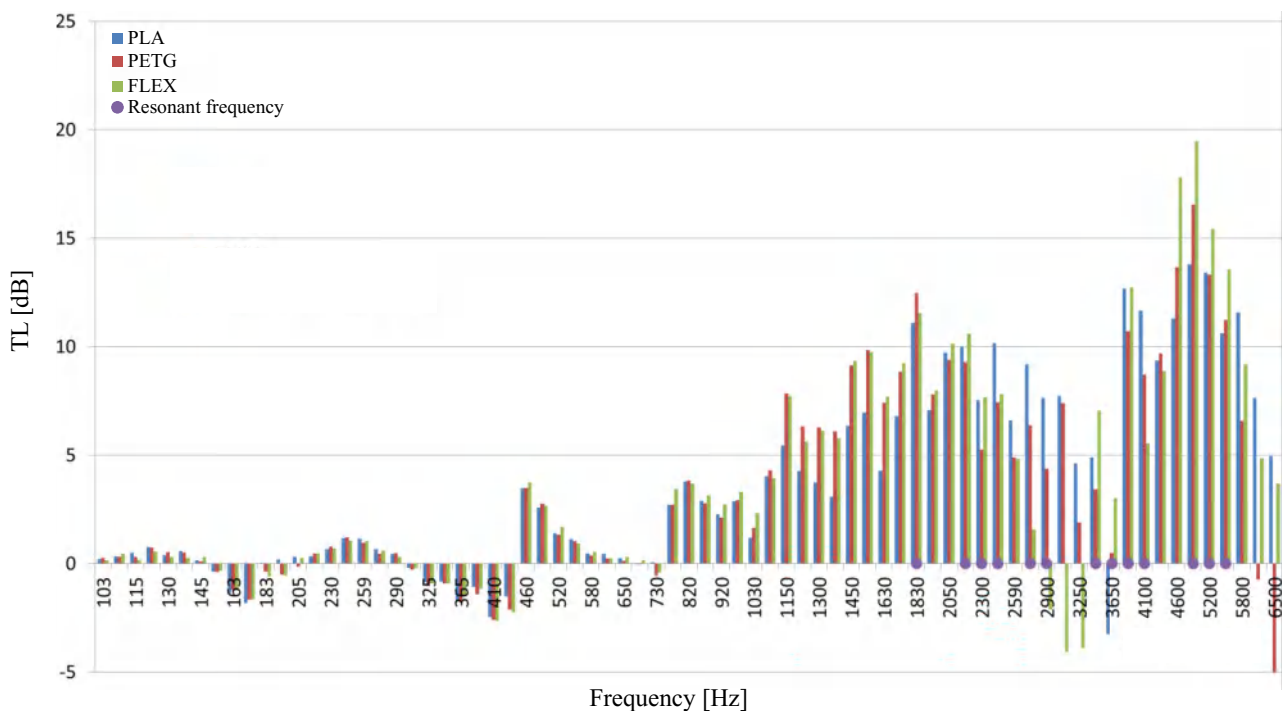


Fig. 9. Transmission loss values for models of acoustic metamaterial with a multi-ring structure made from materials (PETG, PLA and FLEX) for the Mic 3 measuring point.

for the results of measurements after the models were rotated and for the remaining measurement points. Comparison of the transmission attenuation values in $1/12$ octave bands for both sides of a single model (on the example of the Mic 1 measurement point) is shown in Fig. 10.

No significant discrepancies were observed between the results obtained in the transmission loss study for side 1 (Fig. 4, side A) and side 2 (Fig. 4, side B) for each of the physical models. These differences usually did not exceed 2 dB, with the maximum difference being less than 5 dB. These variations may be attributed to the near field effect. The comparison of transmission loss obtained for an individual measurement point of a single model made from PLA on side 2 is shown in Fig. 11.

During the planning phase of the experiment, there was no assumption regarding which of the microphones would be the most representative. Each of the results is representative for a given point in the field. However, the experimental findings indicate that the results for each of the measurement points were similar. The highest values of transmission loss were obtained in the bands with center frequencies ranging from 1830 to 2440 Hz (Mic 1 – from 10.3 to 13.4 dB; Mic 2 – from 7.9 to 12.0 dB; Mic 3 – 7.9 to 11.6 dB) and 3870 to 5500 Hz (Mic 1 – 7.8 to 19.6 dB; Mic 2 – 6.7 to 10.9 dB; Mic 3 – 9.9 to 16.1 dB). For the band with the center frequency of 3650 Hz, a significant decrease in attenuation is observed for acoustic metamaterials made from each type of material (PLA, PETG, and FLEX).

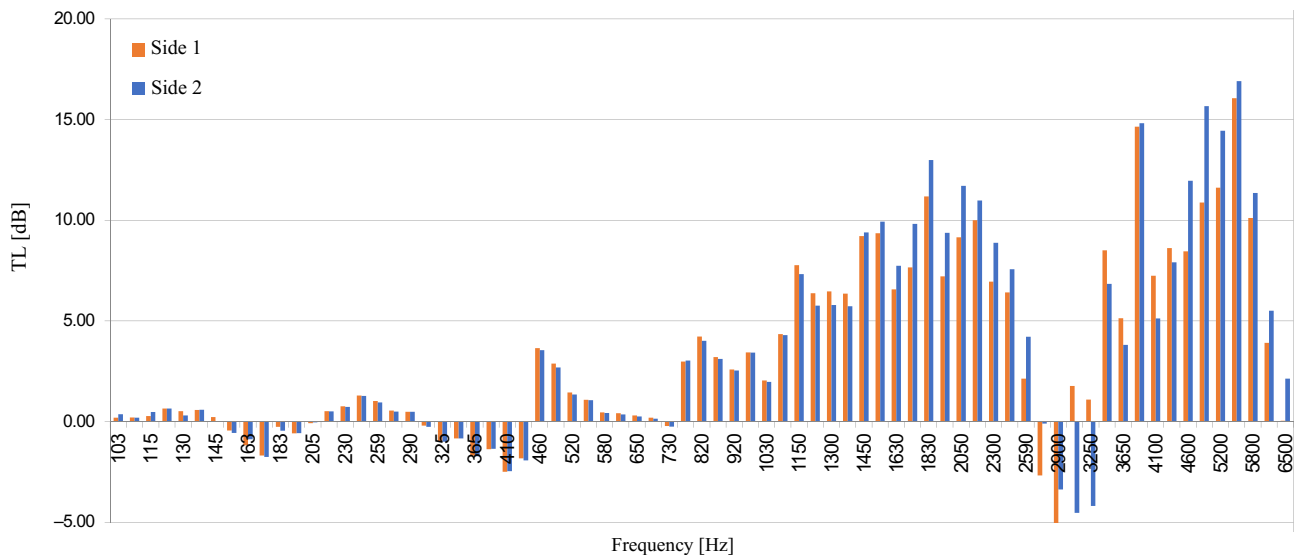


Fig. 10. Transmission loss values for a model of acoustic metamaterial with a multi-ring structure made from FLEX material at the Mic 1 measurement point for both sides of the model.

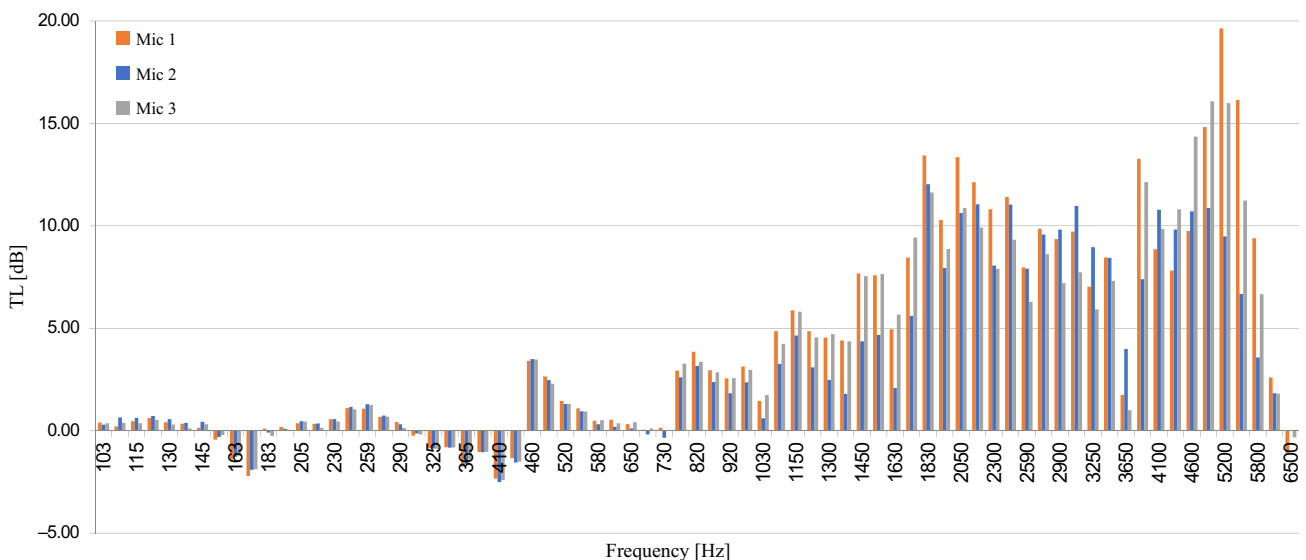


Fig. 11. Transmission loss for the acoustic metamaterial model made out of PLA determined for three measurement points.

5. Conclusions

The conducted numerical analysis with excitation can simulate the conditions similar to those in the experimental transmission loss study. However, due to the different sound pressure levels of the applied excitation and the type of the excitation signal itself (analysis using the pink noise), the values of the sound pressure level in the distributions obtained through numerical research should not be directly compared with the values obtained through experimental research. Additionally, other simplifications used in the numerical study, such as the plane wave assumption, absence of reflections, and no wave propagation on the sides of the structure cause that such results may differ significantly from the results of laboratory tests. For this reason, they were only a reference illustrating the homogeneity of the sound pressure level distribution behind the tested structure.

In most cases, the frequency band in which the highest attenuation was observed coincided with the resonant frequencies obtained through numerical research. Due to the short distance of the microphones from the tested acoustic metamaterial, the results of the transmission loss study were performed in the near field, which could have affected the obtained results. Nonetheless, their purpose was to determine the influence of the material used in the construction of the acoustic metamaterial on the attenuation results. The results prove that the material from which the acoustic metamaterial with a multi-ring structure is made from is of little importance, but the model of such a structure itself must be made with high precision. This precision requirement may pose challenges when using flexible materials in such constructions. Furthermore, the use of 3D printing technique in the production of metamaterials offers a wide range of possible modifications of such structures by affecting their resonant frequencies. The use of various types of materials commonly used in 3D printing for their production, such as rigid materials with special properties (e.g., resistant to high temperatures or weather conditions) can potentially be highly beneficial as well. The presented results for the multi-ring structure demonstrate relatively good values of insertion loss, especially in the medium-frequency and high-frequency ranges, while maintaining small gaps to allow airflow. These attributes make such structures suitable for practical application in sound-absorbing and insulating solutions.

Acknowledgments

This paper is published based on the results of a research task conducted within the scope of the 5th stage of the National Programme “Improvement of safety and working conditions”, supported by resources

from the National Centre for Research and Development. Task no. III.PB.05 titled “Development of acoustic metamaterial for use in soundproofing systems to control noise in industrial environments”. The Central Institute for Labour Protection – National Research Institute is the main coordinator of the program.

References

1. CHEN M., MENG D., JIANG H., WANG, Y. (2018), Investigation on the band gap and negative properties of concentric ring acoustic metamaterial, *Shock and Vibration*, **2018**: 369858, doi: [10.1155/2018/1369858](https://doi.org/10.1155/2018/1369858).
2. DUAN H., SHEN X., WANG E., YANG F., ZHANG X., YIN Q. (2021), Acoustic multi-layer Helmholtz resonance metamaterials with multiple adjustable absorption peaks, *Applied Physics Letter*, **118**(24): 241904, doi: [10.1063/5.0054562](https://doi.org/10.1063/5.0054562).
3. ENGEL Z., PIECHOWICZ J., PLEBAN D., STRYCZNIOWICZ L. (2009), *Industrial Halls, Machines and Devices – Selected Vibroacoustic Problems* [in Polish: *Hale przemysłowe, maszyny i urządzenia – wybrane problemy wibroakustyczne*], Centralny Instytut Ochrony Pracy – Państwowy Instytut Badawczy, Warszawa.
4. GAO N., ZHANG Z., DENG J., GUO X., CHENG B., HOU H. (2022), Acoustic metamaterials for noise reduction: A review, *Advanced Materials Technologies*, **7**(6): 2100698, doi: [10.1002/admt.202100698](https://doi.org/10.1002/admt.202100698).
5. GUS (Central Statistical Office) (2021), *Working Conditions in 2020*, Warsaw, <https://stat.gov.pl/en/topics/labour-market/working-conditions-accidents-at-work/working-conditions-in-2020,1,15.html> (access 11.10.2023).
6. HOWARD C.Q., CAZZOLATO B.S. (2017), *Acoustic Analyses Using Matlab[®] and Ansys[®]*, CRC Press.
7. IANNACE G., CIABURRO G., TREMATERRA A. (2021), Metamaterials acoustic barrier, *Applied Acoustics*, **181**: 108172, doi: [10.1016/j.apacoust.2021.108172](https://doi.org/10.1016/j.apacoust.2021.108172).
8. LIU X., LI X., REN Z. (2020), Miniaturized spiral metamaterial array for a ventilated broadband acoustic absorber, *Shock and Vibration*, **2020**: 8887571, doi: [10.1155/2020/8887571](https://doi.org/10.1155/2020/8887571).
9. MAHESH K., MINI R.S. (2019), Helmholtz resonator based metamaterials for sound manipulation, [in:] *Journal of Physics: Conference Series*, **1355**: 012031, doi: [10.1088/1742-6596/1355/1/012031](https://doi.org/10.1088/1742-6596/1355/1/012031).
10. MAZUR K., WRONA S., PAWELCZYK M. (2018), Design and implementation of multichannel global active structural acoustic control for a device casing, *Mechanical System and Signal Processing*, **98**: 877–889, doi: [10.1016/j.ymsp.2017.05.025](https://doi.org/10.1016/j.ymsp.2017.05.025).
11. MORZYŃSKI L., SZCZEPAŃSKI G. (2018), Double panel structure for active control of noise transmission,

- Archives of Acoustics*, **43**(4): 689–696, doi: [10.24425/aoa.2018.125162](https://doi.org/10.24425/aoa.2018.125162).
12. NAKAYAMA M. *et al.* (2021), A practically designed acoustic metamaterial sheet with two-dimensional connection of local resonators for sound insulation applications, *Journal of Applied Physics*, **129**(10): 105106, doi: [10.1063/5.0041738](https://doi.org/10.1063/5.0041738).
 13. PENNEC Y., DJAFARI-ROUHANI B., VASSEUR J.O., KHELIF A., DEYMIER P.A. (2004), Tunable filtering and demultiplexing in phononic crystals with hollow cylinders, *Physical Review E*, **69**(4): 046608, doi: [10.1103/physreve.69.046608](https://doi.org/10.1103/physreve.69.046608).
 14. RADOSZ J. (2019), Acoustic performance of noise barrier based on sonic crystals with resonant elements, *Applied Acoustics*, **155**: 492–499, doi: [10.1016/j.apacoust.2019.06.003](https://doi.org/10.1016/j.apacoust.2019.06.003).
 15. SIKORA J. (2011), *Rubber Layers in Vibroacoustic Protection Solutions* [in Polish: *Warstwy gumowe w rozwiązaniach zabezpieczeń wibroakustycznych*], Wydawnictwa AGH, Kraków.
 16. SZTYLER B., STRUMILLO P. (2022), Acoustic metamaterials, *Archives of Acoustics*, **47**(1): 3–14, doi: [10.24425/aoa.2022.140727](https://doi.org/10.24425/aoa.2022.140727).
 17. WANG P., CHEN T.-N., YU K.-P., WANG X.-P. (2012), Tunable and large gaps in a two-layer semi-ring structure, *Physica Scripta*, **85**(6): 065402, doi: [10.1088/0031-8949/85/06/065402](https://doi.org/10.1088/0031-8949/85/06/065402).
 18. WRONA S., PAWELCZYK M. (2019), Feedforward control of double-panel casing for active reduction of device noise, *Journal of Low Frequency Noise, Vibration and Active Control*, **38**(2): 787–797, doi: [10.1177/1461348418811429](https://doi.org/10.1177/1461348418811429).
 19. ZHANG X., QU Z., WANG H. (2020), Engineering acoustic metamaterials for sound absorption: From uniform to gradient structures, *iScience*, **23**(5): 101110, doi: [10.1016/j.isci.2020.101110](https://doi.org/10.1016/j.isci.2020.101110).
 20. ZIELIŃSKI T.G. *et al.* (2020), Reproducibility of sound-absorbing periodic porous materials using additive manufacturing technologies: Round robin study, *Additive Manufacturing*, **36**: 101564, doi: [10.1016/j.addma.2020.101564](https://doi.org/10.1016/j.addma.2020.101564).

Research Paper

Impulse Excitation in a Watertight Steel Circular Cylindrical Shell and Influence of Structural Configuration on Underwater Radiated Noise

Chen-I WU*, Gee-Pinn TOO, Bo-Hsien WU

*Department of Systems and Naval Mechatronic Engineering, National Cheng Kung University
Tainan, Taiwan*

*Corresponding Author e-mail: kpssi3006@gmail.com

(received September 4, 2022; accepted June 20, 2023)

This study used experimental measurements and the finite-element method (FEM) simulations to investigate transient underwater radiated noise induced by the impulse excitation of water surrounding a watertight steel-structured circular cylindrical shell submerged in the $176 \times 8 \times 4$ m towing tank. The excitation was caused by dropping an iron block onto a structural bracket in the shell to generate structural vibration. The experimental results were found to be consistent with the FEM results, with the difference between the experimental and simulated sound pressure levels being less than 3 dB. Moreover, it was determined that the structural vibration also generated airborne noise in the cylindrical shell, but this contributed much less than the impulse excitation to the induction of underwater radiated noise. Finally, analysis of the sound field of the underwater noise radiation showed that it was influenced by the wall thickness of the watertight steel cylindrical shell and that of the reinforced bracket seat structure. In particular, the structural reinforcement position proved to be the diffusion breakpoint of the underwater sound radiation. This demonstrates that compared with the studied structure, a thicker and more complex reinforced structure will transmit less or incomplete sound radiation into water.

Keywords: impulse excitation; influence of structural configuration; FEM analysis; underwater noise radiation characteristics.



Copyright © 2023 The Author(s).
This work is licensed under the Creative Commons Attribution 4.0 International CC BY 4.0
(<https://creativecommons.org/licenses/by/4.0/>).

1. Introduction

Understanding the characteristics of noise radiated from underwater vehicles is a key research challenge. As underwater noise radiation is influenced by the structure of underwater vehicles, vehicle-induced underwater noise can be predicted by model simulation, and underwater noise and structure-borne noise caused by vibrating structures can be determined by testing experimental models. In this study, hydrophones were used to measure the underwater noise-radiation sound field caused by an impulse-induced vibration in a model underwater vehicle. In addition, the underwater noise-radiation sound field was numerically simulated using the finite-element method (FEM).

The underwater radiated noise was generated by dropping an iron block onto a section of a model underwater vehicle inside a watertight steel circular cylindrical shell submerged in water in the $176 \times 8 \times 4$ m towing tank. The experimental setup was remotely con-

trolled and a hydrophone line array was used to measure radiating noise in the towing tank. In addition, FEM was used to simulate underwater radiated noise induced by the impulse vibration of a submerged and watertight steel circular cylindrical shell. The effects of the cylindrical shell's structural configuration and the wall thickness on the sound radiation field were investigated. Previous experimental and FEM simulation studies in this area are reviewed below.

In (WAWRZYNOWICZ *et al.*, 2014), the acoustic sound insulation performances of cement and foamed composite materials were studied via FEM simulation to analyze the transient and steady states of two-dimensional and three-dimensional models. In addition, experimental measurements were made to compare sound absorption rates. The results generated by the both models for both transient and steady states agreed with the experimental curve. In (RAWAT *et al.*, 2015), the vibration response of a three-dimensional cylindrical liquid tank subjected to three-

dimensional transient seismic waves was studied by an acoustic-structural FEM. This was used to explore how the force induced by liquid shock water pressure coupled with the vertical force of the seismic wave to dynamically affect the tank bottom.

In (JUNGER, FEIT, 1986), two thin-shelled cylindrical shells with different aspect ratios were subjected to an excitation force, and an analytical solution was obtained for the sound pressure level (SPL) in the far field. In (WU, TOO, 2021), underwater steady-state noise was generated and measured in a watertight steel circular cylindrical shell submerged in a towing tank, and the simulation results of the towing tank were consistent with the experimental results. This verified that FEM is feasible for the analysis of underwater sound radiation induced by continuous machine vibration in a towing tank. Thus, experimental measurements and FEM simulation can be used to analyze the radiated sound field generated by an underwater vehicle containing an operating machine. In an earlier study (WU *et al.*, 2022), the characteristics of the boundary was an important factor to the accuracy of measurements and simulations for underwater radiation in a towing tank. The experiment was conducted to vibrate the watertight cylinder and to measure the underwater sound field, which was significantly impacted by reflections from the tank walls. The experimental measurements and underwater sound field simulations were consistent with each other at 45 and 250 Hz. The simulation and experiment were slightly larger in the 500 Hz case. The result was the simulations investigated the factors affecting the towing tank's boundary effects. In (LEADER *et al.*, 2013), the sound and vibration of a torpedo-shaped structure under axial force excitation were experimentally investigated, and in (WANG *et al.*, 2000), machine vibration-induced underwater acoustic radiation was studied. The simulation theories in the present study and the FEM for fluid-structure interaction have also been applied in (WU, 1989; WU, CHEN, 2017; ETTER, 2018).

Several studies have conducted underwater structure-borne radiated noise experiments and acoustic-structural coupling simulations (YOSHIKAWA, 1993; RUGONYI, BATHE, 2001; MATTHEW, 2004; TONG *et al.*, 2007; QIAN *et al.*, 2012; ZHANG *et al.*, 2016). These studies have used the FEM or the boundary element method to analyze underwater noise and study the fluid-structure coupling vibration performance of a submerged double-cylindrical shell of a ship. The vibroacoustic response of a shaft-hull system was also numerically and experimentally investigated (LIN *et al.*, 2016).

In a boundary study (SACKS *et al.*, 1995), the perfectly matched layer approach (PML) was devised – in which the acoustic pressure on a peripheral boundary is set to 0 – to indicate that the acoustic pressure on a radiation boundary was completely absorbed. This means that an appropriate increase in the ab-

sorption coefficient of the main control equation enables the control equation of the absorption layer to be transformed. In (ALVAREZ-ARAMBERRI *et al.*, 2014), a method for performing calculations for the automatically matched layer (AML) approach, an advanced version of the PML technology, was devised. PML calculation accuracy is affected by absorbing layer parameters, which are determined by researchers. In contrast, the AML approach does not require the manual definition of the absorption layer grid. Instead, the absorption layer parameters are automatically defined based on a model, such that they meet the infinite domain boundary.

2. Basic methodology

Theoretically, the wave equation can obtain the transient and steady-state solutions of acoustic-fluid coupling, and the Helmholtz equation is only suitable for solving steady-state solutions. In this study, the steel block dropped onto the steel cylindrical shell is the transient solution to solve the fluid-solid coupling. Therefore, the ABAQUS software uses the wave equation to derive the transient acoustic-fluid coupling solution first, and then derives the fluid-solid coupling solution.

The response of underwater noise generated from transient structural vibration can be directly derived from the wave equation. That is, the response is discretized from the sound domain, and thus the coupled transient acoustic-structural equation can be derived. The structure is regarded as an elastic body surrounded by fluid, such that structural vibration generates a fluid load at the fluid-solid interface and sound pressure generates an additional force on the structure. Therefore, the structural dynamic equation and the wave equation in the fluid domain must be calculated. The displacement and sound pressure on the fluid-structure interface are obtained via model discretization and from the wave and motion equations, as in (ABAQUS, 2014). Then, based on the assumption that the fluid is an ideal acoustic medium, the wave equation of sound pressure in a three-dimensional space is expressed as:

$$\nabla^2 P - \frac{1}{c^2} \frac{\partial^2 P}{\partial t^2} = 0, \quad (1)$$

where P is the instantaneous sound pressure, t is a time variable, and c is the velocity of sound in the medium, and

$$\nabla^2 = \left(\frac{\partial^2}{\partial x^2} + \frac{\partial^2}{\partial y^2} + \frac{\partial^2}{\partial z^2} \right). \quad (2)$$

The law of finite elements is used as an approximation method to calculate and obtain the solution of the wave equation. Equation (1) is thus rewritten as:

$$\nabla \cdot (\nabla P) - \frac{1}{c^2} \frac{\partial^2 P}{\partial t^2} = 0. \quad (3)$$

By applying the Galerkin approximation method, multiplying a sound pressure function of a boundary condition Φ , and integrating on the sound domain Ω , Eq. (4) is obtained:

$$\int_{\Omega} \Phi [\nabla \cdot (\nabla P)] d\Omega - \int_{\Omega} \Phi \left[\frac{1}{c^2} \frac{\partial^2 P}{\partial t^2} \right] d\Omega = 0. \quad (4)$$

From the chain rules of gradients:

$$u (\nabla \cdot \mathbf{v}) = \nabla \cdot (u \mathbf{v}) - (\nabla u) \cdot \mathbf{v}, \quad (5)$$

where \mathbf{v} is the vector notation and u is a unit direction vector, therefore Eq. (4) can be written as:

$$\begin{aligned} \int_{\Omega} \nabla \cdot (\Phi \nabla P) d\Omega - \int_{\Omega} \nabla \Phi \cdot \nabla P d\Omega \\ - \int_{\Omega} \Phi \left[\frac{1}{c^2} \frac{\partial^2 P}{\partial t^2} \right] d\Omega = 0. \end{aligned} \quad (6)$$

From the divergence theorem:

$$\int_{\Omega} \nabla \cdot \mathbf{A} d\Omega = \int_{\Gamma} \mathbf{A} \cdot \mathbf{n} d\Gamma, \quad (7)$$

where Γ is the boundary, \mathbf{A} is an arbitrary vector, and \mathbf{n} is the vector perpendicular to the boundary. In the fluid-structure interaction problem, Γ represents the water-structure contact surface; accordingly, Eq. (6) can be written as follows:

$$\begin{aligned} \int_{\Gamma} \Phi \nabla P \cdot \mathbf{n} d\Gamma - \int_{\Omega} \nabla \Phi \cdot \nabla P d\Omega \\ - \int_{\Omega} \Phi \left[\frac{1}{c^2} \frac{\partial^2 P}{\partial t^2} \right] d\Omega = 0. \end{aligned} \quad (8)$$

By considering the water and the structure in the normal direction of the contact surface, the relationship between the water pressure gradient and structure is expressed as:

$$\mathbf{n} \cdot \nabla P = -\rho \mathbf{n} \left(\frac{\partial^2 \mathbf{u}}{\partial t^2} \right), \quad (9)$$

where \mathbf{u} is the displacement vector of the structure on the boundary surface. Equation (9) can also be written as:

$$\int_{\Gamma} \Phi \nabla P \cdot \mathbf{n} d\Gamma = \int_{\Gamma} \Phi \left(-\rho \mathbf{n} \frac{\partial^2 \mathbf{u}}{\partial t^2} \right) d\Gamma. \quad (10)$$

Substituting Eq. (10) into Eq. (8) gives the following sound fluid equation:

$$\begin{aligned} \int_{\Omega} \Phi \left[\frac{1}{c^2} \frac{\partial^2 P}{\partial t^2} \right] d\Omega + \int_{\Omega} \nabla \Phi \cdot \nabla P d\Omega \\ = - \int_{\Gamma} \Phi \rho \mathbf{n} \left(\frac{\partial^2 \mathbf{u}}{\partial t^2} \right) d\Gamma. \end{aligned} \quad (11)$$

The known structural motion equation is:

$$[M_s] \{\ddot{U}\} + [C_s] \{\dot{U}\} + [K_s] \{U\} = \{F_s\}. \quad (12)$$

The sound fluid equation (Eq. (11)) is discretized and divided into several finite elements. Any point in the sound pressure elements and the displacement of the mass point are discretized with respect to time. This discretization can be performed through the interpolation of the corresponding value at the node of the element, and the sound pressure boundary condition function Φ can be eliminated. Equations (11) and (12) are thus combined into an acoustic-structural coupling equation as:

$$\begin{aligned} \begin{bmatrix} [M_s] & [0] \\ \rho [R]^T & [M_f] \end{bmatrix} \begin{bmatrix} \{\ddot{U}\} \\ \{\ddot{P}\} \end{bmatrix} + \begin{bmatrix} [C_s] & [0] \\ [0] & [C_f] \end{bmatrix} \begin{bmatrix} \{\dot{U}\} \\ \{\dot{P}\} \end{bmatrix} \\ + \begin{bmatrix} [K_s] & [0] \\ [0] & [K_f] \end{bmatrix} \begin{bmatrix} \{U\} \\ \{P\} \end{bmatrix} = \begin{bmatrix} \{F_s\} \\ [0] \end{bmatrix}, \end{aligned} \quad (13)$$

where $[M_s]$ is the mass matrix of the structure; $[M_f]$ is the mass matrix of the fluid; $[R]$ is the coupling factors; $[C_s]$ is the damping matrix of the structure; $[C_f]$ is the damping matrix of the fluid; $[K_s]$ is the stiffness matrix of the structure; $[K_f]$ is the stiffness matrix of the fluid; and $\{F_s\}$ is the structural load vectors.

The explicit dynamic-solver-analysis method is used with an extremely small time-step increment, as the setting of the time-step increment directly affects the simulation result in dynamic analysis. The central difference integration algorithm is used in the dynamic analysis to solve the overall balance equation for the entire operational process. Then, the dynamic equation is used to calculate the dynamic state of the next time-step increment. The dynamic balance equation for a single-degree-of-freedom system is expressed as:

$$m\ddot{u} + c\dot{u} + ku = p(t). \quad (14)$$

From the central difference theorem:

$$\dot{u}_i = \frac{u_{i+1} - u_{i-1}}{2\Delta t}, \quad (15)$$

$$\ddot{u}_i = \frac{u_{i+1} - 2u_i + u_{i-1}}{(\Delta t)^2}. \quad (16)$$

Substituting Eqs. (15) and (16) into Eq. (14) yields:

$$m \frac{u_{i+1} - 2u_i + u_{i-1}}{(\Delta t)^2} + c \frac{u_{i+1} - u_{i-1}}{2\Delta t} + ku_i = p_i. \quad (17)$$

Equation (17) can be rewritten as:

$$\begin{aligned} \left[\frac{m}{(\Delta t)^2} + \frac{c}{2\Delta t} \right] u_{i+1} = p_i - \left[\frac{m}{(\Delta t)^2} - \frac{c}{2\Delta t} \right] u_{i-1} \\ - \left[k - \frac{2m}{(\Delta t)^2} \right] u_i. \end{aligned} \quad (18)$$

According to Eq. (18), the displacement at a moment is related to that at the previous moment. The displacement, velocity, and acceleration of the model nodes are related to the incremental learning at each step. Therefore, ABAQUS/Explicit uses a very small initial time increment and many increment steps to complete the central difference method.

Equation (19) shows that in the time integration, the time increment directly affects the solution accuracy. The upper limit of the time increment is therefore used to obtain the stable value. In the absence of damping, the stable value of the time increment can be expressed as:

$$\Delta t_{\text{stable}} = \frac{2}{\omega_{\text{max}}}. \quad (19)$$

However, several factors affect the frequency of a system, and sometimes its highest frequency cannot be accurately calculated. Therefore, another method is adopted to obtain a stable value, as shown in Eq. (20):

$$\Delta t_{\text{stable}} = \frac{L^\varepsilon}{C_d}, \quad (20)$$

where L^ε is the minimum length of the grid element, and C_d is the material wave velocity. Therefore, as the size of grid elements reduces, the time increment decreases accordingly, consistent with the time-stable incremental value.

In the FEM calculation, Eq. (13) is solved via the explicit integration method, and the derivatives of acceleration and velocity are replaced by central difference using the central difference method. Then, the state variable equation for the time before the small increment time is solved, and the effective load matrix and the effective load vector are calculated. This method can be used to calculate the dynamic instantaneous displacement condition of the next time increment within each tiny time increment, as in (ABAQUS, 2014).

In the ABAQUS software to perform transient micro-time step calculations, the software itself must have a high number of cores. This study only used a high-performance notebook computer CPU using 8 GB of RAM and one core calculations. Using the explicit dynamic solver, and setting the time period to 0.05 s, and each increment to 0.0001 s, the total calculation of 0.05 s took about 3 to 4 days. The operation time depends on the complexity of the structure and the length of the operation time. To speed up the computing speed, that can increase the computing cores of the software and increase the computing cores of the hardware.

3. Experimental measurement and analysis procedure

In this study, impulse excitation measurements were conducted to obtain the underwater radiation

sound field. The architecture of the entire process was established via several experiments and simulation. The experimental measurement and analysis of the impulse-induced structural noise are described below. The procedure of the impulse-induced structural noise experiment is shown in Fig. 1.

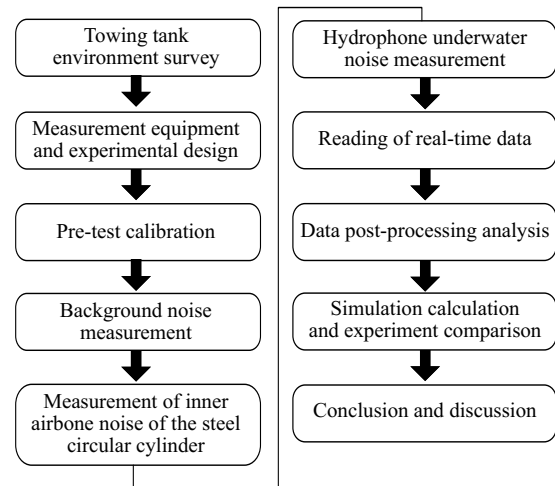


Fig. 1. Procedure of watertight steel circular cylindrical shell underwater measurement, and comparison with simulation results.

First, the towing tank was surveyed to confirm that it was sufficient to contain the watertight steel circular cylindrical shell. To ensure the feasibility of the experiment, the detailed experimental conditions were considered, such as the depth, environment, and background noise of the towing tank, and the capability of the tank to be hoisted on an experimental vehicle.

Second, the measuring vehicle was assembled and prepared. The 1 kg iron block was magnetically attached to the inside roof of the submerged watertight steel circular cylindrical shell and could be dropped by remote control to generate a vibration and noise that simulated an impulse-induced vibration noise radiated from an actual submerged vehicle (Fig. 2). The watertight steel circular cylindrical shell was designed (Fig. 3) so that it could be operated underwater and in air. The measuring instruments (a hydrophone, a sound level meter, and a microphone) were calibrated before measurement.

At the beginning of the underwater measurement, the background noise of the towing tank was measured. The sound level meter was used to measure the SPL of the airborne noise generated by the impulse excitation, and the underwater sound field of the hydrophone was measured. All measured values were converted via the fast Fourier transform (FFT) to obtain the frequency spectrum, and the values of repeated measurements were assessed to evaluate stability.

Many data were post-processed and analyzed to obtain the SPL of the underwater sound field. These data were compared with the FEM simulation data

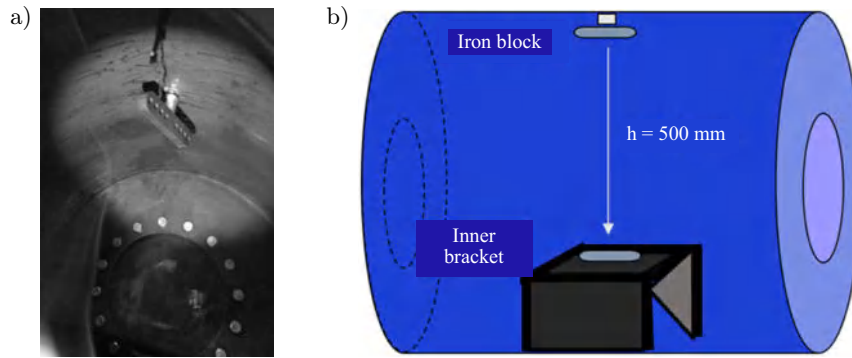


Fig. 2. Photograph of iron block magnetically attached to the roof inside a watertight steel circular cylindrical shell (a) and diagram of the full setup (b).



Fig. 3. Photograph of the watertight steel circular cylindrical shell being loaded into the towing tank (a) and the B&K 8104 hydrophone used to measure underwater noise (b).

for the water course direction of the towing tank. Finally, the characteristics of underwater sound radiation and the structural configuration of the vehicle were explored.

To obtain the radiation underwater sound field, the actual structural vibration of a fluid-structure interaction sound field was simulated using a numerical model and generated in an experimental model, with both models being of the same size and configuration. The underwater noise level was measured, and the results were compared with the FEM simulation results. The experimental measurement was conducted in the towing tank with a length of 176 m, width of 8 m, and depth of 4 m. The center of the watertight steel circular cylindrical shell was 1.5 m beneath the water surface.

The B&K 8104 hydrophone (Fig. 3b) with a measuring frequency of 0.1 Hz–120 kHz was used for the underwater noise measurement. The frequency range and dynamic range of the microphone were 5–20 000 Hz and 182 dB re 20 μ Pa, respectively. The SPL and frequency ranges of the sound-level meter were 28–141 dB and 20 Hz–8 kHz, respectively. In the experimental measurement, a four-by-one hydrophone line array was installed in the watercourse direction at 0.5, 1, 1.5, and 2 m in the towing tank (Fig. 4).

The hydrophones were connected to the signal extractor through an analog-digital converter. The data were collected at a sampling frequency of 100 kHz, the frequency spectrum was obtained via FFT, and data were transmitted to a computer for storage. In addi-

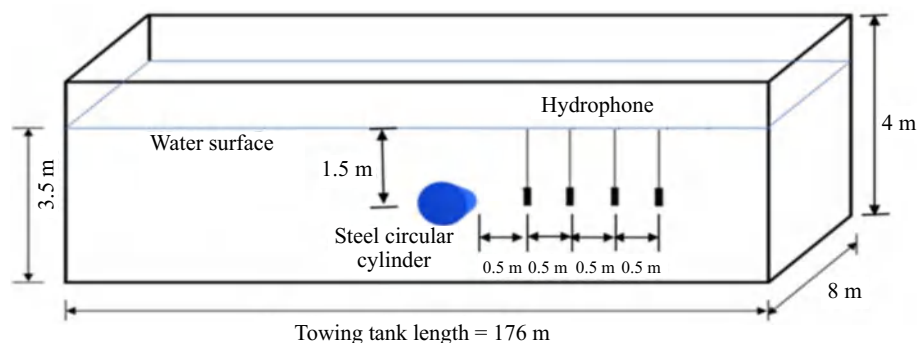


Fig. 4. Underwater configuration of hydrophone line array and the watertight steel circular cylindrical shell.

tion, the SPL of the inner airborne noise in the watertight steel circular cylindrical shell was measured using a sound level meter and was used to estimate the airborne source noise power induced by structural

vibration. The iron block had an initial velocity V_0 of 0 mm/s and was positioned at a height of 500 mm above the bottom of the inner bracket surface of the watertight steel circular cylindrical shell. The velocity

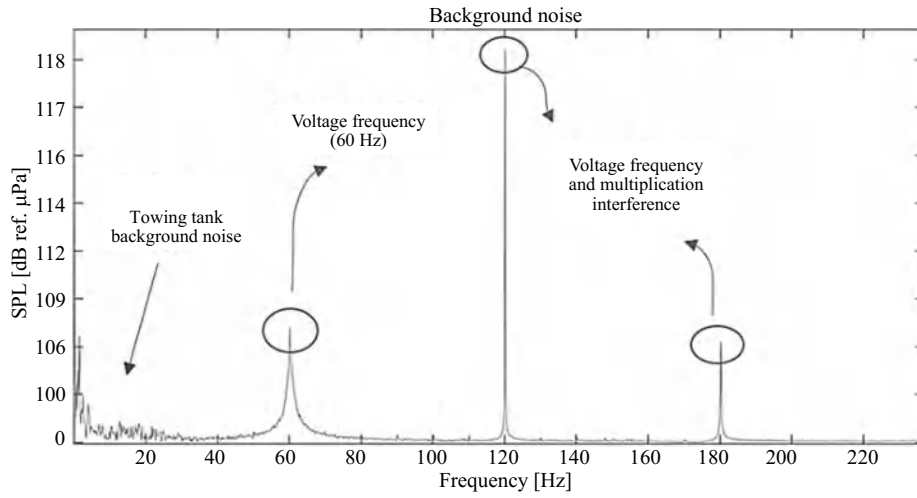


Fig. 5. Towing tank background noise measurement in the frequency domain.

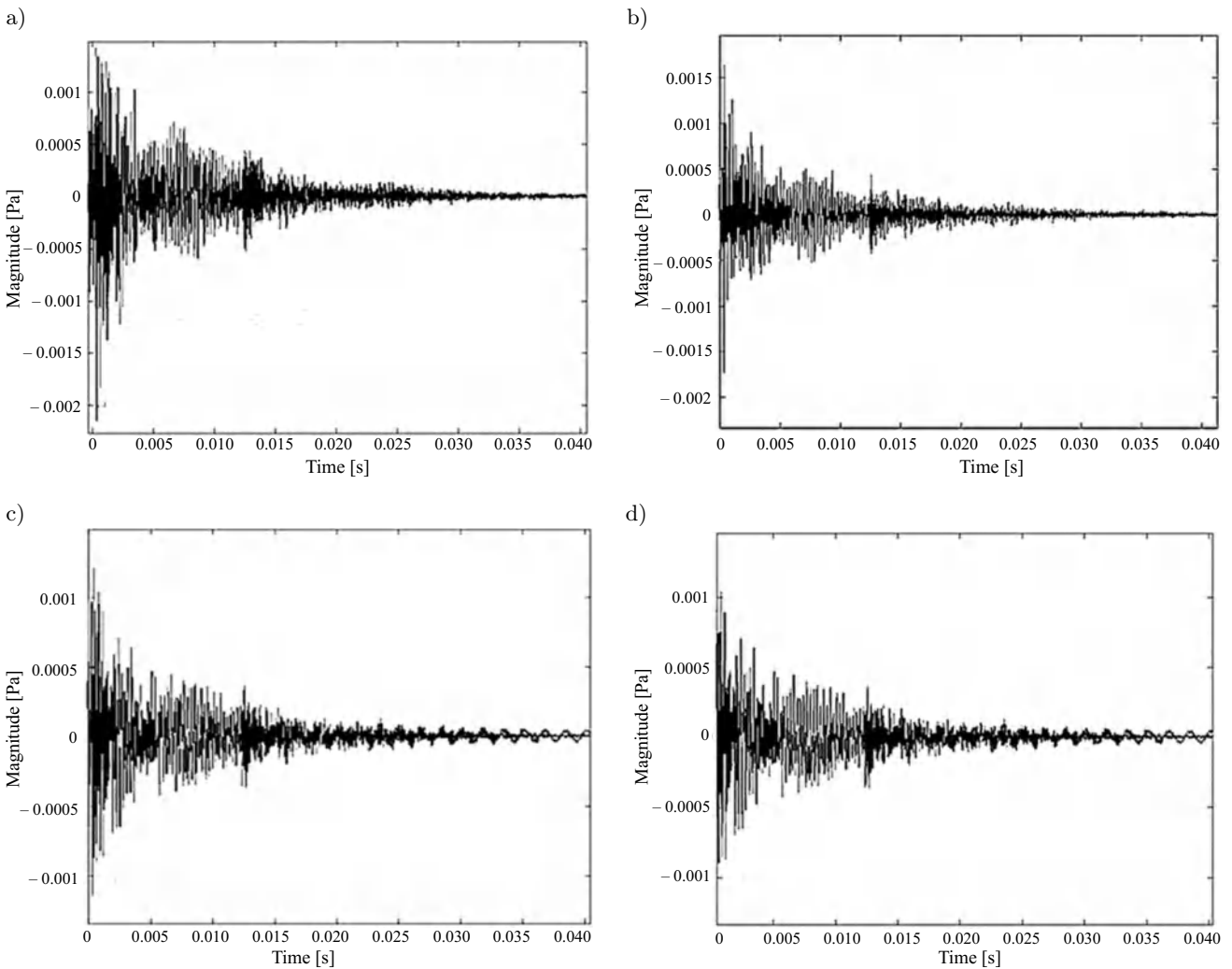


Fig. 6. Measured time series data of underwater acoustic pressure at 0.5 m (a), 1.0 m (b), 1.5 m (c), and 2.0 m (d) from the steel circular cylindrical shell.

of the iron block immediately before its impact with the bracket was calculated according to the conservation of energy from the roof to the impact point. The airborne noise power and the velocity of the block before impact were used as inputs of the FEM model.

The experimental results revealed that the airborne source noise contributed much less than the impulse-induced vibration generated by the impact of the iron block to the underwater radiated noise. Hence, the contribution of airborne noise was ignored and only the velocity of the iron block before its impact with the bracket (i.e., before the impulse excitation) was used as an input for the simulation. Previous studies (WU, TOO, 2021) have indicated that the background noise of this towing tank is low-frequency noise (<20 Hz) as shown in Fig. 5; as this is much lower in frequency than the impulse-induced vibration noise, the towing tank background noise was ignored in the simulation process.

The watertight steel circular cylindrical shell was designed with the following specifications: a ring thin

shell of 8 mm, a two-sided thick shell of 12 mm, and an inner bracket of 8 mm. It was also fitted with watertight adapters and electromagnet device control lines. The steel circular cylindrical shell (Fig. 3a) has a weight of 284 kg, a diameter of 0.803 m, and a length of 1 m. The loading balance block and iron block were 212 and 1 kg, respectively. The steel circular cylindrical shell was suspended in the towing tank with remote controlled cables and a hydrophone array.

Figure 6 shows the time series data measured from the hydrophone line array in the watercourse direction at 0.5, 1.0, 1.5, and 2 m. This indicates the magnitude of the underwater impulse-induced vibration noise and decay within 0.4 s. The measured time series data were converted via FFT to obtain the frequency spectra at 0.5 and 1.0 m (Fig. 7). The transient vibration caused by impulse excitation produced a broadband frequency spectrum. This broadband frequency spectrum was the nature frequencies of steel circular cylinder cylindrical shell in the water and the 374 Hz was the larger amplitude frequency as shown in Fig. 8. Therefore, the

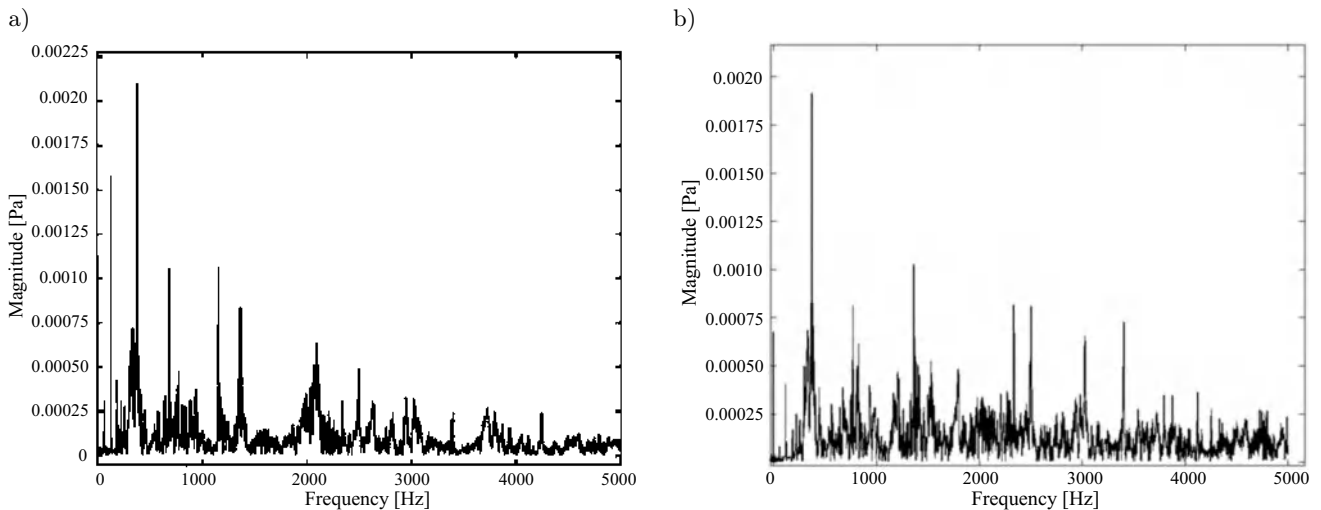


Fig. 7. Measured frequency spectrum of underwater acoustic pressure at 0.5 m (a) and 1.0 m (b) from the steel circular cylindrical shell.

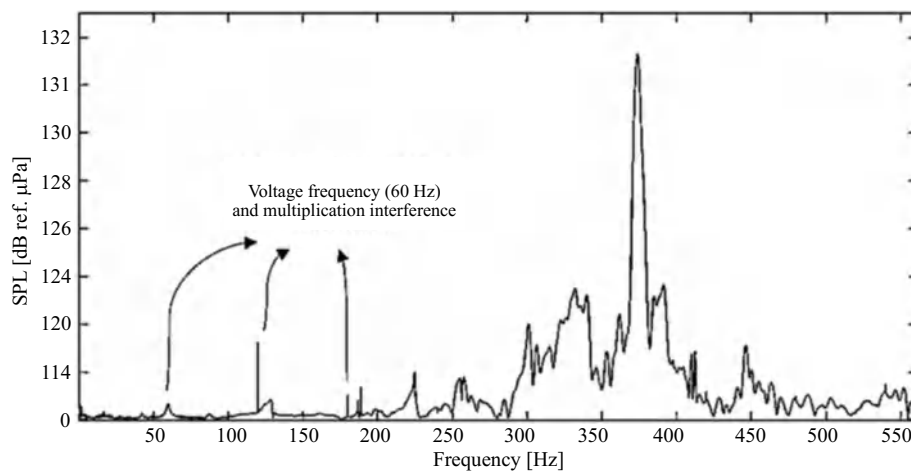


Fig. 8. Nature frequencies of steel circular cylindrical shell in the water and 374 Hz was the larger amplitude frequency.

peak magnitude of time series data was used for SPL calculation. The experimental results were compared with the FEM results, as presented in the next section.

4. Comparison of FEM simulation results with experimental results

The impulse-induced vibration noise radiated from the submerged steel circular cylindrical shell was also simulated via FEM, and the simulation results were compared with the experimental results.

The simulation results of the towing tank are in reasonable agreement with the experiment results, which demonstrates that FEM is a feasible method for analyzing underwater radiated noise. The simulation process is shown in Fig. 9.

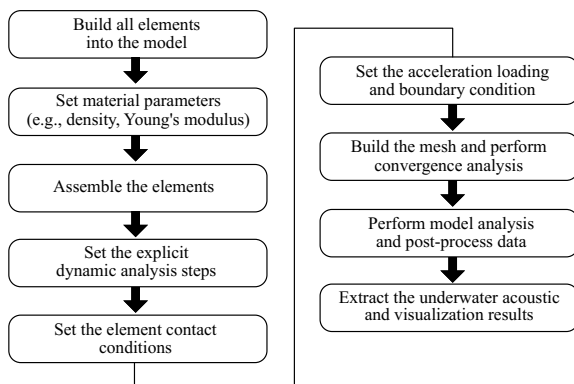


Fig. 9. Set the steps for the explicit dynamic analysis for the underwater vibration noise of impulse-excited structure.

A simulated model of the steel circular cylindrical shell was generated based on the experimental model and is presented in Figs. 10a and 10b, and Table 1, and the steel circular cylindrical shell payload was set to ensure that its weight and buoyancy in water were balanced, as shown in Table 2. The towing tank water model was established under loading and boundary conditions. The boundary condition of the water tank set the acoustic impedance at the bottom and both sides of the tank to approximately $4.3 \times 10^6 \text{ kg/m}^2\text{s}$. The towing tank front and rear walls were far away from the steel cylindrical shell and set non-reflection boundaries. The water surface boundary represents the pressure-release surface. The water surface was located above the steel circular cylinder, which was set in the center of the towing tank (Wu, Too, 2021). The towing tank model and boundaries were shown in Fig. 11 and the parameters were listed in Tables 3 and 4.

In the simulation, a dropped iron block modeled on the top of the bracket (Fig. 10b), as in the experiment. The impulse excitation caused a bracket vibration that was transmitted to the underwater radiated sound field. The parameters of the simulation of the iron block impulse excitation are listed in Table 5.

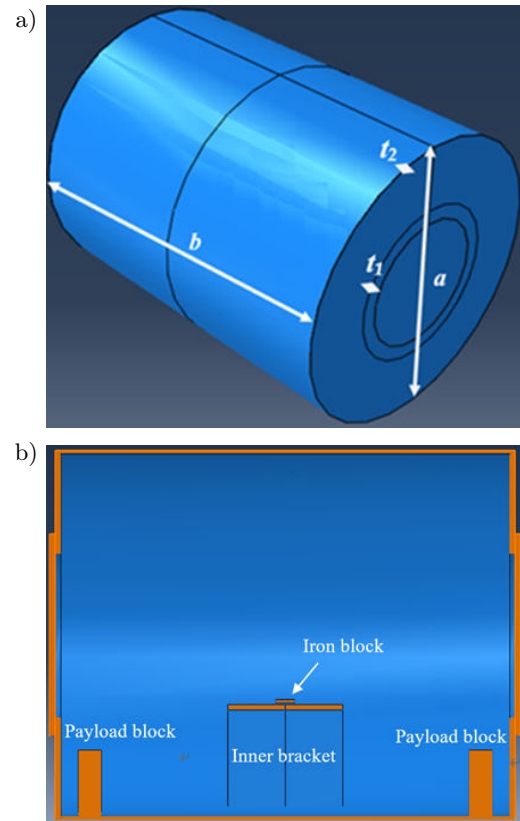


Fig. 10. Diagrams of the steel circular cylindrical shell model (a) and steel circular cylindrical shell inner configuration (b).

Table 1. Dimensions of steel circular cylindrical shell model.

| | |
|---|----------|
| Steel circular cylinder weight | 284 kg |
| Thick round end-plate radius (a) | 0.4015 m |
| Thick round end-plate thickness (t_1) | 0.012 m |
| Thin shell cylindrical length (b) | 1 m |
| Thin shell thickness (t_2) | 0.008 m |

Table 2. Dimensions of steel circular cylindrical shell payload model.

| | |
|-----------------------------|--------|
| Payload weight | 212 kg |
| Payload thickness (t_3) | 0.01 m |

Table 3. Properties of elements of the steel circular cylindrical shell materials in the model.

| Elements | Steel circular, cylindrical shell, inner bracket, payload block and iron block |
|--|--|
| Material | Low-carbon steel |
| Young's coefficient (E) [GPa] | 205 |
| Poisson's ratio (ν) | 0.3 |
| Density (ρ) [kg/m^3] | 7850 |

Table 4. Dimensions of the towing tank model.

| | |
|-----------------------|--------------------------------------|
| Towing tank dimension | $176 \times 8 \times 4 \text{ m}$ |
| Water density | $1.0 \times 10^9 \text{ tonne/mm}^3$ |
| Water bulk modulus | 0.139 MPa |

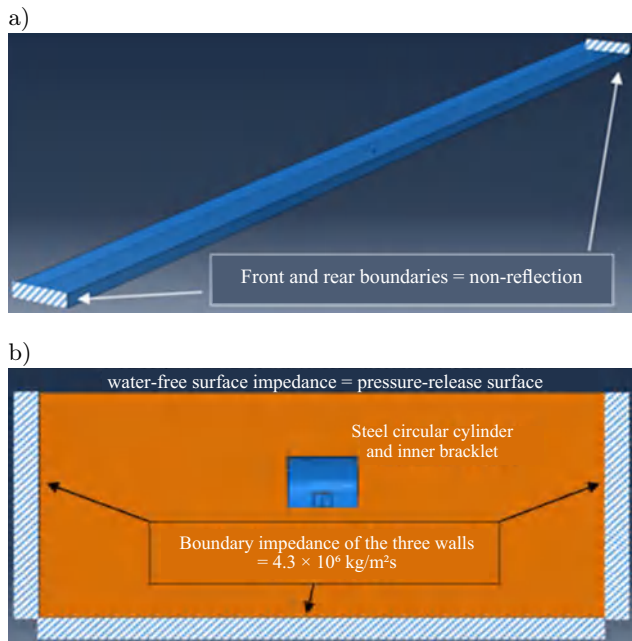


Fig. 11. Diagram of towing tank water model (a) and boundary conditions (b).

Table 5. Parameters of the simulation of the iron block impulse excitation.

| | |
|------------------------------------|-------------------------|
| Iron block weight | 0.001 ton |
| Iron block dropping height (h) | 500 mm |
| Gravitational acceleration (g) | 9 800 mm/s ² |
| Initial speed (V_0) | 0 mm/s |
| Final speed (V_1) | 3 130.5 mm/s |

Seed edges and grid types were set for the mesh grid geometry. Three-dimensional solid elements were used for analysis during the simulation. The mesh elements and grid quantities are shown in Table 6.

Table 6. Types of mesh and grid quantities for elements.

| Element | Mesh grid type | Grid quantity |
|----------------------------------|----------------|---------------|
| Towing tank | AC3D4 | 8 744 042 |
| Steel circular cylindrical shell | C3D4 | 9 190 |
| Inner bracket | C3D8R | 1 872 |
| Payload block | C3D4 | 1 477 |
| Iron block | C3D8R | 156 |

To confirm the correctness of the analysis results, the FEM was used for the convergence analysis. The grid quantity of a mesh directly affects simulation accuracy: a smaller mesh division yields more accurate analysis results than an larger mesh division. However, a mesh grid that is too small may generate too many nodes in a model, which may result in too many degrees of freedom and thereby make the model unstable and increase computational costs.

For the simulation of the sound pressure magnitude, the first hydrophone was placed at a certain dis-

tance from the steel circular cylindrical shell in the water tank. The comparison objects of grid quantity were analyzed. The grid dimension sizes and quantities are shown in Table 7.

Table 7. Mesh grid types and quantity.

| Grid dimension Δx [mm] | Grid quantity |
|--------------------------------|---------------|
| mesh125 | 14 289 405 |
| mesh150 | 8 744 042 |
| mesh175 | 5 681 363 |
| mesh200 | 4 221 977 |
| mesh225 | 3 561 442 |
| mesh250 | 3 015 747 |

The grid analysis comparison was based on the sound pressure magnitude at 0.0008 s, and a convergence analysis of the water grid was performed. Grid dimensions Δx of 250 to 125 mm were used in the convergence analysis. The grid dimension was as shown in Fig. 12a. At a grid size of 150 mm and a quantity of 8 744 042, the sound pressure was 0.0017617 Pa. At a finer grid size (125 mm) and a higher quantity (14 289 405), the sound pressure magnitude did not change significantly (Fig. 12b). Therefore, a water tank grid size of 150 mm was chosen for further simulation analyses.

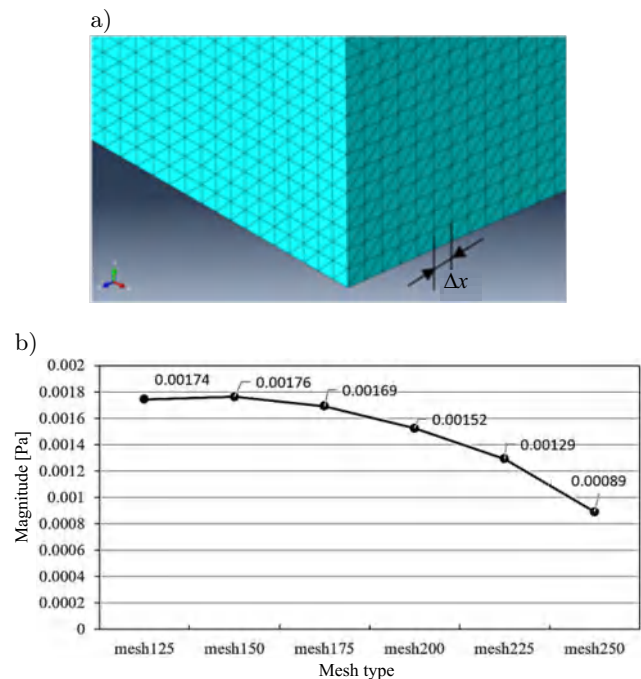


Fig. 12. Diagram of towing tank grid dimension Δx (a) and the convergence analysis of mesh types (b).

In the simulation study, four hydrophones revealed that the main energy occurred at 0–0.01 s. The energy gradually dissipated after 0.05 s and finally tended to be static and stable. The analog data from 0 to 0.001 s show that hydrophones at an interval of 0.5 m exhibited a difference in the vibration start time Δt .

The first hydrophone firstly starts to vibrate, and the second started to vibrate ~ 0.0003 s later, and this trend continued for the third and fourth hydrophones; Δt (0.0003 s) was exactly the time it took for the sound to travel 0.5 m in the water, as shown in Fig. 13.

The simulation analysis time was 0.05 s, and each increment was 0.0001 s. The underwater noise was transmitted through the bracket to the bottom of the steel circular cylindrical shell. The results show that the energy was concentrated within 0–0.01 s, and the energy gradually dissipated after 0.05 s (Fig. 14).

The transient vibration caused by impulse excitation produced a broadband frequency spectrum. Therefore, the peak magnitude of time series data was used for SPL calculation. The peak SPL results of the simulation were compared with the experimental results for each position of the underwater sound field. The peak magnitude of time series data was used for SPL calculation. The difference between the experimental and the simulated SPL was within 3 dB (Fig. 15 and Table 8), which demonstrated the high accuracy of the simulation.

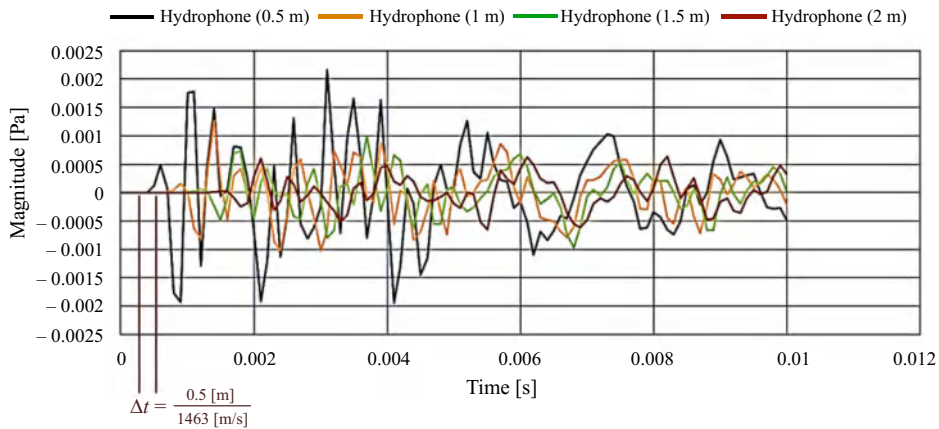


Fig. 13. Simulation of four hydrophones at 0.5, 1, 1.5, and 2 m with time delay Δt versus energy magnitude during $t = 0.01$ s.

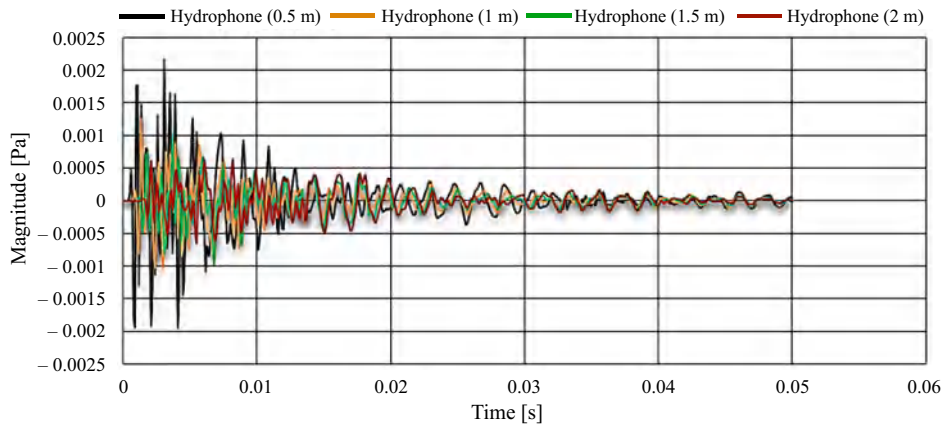


Fig. 14. Simulated underwater acoustic pressure time series data at 0.5, 1, 1.5, and 2 m from the steel circular cylindrical shell.

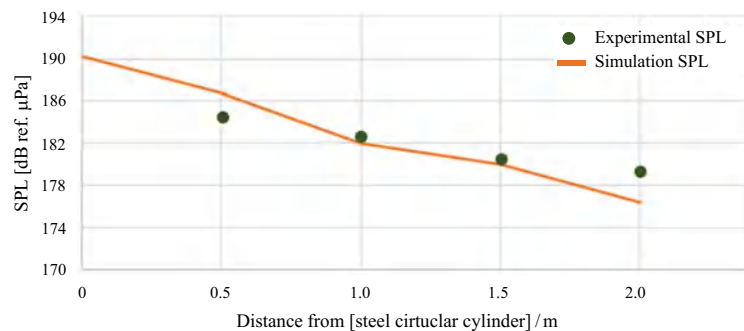


Fig. 15. Peak SPL in the towing tank watercourse direction.

Table 8. Comparisons of the simulated and experimental data of peak SPL in the towing tank watercourse direction.

| Hydrophone location [m] | 0.5 | 1.0 | 1.5 | 2.0 |
|---------------------------|-------|-------|-------|-------|
| Experiment peak SPL [dB] | 184.5 | 183.0 | 181.3 | 179.4 |
| Simulation peak SPL [dB] | 186.3 | 182.1 | 180.1 | 176.5 |
| Discrepancy peak SPL [dB] | +1.8 | -0.9 | -1.2 | -2.9 |

5. Influence of structural configuration on underwater sound radiation

In this section, the effects of structural configuration on sound propagation in the steel circular cylindrical shell and its radiation into water are discussed. The effects of the thickness, configuration, and shape of the steel cylindrical shell structure on the sound field are also discussed. The findings can be used as a design reference for the structural configuration of underwater vehicles. The effects are explored:

1) The dropping of the iron block to impact the base caused the structure below the circular cylindrical shell to vibrate and generate noise in water, which was followed by propagation of a sound wave in water (Figs. 16a–16c). A comparison of the thin

shell with the thick end cap shows that the wave mostly came from the thin shell; that is, the main underwater sound was radiated into the water via the arc surface of the thin shell (Fig. 16).

- 2) After the impact of the iron block, the first acoustic sound wave radiated from the circular cylindrical shell bottom. The second sound wave was circularly diffused by the top arc surface of the thin shell of the cylindrical shell. The reinforced position of the bracket base structure acted as a truncation point for sound radiation in water (Figs. 17a–17c). The underwater sound was radiated from the perimeter of the unreinforced shell of the thin shell arc. This noise radiation behavior shows that the reinforcement position affected the propagation of structural vibration and could block the sound radiation integrity in water. The time series in Fig. 17 shows the sound radiation truncation, as indicated by the red arrows.
- 3) The underwater noise was radiated from the vibrating circular cylindrical shell to the bottom of the towing tank. The noise was diffused and reflected on both sides of the bottom (as indicated by the red circle in Figs. 18c and 18f).

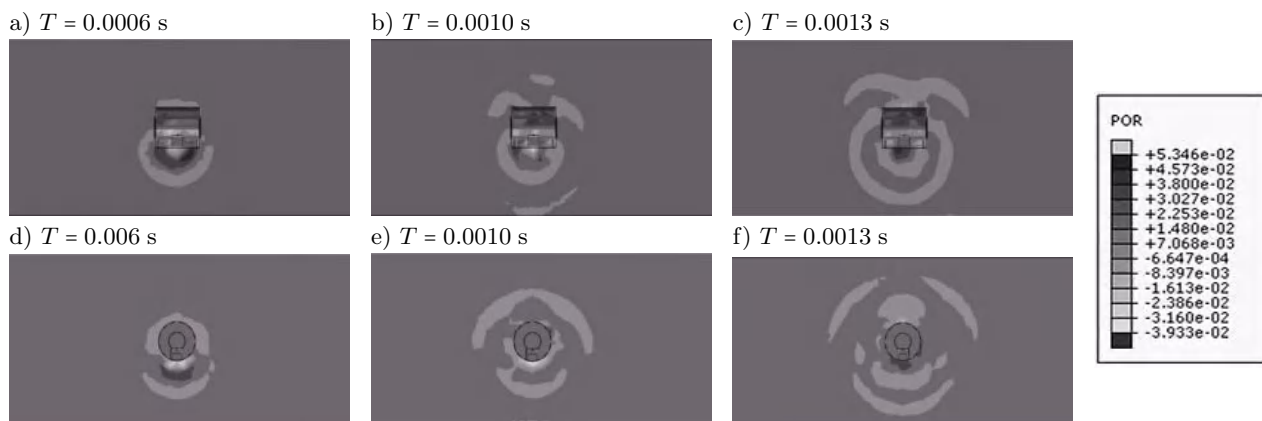


Fig. 16. Simulation diagrams of underwater noise transmitted from the arc surface of the thin shell to the water, where they form sound wave radiation.

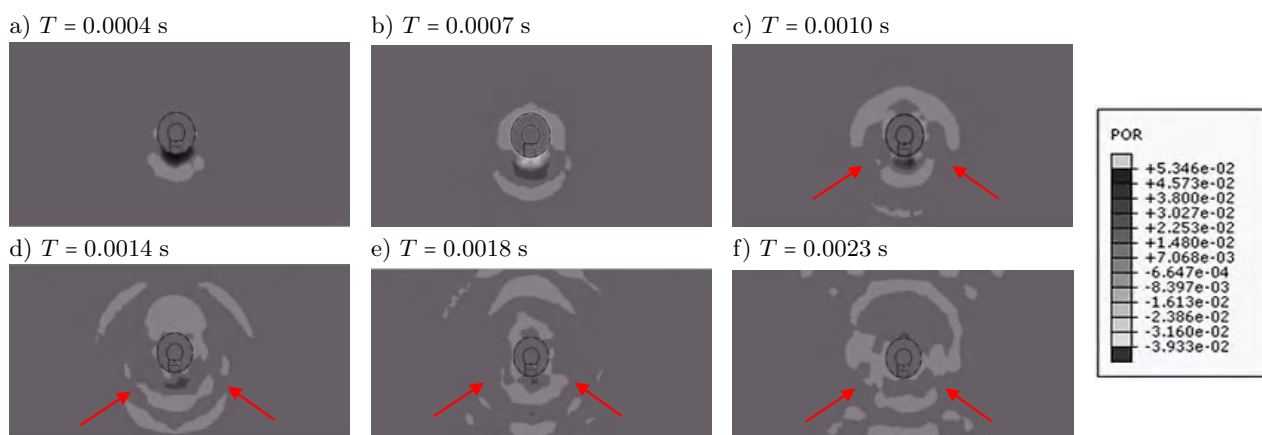


Fig. 17. Reinforced position of the bracket base structure and the truncation point of sound radiation in water.

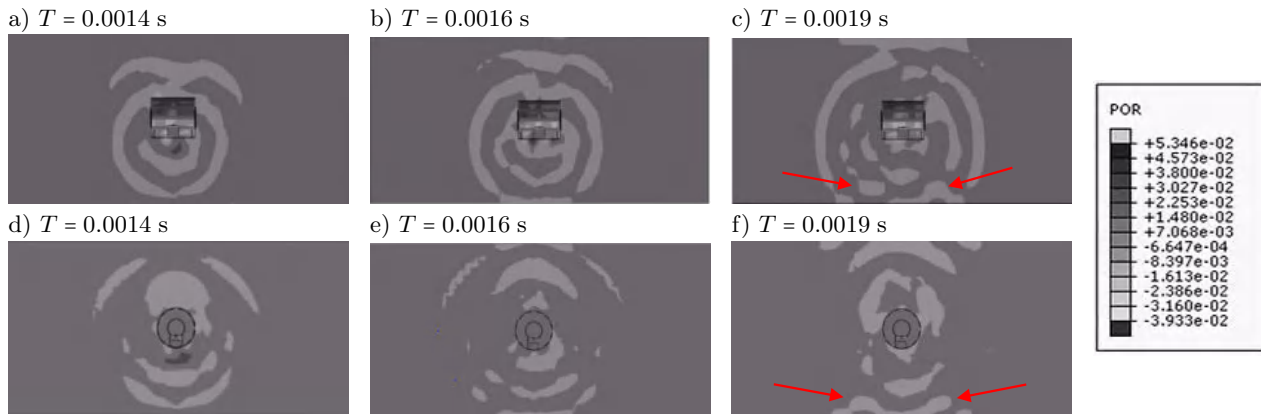


Fig. 18. Noise radiation patterns: noise diffusion and reflection on both sides of the bottom.

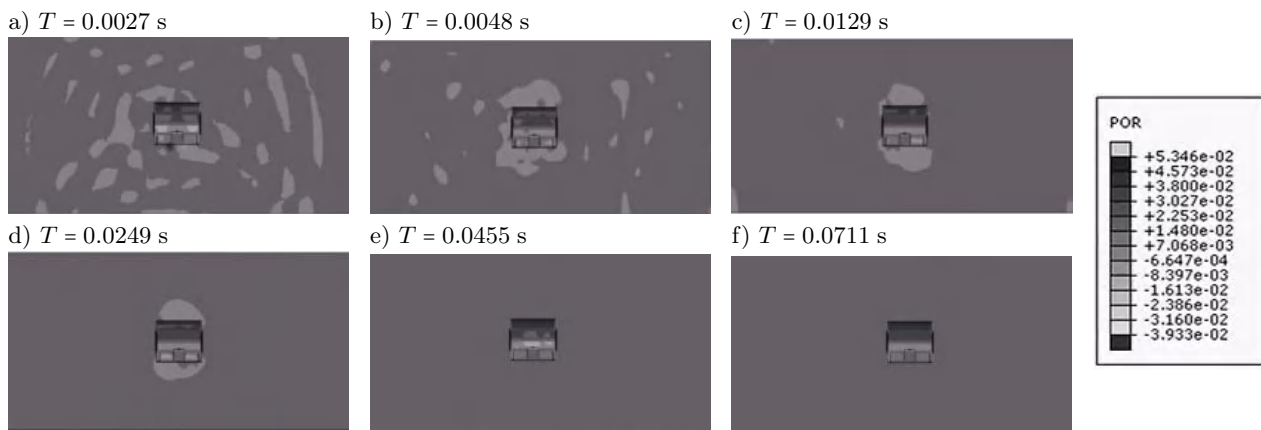


Fig. 19. Transmission of underwater noise from a structure with a gradually declining vibration energy.

- 4) When the vibration energy of the structure in the circular cylindrical shell was large, the vibration alternated from up to down and left to right. The acoustic sound was transmitted by the arc surface of the thin shell and the edges of both sides of the thick end caps (Figs. 17a–17c). With increasing reverberation time, the vibration energy gradually reduced and was transmitted only from the arc surface of the thin shell (Figs. 19c and 19d). Then, with decreasing vibration energy, the acoustic sound reverberated only in the circular cylindrical shell and ultimately disappeared (Figs. 19e and 19f).

6. Conclusions

In this study, impulse-induced structural vibration noise radiated by a watertight steel circular cylindrical shell in a towing tank was measured. Then, this experiment was simulated using the FEM. The accuracy of the simulation results was improved by adding an impulse speed to the loading conditions; as such, the simulation results were consistent with the experimental results. This demonstrates that it is a reliable sim-

ulation method for predicting the radiation of an underwater vehicle sound field caused by transient structural vibration. During the vehicle design process, the underwater noise and observed noise radiation can be predicted and analyzed via the finite-element method.

This study also explored the influence of structural configuration on sound propagation in a circular cylindrical shell and the radiation of this sound into the water. The thickness of the watertight steel cylindrical shell and the reinforced bracket base affected the underwater noise radiation. The thin shell of the structure was the main area from which sound was radiated, while the structural reinforcement position was the diffusion breakpoint of the underwater sound radiation. Therefore, a thicker and more complex reinforced structure will radiate less and incomplete sound into water.

According to the results of this study, although large underwater vehicles have complex structures, usually the main complex and large structures are installed at the bottom of the equipment. Therefore, regardless of the shock vibration of the equipment or the impact of the tool falling, the simpler structure of the upper part of the underwater vehicle is the easiest to radiate noise. The sound-absorbing material can

be covered in the appropriate position of the upper structure. Future research should be able to use the results of this study to conduct more in-depth research and investigate the noise characteristics, structural arrangement and sound-absorbing material performance of specific underwater vehicles.

Acknowledgments

This research was funded by the Ministry of Science and Technology of the Republic of China (project no. MOST111-2221-E-006-071).

References

1. ABAQUS (2014), *Abaqus Analysis User's Guide 6.14: Acoustic, Shock, and Coupled Acoustic-Structural Analysis*, Volume II, Part III, Chapter 6.9.1.
2. ALVAREZ-ARAMBERRI J., PARDO D., BARUCQ H. (2014), Automatically adapted perfectly matched layers for problems with high contrast materials properties, [in:] *14th International Conference on Computational Science*, **29**: 970–979, doi: [10.1016/j.procs.2014.05.087](https://doi.org/10.1016/j.procs.2014.05.087).
3. ETTER P.C. (2018), Noise I: Observations and physical models, [in:] *Underwater Acoustic Modeling and Simulation*, 5th ed., pp. 291–294, CRC Press.
4. JUNGER M.C., FEIT D. (1986), Sound radiation by shells at low and middle frequencies, [in:] *Sound, Structures, and Their Interaction*, pp. 321–365, MIT Press, Cambridge.
5. LEADER J., PAN J., DYLEJKO P., MATTHEWS D. (2013), Experimental investigation into sound and vibration of a torpedo-shaped structure under axial force excitation, *The Journal of the Acoustical Society of America*, **133**(5): 3517, doi: [10.1121/1.4806301](https://doi.org/10.1121/1.4806301).
6. LIN C., WANG J., QU Y., ZHANG Z., HUA H. (2016), Numerical and experimental investigation on vibro-acoustic response of a shaft-hull system, *Engineering Analysis with Boundary Elements*, **71**: 129–139, doi: [10.1016/j.enganabound.2016.07.016](https://doi.org/10.1016/j.enganabound.2016.07.016).
7. MATTHEW H. (2004), The measurement and behavior of vibration, [in:] *Vehicle Refinement: Controlling Noise and Vibration in Road Vehicles*, Cranfield University, pp. 234–268, Elsevier, UK.
8. QIAN D.-J., MIAO X.-H., WANG X.-R. (2012), Sound radiation of underwater structure based on coupled acoustic-structural analysis with ABAQUS, *Applied Mechanics and Materials*, **226–228**: 2249–2252, doi: [10.4028/www.scientific.net/AMM.226-228.2249](https://doi.org/10.4028/www.scientific.net/AMM.226-228.2249).
9. RAWAT A., MATSAGAR V., NAGPAL A.K. (2015), Finite element simulation of cylindrical liquid storage tank under tri-directional components of earthquake, *Journal of Structural Engineering*, **42**(1): 28–39, doi: [10.3850/978-981-09-1139-3_089](https://doi.org/10.3850/978-981-09-1139-3_089).
10. RUGONYI S., BATHE K.J. (2001), On finite element analysis of fluid flows fully coupled with structural interactions, *Computer Modeling in Engineering and Sciences*, **2**(2): 195–212, doi: [10.3970/cmcs.2001.002.195](https://doi.org/10.3970/cmcs.2001.002.195).
11. SACKS Z.S., KINGSLAND D.M., LEE R., LEE J.-F. (1995), A perfectly matched anisotropic absorber for use as an absorbing boundary condition, [in:] *IEEE transactions on Antennas and Propagation*, **43**(22): 1460–1463, doi: [10.1109/8.477075](https://doi.org/10.1109/8.477075).
12. TONG Z., ZHANG Y., ZHANG Z., HUA H. (2007), Dynamic behavior and sound transmission analysis of a fluid-structure coupled system using the direct-BEM/FEM, *Journal of Sound and Vibration*, **299**(3): 645–655, doi: [10.1016/j.jsv.2006.06.063](https://doi.org/10.1016/j.jsv.2006.06.063).
13. WANG W.-H., LIU J.-H., SUTTON R., DOBSON B. (2000), Machine vibration induced underwater acoustic radiation, *Journal of Marine Science and Technology*, **8**(1): 30–40, doi: [10.51400/2709-6998.2451](https://doi.org/10.51400/2709-6998.2451).
14. WAWRZYNOWICZ A., KRZACZEK M., TEJCHMAN J. (2014), Experiments and FE analyses on airborne sound properties of composite structural insulated panels, *Archives of Acoustics*, **39**(3): 351–364, doi: [10.2478/aoa-2014-0040](https://doi.org/10.2478/aoa-2014-0040).
15. WU C.-I., TOO G.-P. (2021), On underwater sound radiation in a towing tank induced by continuous machine vibration in a steel circular cylinder, *Journal of Mechanics*, **37**: 597–608, doi: [10.1093/jom/ufab026](https://doi.org/10.1093/jom/ufab026).
16. WU C.-I., TOO G.-P., WU B.-H. (2022), The boundary acoustic impedance effects of a towing tank underwater sound radiation induced by a steel cylinder continuous vibration, *Applied Acoustics*, **201**: 109101, doi: [10.1016/j.apacoust.2022.109101](https://doi.org/10.1016/j.apacoust.2022.109101).
17. WU H.-T., CHEN P.-T. (2017), Application of coupled FEM/BEM on the analysis of underwater radiated noise of a surface ship induced by hull vibrations, *Journal of Marine Science and Technology*, **25**(2): 196–204, doi: [10.6119/JMST-016-1118-2](https://doi.org/10.6119/JMST-016-1118-2).
18. WU X.-F. (1989), Faster calculations of sound radiation from vibrating cylinders using variational formulations, *Journal of Vibration, Acoustics, Stress, and Reliability in Design*, **111**(1): 101–107, doi: [10.1115/1.3269803](https://doi.org/10.1115/1.3269803).
19. YOSHIKAWA S. (1993), Fluid-structure coupling by the entrained fluid in submerged concentric double-shell vibration, *The Journal of the Acoustical Society of Japan (E)*, **14**(2): 99–111, doi: [10.1250/ast.14.99](https://doi.org/10.1250/ast.14.99).
20. ZHANG Y., LOU J., YU X. (2016), Underwater vibration and acoustic radiation calculation of double cylindrical shell by three-dimensional sono-elasticity of ships, *Journal of Vibroengineering*, **7**: 18–24, <https://www.extrica.com/article/17328>.

Research Paper

Laboratory Tests and Numerical Simulations of Two Anti-Vibration Structures Made by 3D Printing – Comparative Research

Piotr KOWALSKI*, Adrian ALIKOWSKI

*Central Institute for Labour Protection – National Research Institute
Warsaw, Poland*

*Corresponding Author e-mail: pikow@ciop.pl

(received December 22, 2022; accepted May 19, 2023)

This article presents a comparison of test results from two models of anti-vibration systems (I and II) made employing MJF 3D printing technology and two different materials. The research included laboratory tests and numerical simulations, assuming a linear nature of the mechanical properties for the materials and models of structures. The aim of this research was to assess the consistency between laboratory test and numerical simulation results. In addition, evaluation of the suitability of using MJF technology to produce anti-vibration systems was conducted. During the laboratory tests, the response of the two models of structures to vibrations generated by an exciter was recorded using a high-speed camera. Subsequent image analysis was performed using the MOVIAS Neo software. The obtained values of vibration displacements and resonant frequencies were used to validate the numerical model created in the Simcenter Femap software. Relative differences between the values of resonant frequencies obtained experimentally and through simulations were determined. In the case of the structural model I, creating its numerical model without considering the non-linearity of mechanical parameters was found to be unjustified. The comparison of the displacements determined during numerical simulations showed relative differences of less than 16% for both models in relation to the laboratory test results. This comparison result indicates a satisfactory accuracy in simulating this parameter. An assessment of the quality and accuracy of MJF technology-produced prints, led to the conclusion that due to the formation of internal stresses during the print creation, the use of “soft” materials in this technology is problematic.

Keywords: finite element method; 3D printing; mechanical vibrations.



Copyright © 2023 The Author(s).
This work is licensed under the Creative Commons Attribution 4.0 International CC BY 4.0
(<https://creativecommons.org/licenses/by/4.0/>).

1. Introduction

In numerous research centers around the world, developmental research on new materials and systems designed to limit mechanical vibrations generated by machinery and devices is currently underway. Vibrations constitute a potentially harmful factor both for mechanical devices, causing their faster damage or failure, as well as for people, by reducing work comfort or leading to adverse health effects.

An innovative approach to advancing the concept of anti-vibration systems involves the use of 3D printing technology as a quick, precise and easily accessible way to create structures with consistent mechanical properties. The advancement of various 3D printing technologies opens up the possibility of using a wide range of materials with different physical properties that can

be selected based on the expected properties of the prints. For instance, some studies explored the possibility of using a material with shape memory (shape memory polymer, SMP) in 3D printing (YANG *et al.*, 2016). Many studies also attempted to use 3D printing to test new solutions in the field of body protection (PARK, LEE, 2019), metamaterials (ZOLFAGHARIAN *et al.*, 2022) or shock absorbers (SATHYAPRIYA *et al.*, 2022). Confirming the usefulness of 3D printing for the production of anti-vibration systems could reduce both the time and cost of developmental work in this field.

The rising popularity of developing numerical methods together with the increasing computing capabilities of computer systems creates more and more opportunities for testing anti-vibration systems by means of computational simulations. Such an approach is a significantly faster and lower in cost than carrying

out traditional laboratory tests of subsequent physical models subjected to modifications. The potential of using the finite element method (FEM) to study anti-vibration systems is presented in many scientific papers (BURLAYENKO *et al.*, 2019; SARI *et al.*, 2022; DAVID MÜZEL *et al.*, 2020; KAMEL *et al.*, 2019; SHI *et al.*, 1997). Various researches employ the FEM in studies related to limiting the effects of mechanical vibrations, predicting their impact on the environment, as well as analyzing the properties of 3D prints (ABBOT *et al.*, 2019; JINDAL *et al.*, 2020; ŽUR *et al.*, 2019). Verifying compliance between numerical models created using the FEM and laboratory results obtained for real models could accelerate the development of new solutions aimed to reduce mechanical vibrations.

2. Anti-vibration systems – the object of research

In order to assess the possibility of using FEM simulations for the design of 3D anti-vibration structures, comparative tests of two anti-vibration structures produced using the multi jet fusion (MJF) method involving the thermal, selective sintering of powders were carried out. The MJF technology was chosen because of its capacity to employ large printing areas, enabling the printing of over 30 elements in one printing process while maintaining a short printing time. Two materials were used for the prints: nylon PA12 and Ultrasint TPU01, and their parameters are presented in Table 1.

Table 1. Basic mechanical parameters of materials used for 3D printing.

| Material | PA 12 | TPU01 |
|------------------------------|-------|--------|
| Young's modulus [MPa] | 1700 | 56 |
| Density [kg/m ³] | 907.2 | 1206.6 |
| Tensile strength [MPa] | 48 | 8 |

Comparative studies were carried out on structurally distinct models of structures: I and II, as shown in Fig. 1.

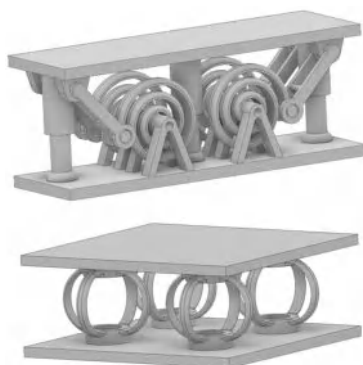


Fig. 1. Developed models of anti-vibration systems with external dimensions: model I – $24 \times 77 \times 29.6$ mm (top); model II – $60 \times 60 \times 25.3$ mm (bottom).

3. Research method

3.1. Laboratory tests

The results of numerical simulations were verified through comparison with measurement data obtained during the tests of real anti-vibration structures subjected to mechanical vibrations. This validation was based on the registered vibration displacements, e.g., the values of the resonance frequencies of both models and the values of displacements of the upper planes of the structures during resonance. The models of anti-vibration systems were tested on the test stand apparatus shown in Fig. 2. The models were excited to oscillate with a tunable sinusoidal signal with a frequency range of 5–100 Hz. During the tests, the models were loaded with masses whose values were selected experimentally. Displacements of elements in the system models were recorded using a high-speed camera. Subsequent image analysis was performed using the MOVIAS Neo software.

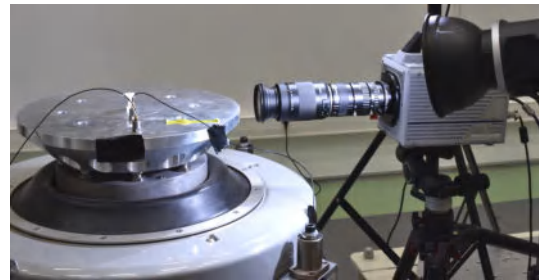


Fig. 2. Laboratory measurement stand consisting of a mechanical vibration exciter and a high-speed camera.

In this way, vibration displacement profiles over time at specific points across the tested system models were obtained. An example of the markers' arrangement at measurement points on the tested models is shown in Fig. 3.

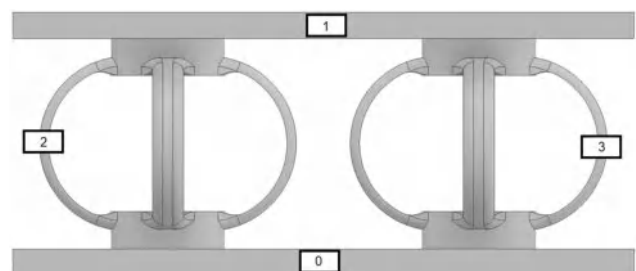


Fig. 3. Arrangement of measurement markers on model II.

The following loading masses were used: 9, 18, and 27 g for structure I, and 60, 120, and 180 g for structure II. The selected loading masses enabled the observation of system resonances without causing any damage to the elements of the tested models. For both models and each applied load, resonant frequencies and their corresponding displacement values were deter-

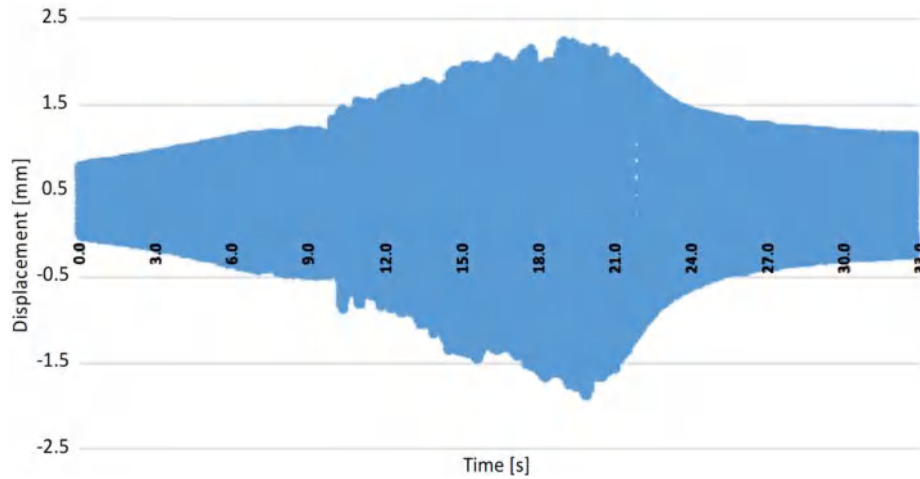


Fig. 4. Diagram of the displacement profile of measurement point 1 for model II loaded with a 60 g mass along the y -direction (vertical to the exciter table).

mined. For further analyses, the displacement values of the measuring point 1 along the y -axis were used. A representative graph of the displacement variation of point 1 over time is shown in Fig. 4.

The data obtained in this process, including resonance frequencies and displacements of individual points in the system models, were used to validate the numerical simulations.

3.2. Numerical simulations

The numerical simulations were performed using the Siemens Simcenter Femap software, a platform designed to conduct engineering analyzes using the FEM. The system models presented in Fig. 1 were subjected to discretization, leading to the generation of a finite number of elements. Next, meshes were generated from the obtained elements for both models. They are presented in Fig. 5.

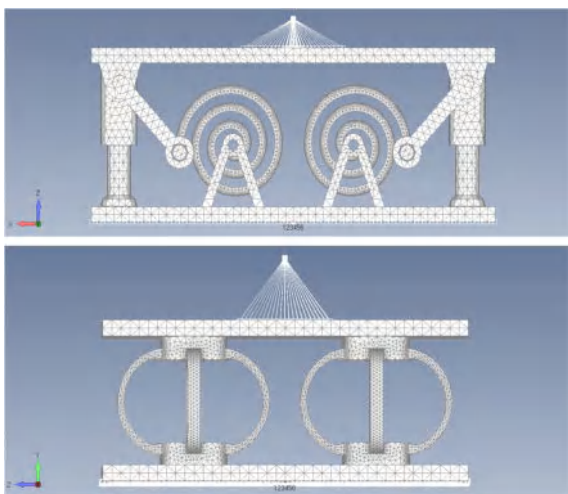


Fig. 5. Grids of the anti-vibration structures generated after the discretization of the continuous 3D models.

In the case of the system model I, a structural element—the central guide, was removed. This removal did not affect the simulation results and increased the number of mesh elements, which ultimately influenced the speed of calculations.

The main assumption of the simulations was the premise of linear characteristics of the material used. The loading of the structures was carried out with the use of RBE2 elements, connecting the upper surface of the models with a designated point that was assigned a mass condition. The same elements were used in the bases of the models to constrain their mobility, by effectively connecting them to the vibration exciter table during laboratory tests. An additional boundary condition used in the frequency analysis involved considering acceleration corresponding to the acceleration of gravity.

In order to determine the resonance frequencies of the system models and their displacements, two numerical analyzes were carried out: modal and frequency.

Modal analysis yields a set of vibration modes of the tested system model together with resonant frequencies. The shape of the modes makes it possible to evaluate the behavior of the model during vibrations of a specific frequency.

On the other hand, frequency analysis makes it possible to determine the actual displacements of individual nodes of the mesh of elements in addition to showing the prevalent stresses and forces. In order to determine the appropriate damping coefficient during the simulation for a given model structure, a number of test simulations were carried out. They involved selecting the damping value for the lowest applied load in such a way that the displacements obtained for the simulation closely matched the values obtained during the experimental tests.

Then, the selected damping coefficient value was used in simulations featuring a different load.

4. Comparison results

The values of resonant frequencies obtained during the laboratory tests and through numerical simulations are presented in Table 2. Comparison of displacements obtained using a high-speed camera and numerical simulations is shown in Table 3. Symbols used in the tables:

- F_{lab} – resonant frequency obtained from laboratory tests [Hz];
- F_{sym} – resonant frequency obtained from numerical simulations [Hz];
- ΔF – relative difference between resonant frequencies from laboratory tests and numerical simulations [%];
- D_{lab} – displacement of measuring point 1 obtained from laboratory tests [mm];
- D_{sym} – displacement of the node coincident with the location of measurement point 1 obtained from numerical simulations [mm];
- ΔD – relative difference between the displacements obtained in the laboratory and from numerical simulations [%].

Table 2. List of resonance frequencies obtained on a laboratory stand and with the use of numerical simulations along with the relative difference of the obtained values.

| Load | Model I | | | Model II | | |
|-----------------------|---------|-------|-------|----------|-------|-------|
| | 9 g | 18 g | 27 g | 60 g | 120 g | 180 g |
| F_{lab} [Hz] | 25.6 | 20.8 | 18.9 | 22.2 | 16.4 | 11.4 |
| F_{sym} [Hz] | 45.3 | 36.1 | 30 | 23.4 | 17.2 | 14.3 |
| ΔF | 77.0% | 73.6% | 58.7% | 5.4% | 4.9% | 25.4% |

Table 3. Summary of the maximum displacements obtained for measuring point 1 using a laboratory stand and numerical simulations along with the relative difference of the obtained values.

| load | Model I | | | Model II | | |
|-----------------------|---------|-------|-------|----------|-------|-------|
| | 9 g | 18 g | 27 g | 60 g | 120 g | 180 g |
| D_{lab} [mm] | 5.4 | 7.2 | 9.9 | 4.0 | 8.5 | 11.7 |
| D_{sym} [mm] | 5.3 | 8.35 | 11.3 | 4.02 | 7.25 | 10.5 |
| ΔD | 2.1% | 16.0% | 13.7% | 0.2% | 15.0% | 10.3% |

By analyzing the obtained relative differences of resonance frequencies ΔF for system I, one can notice large differences between the results of laboratory tests and the ones from simulations. The differences exceed 58% for all loads used. In the case of structure II, the differences for loads of 60 g and 120 g do not exceed 5.5%, while for the highest load of 180 g the difference increases significantly and exceeds 25%. However, in the case of system II, despite a large relative difference expressed in percentage, the difference between the resonance frequency values is only 3 Hz.

For both models of anti-vibration systems, the relative differences in the obtained displacements did not exceed 16%, which can be considered a satisfactory result. The obtained relative differences correspond to the real displacement differences of about 1.4 mm.

5. Conclusions

The presented research showed the potential of using numerical methods to predict resonance frequencies and displacements of 3D-printed anti-vibration structures made. The tests of the two presented models showed that obtaining reliable results through numerical simulations strongly depends on the construction of the anti-vibration system model.

The uncomplicated construction of models, such as tested model II, in which the vibration energy is dissipated only in the structure of the material, allows the use of a linear model to a limited extent. However, this approach is associated with low accuracy of the obtained simulation results. This is confirmed by the obtained increased differences in the determined values of the resonance frequency (laboratory and FEM simulation) for model II under a load of 180 g, at which the model of the structure probably behaves non-linearly.

In the case of models with more complex structures, such as model I, the correct determination of resonant frequencies may require taking into account not only the material property non-linearities, but also non-linearities resulting from the structure of the system.

The relative differences in displacements obtained experimentally and through simulation can be considered acceptable. However, due to large differences in the obtained resonant frequencies, the reliability of displacement values determined for model I might be questionable.

The obtained differences in results could be influenced not only by non-linearities in the mechanical parameters of the structures and the materials used, but also by inaccuracies in workmanship and internal stresses generated during the printing of the model structures.

When analyzing the applicability of MJF technology based on powder sintering at high temperatures for producing 3D anti-vibration structures (model made of TPU01 material), an uneven distribution of the generated thermal energy was noticed during the printing process. This indicates that different elements of the same structure may have significantly different temperatures during printing. A high temperature gradient in the structure itself can cause high internal stresses that affect both the accuracy and quality of prints (deformations) and their mechanical properties.

Numerical modeling of models produced in this way may pose significant challenges and lead to unreliable simulation results.

Acknowledgments

This article was based on the results of a research task carried out as part of the 5th phase of the National Program “Improvement of Safety and Working Conditions” partially supported in the years 2020–2022 – in the field of research and development – by the National Center for Research and Development (project no. III.PB.02 entitled “Development of Anti-Vibration Systems with Innovative 3D structures”). The main coordinator of the Program is the Central Institute for Labour Protection – National Research Institute.

References

1. ABBOT D.W., KALLON D.V.V., ANGHEL C., DUBE P. (2019), Finite element analysis of 3D printed model via compression tests, *Procedia Manufacturing*, **35**: 164–173, doi: [10.1016/j.promfg.2019.06.001](https://doi.org/10.1016/j.promfg.2019.06.001).
2. BURLAYENKO V.N., SADOWSKI T., ALTENBACH H., DIMITROVA S. (2019), Three-dimensional finite element modelling of free vibrations of functionally graded sandwich panels, [in:] *Recent Developments in the Theory of Shells*, Altenbach H., Chróścielewski J., Eremeyev V., Wiśniewski K. [Eds], pp. 157–177, Springer.
3. DAVID MÜZEL S., BONHIN E.P., GUIMARÃES N.M., GUIDI E.S. (2020), Application of the finite element method in the analysis of composite materials: A review, *Polymers*, **12**(4): 818, doi: [10.3390/polym12040818](https://doi.org/10.3390/polym12040818).
4. JINDAL P., WORCESTER F., SIENA F.L., FORBES C., JUNEJA M., BREEDON P. (2020), Mechanical behaviour of 3D printed vs thermoformed clear dental aligner materials under non-linear compressive loading using FEM, *Journal of the Mechanical Behavior of Biomedical Materials*, **112**: 104045, doi: [10.1016/j.jmbbm.2020.104045](https://doi.org/10.1016/j.jmbbm.2020.104045).
5. KAMEL M.A., IBRAHIM K., EL-MAKAREM AHMED A. (2019), Vibration control of smart cantilever beam using finite element method, *Alexandria Engineering Journal*, **58**(2): 591–601, doi: [10.1016/j.aej.2019.05.009](https://doi.org/10.1016/j.aej.2019.05.009).
6. PARK J.H., LEE J.R. (2019), Developing fall-impact protection pad with 3D mesh curved surface structure using 3D printing technology, *Polymers*, **11**(11): 1800, doi: [10.3390/polym11111800](https://doi.org/10.3390/polym11111800).
7. SARI B., KAZEMI LICHAEI M., YILDIRIM S. (2022), Free vibration analysis of tapered composite aircraft wing via the finite element method, *Cukurova University Journal of the Faculty of Engineering*, **37**(3): 741–752, doi: [10.21605/cukurovaumfd.1190386](https://doi.org/10.21605/cukurovaumfd.1190386).
8. SATHYAPRIYA G. *et al.* (2022), Development of compliant vibration isolation damper and its performance analysis in turning operation, *Advances in Materials Science and Engineering*, **2022**: 6860178, doi: [10.1155/2022/6860178](https://doi.org/10.1155/2022/6860178).
9. SHI Y., LEE R.Y.Y., MEI C. (1997), Finite element method for nonlinear free vibrations of composite plates, *AIAA Journal*, **35**(1): 159–166, doi: [10.2514/2.78](https://doi.org/10.2514/2.78).
10. YANG Y., CHEN Y., WEI Y., LI Y. (2016), 3D printing of shape memory polymer for functional part fabrication, *The International Journal of Advanced Manufacturing Technology*, **84**(9): 2079–2095, doi: [10.1007/s00170-015-7843-2](https://doi.org/10.1007/s00170-015-7843-2).
11. ZOLFAGHARIAN A., BODAGHI M., HAMZEHEI R., PARR L., FARD M., ROLFE B.F. (2022), 3D-printed programmable mechanical metamaterials for vibration isolation and buckling control, *Sustainability*, **14**(11): 6831, doi: [10.3390/su14116831](https://doi.org/10.3390/su14116831).
12. ŽUR P., KOŁODZIEJ A., BAIER A. (2019), Finite elements analysis of PLA 3D-printed elements and shape optimization, *European Journal of Engineering Science and Technology*, **2**(1): 59–64, doi: [10.33422/EJEST.2019.01.51](https://doi.org/10.33422/EJEST.2019.01.51).

Research Paper

A Multi-Layer Micro-Perforated Panel Structure Based on Curled Space for Broadband Sound Absorption at Low Frequencies

Jiaming CHU⁽¹⁾, Xiao LIANG^{(1),(2)*}, Zhen YANG⁽¹⁾, Haofeng LIANG⁽¹⁾,
Tao CHEN⁽¹⁾, Liang SU⁽¹⁾, Zhuo ZHOU^{(3)*}

⁽¹⁾ School of Mechanical Engineering, Xiangtan University
Xiangtan, China

⁽²⁾ Foshan Green Intelligent Manufacturing Research Institute of Xiangtan University
Foshan, Guangdong, China

⁽³⁾ School of Mechanical Engineering and State Key Laboratory for Strength and Vibration of Mechanical Structures
Xi'an Jiaotong University
Xi'an, Shanxi, China

*Corresponding Authors e-mails: liangxiao@xtu.edu.cn (Xiao Liang); zhouzhuo221@163.com (Zhuo Zhou)

(received February 16, 2023; accepted May 19, 2023)

In this paper, we propose a multi-layer micro-perforated panel structure based on a curled space for broadband sound absorption at low frequencies, which increases the number of perforated panel layers in a limited space using a curled space. The absorption coefficients of the structure under plane wave conditions were calculated using the transfer matrix method and the finite element method. It is demonstrated that the multi-layer micro-perforated panel structure can ensure high absorption (consistently over 90%) in the frequency range of 400~5000 Hz. The sound absorption mechanism of the multi-layer micro-perforated panel structure is investigated by using the acoustic impedance along with the reflection coefficient of the complex frequency surface. In addition, we also discuss the effects of the micro-perforated panel parameters on the structural sound absorption coefficient. The results show that the proposed multi-layer micro-perforated panel structure provides an excellent solution for sound absorption in a limited space.

Keywords: micro-perforated plate; curled space; broadband sound absorption; complex frequency plane method.



Copyright © 2023 The Author(s).
This work is licensed under the Creative Commons Attribution 4.0 International CC BY 4.0
(<https://creativecommons.org/licenses/by/4.0/>).

1. Introduction

The micro-perforated plate (MPP) has an excellent broadband sound absorption ability, as well as high-temperature resistance, corrosion resistance, and non-pollution, which is regarded as one of the most promising next-generation sound absorption materials. MAA (1983) first proposed the concept of the MPP absorber by reducing the diameter of perforations in conventional perforated plates to less than one millimeter, thus obtaining the MPP structure with high acoustic resistance and low acoustic impedance. Since then, MPP absorbers have received widespread attention in various acoustic applications.

Currently, the theory of MPP has been widely studied (CHENG, 2018; RAFIQUE *et al.*, 2021; LI, 2018). MAA (1984, 1994) provided the MPP theoretical analysis and design principles. In addition, the double-layer MPP structure was developed to expand further the sound absorption band (MAA, LIU, 2000). As compared to the narrower absorption band of the single-layer MPP structure, the double-layer MPP produces two different absorption peaks, thus obtaining a wider absorption band. MOSA *et al.* (2020b) introduced inhomogeneous perforations on top of the double-layered MPP, which further increased the absorption band. At the same time as introducing inhomogeneous perforations, MOSA *et al.* (2020a) set up multiple cavities

with different depths to produce a wider absorption band. Due to the mutual coupling of multiple absorption peaks, the MPP can form a wide band of sound absorption, therefore, there are several studies based on a multi-layer MPP. For example, COBO *et al.* (2019) designed a three-layer MPP and optimized the MPP parameters by a simulated annealing method. BUCIARELLI *et al.* (2019) established an analytical model for the design of multi-layer MPP absorbers and found that adding more MPP leads to resonant coupling, which is beneficial to improve the absorption band. In addition, it obtained the 5-layer MPP structure. By optimizing the parameters of the MPP structure, the absorption coefficient of this structure at 400~2000 Hz is all over 0.9. Using the transmission matrix method is more convenient than the equivalent circuit analysis method to study a multi-layer MPP (LEE, KWON, 2004). CARBAJO *et al.* (2020) proposed the multi-layer MPP absorber with inclined perforations and investigated its acoustic properties using the transfer matrix method, which promotes the application of a multi-layer MPP in the field of noise reduction.

A multi-layer MPP has broad-frequency sound absorption characteristics, however, a large cavity is often required for low-frequency sound absorption, which significantly limits its application (ZHAO, LIN, 2022). Many studies have proposed solutions to this problem. Firstly, in response to the crisis of excessive cavity volume, LI and ASSOUAR (2016) significantly reduced the structural volume by converting the cavity into a coiled coplanar air chamber, which absorbed sound perfectly at 125 Hz. Similarly, PRASETIYO *et al.* (2021) introduced a coiled structure in the cavity to reduce the cavity volume, and the absorption coefficients exceeded 0.8 from 250 to 1000 Hz. CUI *et al.* (2022) also obtained a composite spatially folded metamaterial structure by a curled space and achieved a large broadband absorption above 200 Hz. It is a simple and practical way to reduce the cavity volume by spatially coiled structures, and there are many similar studies (LIU *et al.*, 2019; 2020; WU *et al.*, 2019). Secondly, MPP structures are often used together with other structures to improve low-frequency sound absorption further to obtain new acoustic metamaterials (CHENG *et al.*, 2022; GAO *et al.*, 2017; RAFIQUE *et al.*, 2022). XIAOQI and CHENG (2021) achieved broadband and low-frequency sound absorption by setting MPP boundaries in an acoustic black hole structure. SHAO *et al.* (2022) designed a tunable multi-layer composite structure by combining the Helmholtz structure, MPP, and porous material, which has absorption coefficients exceeding 0.9 at 400~3000 Hz. XIE *et al.* (2022) combined the MPP structure with a conchoidal cavity structure. The structural absorption band can be changed by adjusting the structural parameters.

A multi-layer MPP has broad frequency sound absorption characteristics and the coiled structure can

reduce the volume of the structure. Based on these two characteristics, this paper investigates the acoustic performance of the multi-layer MPP with a coiled structure. Moreover, we study the sound absorption mechanism using the complex frequency surface acoustic impedance and the reflection coefficient. In addition, we discuss the effect of perforated panel parameters on the sound absorption coefficient of the structure. Finally, it is shown that sound absorption can be achieved at different frequency bands by changing the perforated panel parameters and structure dimensions.

2. Theoretical analysis

2.1. Basic formulations

According to Maa's approximation formula (MAA, 1998), the single-layer MPP relative acoustic impedance can be written as:

$$z_{\text{MPP}} = r + j\omega m, \quad (1)$$

where j is the imaginary number, ω is the angular frequency, r is the relative acoustic resistance, and m is the relative acoustic mass, which are defined as:

$$r = \frac{32\eta t}{\rho c \sigma d^2} \left[\left(1 + \frac{x^2}{32}\right)^{\frac{1}{2}} + \frac{\sqrt{2}}{8} \frac{xd}{t} \right], \quad (2)$$

$$m = \frac{t}{\sigma c} \left[1 + \left(9 + \frac{x^2}{2}\right)^{-\frac{1}{2}} + 0.85 \frac{d}{t} \right], \quad (3)$$

where $\eta = 1.8 \times 10^{-5}$ Pa·s, $\rho = 1.25$ kg/m³, $c = 343$ m/s are the dynamic viscosity coefficient, the density, and sound speed of the air, t is the panel thickness, σ is the perforation ratio, and d is the diameter of the perforation hole, x is the perforation constant, and it is given by:

$$x = \frac{d}{2} \sqrt{\frac{\omega \rho}{\eta}}. \quad (4)$$

At the vertical incidence of plane waves, the sound absorption coefficient of a single-layer MPP can be expressed as:

$$\alpha = \frac{4r}{(1+r)^2 + (\omega m - \cot(\omega D/c))^2}, \quad (5)$$

where D is the depth of the dorsal cavity of the MPP.

Further, we can simplify it to the following equation:

$$\alpha = \frac{4r}{(1+r)^2 + m'^2}. \quad (6)$$

By analyzing Eq. (6), we can discover that perfect sound absorption can only be achieved if $r = 1$ and $m' = 0$. In general, achieving an ideal acoustic impedance match for a wide frequency absorption

is not easy. However, in most practical applications, achieving perfect sound absorption is unnecessary, and absorbing most of the sound energy can also achieve the purpose. Therefore, this gives a larger range of acoustic impedance matches. As shown in Fig. 1, the sound absorption coefficients are shown for different relative sound impedances and sound masses. When the relative acoustic impedance is within the blue elliptical region in Fig. 1b, the sound absorption coefficient is above 0.8. At this time, the relative acoustic impedance region is significantly larger, dramatically reducing the structure requirements. For example, the MPP achieves the maximum absorption coefficient of 0.99 at 125 Hz when d , t , D , and σ are taken as 3.5, 0.2, 734 mm, and 0.096%, respectively. At this time, r and m' are 0.99 and -0.06 , respectively, which are very close to the parameters at the theoretical maximum absorption coefficient. However, the sound absorption frequency band of a MPP is very narrow under this parameter. Moreover, the depth of the back cavity is too large. When D changed to 200 mm, the absorption coefficient of a MPP would reach 0.88 at 551 Hz ($r = 2.06$, $m' = 0.05$), and almost no absorption effect at 125 Hz ($r = 0.99$, $m' = 148.5$).

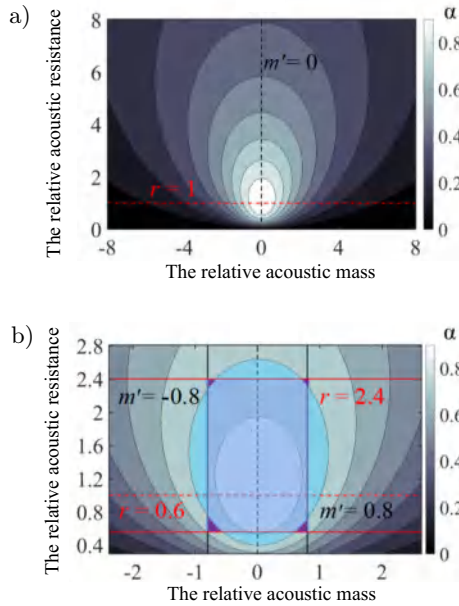


Fig. 1. MPP absorption coefficients at different relative acoustic impedances: a) the red and black dashed lines and intersection points represent $r = 1$, $m' = 0$, and $\alpha = 1$, respectively; b) most of the region with $\alpha \geq 0.8$ is in the region bounded by $2.4 \geq r \geq 0.6$ and $-0.8 \geq m' \geq 0.8$ (except for the purple region), which we refer to as region A.

2.2. Transfer matrix method

The transfer matrix method (TMM) is a simple method for the study of a multi-layer MPP. According to (LEE, KWON, 2004), we can initially write the MPP and cavity transfer matrix, respectively:

$$[\mathbf{P}] = \begin{bmatrix} 1 & \rho c z_{\text{MPP}} \\ 0 & 1 \end{bmatrix}, \quad (7)$$

$$[\mathbf{S}] = \begin{bmatrix} \cos(kh) & (j\rho c) \sin(kh) \\ (j/\rho c) \sin(kh) & \cos(kh) \end{bmatrix}, \quad (8)$$

where $k = \omega/c$ is the wave number, and h is the air cavity depth.

For a multi-layer MPP shown in Fig. 2, we can multiply the transfer matrix \mathbf{P}_i of each MPP with the transfer matrix \mathbf{S}_i of the air cavity sequentially, thus obtaining the total transfer matrix:

$$[\mathbf{T}] = [\mathbf{P}]_1 [\mathbf{S}]_1 \cdots [\mathbf{P}]_n [\mathbf{S}]_n = \begin{bmatrix} T_{11} & T_{12} \\ T_{21} & T_{22} \end{bmatrix}. \quad (9)$$

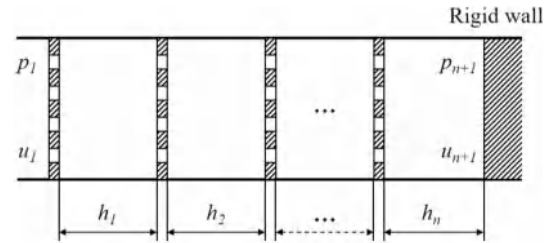


Fig. 2. Schematic diagram of the multi-layer MPP structure.

At the vertical incidence of plane waves, the reflection and absorption coefficients of a multi-layer MPP can be expressed as:

$$\gamma = \frac{T_{11} - \rho c T_{21}}{T_{11} + \rho c T_{21}}, \quad (10)$$

$$\alpha = \frac{4 \operatorname{Re} \left(\frac{T_{11}/T_{21}}{\rho c} \right)}{\left[1 + \operatorname{Re} \left(\frac{T_{11}/T_{21}}{\rho c} \right) \right]^2 + \left[\operatorname{Im} \left(\frac{T_{11}/T_{21}}{\rho c} \right) \right]^2}. \quad (11)$$

The equivalent relative acoustic impedance and equivalent relative sound mass of a multi-layer MPP can also be calculated as:

$$z_0 = \frac{T_{11}/T_{21}}{\rho c}, \quad (12)$$

$$r_0 = \operatorname{Re} \left(\frac{T_{11}/T_{21}}{\rho c} \right), \quad (13)$$

$$m_0 = \operatorname{Re} \left(\frac{T_{11}/T_{21}}{\rho c} \right). \quad (14)$$

2.3. Finite element method

The 3D model of the structure is shown in Fig. 3a, where $L = 121$ mm and $W = 48$ mm are the length and width of the structure, respectively. As a result

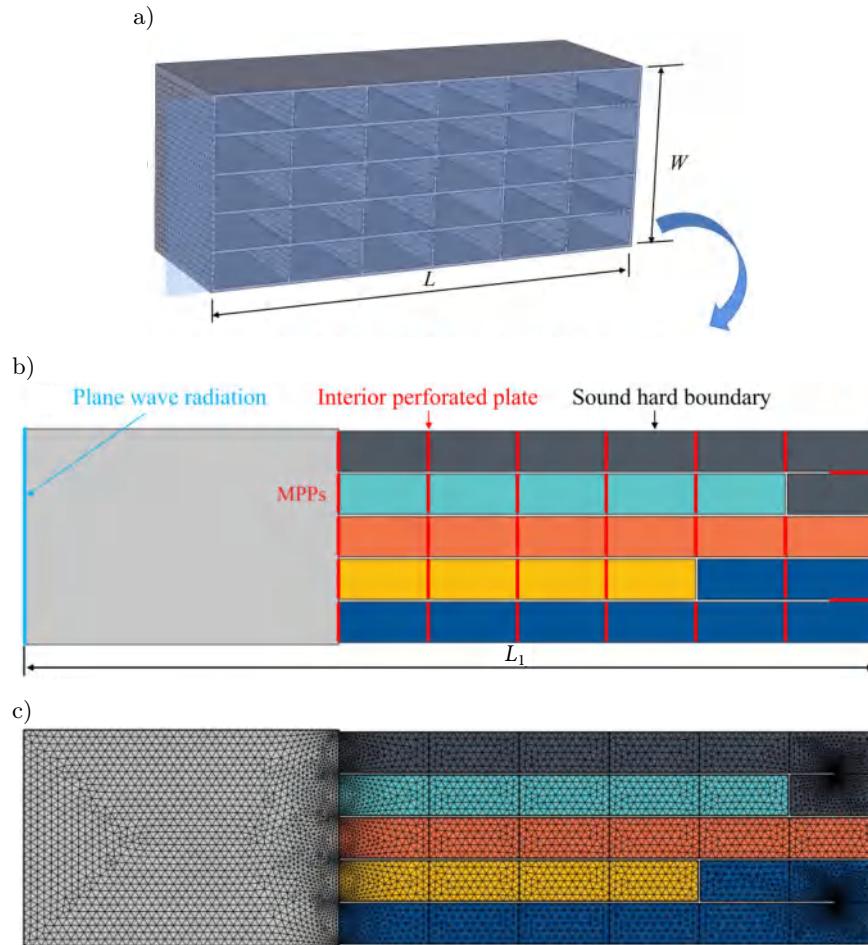


Fig. 3. Diagram of multi-layer MPP structure based on curl space: a) schematic diagram of the 3D model of the structure; b) finite element boundary conditions; c) finite element meshing.

of the symmetry of the 3D model, we reduce the 3D model to a 2D planar model when performing the finite element simulation, as shown in Fig. 3b. The physical field under study is the Pressure Acoustic Frequency Domain and the entire study domain is the air domain, moreover the entire air domain length $L_1 = 190$ mm. The aero-domain and internal MPPs are modeled with a linear elastic fluid model and a thin-plate MPP model from COMSOL, respectively. In addition, the mesh is divided into free triangular meshes, and the maximum mesh is $1/12$ of the minimum wavelength to ensure the accuracy of the calculation. The sound incident field is a plane wave incident vertically, as shown by the blue line in Fig. 3b, and it is:

$$p_b = p_0 e^{-jkx}, \quad (15)$$

where $p_0 = 1$ Pa is the pressure amplitude.

The red line represents the interior perforated plate, whose diameter, thickness, and perforation rate are $d = 0.2$ mm, $t = 0.1$ mm, and $\sigma = 0.03$, respectively, and whose relative acoustic impedance can be expressed as:

$$z = \frac{j\omega(t + 8df_{\text{int}}/3\pi)/c\sigma C_D}{J_2(d\sqrt{-ik}/2)/J_0(d\sqrt{-ik}/2)}, \quad (16)$$

where $C_D = 1$ and f_{int} represent the flow coefficient and the hole-hole interaction function, respectively; J_2 and J_0 are Bessel functions of the first kind of the second and first order.

The other boundaries of the model are the sound hard boundary, which means that the normal derivative of the pressure is zero at the boundary and they are:

$$\frac{\partial p_t}{\partial \mathbf{n}} = 0. \quad (17)$$

2.4. Sound absorption coefficient

According to (ZHAO, LIN, 2022), the double-layer MPP can be flipped and thus reduce the back cavity space, as shown in Figs. 4a and 4b. Among them, the main parameters of the MPP structures include the plate thickness $t_1 = 0.4$ mm, hole diameter $d_1 = 0.3$ mm, the perforation rate $\sigma_1 = 0.01$, and the back cavity depth $D_1 = D_2 = 75$ mm. The research results show that the sound absorption coefficients of both are almost the same (ZHAO, LIN, 2022). Therefore, we can approximate the equivalence of the two in our study, thus simplifying the calculation. The simplified model

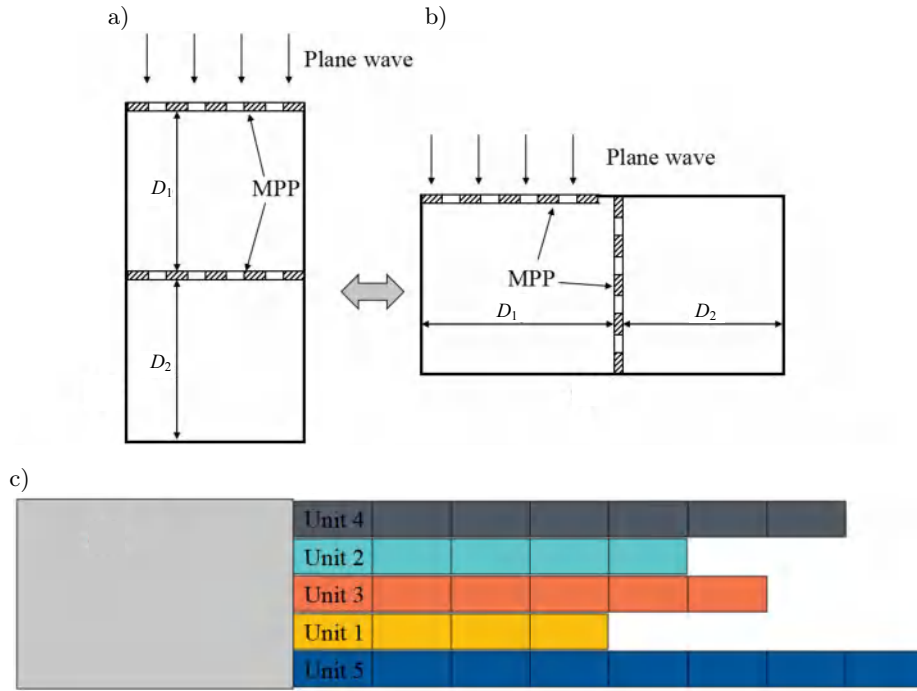


Fig. 4. Schematic diagram of two double-layer MPP structures and simplified model structure diagram: a) a conventional double-layer MPP; b) a turned double-layer MPP; c) a simplified model structure diagram.

structure is shown in Fig. 4c. The structure can be divided into 5 units, each of which is a multi-layered MPP structure and the number of layers increases from 4 to 8 layers sequentially. Furthermore, we number the units sequentially according to the number of layers of the MPP. Further, each unit can again be understood as a concrete example of the structure of Fig. 2.

Since the parameters of a MPP ($d = 0.2 \text{ mm}$, $t = 0.1 \text{ mm}$, $\sigma = 0.03$, and the spacing between adjacent MPPs is 20 mm) are consistent across the layers studied, Eq. (9) can be simplified and the transfer matrix of each unit can be expressed as:

$$[\mathbf{T}]_m = \{[\mathbf{P}][\mathbf{S}]\}^n \begin{cases} m = 1, 2, \dots, 5, \\ n = 4, 5, \dots, 8. \end{cases} \quad (18)$$

The equivalent relative acoustic impedance of each unit can be obtained by Eq. (12), and then the relative acoustic impedance of the structure as a whole can be obtained by the following equation:

$$\frac{S}{z_{eq}} = \frac{1}{\sum_{m=1}^5 \frac{S_m}{z_m}}, \quad (19)$$

where S and S_m represent the acoustic incident area and the unit acoustic incident area, respectively, and $S = 5S_m$.

Eventually, at the vertical incidence of plane waves, the sound absorption coefficient of the structure can be expressed as:

$$\alpha = \frac{4 \operatorname{Re}(z_{eq})}{[1 + \operatorname{Re}(z_{eq})]^2 + [\operatorname{Im}(z_{eq})]^2}. \quad (20)$$

The sound absorption coefficients calculated by FEM and TMM are shown in Fig. 5a, and the results of both calculations match satisfactorily. The reason for the slight error is that the FEM modeling considers the structure thickness. However, the effect of this on the analytical study is not significant. The absorption coefficient of the structure at $400 \sim 5000 \text{ Hz}$ consistently exceeds 0.9 , which has a wide absorption band. The equivalent acoustic impedance of the structure

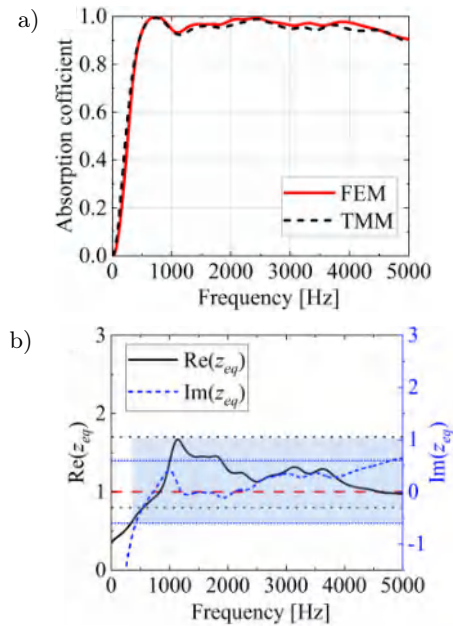


Fig. 5. Diagram of: a) the structural sound absorption coefficient; b) the relative acoustic impedance of the structure.

that will be derived according to Eq. (19) is shown in Fig. 5b. It can be seen from the figure that the relative acoustic impedance is not perfectly matched, but most of them are in region A (the region shown in Fig. 1b). Therefore, the absorption coefficient is more extensive than 0.8 in these frequency bands, which is an excellent verification of the sound absorption effect of the structure.

3. Parametric study

To better understand the effects of different design parameters on the sound absorption performance of the structure, a series of parametric studies are conducted in this section by varying parameters such as perforated plate thickness, perforation hole diameter, and perforation rate by using FEM simulations. In addition, the number of perforated plate layers, the unit distribution, and the size of the structure are also analyzed.

3.1. Effects of the perforation hole diameter

In order to better find out the effect of a perforation hole diameter on the sound absorption performance of the multi-layer MPP structure based on a curl space, we only change the value of the hole diameter d and keep other parameters constant. The results are shown in Fig. 6a, and it can be seen that choosing the proper aperture size is necessary to get the effect of broadband-efficient sound absorption. As the aperture

diameter gradually increases, the peak absorption coefficient moves toward lower frequencies and more absorption lows appear. In the latter case, it is caused by an acoustic impedance mismatch. For the former, we analyzed the single small hole of the MPP and the air back cavity, which would be the Helmholtz resonator. Furthermore, it can be reduced to a spring oscillator and its resonant frequency is proportional to $\sqrt{K/M}$. As the hole diameter increases, the stiffness factor of the equivalent air spring K decreases. These are because at the constant perforation rate σ , an increase in the hole diameter causes a decrease in the number of holes and thus an increase in the volume of the air back cavity corresponding to each small hole. There is also an increase in the oscillator mass M due to the increase in the aperture diameter. Therefore, the peak absorption coefficient will be shifted towards the lower frequencies.

3.2. Effects of the panel thickness

As shown in Fig. 6b, the effect of the thickness of the MPP on the absorption coefficient of the multi-layer MPP structure based on a curl space is shown. It can be seen from the figure that as the thickness of the MPP increases, the sound absorption coefficient decreases. According to Eq. (16), the acoustic impedance of the MPP increases when t rises, which leads to a decrease in the absorption coefficient. Moreover, this parameter has a significant influence on the sound absorption coefficient, thus, it must be chosen reasonably.

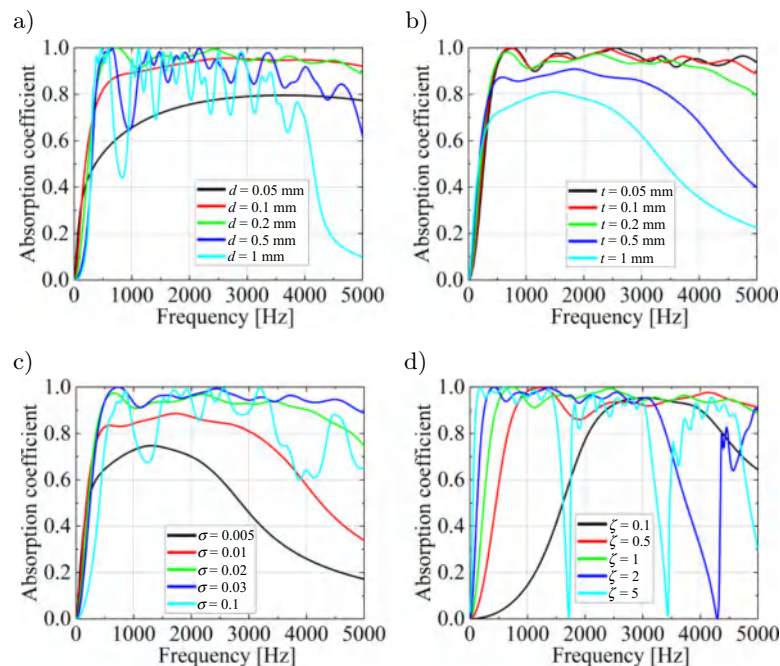


Fig. 6. Effect of different design parameters on the sound absorption coefficient of multi-layer MPP structure based on curl space: a) effects of the perforation hole diameter, $t = 0.1$ mm, $\sigma = 0.03$, $h = 20$ mm; b) effects of the panel thickness, $d = 0.2$ mm, $\sigma = 0.03$, $h = 20$ mm; c) effects of the perforation ratio, $d = 0.2$ mm, $t = 0.1$ mm, $h = 20$ mm; d) sound absorption coefficients of the structure with a different scale size, $d = 0.2$ mm, $t = 0.1$ mm, $\sigma = 0.03$, $h = 20$ mm.

3.3. Effects of the perforation ratio

In this subsection, we investigate the effect of the perforation rate σ on the structural absorption coefficient. The results are shown in Fig. 6c, the absorption coefficient increases, and the peak shifts to high frequencies when the perforation rate σ is increased. According to Eqs. (2), (3), and (16), we can know that the relative acoustic impedance of the MPP decreases as σ increases, which leads to an increase in the absorption coefficient. Similarly, by analogy with the spring oscillator model, we can find the reason for the peak shift to high frequencies. As σ increases, the equivalent air spring stiffness factor K increases, and M is constant, therefore the peak absorption coefficient moves to higher frequencies.

3.4. Effects of the structure with different scale sizes

In this subsection, the effect of the structure size on the absorption coefficient is studied, with ζ being the scaling ratio of the structure. The results are shown in Fig. 6d, the absorption coefficient peak will be moved to high frequencies when scaling down the structure as a whole. When scaled down to 0.5 times the structure, the sound absorption band will be in the middle and high frequencies (above 1000 Hz). When the structure is reduced to 0.1 times the structure, the absorption band will be at a high frequency (above 2400 Hz). On the contrary, the low-frequency sound absorption effect is enhanced by enlarging the structure. This is mainly

caused by the change of cavity in the structure, the large cavity is more suitable for low-frequency sound absorption, but the larger structure size will also be detrimental to the actual use. Therefore, we can choose the corresponding structure size according to the real situation.

4. Sound absorption mechanism

4.1. Acoustic impedance analysis

In order to explain the principle of efficient sound absorption by MPP broadband, the relative acoustic impedance of the overall structure and each unit is analyzed in this subsection, and the calculation results are shown in Fig. 7. Also, all MPP parameters studied are the identical, $d = 0.2$ mm, $t = 0.1$ mm, $\sigma = 0.03$. In Fig. 7, the thick black solid line and the thick blue dashed line indicate the relative sound resistance and the relative sound mass, respectively. The critical values in Fig. 1b are shown as thin dashed lines in Fig. 7, where the blue shading is the frequency band when the absorption coefficient is more significant than 0.8. From Figs. 7a–7e, it can be seen that as the number of MPP layers increases, the peak of the relative acoustic impedance increases and moves toward the lower frequencies. In addition, the sound absorption band becomes gradually wider. This indicates that the multi-layer MPP structure favors low-frequency broadband sound absorption. For the multi-layer MPP structure based on a curl space,

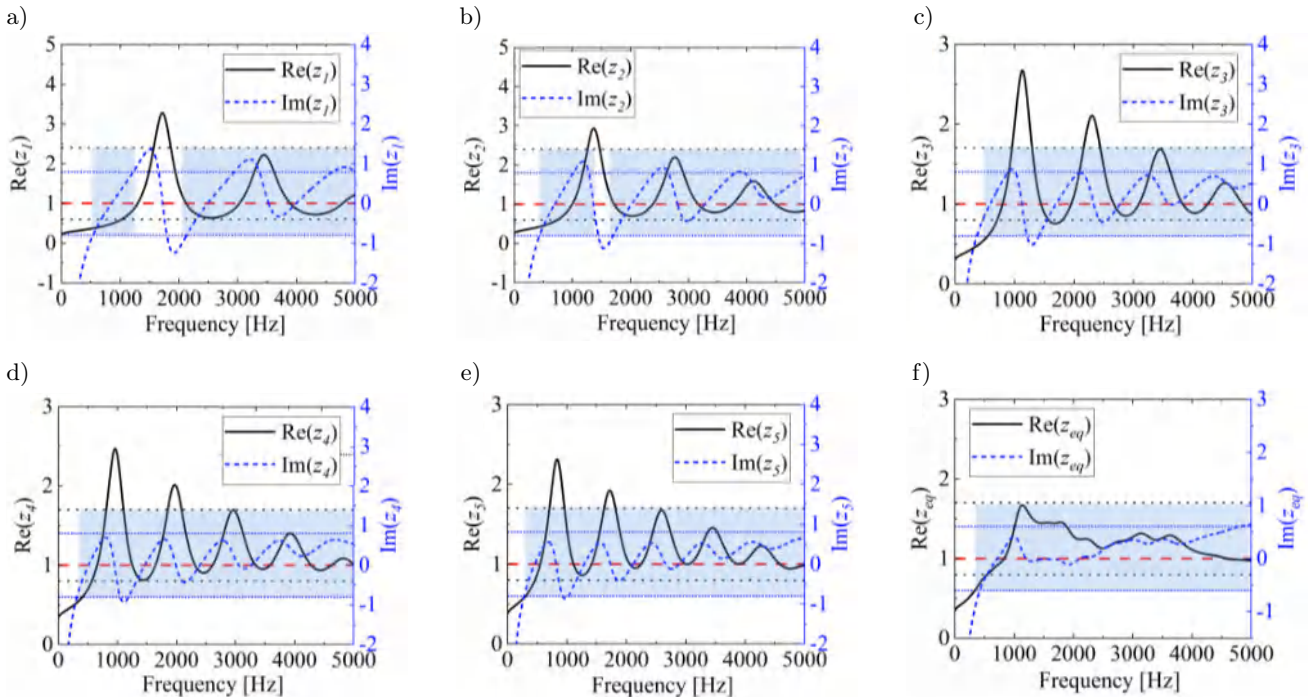


Fig. 7. Relative acoustic impedance of multi-layer MPP structures and their structural units based on curled space: a) unit 1 (4-layer MPP); b) unit 2 (5-layer MPP); c) unit 3 (6-layer MPP); d) unit 4 (7-layer MPP); e) unit 5 (8-layer MPP); f) the overall structure.

the parallel coupling of five units dramatically reduces the peak of the relative acoustic impedance, making the relative acoustic resistance and the relative sound mass closer to 1 and 0, respectively. Therefore, this also ensures the sound absorption effect at low frequencies and broadband sound absorption.

4.2. Complex frequency plane analysis

To further understand the absorption mechanism, we use a graphic approach to evaluate the reflection coefficient r in the complex plane (JIMÉNEZ *et al.*,

2017a; 2017b; ROMERO-GARCÍA *et al.*, 2016). In general, in the lossless case, the reflection coefficient has a complex conjugate zero and a conjugate pole. When the loss balances the energy leakage, the zero falls exactly on the real frequency axis, meaning that the critical coupling condition is satisfied. In addition, the leakage rate between the zero point and the pole can determine the absorption bandwidth (ROMERO-GARCÍA *et al.*, 2016). For example, as shown in Fig. 8c, there are three zeros and three poles, respectively. The zero point at 4000 Hz is very close to the real frequency axis, thus it will tend to perfect sound absorption.

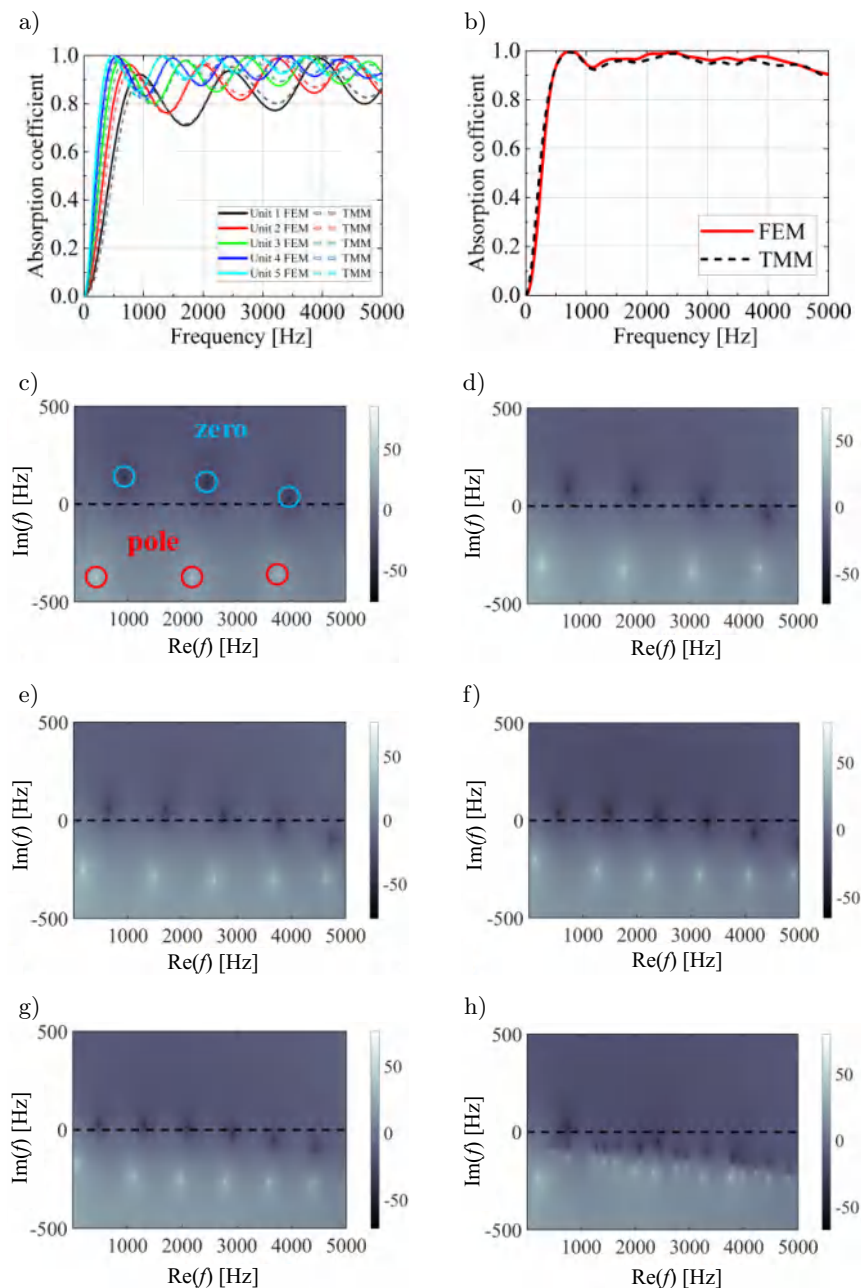


Fig. 8. a) and b) are the sound absorption coefficients of the five units and the overall structure, respectively; c)–h) are the representation of the $20 \log_{10} |\gamma|$ in the complex frequency plane for the multi-layer MPP structures and their structural units based on curled space; c) unit 1 (4-layer MPP); d) unit 2 (5-layer MPP); e) unit 3 (6-layer MPP); f) unit 4 (7-layer MPP); g) unit 5 (8-layer MPP); h) the overall structure.

In addition, there is a large leakage rate between the zero and pole points that extends the absorption band. However, the absorption valley will be lower because of fewer resonance peaks. These can be seen from the absorption curves in Fig. 8a. As can be seen in Figs. 8c–8g, further increasing the number of layers of MPP can obtain more resonance peaks, yet it is not effective in reducing the leakage rate. Therefore, there are still many sound absorption valleys in multi-layer MPP structures.

The zero point is almost always below the real frequency axis for the multi-layer MPP with a coiled structure, as shown in Fig. 8h. Although the critical coupling condition is not fully satisfied, a high absorption is still obtained at the resonant frequency. In addition, the leakage rate between zero and the pole is small and the number of resonance peaks is large. With the combined effect of these two reasons, both lower absorption valleys are eliminated and broadband absorption is achieved. As shown in Fig. 8b, the absorption curve consistently exceeds 0.9 in the 400~5000 Hz frequency range, and half absorption is achieved at 230 Hz.

5. Conclusions

This paper proposes a multi-layer micro-perforated panel structure based on a curled space for broadband sound absorption at low frequencies. The structure is approximated as a parallel composition of five multi-layer MPPs with different layers. The absorption coefficients of the structure have been computed under plane wave conditions using the TMM and the FEM methods, and the numerical results are matched perfectly. The results show that the multi-layer MPP structure can guarantee a high absorption rate (consistently over 90%) in the frequency range of 400~5000 Hz. The sound absorption mechanism of the multi-layer MPP structure was investigated using the acoustic impedance and the reflection coefficient of the complex frequency surface. In addition, the proposed structure is a subwavelength absorber because the low-frequency wavelengths in the air are 12 times larger in magnitude than the overall length of the structure and 31 times larger in volume than the width of the prototype.

Conflict of interest statement

The authors reported no potential conflict of interest.

Acknowledgments

This study was supported by the National Science Foundation of China (NSFC) under the grant no. 12104386; The science and technology innova-

tion Program of Hunan Province under the grant no. 2021RC2097; The Guangdong Basic and Applied Basic Research Fund Regional Joint Fund Youth Fund Project under the grant no. 2019A1515111118; China Postdoctoral Science Foundation under the grant no. 2022M711354; Natural Science Foundation of Hunan Province Youth Project under the grant no. 2022JJ40421.

References

- BUCCIARELLI F., MALFENSE FIERRO G.P., MEO M. (2019), A multilayer microperforated panel prototype for broadband sound absorption at low frequencies, *Applied Acoustics*, **146**: 134–144, doi: [10.1016/j.apacoust.2018.11.014](https://doi.org/10.1016/j.apacoust.2018.11.014).
- CARBAJO J., GHAFARI MOSANENZADEH S., KIM S., FANG N.X. (2020), Multi-layer perforated panel absorbers with oblique perforations, *Applied Acoustics*, **169**: 107496, doi: [10.1016/j.apacoust.2020.107496](https://doi.org/10.1016/j.apacoust.2020.107496).
- CHENG B., GAO N., HUANG Y., HOU H. (2022), Broadening perfect sound absorption by composite absorber filled with porous material at low frequency, *Journal of Vibration and Control*, **28**(3–4): 410–424, doi: [10.1177/1077546320980214](https://doi.org/10.1177/1077546320980214).
- CHENG Y. (2018), Acoustic absorption of a microperforated panel without the backing cavity, [in:] *INTER-NOISE and NOISE-CON Congress and Conference Proceedings*, pp. 171–180.
- COBO P., DE LA COLINA C., ROIBÁS-MILLÁN E., CHIMENO M., SIMÓN F. (2019), A wideband triple-layer microperforated panel sound absorber, *Composite Structures*, **226**: 111226, doi: [10.1016/j.compstruct.2019.111226](https://doi.org/10.1016/j.compstruct.2019.111226).
- CUI H., HU Z., HU H. (2022), Research on the low-frequency sound absorption characteristics of coiled Helmholtz cavity acoustic metamaterials, *Advances in Mechanical Engineering*, **14**(8), doi: [10.1177/16878132221119996](https://doi.org/10.1177/16878132221119996).
- GAO N., WU J.H., HOU H., YU L. (2017), Excellent low-frequency sound absorption of radial membrane acoustic metamaterial, *International Journal of Modern Physics B*, **31**(03): 1750011, doi: [10.1142/S0217979217500114](https://doi.org/10.1142/S0217979217500114).
- JIMÉNEZ N., ROMERO-GARCÍA V., PAGNEUX V., GROBY J.-P. (2017a), Quasiperfect absorption by subwavelength acoustic panels in transmission using accumulation of resonances due to slow sound, *Physical Review B*, **95**(1): 014205, doi: [10.1103/PhysRevB.95.014205](https://doi.org/10.1103/PhysRevB.95.014205).
- JIMÉNEZ N., ROMERO-GARCÍA V., PAGNEUX V., GROBY J.-P. (2017b), Rainbow-trapping absorbers: Broadband, perfect and asymmetric sound absorption by subwavelength panels for transmission problems, *Scientific Reports*, **7**(1): 13595, doi: [10.1038/s41598-017-13706-4](https://doi.org/10.1038/s41598-017-13706-4).
- LEE D.H., KWON Y.P. (2004), Estimation of the absorption performance of multiple layer perforated panel systems by transfer matrix method, *Journal of Sound*

- and *Vibration*, **278**(4–5): 847–860, doi: [10.1016/j.jsv.2003.10.017](https://doi.org/10.1016/j.jsv.2003.10.017).
11. LI C. (2018), Sound absorption of microperforated panels in complex vibroacoustic environments, [in:] *INTER-NOISE and NOISE-CON Congress and Conference Proceedings*, pp. 6237–6249.
 12. LI Y., ASSOUAR B.M. (2016), Acoustic metasurface-based perfect absorber with deep subwavelength thickness, *Applied Physics Letters*, **108**(6): 063502, doi: [10.1063/1.4941338](https://doi.org/10.1063/1.4941338).
 13. LIU C.R., WU J.H., CHEN X., MA F. (2019), A thin low-frequency broadband metasurface with multi-order sound absorption, *Journal of Physics D: Applied Physics*, **52**(10): 105302, doi: [10.1088/1361-6463/aafaa3](https://doi.org/10.1088/1361-6463/aafaa3).
 14. LIU C.R., WU J.H., YANG Z., MA F. (2020), Ultra-broadband acoustic absorption of a thin microperforated panel metamaterial with multi-order resonance, *Composite Structures*, **246**: 112366, doi: [10.1016/j.compstruct.2020.112366](https://doi.org/10.1016/j.compstruct.2020.112366).
 15. MAA D.-Y. (1983), Direct and accurate impedance measurement of microperforated panel, [in:] *INTER-NOISE and NOISE-CON Congress and Conference Proceedings*, pp. 363–366.
 16. MAA D.-Y. (1984), Wide-band sound absorber based on microperforated panels, [in:] *INTER-NOISE and NOISE-CON Congress and Conference Proceedings*, pp. 415–420.
 17. MAA D.-Y. (1994), Microperforated panel at high sound intensity, [in:] *INTER-NOISE and NOISE-CON Congress and Conference Proceedings*, pp. 1511–1514.
 18. MAA D.-Y., LIU K. (2000), Sound absorption characteristics of microperforated absorbers for random incidence, *Chinese Journal of Acoustics*, **19**(4): 289–298, doi: [10.15949/j.cnki.0217-9776.2000.04.001](https://doi.org/10.15949/j.cnki.0217-9776.2000.04.001).
 19. MAA D.-Y. (1998), Potential of microperforated panel absorber, *The Journal of the Acoustical Society of America*, **104**(5): 2861–2866, doi: [10.1121/1.423870](https://doi.org/10.1121/1.423870).
 20. MOSA A.I., PUTRA A., RAMLAN R., ESRAA A.-A. (2020a), Absorption coefficient of a double-layer inhomogeneous micro-perforated panel backed with multiple cavity depths, *Acoustics Australia*, **48**(1): 69–78, doi: [10.1007/s40857-020-00176-4](https://doi.org/10.1007/s40857-020-00176-4).
 21. MOSA A.I., PUTRA A., RAMLAN R., ESRAA A.-A. (2020b), Wideband sound absorption of a double-layer microperforated panel with inhomogeneous perforation, *Applied Acoustics*, **161**: 107167, doi: [10.1016/j.apacoust.2019.107167](https://doi.org/10.1016/j.apacoust.2019.107167).
 22. PRASETIYO I., SIHAR I., SUDARSONO A.S. (2021), Realization of a thin and broadband microperforated panel (MPP) sound absorber, *Applied Acoustics*, **183**: 108295, doi: [10.1016/j.apacoust.2021.108295](https://doi.org/10.1016/j.apacoust.2021.108295).
 23. RAFIQUE F., WU J.H., LIU C.R., MA F. (2022), Low-frequency sound absorption of an inhomogeneous micro-perforated panel with j-shaped cavities of different depths, *Acoustics Australia*, **50**(2): 203–214, doi: [10.1007/s40857-021-00261-2](https://doi.org/10.1007/s40857-021-00261-2).
 24. RAFIQUE F., WU J.H., WAQUAS M., LUSHUAI X., MA F. (2021), A thin double-layer multiple parallel-arranged inhomogeneous microperforated panel absorber for wideband low-frequency sound absorption, *Journal of the Brazilian Society of Mechanical Sciences and Engineering*, **44**(1): 1–18, doi: [10.1007/S40430-021-03327-4](https://doi.org/10.1007/S40430-021-03327-4).
 25. ROMERO-GARCÍA V., THEOCHARIS G., RICHOUX O., PAGNEUX V. (2016), Use of complex frequency plane to design broadband and sub-wavelength absorbers, *The Journal of the Acoustical Society of America*, **139**(6): 3394–3402, doi: [10.1121/1.4950708](https://doi.org/10.1121/1.4950708).
 26. SHAO H., HE J., ZHU J., CHEN G., HE H. (2022), Low-frequency sound absorption of a tunable multi-layer composite structure, *Journal of Vibration and Control*, **28**(17–18): 2279–2287, doi: [10.1177/10775463211008279](https://doi.org/10.1177/10775463211008279).
 27. WU F., XIAO Y., YU D., ZHAO H., WANG Y., WEN J. (2019), Low-frequency sound absorption of hybrid absorber based on micro-perforated panel and coiled-up channels, *Applied Physics Letters*, **114**(15): 151901, doi: [10.1063/1.5090355](https://doi.org/10.1063/1.5090355).
 28. XIAOQI Z., CHENG L. (2021), Broadband and low frequency sound absorption by Sonic black holes with micro-perforated boundaries, *Journal of Sound and Vibration*, **512**: 116401, doi: [10.1016/j.jsv.2021.116401](https://doi.org/10.1016/j.jsv.2021.116401).
 29. XIE S., YANG S., YAN H., LI Z. (2022), Sound absorption performance of a conch-imitating cavity structure, *Science Progress*, **105**(1): 00368504221075167, doi: [10.1177/00368504221075167](https://doi.org/10.1177/00368504221075167).
 30. ZHAO L., LIN T.R. (2022), A turned double-layer microperforated panel for low frequency sound absorption in enclosures with limited cavity space, *Applied Acoustics*, **188**: 108594, doi: [10.1016/j.apacoust.2021.108594](https://doi.org/10.1016/j.apacoust.2021.108594).

Research Paper

Evaluation of the Sedimentation Process in the Thickener by Using the Parameters of Longitudinal Ultrasonic Oscillations and Lamb Waves

Vladimir MORKUN, Natalia MORKUN, Vitalii TRON*,
Oleksandra SERDIUK, Alona HAPONENKO

Kyryvi Rih National University
Kyryvi Rih, Ukraine

*Corresponding Author e-mail: vtron@knu.edu.ua

(received September 4, 2022; accepted June 2, 2023)

Water is widely used in the mining industry, particularly in mineral enrichment processes. In the process of magnetic separation or flotation of crushed ore, a concentrate (an enriched product), and tailings (a product with a low content of a useful component) are obtained. One of the main tasks of enrichment processes is the efficient use of water resources. This is achieved by reclaiming and subsequent reusing water contained in ore beneficiation products by extracting it in industrial thickeners. Optimizing this process makes it possible to reduce water usage in the mining industry, reduce costs of mineral enrichment processes, and address extremely urgent environmental protection problems. To evaluate the process of sedimentation of the solid phase in the pulp within the thickener, measurements of parameters of longitudinal ultrasonic oscillations and Lamb waves that have traveled a fixed distance in the pulp and along the measuring surface in contact with it are used. The proposed approach allows for the consideration of pulp density, particle size of the solid phase in the ore material and the dynamics of changes in these parameters in the thickener at the initial stage of the sedimentation process. Based on the obtained values, adjustments can be made to the characteristics of its initial product, leading to reduced water usage and minimized loss of a useful component.

Keywords: thickener; ultrasound; automatic control; modeling; parameter estimation.



Copyright © 2023 The Author(s).
This work is licensed under the Creative Commons Attribution 4.0 International CC BY 4.0
(<https://creativecommons.org/licenses/by/4.0/>).

1. Introduction

In ore enrichment processes thickeners are used to separate, under the gravity action, a mixture of solid and liquid pulp phases into two products: a clarified aqueous solution in the overflow stream and a concentrated thick suspension in the underflow stream. Flocculants are also supplied to the system to increase the rate of solid particle sedimentation. As shown in several papers (BÜRGER *et al.*, 2013; SEGOVIA *et al.*, 2011; SMITH, n.d.), during the sedimentation process of particles of the solid phase in the pulp, several zones can be categorized (Fig. 1): 1 – particle sedimentation at a constant rate, 2 – variable rate of particle sedimentation, 3 – formation and compaction of the sediment.

The thickening process is controlled by changing the sedimentation parameters of crushed ore particles, which leads to increasing the transparency of the over-

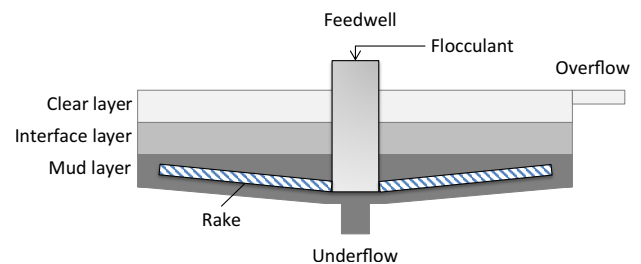


Fig. 1. Layers of the solid phase sedimentation in thickener.

flow (in order to achieve the minimum content of solid particles in the overflow) and increasing the density of the underflow product (in order to extract the maximum amount of solid particles). Control of the thickening process is usually achieved by adjusting the rate of release of the condensed product and adding a flocculant.

In the paper (Sinonine Tech, n.d.), it was demonstrated that the mechanism governing the solid phase particle sedimentation in the thickener is extremely complex. Different types of ore, particles size and variations in pulp concentration lead to diverse sedimentation characteristics. A higher rate of the sedimentation rate results in a shorter time for the pulp to remain in the thickener, otherwise the rate of the sediment layer growth turns out to be fast. This leads to the need to increase in the torque the thickener's rake drive motor, and, in extreme cases, to its overload and the shutdown of the thickener by the protection device. Conversely, a slow sedimentation rate requires that the pulp residence time in the thickener should be increased, otherwise the concentration of the solid phase in the unloaded material decreases, which leads to low dehydration efficiency and increases energy consumption for this process. It is concluded that the control of the performance of the thickener unloading slurry pump and the operational speed control of its drive motor in accordance with the current characteristics of the sedimentation process is of critical importance and central to optimizing the sedimentation process in thickeners.

In another work (Metso, 2017), the control of a thickener is considered from the perspective of measuring process characteristics and simple reaction to their changes. In the thickener, it is rather difficult to see or measure what is happening, and therefore the reaction time from the beginning of the deviation of any parameter to corresponding adjustments in process productivity and efficiency can be quite long. At the same time, the control of the thickener should take into account fluctuations in technological flow characteristics. This is achieved by regulating both the amount of flocculant supplied to the process and the speed of pumping out the thickener unloading product. Figure shows (in accordance with ISO 14617-6:2012) the proposed thickener control circuits: dosing of flocculant (MF – device for the flow measuring) depending on the mass flow rate of the initial material with feedback from the level of the sediment layer (LT – device for the level measuring) or the pressure of the sedimented material layer (PT – device for the pressure measuring), and the performance of the thickener discharge pump depending on either the concentration of the solid phase (DT – device for the density measuring) or the overflow turbidity. The torque of the rake drive motor (M) is also controlled to prevent overloading. In practice, thickened product pumps and flocculant dosing pumps must be controlled based on the measured parameters of the sedimentation process to achieve the thickener's desired operating point under various production scenarios and meet target quality indicators.

However, as noted in the paper by OJEDA *et al.* (2014), conventional feedback control is ineffective for stabilizing the process when the properties of the raw material fluctuate significantly over time, primarily be-

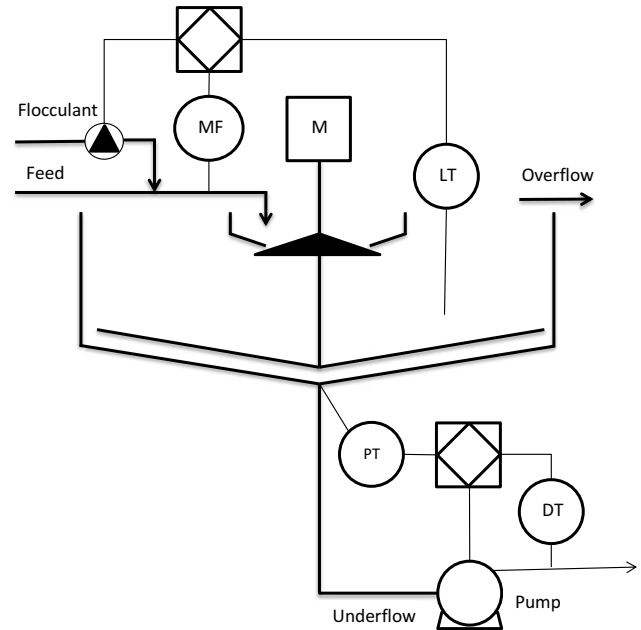


Fig. 2. General contours of the thickener control.

cause the dynamics of the process demonstrates high nonlinearity. This paper presents innovative approach based on an expert system for an industrial thickener with a diameter of 125 m and processing 13 000 m³/h of concentrate containing 27% solids. It is noted that the proposed expert system should be based on an information base encompassing all possible operating scenarios and real-time measurements of the main technological variables.

Thus, the control of sedimentation process variables is crucial for the effective operation of a thickener. In the study conducted by ZUZUNAGA *et al.* (2018), attention is paid to three important control parameters within the thickening technological process: pulp flow speed at the thickener inlet, thickened product flow speed at its outlet, and clarified water flow into the overflow. These measurements have certain problems that can potentially affect the ability to accurately determine the flow rate: pipe size, the medium density in the flow, pump type, the involved air, access to the pipe, etc. Taking these factors into consideration is important for obtaining reliable measurement results that can serve as an indirect indicators of the efficiency of the thickening process.

Currently, the evaluation of the sedimentation process of crushed ore particles entering the thickener relies on the recognition of sediment level and the boundary between different media (MORKUN *et al.*, 2014b; 2014c; 2015b; KANSAI Automation Co., n.d.; SMITH, n.d.). This assessment characterizes the dynamics of particles with specific concentration and sizes in the pulp. Since these estimates are used to regulate the density of the discharge product and the flow of flocculant, inaccurate measurement of these pa-

rameters can lead to water entering into the thickener discharge, solid particles entering the overflow or problems with flocculation. All these problems, in turn, lead to additional costs associated with increased flocculant consumption or the need for reprocessing of ore pulp.

There are several methods of measuring sediment levels and media interfaces in thickeners: manual core sampling (manual core sampling), measurement of hydrostatic pressure, buoyancy-based system, ultrasonic measurements with fixed position ultrasound, mechanical lowering sample analyzers – mud diver (SMITH, n.d.).

Taking core samples manually is a complex, risky, and time-consuming test. When used in combination with a thickener rake torque measurement, this method can actually be used to estimate the sediment level. However, it does not yield high accuracy of estimation. Depending on the rheology of the sediment, the torque and reservoir pressure do not always align. Moreover, this method also requires frequent maintenance.

The float method can incur high operational costs. Floats also often leak and fill with substances they are meant to float in, and as a result they sink. It is not easy to maintain their operational filling with the required liquid density. The boundary of media separation is difficult to detect using this method, especially when the difference in density between the layers can be very small (Markland Specialty Engineering Ltd., n.d.).

Ultrasonic devices based on the measurement of the signal's transit time to reflective surfaces capture the sediment level effectively, provided the medium does not weaken the probing signal's energy before it reaches the sediment layer. However, when using this method, it is difficult to detect the layer of interest, especially if its boundary is not clearly defined (MORKUN *et al.*, 2014b; 2014c; KANSAI Automation Co., n.d.).

A mud diver is an automated device that mechanically lowers a probe into a thickener. This probe can use various measurement methods (for example, optical, ultrasonic, etc.) to determine the depth of layers in the reservoir in real-time (PLA Process Analysers, n.d.). The dives of the mud diver are synchronized with the rotation of the thickener's rake, which prevents entanglement of the probe in the rake arms. Additionally, mud divers are usually equipped with a washing station that cleans the probe after each dive, preventing its contamination. However, this method cannot ensure the efficiency and continuous data acquisition necessary for the operation of automatic thickener control systems. Moreover, like all mechanical devices, mud divers require high maintenance costs.

Therefore, for effective thickener control, it is essential to obtain operational information about the process of sedimentation of particles of the solid phase in the pulp. Having such an estimate applied to its ini-

tial stage allows one to predict the characteristics of final product. The assessment of this process should be based on measurements of the dynamics of changes in the concentration of the solid phase within the pulp and the size of its particles at a certain depth of the thickener.

The objective of this research is to develop methods for gathering information about the ore pulp thickening process in an industrial thickener. This information allows to improve the quality of control, ensuring the desired concentration of the solid phase in the final product, and ultimately reducing production costs. Existing automatic control systems for industrial thickeners are characterized by prolonged response dynamics to disturbing influences and extended transient processes. In contrast, the proposed method of ultrasonic control of the process of sedimentation of crushed ore particles in the thickener is based on measuring the concentration of solid-phase particles and their size in the initial stage of sedimentation. This enables obtaining highly accurate forecast of final product characteristics.

2. Proposed methodology

In the mining industry, water is widely used in hydrometallurgical and mineral enrichment processes (GOLIK *et al.*, 2015a; 2015b; MORKUN *et al.*, 2017). In the beneficiation based on the magnetic separation method, ore particles are ground to a size that is approximately equal to that of the useful component size, which consequently allows the magnetic separator to extract the valuable component from the ore pulp. Before entering the crushing unit, the ore is mixed with water and brought to the optimal size in several stages before being fed into the magnetic separator. Each of these stages includes the following essential technological operations: grinding, classification, and magnetic separation (MORKUN *et al.*, 2015a; SHUKLA, 2021).

In the process of magnetic separation, two products are obtained: concentrate and tails, which are then sent to dehydration systems (ARJMAND *et al.*, 2019; GARM-SIRI, UNESI, 2018; TRIPATHY *et al.*, 2021).

Figure 3 presents a technological diagram of the beneficiation process at the Northern Mining and Beneficiation Plant in Kryvyi Rih, Ukraine (MORKUN *et al.*, 2015a). In this figure, the following symbols are used: mill denotes the ball mill (a technological apparatus for reducing the size of ore particles) and numbers denote the stages of ore particle separation (1 – first stage, 2 – second stage, 3 – third stage, 4 – fourth stage); MS denotes the magnetic separator (a technological apparatus for separating ore particles according to their magnetic properties), while sizer (classifier), H/c (hydrocyclone) and T-r (thickener) are technological apparatus for separating ore particles based on their size.

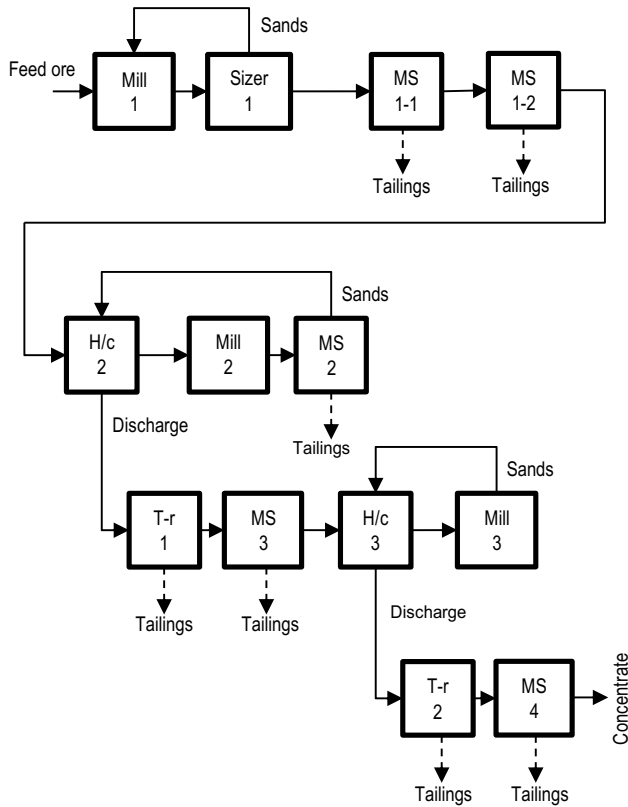


Fig. 3. Technological scheme of the iron ore beneficiation process.

The main internal control influences in the beneficiation line, presented in Fig. 3, are water flows into technological units. In Figs. 4 and 5, examples of obtained qualitative-quantitative dependencies that characterize the influence of this parameter on the technological process are presented.

The dependence of the output of the -0.044 mm grain size class on the flow of water to technological units distributed along the enrichment line is presented in Fig. 4. Here, L denotes the measuring point numbers after the technological devices (1 – mill 1; 2 – sizer, etc.).

The dependence of the mass fraction of iron in the industrial product on the water flow to the technological units is presented in Fig. 5.

The slurry enters the dirt separators at the first stage (point 8), where the solid phase is crushed to a fineness of 91% in the -0.074 mm class. In the dirt separators at the second stage (point 13) the fineness reaches 98% in the -0.074 mm class. Under these conditions, the measurement error for the concentration of the solid phase in the pulp at a level of 0.5–1.5 m from the surface of the pulp in the desludger is 1.8–2.1%, and the concentration of the control size class -0.074 mm showed a deviation in the range of 1.5–1.7% compared to the results of laboratory analysis.

The technological process of ore beneficiation (Fig. 4) involves the pulp entering the thickener, where the solid phase is crushed to expose the ore joints (MORKUN *et al.*, 2014a).

According to the proposed method, a measuring module is placed in the thickener, which enabling for conducting ultrasonic measurements using longitudinal ultrasonic oscillations and Lamb waves. The measuring module placed in the upper part of the thickener vertically along the depth of the thickener. It can function as either a stationary or mobile unit.

First, a reference liquid, in this case, water, is supplied to the measuring module. In the measuring module, high-frequency ultrasonic vibrations are formed and travel a fixed distance in it. The obtained results

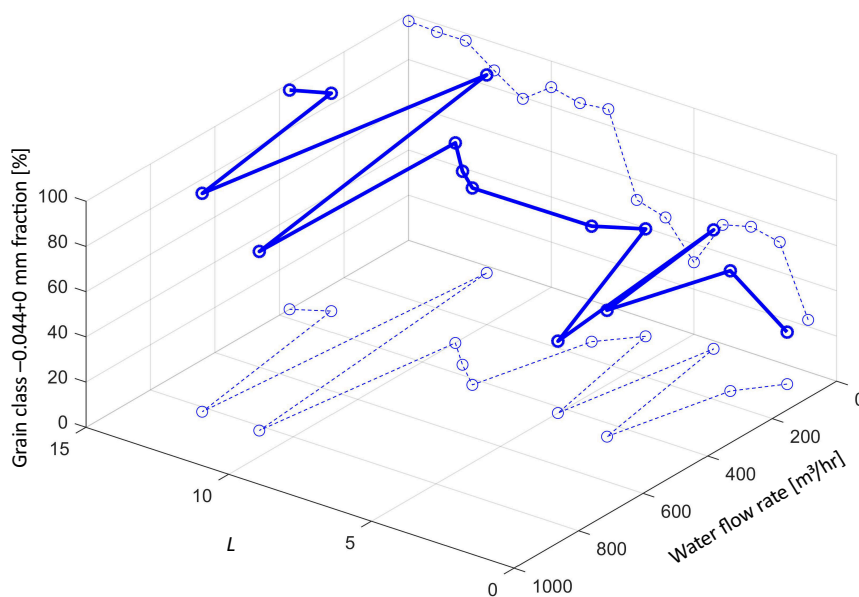


Fig. 4. Output of the grain size class -0.044 mm depending on the water flow to the technological units: the solid line represents a distributed function; the dashed lines are projections on coordinate planes.

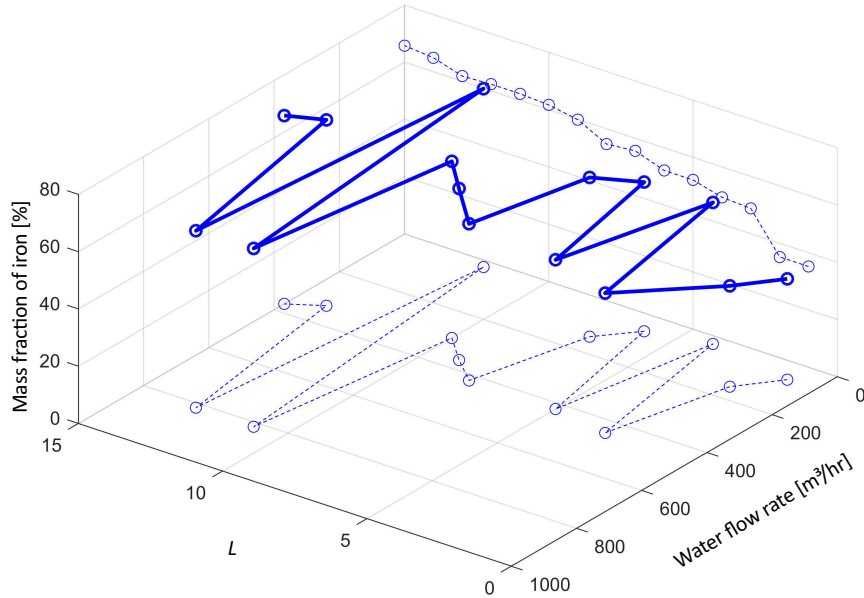


Fig. 5. The mass fraction of iron in the industrial product depending on the water flow to the technological units: the solid line is a distributed function; the dashed lines are projections on coordinate planes.

measure the attenuation of the intensity of high-frequency ultrasonic vibrations serving as reference (basic). In the operational state, an ore suspension flow is formed in the measuring chamber of the thickener. This flow generates high-frequency ultrasonic vibrations that travel a fixed distance when there is a flow of ore suspension in the measuring chamber. For high-frequency ultrasonic vibrations that have traveled a fixed distance throughout the flow of water and ore suspension, the ratio of ultrasound intensities S_1 is determined:

$$S_1 = \ln \frac{I_{B1}^{\text{vol}}}{\langle I_{v1}(z) \rangle}, \quad (1)$$

where I_{B1}^{vol} is the intensity of high-frequency bulk ultrasonic waves that have traveled a fixed distance z throughout the water flow, z is a fixed distance of the ultrasonic waves travelling throughout the water flow, and $\langle I_{v1}(z) \rangle$ is the intensity of high-frequency bulk ultrasonic waves that have traveled a fixed distance z throughout the flow of ore suspension.

The equation for $\langle I_{v1}(z) \rangle = I_{B1}^{\text{vol}}$ is:

$$\langle I_{v1}(z) \rangle = I_{B1}^{\text{vol}} \exp \left(-\frac{W \cdot z}{\varkappa} \int_0^{r_m} \sigma(v_1, r) F(r) dr \right), \quad (2)$$

where $\varkappa = \int_0^{r_m} \frac{4\pi r^3}{3} F(r) dr$, $F(r)$ is the distribution function of solid-phase particles in the ore suspension based on their size r , r_m is the maximum size of solid-phase particles in the ore suspension, and $\sigma(v_1, r)$ is the attenuation cross-section of high-frequency bulk ultrasonic waves with frequency v on a particle of size r .

The size $\sigma(v, r)$ for any frequency bulk ultrasonic waves is determined by the sum of absorption cross-

sections $\sigma_s(v, r)$ and scattering $\sigma_c(v, r)$ ultrasound (MORKUN *et al.*, 2014b; 2019):

$$\sigma(v, r) = \sigma_c(v, r) + \sigma_s(v, r) \quad (3)$$

In the high-frequency region ($v_1 \geq 5 \cdot 10^6$ Hz), the attenuation of ultrasound is primarily caused by the scattering of ultrasonic waves on the solid-phase particles: $\sigma(v_1, r) \approx \sigma_c(v_1, r)$. Therefore, the attenuation formed in the frequency region $v_1 \geq 5 \cdot 10^6$ Hz is determined by the size and concentration of the solid phase particles in the ore suspension.

In (MORKUN *et al.*, 2019) it was concluded that Lamb waves can be used to obtain a value proportional only to the concentration of the solid phase. In the metal plate, which is a component of the measuring module, Lamb waves are formed, which propagate along its entire length. In this case, the attenuation coefficient of ultrasonic Lamb waves that have traveled a fixed distance along the metal plate is determined by the expression:

$$\alpha = \left[(1 - W) \frac{\rho_w}{\rho} + W \frac{\rho_s}{\rho} \right] C_v, \quad (4)$$

where W is the mass concentration of the solid phase in the suspension, while ρ_w , ρ_s , ρ are the specific densities of water, solid phase particles, and the material of the metal plate. In Eq. (4), the value C_v does not depend on the parameters of the surrounding environment whose parameters are controlled, and is a function of the wave numbers of ultrasonic Lamb waves, including both longitudinal and transverse waves of the metal plate material.

The intensity of Lamb waves is measured after they travel a certain distance along a metal plate. The in-

tensity of Lamb waves that have traveled a fixed distance through a metal plate l_n ($n = 1, 2, 3, \dots, m$) can be determined by the expression:

$$I_{nL} = I_{0L} \exp\left(-\left[(1-W)\frac{\rho_w}{\rho} + W\frac{\rho_s}{\rho}\right]C_v l_n\right), \quad (5)$$

where I_{0L} and I_{nL} are the intensity of Lamb ultrasonic waves emitted and the intensity of Lamb ultrasonic waves after they have traveled the distance l_n ($n = 1, 2, 3, \dots, m$), respectively.

If the metal plate is in contact with pure water, then the intensity of ultrasonic Lamb waves in this case is:

$$I_{nBL} = I_{0L} \exp\left(-\frac{\rho_w}{\rho}C_v l_n\right). \quad (6)$$

It follows from Eqs. (5) and (6):

$$I_{nL} = I_{nBL} \exp\left(-\frac{WC_v l_n}{\rho}(\rho_s - \rho_w)\right), \quad (7)$$

that is, the intensity of the received signal is determined by the concentration of the solid phase of the ore suspension and the length of the measurement section l_n ($n = 1, 2, 3, \dots, m$) – the length of the segment of the metal plate along which the Lamb waves have travelled.

According to the proposed method, the value S_2 is calculated as:

$$S_2 = \ln \frac{I_{nBL}}{I_{nL}} = W_n \frac{(\rho_s - \rho_w)}{\rho} C_v l_n. \quad (8)$$

Thus, the value S_2 is determined exclusively by the solid-phase concentration of the ore suspension at a certain depth of the thickener and uniquely characterizes its changes during the sedimentation process. The schematic for measuring changes in the solid-phase concentration of the ore suspension during its sedimentation in the thickener is shown in Fig. 6. To generate and shape ultrasonic waves, as well as to receive, amplify, filter, and select their frequency and timing, we use the corresponding sub-units of our self-designed “Pulsar” ultrasonic granulometer. All other components are standard units of computerized automated process control systems employed in ore beneficiation plants.

The ratio of values S_1 and S_2 characterizes the granulometric composition of the controlled medium:

$$S = \frac{S_1}{S_2} = \frac{z \cdot \rho}{l C_v \kappa (\rho_s - \rho_w)} \int_0^{r_m} \sigma(v, r) F(r) dr. \quad (9)$$

The size S depends only on the size distribution of solid particles, which means that it unambiguously determines the concentration of the controlled particle size class of the solid phase in the thickener’s controlled zone.

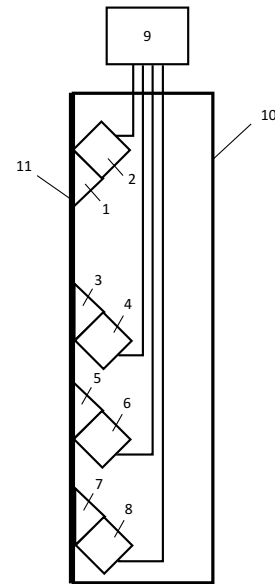


Fig. 6. Scheme for measuring changes in the solid-phase concentration of the ore suspension during its sedimentation in the thickener: 1, 3, 5, 7 – prisms that form an ultrasonic signal; 2, 4, 6, 8 – piezo transducers; 9 – control unit; 10 – measuring module; 11 – measuring surface.

Therefore, the proposed method makes it possible to determine the concentration of the solid-phase concentration and the content of crushed material particles in the control size class, enabling an assessment of the sedimentation process of the solid-phase pulp particles in the thickener.

3. Results

Tests of the measuring system, implementing the proposed method, were carried out at the ore beneficiation factory to verify its metrological and operational characteristics under real industrial conditions. The tests were conducted in two stages. During the first stage, the installation, adjustment, and calibration of the measuring system was carried out in relation to the technological process of the beneficiation factory. In the second stage, the metrological and operational-technical characteristics of the measuring system were determined. To record the metrological characteristics, measurements were taken of the solid-phase concentration and the content of the controlled size class (-0.074 mm) in the precipitated product, with simultaneous sampling for sieve analysis. Measurements were carried out at the minimum, nominal, and maximum consumption of the thickener’s input product. The estimation of the measurement error for both the solids content in the pulp and the content of the controlled size class was made by comparing the readings of the measuring system with the results of a carefully performed sieve analysis of the samples.

The analysis of the obtained results is of interest concerning the ratio of the values between equipment error and the error in the measurement method itself. As it was shown above, the operation of the measuring system relies on determining the characteristics of ultrasonic vibrations propagating in the controlled volume of the pulp and in the plate in contact with it. This device generates two main signals S and S_2 , which characterize the measured technological parameters. Due to the fact that pulp is a randomly inhomogeneous medium in which there are fluctuations in both the number and size of crushed ore particles, along with density variations in the controlled volume of the pulp, the signals generated by the measuring system are also subject to fluctuations. These factors are the primary causes of the inaccuracy in the ultrasonic measurement method used to determine pulp parameters.

Let η be the value characterizing the granulometric composition of the pulp, i.e., the mass fraction of solid particles whose sizes are smaller (or larger) than a given value, for example, 0.074 mm. Fluctuations in the above-mentioned physical quantities lead to scattered values η by size $\Delta\eta$, which, as the analysis showed, can be determined by the expression:

$$\begin{aligned} \Delta\eta = & K \frac{1}{S_2} \left(\left[\exp \left\{ \frac{\overline{W}V_1}{\aleph} (1-\lambda)^2 \right\} - 1 \right] \right. \\ & + S^2 \left[\exp \left\{ \frac{\overline{W}V_2}{\aleph} (1-\theta)^2 \right\} - 1 \right] \\ & \left. + S^2 \theta^2 \left(\frac{\Delta\rho_s}{\overline{\rho}_s - \rho_w} \right)^2 \right)^{\frac{1}{2}}. \end{aligned} \tag{10}$$

Here, the magnitude

$$K = \left| \frac{d\eta}{dS} \right|$$

characterizes the sensitivity of the measurement method. The size η can be represented as a linear or quadratic dependence on the signal S generated by the device based on the measurements results. As the tests showed, this dependence in the working range is linear and can be presented in the form:

$$\eta = a_0 + a_1 S,$$

where the coefficients a_0 and a_1 are determined by the method of least squares based on the results of the sieve analysis of the samples and the readings of the device.

In this case, the sensitivity of the measurement method is given by:

$$K = \left| \frac{d\eta}{dS} \right| = |a_1|.$$

Taking into account Eq. (9), the signal S generated by the measuring system is determined by the expression:

$$S = \frac{V_1(1-\lambda)}{V_2(1-\theta)}, \tag{11}$$

where

$$\lambda = \int_0^\infty F_\eta(r) dr \exp \left[-\frac{\sigma(v,r)z}{V} \right],$$

and $\sigma(v,r)$ is the full frequency ultrasound scattering cross-section v on a particle of radius r , and V_1, V_2, z are the values characterizing the geometric parameters of the measurements.

The signal S_1 generated by the measuring system is determined by the equation:

$$S_2 = \frac{\overline{W}V_2}{\aleph} (1-\theta), \tag{12}$$

where \overline{W} is the mean value of the volume fraction (concentration) of the solid in the controlled volume V of the pulp; $\theta = \exp \left\{ -\frac{\aleph}{V_2} (\overline{\rho}_s - \rho_w) C_v l \right\}$; $F_\eta(r)$ is the size distribution function of particles at a certain mass fraction of the size class η ; $\overline{\rho}_s$ is the average pulp density; C_v is the constant value; l is the length of the measuring plate; \aleph is the distribution function of particles of the solid phase in the ore suspension by size.

Using some approximations and transformations, Eq. (10) can be reduced to a simpler form:

$$\Delta\eta = KS \sqrt{\frac{\aleph}{\overline{W}} \left(\frac{1}{V_1} + \frac{1}{V_2} \right) + \frac{\theta \Delta\rho_s^2}{(\overline{\rho}_s - \rho_w)^2}}. \tag{13}$$

It should be noted that complete a priori information for calculating the value $\Delta\eta$ according to Eq. (13) is not available, but these data can be obtained indirectly.

Let us first focus on the determination of the measurement error of the mass fraction of the solid in the pulp β :

$$\beta = bS_2, \tag{14}$$

where b is the coefficient determined by experimental data. Equation (14) describes the dependence of the results of evaluation measurements with specific values of the concentration of the solid phase of the pulp, obtained as a result of laboratory analysis of selected pulp samples, i.e., it actually scales the measurement results and converts them into a commonly used concentration scale.

The error of this magnitude $\Delta\beta$ in general, it can be presented in the form:

$$\Delta\beta = \beta \sqrt{\frac{\aleph}{\eta \overline{W} V_2} + \frac{\theta \Delta\rho_s^2}{(\overline{\rho}_s - \rho_w)^2}}. \tag{15}$$

It follows from Eqs. (13) and (15) that the error in measuring the granulometric composition $\Delta\eta$ can be expressed due to the measurement error of the mass fraction of the solid $\Delta\beta$:

$$\Delta\eta = KS \sqrt{\left(\frac{\Delta\beta}{\beta} \right)^2 + \frac{\aleph}{\overline{W}V}}. \tag{16}$$

The analysis showed that

$$\frac{\varkappa}{\overline{WV}} \ll \left(\frac{\Delta\beta}{\beta} \right)^2,$$

therefore, it is possible to obtain an even simpler expression for estimating the error value $\Delta\eta$:

$$\Delta\eta \approx KS \frac{\Delta\beta}{\beta} = |\eta - a_0| \frac{\Delta\beta}{\beta}. \quad (17)$$

In the process of experimental studies, pulp samples were taken at fixed points along the depth of the thickener. Samples were collected into a measuring container and then processed using proven laboratory methods. The volume and mass concentration of the solid phase of the pulp, its density, as well as the content of the control size class -0.074 mm were determined. The determination of the granulometric composition of crushed ore in the pulp was carried out by the dry sieve method, i.e., by sieving through a set of standard sieves with holes of normalized sizes: +3, 3+1, 1+0.5, 0.5+0.25, 0.25+0.125, 0.125+0.074, 0.074+0.056, 0.056+0.044, 0.044+0. The density of the crushed material was determined by the pycnometer method. Samples were analyzed with a density ranging from 1050 to 1550 kg/m³, with a fineness class of -0.074 mm ranging from 30 to 98% and a crushed ore density ranging from 1900 to 4500 kg/m³. The results of industrial tests testify to the fact that the uncertainty in determining the mass fraction of solids $\Delta\beta$ makes up $\sim 2\%$. This value is used as the initial value for calculating the value $\Delta\eta$ according to Eq. (17), and the results are given in Table 1.

Table 1. Calculation results $\Delta\eta$.

| | | | | | |
|---------------------|-----|-----|-----|-----|-----|
| $\eta_{-0.074}$ [%] | 50 | 55 | 60 | 65 | 70 |
| $\Delta\eta$ [%] | 1.6 | 1.4 | 1.2 | 1.0 | 0.7 |

Therefore, the accuracy of measuring the granulometric composition of the pulp at the thickener's depth depends on the size range of the measurements. With a high mass fraction of the controlled size class (65% or more), the uncertainty of the measurement method is approximately 1%. However, as the mass fraction of the controlled size class decreases to 50% and below, the method's uncertainty doubles.

Based on the results of the conducted tests, it can be concluded that the error values associated with the measurement method and the instrument's error in the measuring system itself are practically comparable. In the actual operational conditions of the processing plant, it is possible to ensure the measurement of the controlled technological parameters with an uncertainty ranging from 1 to 2%.

The proposed method for estimating pulp density and particle size of its solid phase in the initial stage of

the sedimentation process allows to implement thickener control based on the MPC (model-predictive control) algorithm and, for example, a widespread phenomenological model (BARTH *et al.*, 2016; BETANCOURT *et al.*, 2014; BÜRGER *et al.*, 2019). It is also possible to use expert control systems based on fuzzy rules, and other algorithms for optimal control of a thickener (CHAI *et al.*, 2014; TAN *et al.*, 2015; XU *et al.*, 2015; ZHANG *et al.*, 2016).

According to the industrial test results of the automatic control system of the thickener using ultrasonic control means, it was determined that its use as part of the automatic control system of the processes of iron ore enrichment at the Northern Iron Ore Beneficiation Works can lead to a reduction in water consumption by 3.5% and a decrease in iron-magnetite losses by 0.6–0.7%.

4. Conclusion

To evaluate the sedimentation process of the solid phase of the pulp in the thickener, measurements of longitudinal ultrasonic oscillations and Lamb waves that have traveled a fixed distance in the pulp and on the measuring surface in contact with it were used.

As a result of industrial tests of the measuring system, the following was established: the proposed method ensures stable measurement of the content of solid and the controlled size class of crushed materials, with measurement errors not exceeding the specified technological parameters $\pm 2\%$.

Since all calculations in the proposed automatic control method are carried out based on measurements relative to the characteristics of water, which serves as the reference substance, the results obtained are resilient against various disturbing factors that reduce the accuracy of measurements of the solid-phase parameters in the ore suspension.

The proposed approach allows to take into account pulp density, particle size of the solid phase in the ore material and the dynamics of changes in these parameters in the thickener at the initial stage of the sedimentation process. Based on these obtained values, adjustments can be made to the characteristics of the initial product, leading to a reduction in water consumption by 3.5% and a decrease in the loss of the useful component by 0.6–0.7%.

Acknowledgments

Funded by the Alexander von Humboldt Foundation.

References

1. ARJMAND R., MASSINAEI M., BEHNAMFARD A. (2019), Improving flocculation and dewatering performance of

- iron tailings thickeners, *Journal of Water Process Engineering*, **31**: 100873, doi: [10.1016/j.jwpe.2019.100873](https://doi.org/10.1016/j.jwpe.2019.100873).
2. BARTH A., BÜRGER R., KRÖKER I., ROHDE C. (2016), Computational uncertainty quantification for a clarifier-thickener model with several random perturbations: A hybrid stochastic Galerkin approach, *Computers & Chemical Engineering*, **89**: 11–26, doi: [10.1016/j.compchemeng.2016.02.016](https://doi.org/10.1016/j.compchemeng.2016.02.016).
 3. BETANCOURT F., BÜRGER R., DIEHL S., FARÅS S. (2014), A model of clarifier-thickener control with time-dependent feed properties, Presented at Physical Separation '13, Falmouth, UK, *Minerals Engineering*, **62**: 91–101, doi: [10.1016/j.mineng.2013.12.011](https://doi.org/10.1016/j.mineng.2013.12.011).
 4. BÜRGER R., CHOWELL G., GAVILÁN E., MULET P., VILLADA L.M. (2019), Numerical solution of a spatio-temporal predator-prey model with infected prey, *Mathematical Biosciences and Engineering*, **16**(1): 438–473, doi: [10.3934/mbe.2019021](https://doi.org/10.3934/mbe.2019021).
 5. BÜRGER R., DIEHL S., FARÅS S., NOPENS I., TORFS E. (2013), A consistent modelling methodology for secondary settling tanks: A reliable numerical method, *Water Science & Technology*, **68**(1): 192–208, doi: [10.2166/wst.2013.239](https://doi.org/10.2166/wst.2013.239).
 6. CHAI T., LI H., WANG H. (2014), An intelligent switching control for the intervals of concentration and flow-rate of underflow slurry in a mixed separation thickener, *IFAC Proceedings Volumes*, **47**(3): 338–345, doi: [10.3182/20140824-6-ZA-1003.02114](https://doi.org/10.3182/20140824-6-ZA-1003.02114).
 7. GARMSIRI M.R., UNESI M. (2018), Challenges and opportunities of hydrocyclone-thickener dewatering circuit: A pilot scale study, *Minerals Engineering*, **122**: 206–210, doi: [10.1016/j.mineng.2018.04.001](https://doi.org/10.1016/j.mineng.2018.04.001).
 8. GOLIK V., KOMASHCHENKO V., MORKUN V., GAPO-NENKO I. (2015a), Improving the effectiveness of explosive breaking on the basis of new methods of borehole charge initiation in quarries, *Metallurgical and Mining Industry*, **7**(7): 383–387.
 9. GOLIK V., KOMASHCHENKO V., MORKUN V., ZAALISHVILI V. (2015b), Enhancement of lost ore production efficiency by usage of canopies, *Metallurgical and Mining Industry*, **7**(4): 325–329.
 10. KANSAI Automation Co., Ltd. (n.d.), *Ultrasonic sludge blanket level meter*, https://kansai-automation.co.jp/en/product/flow_meter_etc/sludge_interface.php (access: 22.08.2022).
 11. Markland Specialty Engineering Ltd. (n.d.), *Portable sludge blanket level detector*, <https://sludgecontrols.com/our-products/portable-sludge-level-detector> (access: 22.08.2022).
 12. Metso (2017), *Advanced thickener control*, <https://www.mogroup.com/insights/blog/mining-and-metals/advanced-thickener-control/> (access: 22.08.2022).
 13. MORKUN V., MORKUN N., TRON V. (2015a), Distributed closed-loop control formation for technological line of iron ore raw materials beneficiation, *Metallurgical and Mining Industry*, **7**(7): 16–19.
 14. MORKUN V., MORKUN N., TRON V. (2015b), Distributed control of ore beneficiation interrelated processes under parametric uncertainty, *Metallurgical and Mining Industry*, **7**(8): 18–21.
 15. MORKUN V., MORKUN N., PIKILNYAK A. (2014a), Iron ore flotation process control and optimization using high-energy ultrasound, *Metallurgical and Mining Industry*, **6**(2): 36–42.
 16. MORKUN V., MORKUN N., PIKILNYAK A. (2014b), Modeling of ultrasonic waves propagation in inhomogeneous medium using fibered spaces method (k-space), *Metallurgical and Mining Industry*, **6**(2): 43–48.
 17. MORKUN V., MORKUN N., PIKILNYAK A. (2014c), The gas bubble size distribution control formation in the flotation process, *Metallurgical and Mining Industry*, **6**(4): 42–45.
 18. MORKUN V., MORKUN N., TRON V., HRYSHCHENKO S., SERDIUK O., DOTSENKO I. (2019), Basic regularities of assessing ore pulp parameters in gravity settling of solid phase particles based on ultrasonic measurements, *Archives of Acoustics*, **44**(1): 161–167, doi: [10.24425/aoa.2019.126362](https://doi.org/10.24425/aoa.2019.126362).
 19. MORKUN V., SEMERIKOV S.O., HRYSHCHENKO S.M., SLOVAK K.I. (2017), Environmental geo-information technologies as a tool of pre-service mining engineer's training for sustainable development of mining industry, *CEUR Workshop Proceedings*, **1844**: 303–310.
 20. OJEDA P., BERGH L.G., TORRES L. (2014), Intelligent control of an industrial thickener, *13th International Conference on Control Automation Robotics & Vision (ICARCV)*, pp. 505–510, doi: [10.1109/ICARCV.2014.7064356](https://doi.org/10.1109/ICARCV.2014.7064356).
 21. PLA Process Analysers (n.d.), *Automatic mud-diver, tank profiling & interface detection system for clarifiers, thickeners & CCD's*, <https://www.plapl.com.au/mud-diver/> (access: 22.08.2022).
 22. SEGOVIA J.P., CONCHA F., SBARBARO D. (2011), On the control of sludge level and underflow concentration in industrial thickeners, *IFAC Proceedings Volumes*, **44**(1): 8571–8576, doi: [10.3182/20110828-6-IT-1002.02667](https://doi.org/10.3182/20110828-6-IT-1002.02667).
 23. SHUKLA V., KUMAR C.R., CHAKRABORTY D.P., SHIVANGI U., DU J. (2021), Iron ore tailing beneficiation – A potential resource for future, *International Journal of Engineering Research & Technology (IJERT)*, **10**(9): 787–791.
 24. Sinonine Tech (n.d.), *Thickener automatic control*, <https://www.sinoninetech.com/index.php/Home/News/show/id/108.html> (access: 22.08.2022).
 25. SMITH M. (n.d.), *5 ways to measure bed level in thickeners*, PLA Process Analysers, <https://www.plapl.com>.

- [com.au/5-ways-to-measure-bed-level-in-thickeners/](https://www.com.au/5-ways-to-measure-bed-level-in-thickeners/) (access: 22.08.2022).
26. TAN C.K., SETIAWAN R., BAO J., BICKERT G. (2015), Studies on parameter estimation and model predictive control of paste thickeners, *Journal of Process Control*, **28**: 1–8, doi: [10.1016/j.jprocont.2015.02.002](https://doi.org/10.1016/j.jprocont.2015.02.002).
 27. TRIPATHY S.K., MURTHY Y.R., FARROKHPAY S., FILIPPOV L.O. (2021), Design and analysis of dewatering circuits for a chromite processing plant tailing slurry, *Mineral Processing and Extractive Metallurgy Review*, **42**(2): 102–114, doi: [10.1080/08827508.2019.1700983](https://doi.org/10.1080/08827508.2019.1700983).
 28. XU N., WANG X., ZHOU J., WANG Q., FANG W., PENG X. (2015), An intelligent control strategy for thickening process, *International Journal of Mineral Processing*, **142**: 56–62, doi: [10.1016/j.minpro.2015.01.007](https://doi.org/10.1016/j.minpro.2015.01.007).
 29. ZHANG J., YIN X., LIU J. (2016), Economic MPC of deep cone thickeners in coal beneficiation, *The Canadian Journal of Chemical Engineering*, **94**(3): 498–505, doi: [10.1002/cjce.22419](https://doi.org/10.1002/cjce.22419).
 30. ZUZUNAGA A., VAN DER SPEK A., URQUIOLA R., MARON R. (2018), Uses and benefits of flow measurement in the operation of tailings thickeners, *5th International Seminar on Tailings Management*.

Research Paper

Algorithm for Computationally Efficient Imaging of Sound Speed in Conventional Ultrasound Sonography

Piotr KARWAT

*Department of Ultrasound, Institute of Fundamental Technological Research
Polish Academy of Sciences*

Warsaw, Poland; e-mail: pkarwat@ippt.pan.pl

(received December 19, 2022; accepted May 11, 2023)

The speed of sound (SoS) in tissues reflects their mechanical properties and therefore can carry valuable diagnostic information. In conventional ultrasound sonography (US), however, this information is not readily available. Furthermore, since the actual SoS is unknown, image reconstruction is carried out using an average SoS value for soft tissues. The resulting local deviations from the actual SoS lead to aberrations in US images. Methods for SoS imaging in US therefore have the potential to enable the correction of aberrations in classical US. In addition, they could also become a new US modality.

There are several approaches to SoS image reconstruction. They differ in terms of input data requirements, computational complexity, imaging quality, and the potential for signal analysis at the intermediate stages of processing. This article presents an algorithm with multi-stage processing and low computational complexity.

The algorithm was verified through numerical simulations and phantom measurements. The obtained results show that it can correctly estimate SoS in layered media, which in most cases model the tissue structure well. With its computational complexity of $O(n)$, the algorithm can be implemented in real-time ultrasound imaging systems with limited hardware performance, such as portable ultrasound devices.

Keywords: speed of sound; ultrasound imaging; computational complexity.



Copyright © 2023 The Author(s).
This work is licensed under the Creative Commons Attribution 4.0 International CC BY 4.0
(<https://creativecommons.org/licenses/by/4.0/>).

1. Introduction

The speed of sound (SoS) in tissues reflects their mechanical properties and depends on many aspects. Various soft tissue types can be characterized by an SoS ranging approximately from 1440 m/s in fat to 1620 m/s in skin (COBBOLD, 2007; Foundation for Research on Information Technologies in Society, n.d.). Moreover, the SoS can vary with tissue composition. For example, excess fat content leads to a decreased SoS, as in fatty liver (GHOSHAL *et al.*, 2012). It can also be altered due to pathological changes in the extracellular matrix, specifically the excessive accumulation of collagen and the development of fibrosis, which often accompany inflammatory diseases and tumors.

The SoS can therefore provide information on tissue type and condition. It has already proven usable in the assessment of breast tumor malignancy in ultrasound computed tomography (UCT) (ANDRE *et al.*, 2012). This technique, however, requires that the examined tissue is accessible from all sides in the imag-

ing plane, and preferably contains no bones. As a result, UCT has a very narrow field of application, limited mainly to breast imaging. Implementing the SoS modality into conventional ultrasound sonography (US) could allow for utilizing the SoS information on a much larger scale and in the context of many other organs and diseases.

The existing solutions for SoS imaging in conventional US are relatively new. JAEGER *et al.* (2014; 2015) introduced a mathematical model and an algorithm for SoS reconstruction, which they called the computed ultrasound tomography in echo mode (CUTE). It utilized phase differences between complex images obtained for a number of plane wave transmissions at different angles. The authors proposed a model describing these phase differences as a function of SoS local errors made in image reconstruction. To solve the inverse problem, they proposed the use of the pseudoinverse of the transformation matrix based on their model. At first, the processing was conducted in the frequency domain, which made the algorithm compu-

tationally efficient. However, it also made it impossible to consider imaging dead zones, which in turn led to bias in the resulting SoS estimates. To address this problem, a spatial domain version of CUTE processing was proposed (JAEGER, FRENZ, 2015; SANABRIA *et al.*, 2018). This led to an improvement in the quality of resulting SoS images to the point where CUTE could be referred to as a quantitative method. This improvement, however, was accompanied by a significant increase in computational complexity. In another paper (STÄHLI *et al.*, 2020), the authors indicated that certain assumptions made in the CUTE method are wrong. As a solution, they proposed a new algorithm and a modification in the input data to ensure the same transmit-receive mid-angle in the compared images. In exchange for more complex preprocessing and a reduced resolution, this method offers more accurate SoS estimates.

Another group of methods for SoS imaging uses convolutional neural networks (CNNs). In some studies (FEIGIN *et al.*, 2020; YOUNG *et al.*, 2022), CNNs were trained using raw echo data obtained through numerous simulations with the k-Wave toolbox (TREEBY, COX, 2010) for Matlab. SoS imaging using CNNs does not require the initial image reconstruction. Moreover, the reported models demonstrated good performance with data from just three transmissions, a notably smaller number to what is reported in the case of CUTE methods. Finally, CNNs are fast enough to be implemented in real-time imaging systems. On the other hand, analyzing and understanding the CNN's way of interpreting the signal in order to find a correlation with some physical model poses challenges for researchers.

In (KARWAT, 2019), the author proposed a modification to the CUTE mathematical model and introduced a corresponding SoS reconstruction algorithm based on it. This modification made it possible to solve the inverse problem at low computational cost and was therefore called Quick-CUTE (Q-CUTE). The algorithm was validated using simulation data.

In this study, the input signal of the CUTE method is analyzed with respect to its compliance with the modified mathematical model. Moreover, the algorithm is described in more detail, including an analysis of the signal at individual stages of the processing. Finally, the results of the measurement-based validation are presented.

2. Methodology

2.1. General CUTE model

The general idea behind the spatial domain CUTE method is presented in (JAEGER, FRENZ, 2015; SANABRIA *et al.*, 2018), but for clarity, it will also be explained here. Reconstruction of images in conventional

US is usually performed according to the delay-and-sum (DAS) algorithm that includes, inter alia, compensation for the ultrasound pulse propagation delays t . The calculation of these delays requires knowledge of the SoS value c along the pulse propagation path r from the probe to the pixel of interest and back to the probe:

$$t = \int_r \frac{dr}{c}. \quad (1)$$

However, the value of c is not known precisely, therefore its approximation is used. Typically, an average SoS value for soft tissues is used for this purpose. Any discrepancies between the SoS value c_R adopted for reconstruction and the actual SoS spatial distribution c result in calculated propagation delays t_r being different from the actual delays t . Consequently, these discrepancies lead to time delay errors τ :

$$\begin{aligned} \tau &= t - t_r = \int_r \frac{dr}{c} - \int_r \frac{dr}{c_R} \\ &= \int_r \sigma dr - \int_r \sigma_R dr = \int_r \Delta\sigma dr. \end{aligned} \quad (2)$$

For notation simplicity, σ , σ_R , and $\Delta\sigma$ terms are introduced in the aforementioned equation. The first two represent actual and approximated values of sound slowness (inverse of SoS), respectively. The last one stands for the error in sound slowness:

$$\Delta\sigma(z, x) = \sigma(z, x) - \sigma_R = \frac{1}{c(z, x)} - \frac{1}{c_R}. \quad (3)$$

Coming back to the time delay errors τ , they lead to phase aberrations φ in the reconstructed complex radio-frequency (CRF) images. These phase aberrations cannot be measured directly for an individual CRF image but can be estimated as local phase differences $\Delta\varphi$ with respect to another CRF image acquired for different propagation paths r . Based on the $\Delta\varphi$, however, only relative values of τ can be obtained. Therefore, instead of τ , time delay error differences $\Delta\tau$ will be further considered:

$$\Delta\tau_{m,n} = \tau_n - \tau_m = \int_{r_n} \Delta\sigma dr - \int_{r_m} \Delta\sigma dr, \quad (4)$$

where m and n subscripts identify the m -th and n -th images being compared. The above equation describes the forward problem, i.e., it defines the observed $\Delta\tau$ as a function of the error in sound slowness $\Delta\sigma$. The CUTE algorithms are designed to solve the inverse problem, that is to estimate the SoS corrections based on the observed $\Delta\tau$. To make this feasible, some assumptions are made. First, similarly to the classical DAS reconstruction algorithm, the concept of rays known from geometrical optics is used to describe the propagation of ultrasound. Given that relative SoS variations in soft tissues are relatively low (up to approximately $\pm 6\%$ from the SoS mean value), it is also assumed that the ultrasound rays do not refract.

Furthermore, if the receive aperture and apodization used for reconstructing each pixel remain the same for the images being compared, the parts of time delay errors τ_m and τ_n associated with the return paths (from pixel to probe) are assumed to be equal. The time delay error differences $\Delta\tau_{m,n}$ are therefore a consequence of the errors committed on the transmit paths (from probe to pixel) only, as the return paths errors cancel each other out. With the above assumptions, and bearing in mind that CUTE methods typically use images obtained for plane wave emissions at various angles θ , r represents a rectilinear transmit propagation path taken at angle θ from a probe to a pixel of interest P .

The formulation of the forward problem in Eq. (4) can be further modified. Its frequency domain version is utilized in the first reported version of CUTE (JAEGER *et al.*, 2014; 2015). Its original form is the foundation for the spatial domain CUTE algorithm (JAEGER, FRENZ, 2015; SANABRIA *et al.*, 2018). Finally, it can be linearly approximated to obtain a common integration path, as in Q-CUTE (KARWAT, 2019). Depending on the formulation of the forward problem, solving the inverse problem can be conducted in various ways. This, in turn, leads to multiple CUTE versions differing in terms of SoS imaging quality and computational complexity.

2.2. Spatial domain CUTE processing

The model described in Eq. (4) is the basis for the spatial domain CUTE algorithm. It is used for the determination of the forward problem (calculation of $\Delta\tau$ based on $\Delta\sigma$) transformation matrix. Next, its pseudo-inverse is computed for subsequent use in solving the inverse problem (calculation of $\Delta\sigma$ based on $\Delta\tau$). Due to the ill-conditioning of the inverse problem, spatial gradient regularization is used.

Having the pre-calculated inverse transformation matrix, it only takes $\Delta\tau$ to compute $\Delta\sigma$. The time delay errors $\Delta\tau_{m,n}$ are estimated from the local phase differences $\Delta\varphi_{m,n}$ between CRF_m and CRF_n complex images as well as the signal frequency f :

$$\Delta\tau_{m,n} = \frac{\Delta\varphi_{m,n}}{2\pi f}. \quad (5)$$

Due to the interference nature of the CRF images, to obtain a usable signal, the local phase differences $\Delta\varphi_{m,n}$ are estimated according to the equation:

$$\Delta\varphi_{m,n} = \arg[\text{filt}(\text{CRF}_n \circ \text{CRF}_m^*)], \quad (6)$$

where $*$ and \circ operators are the complex conjugate and Hadamard (element-wise) product, respectively. The term “filt” denotes spatial smoothing filtration, and “arg” returns the arguments of complex numbers.

The $\Delta\tau$ maps obtained using the above methodology are of poor lateral resolution due to the absence

of transmit focusing in the CRF images. In order to enhance the resolution, the input CRF images can be obtained through coherent compounding for a number of closely spaced transmit angles θ . Another issue is the aliasing and decoherence, which may occur if the difference between θ_m and θ_n angles is substantial. On the other hand, if the difference between θ_m and θ_n is small, the amplitude of the useful part of $\Delta\tau$ is low compared to the interference part, adversely affecting the sensitivity of the method. To avoid the aliasing and limit the decoherence while maintaining the sensitivity, $\Delta\tau_{m,n}$ is estimated using a number of closely spaced θ angles that cover the angular space between the target pair of θ_m and θ_n angles.

To illustrate it, let us consider the objective of obtaining $\Delta\tau_{m,n}$ map for transmit angles $[\theta_m, \theta_n] = [0^\circ, 8^\circ]$. To avoid the aliasing and preserve the coherence of the paired CRF images, one would reduce the difference in θ from 8° to 2° , and this involves using a set of CRF images for transmit angles $\theta = \{0^\circ, 2^\circ, 4^\circ, 6^\circ, 8^\circ\}$. For each pair of consecutive θ angles, $\Delta\tau$ is calculated. The final $\Delta\tau_{m,n}$ is the sum of the $\Delta\tau$ maps obtained for θ pairs $\{[0^\circ, 2^\circ], [2^\circ, 4^\circ], [4^\circ, 6^\circ], [6^\circ, 8^\circ]\}$. Furthermore, in order to enhance the $\Delta\tau$ lateral resolution, each CRF image would be obtained through coherent compounding for angles, e.g., being $\{-1^\circ, -0.5^\circ, 0^\circ, 0.5^\circ, 1^\circ\}$ around the base angle θ . This means that a single $\Delta\tau_{m,n}$ map would require plane wave transmissions at angles in the range $[-1^\circ, 9^\circ]$ with a step of 0.5° , which amounts to 21 transmissions.

More details on the spatial domain CUTE algorithm can be found in the presentation by JAEGER *et al.* (2015) and the paper by SANABRIA *et al.* (2018). For simplicity, in the remaining sections of this paper, the term CUTE will be used to refer to the spatial domain version of the CUTE method.

2.3. Q-CUTE model

The method being the subject of this article is the Q-CUTE technique, presented briefly in (KARWAT, 2019). It is based on a model that is a modified version of the general CUTE model described by Eq. (4). The aim of the modification is to obtain a common integration path. This, in turn, enables a different approach to the input signal $\Delta\tau$ and opens new ways of solving the inverse problem. Let us start from the beginning, though.

Because $dr = dz'/\cos\theta$, Eq. (4) can be rewritten as:

$$\Delta\tau_{m,n}(z, x) = \frac{1}{\cos\theta_n} \int_0^z \Delta\sigma(r_n) dz' - \frac{1}{\cos\theta_m} \int_0^z \Delta\sigma(r_m) dz'. \quad (7)$$

Let us approximate linearly $\Delta\sigma$ along r_m and r_n paths using $\Delta\sigma$ and its x -derivative $\Delta\sigma_x$ along a path $r_{m,n}$ that is horizontally equidistant from r_m and r_n , as shown in Fig. 1.

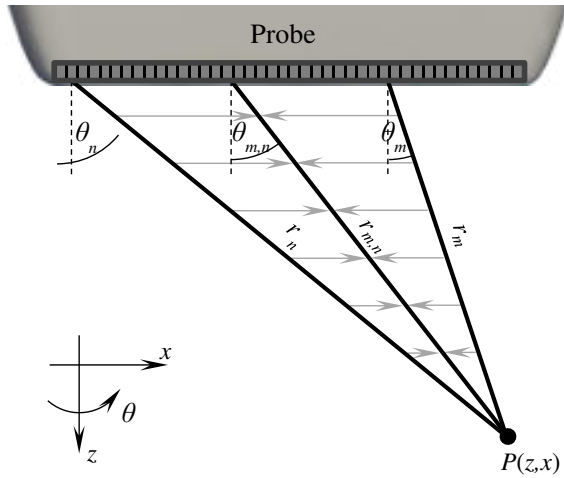


Fig. 1. Sketch of the linear approximation approach used in the Q-CUTE model. The approximation is done horizontally as indicated by gray arrows.

The corresponding angle $\theta_{m,n}$ equals:

$$\theta_{m,n} = \tan^{-1} \left(\frac{\tan \theta_m + \tan \theta_n}{2} \right), \quad (8)$$

and the linear approximations of $\Delta\sigma$ along the r_m and r_n paths are:

$$\begin{aligned} \Delta\sigma(r_m) &\approx \Delta\sigma(r_{m,n}) \\ &+ \Delta\sigma_x(r_{m,n})(z - z') \left(\frac{\tan \theta_n - \tan \theta_m}{2} \right), \end{aligned} \quad (9)$$

$$\begin{aligned} \Delta\sigma(r_n) &\approx \Delta\sigma(r_{m,n}) \\ &- \Delta\sigma_x(r_{m,n})(z - z') \left(\frac{\tan \theta_n - \tan \theta_m}{2} \right). \end{aligned}$$

With this modification, the $r_{m,n}$ becomes the new, common integration path, and Eq. (7) takes the form:

$$\begin{aligned} \Delta\tau_{m,n}(z, x) &= a_{m,n} \int_0^z \Delta\sigma(r_{m,n}) dz' \\ &+ b_{m,n} \int_0^z (z' - z) \Delta\sigma_x(r_{m,n}) dz'. \end{aligned} \quad (10)$$

Terms $a_{m,n}$ and $b_{m,n}$ in Eq. (10) are functions of θ_m and θ_n :

$$\begin{aligned} a_{m,n} &= \left(\frac{1}{\cos \theta_n} - \frac{1}{\cos \theta_m} \right), \\ b_{m,n} &= \left(\frac{1}{\cos \theta_n} + \frac{1}{\cos \theta_m} \right) \left(\frac{\tan \theta_n - \tan \theta_m}{2} \right), \end{aligned} \quad (11)$$

and are shown in Fig. 2.

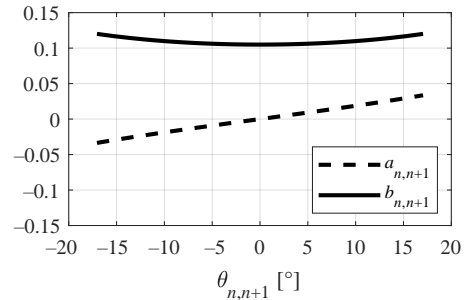


Fig. 2. Graphs of $a_{m,n}$ and $b_{m,n}$ terms as functions of $\theta_{m,n}$.

Integration by parts of the second integral in Eq. (10), after some rearrangements, yields:

$$\begin{aligned} \Delta\tau_{m,n}(z, x) &= a_{m,n} \int_0^z \Delta\sigma(r_{m,n}) dz' \\ &- b_{m,n} \iint_0^z \Delta\sigma_x(r_{m,n}) dz'^2. \end{aligned} \quad (12)$$

The aforementioned forward problem model is the basis for the Q-CUTE method.

2.4. Q-CUTE processing

The estimation of $\Delta\tau$ in the Q-CUTE method is conducted in the same way as in CUTE, i.e., according to Eqs. (5) and (6). Solving the inverse problem, in turn, is done in two steps.

First, by using the properties of $a_{m,n}$ and $b_{m,n}$, i.e., parity and amplitude ratio, especially for $\theta_{m,n}$ close to zero (Fig. 2), Eq. (12) is simplified by neglecting the first integral on the right side of the equation:

$$\Delta\tau_{m,n}(z, x) \approx -b_{m,n} \iint_0^z \Delta\sigma_x(r_{m,n}) dz'^2. \quad (13)$$

This allows a direct calculation of $\Delta\sigma_x$ for each $[m, n]$ pair:

$$\Delta\sigma_x(z, x, [m, n]) \approx \frac{-1}{b_{m,n}} \left[\frac{d^2}{dz'^2} \Delta\tau_{m,n}(r_{m,n}) \right]_{z'=z}. \quad (14)$$

The $\Delta\sigma_x$ is next averaged over $[m, n]$ pairs, yielding $\overline{\Delta\sigma_x}$. This, in turn, is integrated with respect to x to obtain the estimate of $\Delta\sigma$:

$$\Delta\sigma(z, x) = \int_{-\infty}^x \overline{\Delta\sigma_x}(z, x') dx' + C(z), \quad (15)$$

where C is the constant of integration (it is constant along the x -direction, but may vary with z).

In the second step of the Q-CUTE algorithm, the missing $C(z)$ is determined. The formula for C can be derived using the unmodified form of Eq. (12). Substituting $\overline{\Delta\sigma_x}$ for $\Delta\sigma_x$, and expanding $\Delta\sigma$ according to

Eq. (15), after rearrangements, yields the C estimates based on individual $[m, n]$ pairs:

$$C_{m,n}(z, x) = \frac{1}{a_{m,n}} \left[\frac{d}{dz'} \Delta\tau_{m,n}(r_{m,n}) \right]_{z'=z} - \int_{-\infty}^x \overline{\Delta\sigma_x}(z, x') dx' + \frac{b_{m,n}}{a_{m,n}} \int_0^z \overline{\Delta\sigma_x}(r_{m,n}) dz'. \quad (16)$$

To obtain the final estimate for C , the values calculated using the above formula need to be averaged over $[m, n]$ pairs and the x -dimension. However, for $\theta_{m,n}$ close to zero, $a_{m,n}$ is close to zero as well. This means that $\Delta\tau_{m,n}$ for small $|\theta_{m,n}|$ does not provide much information on C , and dividing by $a_{m,n}$, in this case, would only amplify distortions in $\frac{d}{dz} \Delta\tau_{m,n}$. To prevent this, the averaging over $[m, n]$ pairs uses $a_{m,n}^2$ as weights, which leads to inverse variance weighting.

Finally, knowing the $\Delta\sigma$ (including the constant of integration C), one can calculate the speed of sound c using a reorganized version of Eq. (3):

$$c(z, x) = \frac{c_0}{1 + c_0 \Delta\sigma(z, x)}. \quad (17)$$

2.5. Regularized derivative operator

As in the case of the CUTE algorithm, Q-CUTE needs regularization to prevent amplification of interference present in the $\Delta\tau$ data. In the Q-CUTE algorithm, this is realized by replacing the derivative operators that act on $\Delta\tau$ with regularized ones. As a matrix model \mathbf{D}_{reg} of the regularized derivative operator, a pseudo-inverse of integration operator matrix \mathbf{J} (Fig. 3a) with gradient regularization (gradient operator \mathbf{D} shown in Fig. 3b) was adopted:

$$\mathbf{D}_{\text{reg}} = (\mathbf{J}^T \mathbf{J} + \lambda \mathbf{D}^T \mathbf{D})^{-1} \mathbf{J}^T, \quad (18)$$

where λ denotes the regularization factor. Figure 3c shows an exemplary \mathbf{D}_{reg} matrix, while Fig. 3d presents selected impulse responses from \mathbf{D}_{reg} .

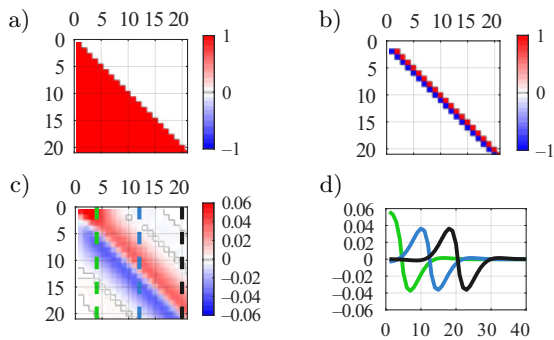


Fig. 3. Examples of a) integration operator matrix \mathbf{J} ; b) gradient operator matrix \mathbf{D} ; c) regularized derivative operator matrix \mathbf{D}_{reg} ; d) selected impulse responses of \mathbf{D}_{reg} . The first quarter of matrices is shown in a)–c).

These types of impulse responses can be precisely approximated using pairs of computationally efficient infinite impulse response (IIR) filters (LYONS, 2004) operating one in forward and the other backward direction. Implementation of the regularized derivative operator depicted in Figs. 3c and 3d requires the use of second-order IIR filters. The IIR filter coefficients were precomputed to approximate the central, anti-symmetric impulse response of \mathbf{D}_{reg} for a chosen value of λ . However, as shown in Figs. 3c and 3d, impulse responses close to signal boundaries are more complex. To reflect the changes in the \mathbf{D}_{reg} impulse responses and thus ensure proper derivative operation when approaching signal boundaries, the output of each filter is multiplied by a precalculated correction vector. The vector compensates for two effects resulting from clipping the forward or backward impulse responses. Firstly, it equalizes the areas under both impulse responses so that the derivative of a constant signal is always 0. Secondly, it corrects the change in the distance between the centers of mass of the impulse responses so that the derivative of a linear signal is always constant.

2.6. Computational complexity

The implementation of preprocessing, i.e., the estimation of $\Delta\tau$ based on a set of CRF images, can be done in a variety of ways. They can differ in terms of optional CRF images compounding, pairing strategy, or type and order of the smoothing filter used in Eq. (6). As a result, the discussion of the computational complexity of the preprocessing becomes hindered. However, the preprocessing for the Q-CUTE algorithm is the same as in other CUTE methods based on the model presented in Eq. (4). Hence, it does not introduce computational differences between the compared SoS imaging algorithms. Therefore, the description of computational complexity is limited to the subsequent processing.

Let us define n_{PIX} as the number of pixels in a single $\Delta\tau$ map, and $n_{\Delta\tau}$ as the number of $\Delta\tau$ maps. Then the size of the $\Delta\tau$ to $\Delta\sigma$ transformation matrix in the CUTE algorithm is $n_{\text{PIX}} \times (n_{\text{PIX}} \cdot n_{\Delta\tau})$. Although the forward problem transformation matrix is sparse, the inverse problem transformation matrix is not. The CUTE computational complexity, expressed as a number of multiply-add operations, is therefore equal $n_{\Delta\tau} \cdot n_{\text{PIX}}^2$.

In the case of Q-CUTE algorithms, the computational complexity is a sum of the complexities of their components. Apart from the operations directly represented in the equations (derivatives, integrations, and weighted sums), they also include 1-D linear interpolation every time some operation is performed along a direction that is not aligned with rows or columns of the data array. The computational cost of each operation

and their total cost in the Q-CUTE algorithms are presented in Table 1. The total computational complexity of the Q-CUTE algorithm is equal to $35 \cdot n_{\Delta\tau} \cdot n_{\text{PIX}}$.

Table 1. List of the operations, their computational cost per pixel of the $\Delta\tau$ map, and the number of calls per single $\Delta\tau$ map in the Q-CUTE algorithm.

| Operation name | Unit cost | # of calls | Cost |
|---|-----------|------------|-----------|
| 1-D linear interpolation | 2 | 3 | 6 |
| Derivative (regularized) (two 2nd order IIR filters) | 12 | 2 | 24 |
| Integration | 1 | 1 | 1 |
| Weighted sum | 1 | 4 | 4 |
| Total | | | 35 |

2.7. Validation/input data

The Q-CUTE algorithm was tested and validated based on data obtained from phantom measurements as well as from numerical simulations.

Measurements were carried out with the use of the us4R-lite system (us4us, Warsaw, Poland) (CACKO, LEWANDOWSKI, 2022) and a linear array probe SL1543 (Esaote, Genoa, Italy) with 192 elements, a pitch of 0.245 mm, and a center frequency of 8 MHz. The data were acquired from a phantom model 1438 (Dansk Phantom Service, Frederikssund, Denmark). The main material of this phantom is characterized by an SoS of 1540 m/s. The phantom also contains four cylindrical targets, 10 mm in diameter, with SoS values equal to 1480, 1510, 1570, and 1600 m/s.

Numerical simulations were performed with probe parameters identical to those for SL1543, using a custom-developed MATLAB-based simulator tool. The simulator follows a similar principle to the Field software (JENSEN, 1996), i.e., it is based on linear acoustics and uses the concept of scattering points. Unlike Field, however, it can simulate any SoS maps (refraction is still omitted). Furthermore, it makes possible to simulate a medium in which the SoS map is different for the transmit and receive paths, which also distinguishes it from the k-Wave toolbox (TREEBY, COX, 2010). This feature proves useful in the separation of $\Delta\tau$ signal components presented in the Results section.

In both cases, i.e., measurements and simulations, the raw echo data were acquired using the single-element synthetic transmit aperture (SSTA) technique, elsewhere referred to as full matrix capture (FMC). It involves the separate transmission through each individual probe element and receiving the echoes each time with the entire probe. This strategy was used in the case of changing the transmission angles θ or SoS value c_R , because it does not require repeating measurements or simulations, just the FMC data need to be properly converted into a form corresponding to the plane wave imaging.

The obtained raw echo data underwent processing through a digital down converter (DDC), i.e., they were quadrature demodulated, low-pass filtered and decimated. The resulting complex echo signal was next reconstructed into CRF images using the delay-and-sum (DAS) algorithm with phase-error-free quadrature sampling (CHANG *et al.*, 1993).

The CRF images were reconstructed for diverging waves, so they had to be converted into a form corresponding to plane waves. This was done through the proper recombination of the CRF images. This conversion was done for transmit angles θ ranging from -17° to $+17^\circ$ in a step of 0.25° , resulting in a set of 137 CRF images. In the next step, a subset of CRF images with θ in a $\pm 2^\circ$ range around a selected θ was coherently summed. The selected θ were in the range from -15° to $+15^\circ$ in a step of 2° , resulting in a set of 16 compounded CRF images. Then, based on pairs of compounded CRF images with consecutive θ values, $\Delta\tau$ maps were estimated using Eqs. (5) and (6). Next, the $\Delta\tau$ maps were summed in groups so that $\theta_n - \theta_m$ equaled 6° , which resulted in a set of five $\Delta\tau$ maps further processed to obtain a single SoS output image. A diagram of this procedure for a single $\Delta\tau$ map is presented in Fig. 4.

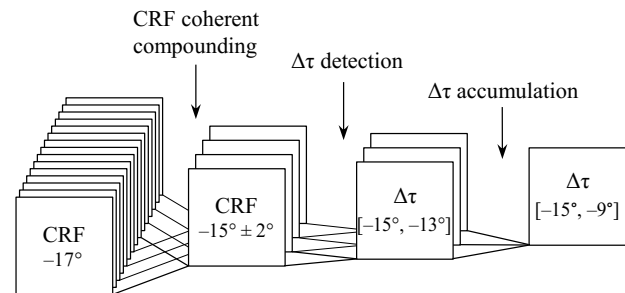


Fig. 4. Diagram of processing a set of CRF images to obtain a single $\Delta\tau$ map.

The SoS spatial distributions used in this study included uniform cases, horizontal layer cases, and circular inclusion cases. The layers and circular inclusions in measurement data were obtained through positioning the probe along and across cylindrical objects in the phantom, respectively.

In order to assess the SoS imaging quality, the results of the Q-CUTE method were compared with those obtained from the spatial domain CUTE algorithm considered as a reference at this stage of the research.

The appearance of the resulting SoS images depends on the regularization factors (CUTE) and the corresponding filters in the regularized derivative operators (Q-CUTE). Increasing the regularization factor results in smoother SoS images. The level of regularization was therefore a compromise between reducing the variance and maintaining the details of the SoS

images. It was also adjusted so that the average image of a simulated circular inclusion was reproduced with similar amplitudes and slopes by both algorithms.

All the raw echo data simulations and conversions, CRF image reconstructions, CUTE processing, and preparation of the results were executed using MATLAB 2021b (Mathworks, Inc., Natick, Massachusetts).

3. Results

The SoS images reconstructed using the CUTE and Q-CUTE algorithms are depicted in Figs. 5–8. Figure 5

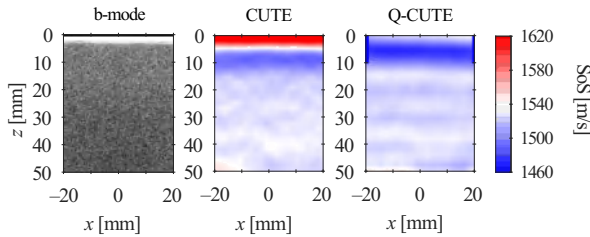


Fig. 5. Images of the homogeneous 1540 m/s part of the phantom: b-mode (left), SoS images obtained with the use of CUTE (middle), and with Q-CUTE (right).

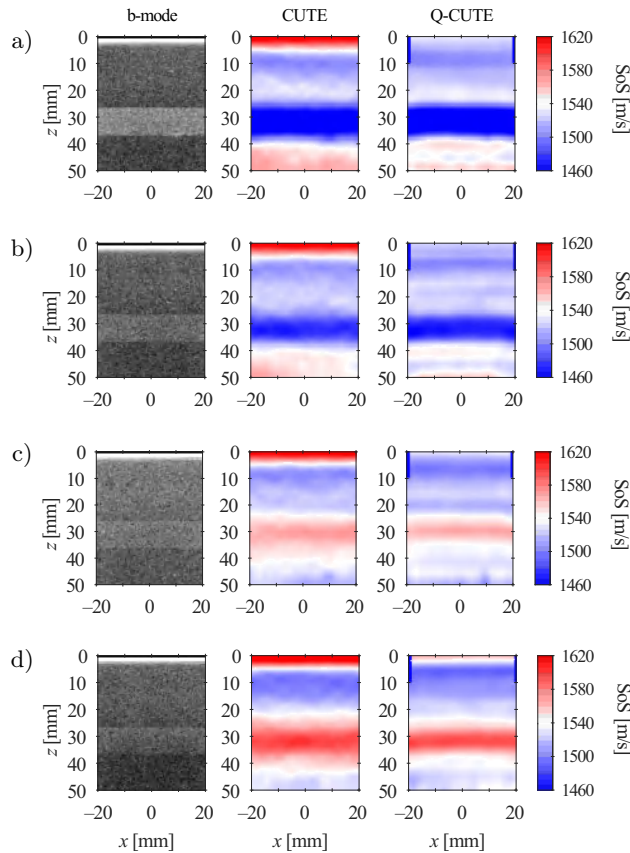


Fig. 6. Images of layers: b-mode (left), SoS images obtained with the use of CUTE (middle), and with Q-CUTE (right). SoS in the layers is: a) 1480 m/s; b) 1510 m/s; c) 1570 m/s; d) 1600 m/s.

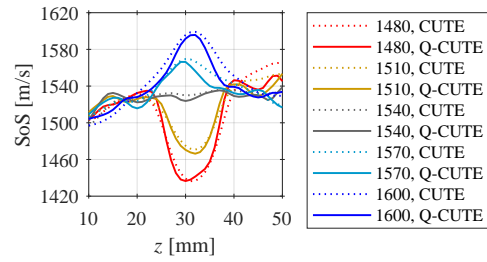


Fig. 7. SoS z -profiles for the homogeneous and layer cases for CUTE (dotted lines) and Q-CUTE (solid lines).

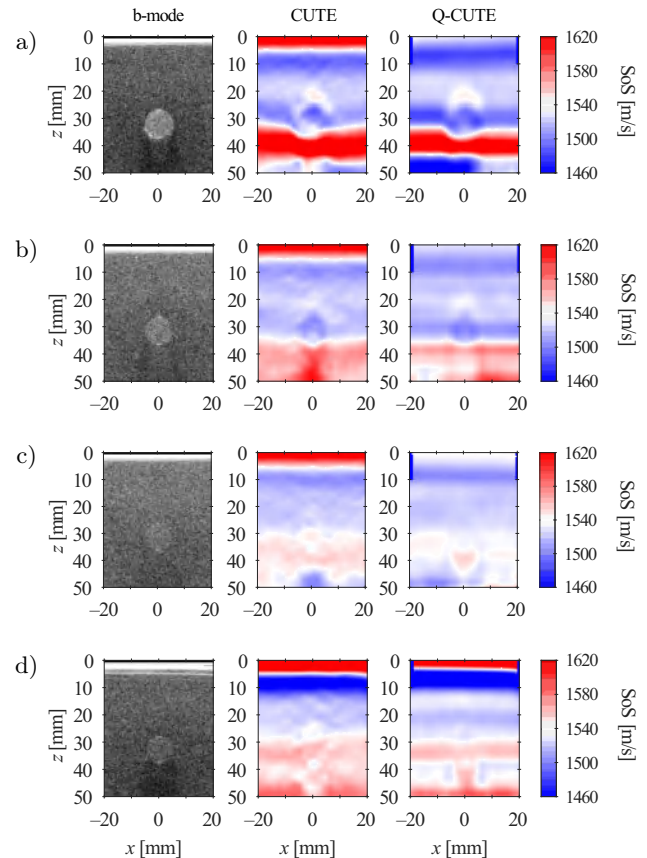


Fig. 8. Images of circular objects: b-mode (left), SoS images obtained with the use of CUTE (middle), and with Q-CUTE (right). SoS in the objects is: a) 1480 m/s; b) 1510 m/s; c) 1570 m/s; d) 1600 m/s.

presents the case of a homogeneous SoS spatial distribution, while layer cases are shown in Fig. 6, and circular object cases are presented in Fig. 8. For a better assessment of the layer images, Fig. 7 shows the averaged z -profiles of the SoS maps shown in Fig. 6.

In the cases shown in Fig. 8, both SoS imaging algorithms fail to reveal the presence of circular objects. To better understand the reasons behind these results, let us analyze the $\Delta\tau$ signal. Each row in Fig. 9 contains $\Delta\tau$ maps for a few angle pairs $[\theta_m, \theta_n]$. The first row (Fig. 9a) shows the same measurement case for which the results in Fig. 8 were computed. The fol-

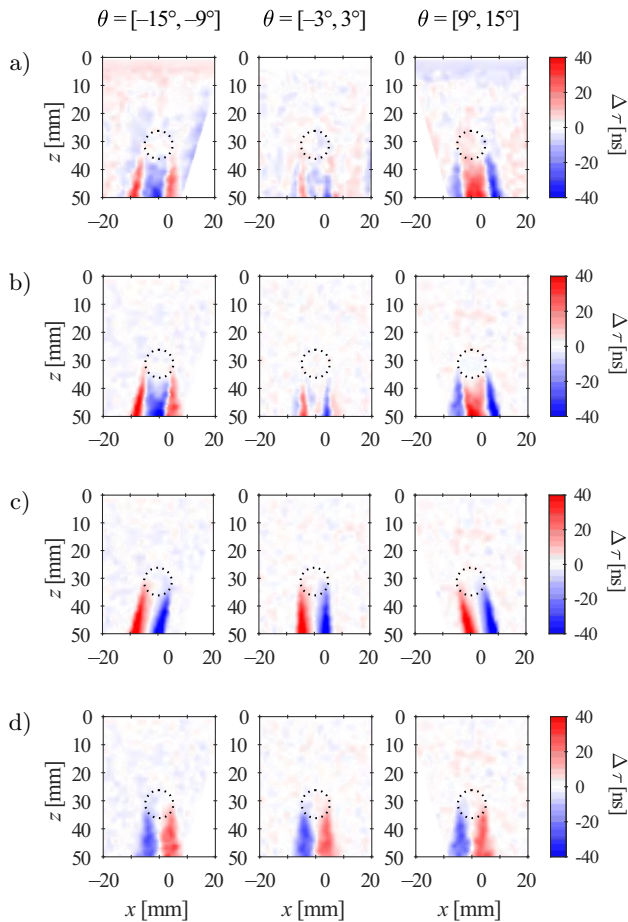


Fig. 9. Images of $\Delta\tau$ for a circular object with an SoS of 1570 m/s for a) measurement data, and for simulated data with the object present in: b) both transmit and receive paths; c) transmit path only; d) receive path only.

lowing rows (Figs. 9b–9d) present $\Delta\tau$ maps for the simulated data. In the second row (Fig. 9b), the simulated SoS map was the same as in the measurement case, i.e., it contained a circular object with an SoS of 1570 m/s. Subsequently, the presence of the object was limited to the transmit propagation paths only, which led to $\Delta\tau$ maps shown in the third row (Fig. 9c). Analogously, the fourth row (Fig. 9d) illustrates the case with the object being present along the receive propagation paths only.

There is a similarity between the $\Delta\tau$ maps obtained for the measurement (Fig. 9a) and simulation (Fig. 9b). In both cases, they contain a strong component that changes its orientation and a weaker, stationary component in the background. These components are well separated in Figs. 9c and 9d.

The $\Delta\tau$ maps obtained through the simulations (Figs. 9b–9d) were subjected to further processing, resulting in the final SoS images shown in Fig. 10. The signal at intermediate processing steps in the Q-CUTE algorithm for the $\Delta\tau$ data as in Fig. 9c is presented in Fig. 11.

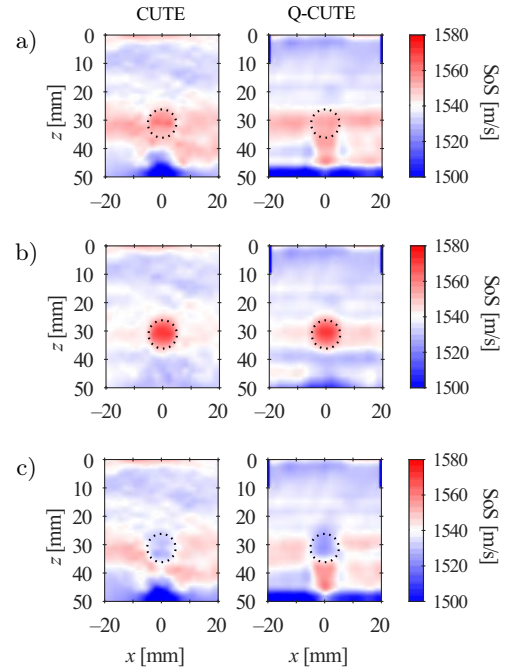


Fig. 10. Images of SoS obtained with the use of CUTE (left) and Q-CUTE (right) algorithms from simulation data. The SoS map used in simulations contained a circular object with an SoS of 1570 m/s present in: a) both transmit and receive paths; b) transmit path only; c) receive path only. The object position is marked with a dashed line.

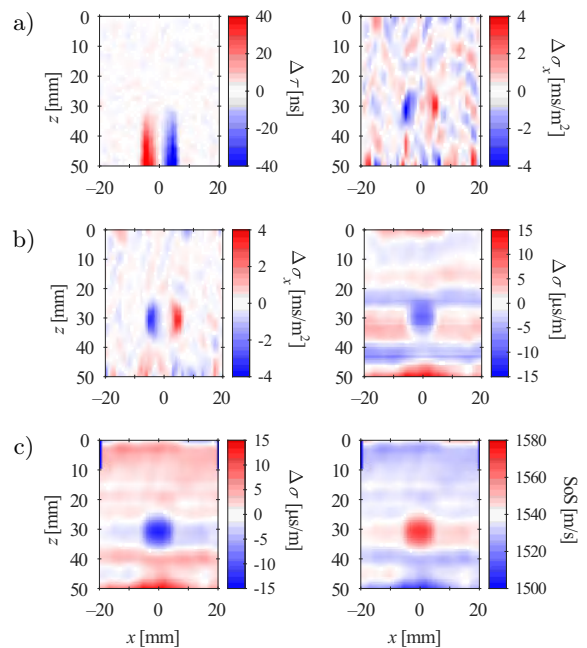


Fig. 11. Images of the signal at selected stages of Q-CUTE processing: a) $\Delta\tau$ ($-3^\circ, 3^\circ$); b) $\Delta\sigma_x$ ($-3^\circ, 3^\circ$); c) $\Delta\sigma_x$; d) $\Delta\sigma$ without C correction; e) $\Delta\sigma$ with C correction; f) final SoS estimate.

4. Discussion

The presented results allow an evaluation and comparison of the Q-CUTE algorithm with the spatial do-

main CUTE method in terms of SoS imaging quality. As shown in the homogeneous medium case (Fig. 5), both algorithms produce similar artifacts in the shallow area (up to approximately 15 mm depth). Moreover, both methods tend to underestimate the global SoS. Moving on to the layer cases (Figs. 6, 7), the imaging of horizontal objects shows similar dynamics, and the overall underestimation is visible here as well. Further problems appear when a non-layered SoS case is considered. The circular inclusion was not exposed by any of the algorithms (Fig. 8).

The reason for this is the fact that in the $\Delta\tau$ signal, there is a component (Fig. 9d) related to the receive propagation paths passing through the circular object. This component was assumed to be zero and was therefore neglected in the mathematical model. However, as shown through simulations (Fig. 9), it significantly contributes to the $\Delta\tau$ signal. Unfortunately, this contribution is opposite to the useful part of the signal related to the circular object. As a result, imaging of local, non-layered inclusions with CUTE algorithms based on Eq. (4) becomes difficult (Fig. 10).

This problem was already identified in (STÄHLI *et al.*, 2020). The authors proposed to abandon the assumption of canceling the return path influence. They introduced a new version of the CUTE algorithm that takes into account the receive paths. In the computation of the $\Delta\tau$ signal, the algorithm requires that the transmit-receive mid-angle in the compared CRF images remains the same.

The Q-CUTE algorithm cannot be easily adapted to this new approach. Representing four propagation paths (transmit and receive paths for two acquisitions) with a single common integration path would impose narrow limits on transmit and receive angles. Moreover, at least a quadratic approximation would be required in place of Eq. (9), which could cause further complications.

A more promising way might be to separate or filter out the unwanted receive component. One of the options is to replace the $\Delta\tau$ with differences between $\Delta\tau$ obtained for different sets of θ angles. This approach would eliminate the stationary receive component. This, of course, would require major modifications to the algorithm to account for the change in the $\Delta\tau$ signal definition.

Having discussed the quality of the SoS imaging, it is also worth mentioning other features of the Q-CUTE algorithm. One of its advantages is the modular structure. It makes it possible to control the data at each stage of the processing (Fig. 11), helping to understand the signal and allowing for easy optimization of the algorithm. By contrast, in the case of the CUTE method, a deeper analysis of the signal and its processing is difficult as the algorithm is not modular and is predetermined by the matrix inversion process. One can

analyze the impulse responses included in the inverse transformation matrix, but without descriptions like in Eq. (12) it is hard to understand them. There are also other approaches to SoS imaging that hold promise but provide little in terms of understanding the signal. This especially applies to deep learning methods, which have become popular in many areas and have also been used in SoS imaging (FEIGIN *et al.*, 2020; YOUNG *et al.*, 2022). Their cognitive value, however, is limited to the so-called maps of attention.

Another aspect is the computational complexity. As described in the Methods section, the computational complexity of Q-CUTE is $O(n)$ and, in most cases, it will be significantly lower than the complexity of the spatial domain CUTE which is $O(n^2)$. In practice, it translates into shorter execution times, which was observed when generating the images presented in the Results section. The algorithms were run in MATLAB on a PC with an Intel Core i7-6900K CPU. The common preprocessing took 340 ms, while the remaining parts of the algorithms took 30 ms and 310 ms for Q-CUTE and CUTE, respectively. Consequently, Q-CUTE ran nearly twice as fast as CUTE (2.7 fps versus 1.5 fps). This was the case with the common preprocessing designed with a focus on high-quality $\Delta\tau$ signal. A more balanced quality/performance ratio would lead to overall higher frame rates with a larger difference between Q-CUTE and CUTE. Obviously, single frames per second cannot be considered a satisfactory result in the target applications, but this can be improved for both algorithms through balanced preprocessing, optimized implementations, and of course, the usage of more powerful hardware. In the case of large US devices with high computing power, the computational complexity of the algorithms may not be a decisive factor. However, there is an emerging market of portable medical devices with their limitations. They are battery-powered and are enclosed in tight housing, impeding heat dissipation. For these reasons, power consumption has to be kept at relatively low level. This, in turn, puts constraints on the hardware, limiting its computing power. In this type of US devices, the algorithms such as Q-CUTE can find their use.

5. Conclusions

In this paper, an algorithm for SoS imaging in conventional ultrasound sonography was presented. The algorithm, called Q-CUTE, is characterized by low computational complexity, which allows implementing it on US devices with hardware limitations, e.g., on portable US devices. Its modular structure makes it possible to analyze the data at each stage, helping to understand the signal and optimize the processing.

The Q-CUTE algorithm performs on a similar level as the reference CUTE algorithm. It allows for imaging

the horizontally layered structures, a frequent case in US. These structures include tissues such as skin, fat, muscles, etc., forming layers of different SoS. Therefore, the Q-CUTE algorithm might be used for determining SoS profiles for aberration correction in conventional US.

However, problems arise when revealing non-layered structures, such as circular inclusions. To overcome them, a new approach to the $\Delta\tau$ computation will be analyzed in the future research. This will require further modifications to the mathematical model and the implementation of the Q-CUTE algorithm.

Acknowledgments

This study was funded by the National Science Centre, Poland (grant no. 2016/21/N/ST7/03029).

References

- ANDRÉ M., WISKIN J., BORUP D., JOHNSON S., OJEDA-FOURNIER H., OLSON L. (2012), Quantitative volumetric breast imaging with 3D inverse scatter computed tomography, [in:] *2012 Annual International Conference of the IEEE Engineering in Medicine and Biology Society*, **34**: 1110–1113, doi: [10.1109/embc.2012.6346129](https://doi.org/10.1109/embc.2012.6346129).
- CACKO D., LEWANDOWSKI M. (2022), Shear wave elastography implementation on a portable research ultrasound system: Initial results, *Applied Sciences*, **12**(12): 6210, doi: [10.3390/app12126210](https://doi.org/10.3390/app12126210).
- CHANG S.H., PARK S.B., CHO G.H. (1993), Phase-error-free quadrature sampling technique in the ultrasonic B-scan imaging system and its application to the synthetic focusing system, *IEEE Transactions on Ultrasonics, Ferroelectrics, and Frequency Control*, **40**(3): 216–223, doi: [10.1109/58.216834](https://doi.org/10.1109/58.216834).
- COBBOLD R.S.C. (2007), *Foundations of Biomedical Ultrasound*, Oxford University Press.
- FEIGIN M., FREEDMAN D., ANTHONY B.W. (2020), A deep learning framework for single-sided sound speed inversion in medical ultrasound, *IEEE Transactions on Biomedical Engineering*, **67**(4): 1142–1151, doi: [10.1109/tbme.2019.2931195](https://doi.org/10.1109/tbme.2019.2931195).
- Foundation for Research on Information Technologies in Society (n.d.), *Speed of Sound*, <https://itis.swiss/virtual-population/tissue-properties/database/acoustic-properties/speed-of-sound/> (access: 12.10.2023).
- GHOSHAL G., LAVARELLO R.J., KEMMERER J.P., MILLER R.J., OELZE M.L. (2012), Ex vivo study of quantitative ultrasound parameters in fatty rabbit livers, *Ultrasound in Medicine and Biology*, **38**(12): 2238–2248, doi: [10.1016/j.ultrasmedbio.2012.08.010](https://doi.org/10.1016/j.ultrasmedbio.2012.08.010).
- JAEGER M., HELD G., PREISSER S., PEETERS S., GRÜNING M., FRENZ M. (2014), Computed ultrasound tomography in echo mode (CUTE) of speed of sound for diagnosis and for aberration correction in pulse-echo sonography, [in:] *Proceedings of SPIE 9040, Medical Imaging 2014: Ultrasonic Imaging and Tomography*, **9040**: 90400A, doi: [10.1117/12.2042993](https://doi.org/10.1117/12.2042993).
- JAEGER M., HELD G., PEETERS S., PREISSER S., GRÜNING M., FRENZ M. (2015), Computed ultrasound tomography in echo mode for imaging speed of sound using pulse-echo sonography: Proof of principle, *Ultrasound in Medicine and Biology*, **41**(1): 235–250, doi: [10.1016/j.ultrasmedbio.2014.05.019](https://doi.org/10.1016/j.ultrasmedbio.2014.05.019).
- JAEGER M., FRENZ M. (2015), Quantitative imaging of speed of sound in echo ultrasonography, [in:] *IEEE International Ultrasound Symposium*, <https://www.youtube.com/watch?v=Ck75XbflQtY> (access: 12.10.2023).
- JENSEN J.A. (1996), Field: A program for simulating ultrasound systems, [in:] *Medical & Biological Engineering & Computing*, **34**(1): 351–353.
- KARWAT P. (2019), Computationally efficient algorithm for sound speed imaging in pulse-echo ultrasound, *Proceedings of Meetings on Acoustics*, **38**(1): 020005, doi: [10.1121/2.0001109](https://doi.org/10.1121/2.0001109).
- LYONS R.G. (2004), *Understanding Digital Signal Processing*, 2nd ed., Prentice Hall.
- SANABRIA S.J., OZKAN E., ROMINGER M., GOKSEL O. (2018), Spatial domain reconstruction for imaging speed-of-sound with pulse-echo ultrasound: Simulation and in vivo study, *Physics in Medicine and Biology*, **63**(21): 215015, doi: [10.1088/1361-6560/aae2fb](https://doi.org/10.1088/1361-6560/aae2fb).
- STÄHLI P., KURIAKOSE M., FRENZ M., JAEGER M. (2020), Improved forward model for quantitative pulse-echo speed-of-sound imaging, *Ultrasonics*, **108**: 106168, doi: [10.1016/j.ultras.2020.106168](https://doi.org/10.1016/j.ultras.2020.106168).
- TREEBY B.E., COX B.T. (2010), k-Wave: MATLAB toolbox for the simulation and reconstruction of photoacoustic wave fields, *Journal of Biomedical Optics*, **15**(2): 021314, doi: [10.1117/1.3360308](https://doi.org/10.1117/1.3360308).
- YOUNG J.R., SCHOEN S., KUMAR V., THOMENIUS K., SAMIR A.E. (2022), SoundAI: Improved imaging with learned sound speed maps, [in:] *2022 IEEE International Ultrasonics Symposium*, doi: [10.1109/IUS54386.2022.9958284](https://doi.org/10.1109/IUS54386.2022.9958284).

Research Paper

3D Synthetic Aperture Imaging Method in Spectrum Domain for Low-Cost Portable Ultrasound Systems

Jurij TASINKIEWICZ

*Institute of the Fundamental Technological Research, Polish Academy of Sciences
Warsaw, Poland; e-mail: yurijtas@ippt.pan.pl*

(received December 30, 2022; accepted March 7, 2023)

Portable, hand-held ultrasound devices capable of 3D imaging in real time are the next generation of the medical imaging apparatus adapted not only for professional medical staff but for a wide group of less advanced users. Limited power supply capacity and the relatively small number of channels used for the ultrasound data acquisition are the most important limitations that should be taken into account when designing such devices and when developing the corresponding image reconstruction algorithms.

The aim of this study was to develop a new 3D ultrasound imaging method which would take into account the above-mentioned features of the new generation of ultrasonic devices – low-cost portable general access scanners.

It was based on the synthetic transmit aperture (STA) method combined with the Fourier spectrum domain (SD) acoustic data processing. The STA using a limited number of elements in transmit and receive modes for ultrasound data acquisition allowed both aforementioned constraints to be obeyed simultaneously. Moreover, the computational speed of the fast Fourier transform (FFT) algorithm utilized for the ultrasound image synthesis in the spectrum domain makes the proposed method to be more competitive compared to the conventional time domain (TD) STA method based on the delay-and-sum (DAS) technique, especially in the case of 3D imaging in real time mode.

Performance of the proposed method was verified using numerical 3D acoustic data simulated in the Field II program for MATLAB and using experimental data from the custom design 3D scattering phantom collected by means of the Verasonics Vantage 256™ research ultrasound system equipped with the dedicated 1024-element 2D matrix transducer.

The method proposed in this paper was about 80 times faster than its counterpart based on the time domain synthetic transmit aperture (TD-STA) approach in the numerical example of a single 3D ultrasound image synthesized from 4 partial images each containing $64 \times 64 \times 512$ pixels.

It was also shown that the acceleration of the image reconstruction was achieved at the cost of a slight deterioration in the image quality assessed by the contrast and contrast-to-noise ratio (CNR).

Keywords: ultrasound imaging; matrix transducer; delay-and-sum; Fourier transform; synthetic aperture.



Copyright © 2023 The Author(s).
This work is licensed under the Creative Commons Attribution 4.0 International CC BY 4.0
(<https://creativecommons.org/licenses/by/4.0/>).

1. Introduction

Medical ultrasonography is the most used imaging modality for its speed, flexibility, cost-effectiveness and non-invasive nature. These features make the ultrasound imaging more competitive than the other imaging techniques, especially for preliminary diagnosis. Recently, the 3D or volumetric ultrasound imaging technology has been rapidly developed as the researchers started exploring innovative and new applications (FENSTER *et al.*, 2001; JI *et al.*, 2011). The volumetric imaging provides the physicians with much

deeper and realistic insight into the examined part of the human body (CAMPBELL *et al.*, 2005; LANDRY *et al.*, 2005). For instance, 3D ultrasound provides the capabilities of surface characterization of the fetus offering a better view of fetal defects like a cleft lip or clubfoot. Also, reduction in breast examination time with 3D ultrasound is currently under investigation (KOTSIANOS-HERMLE *et al.*, 2009; PADILLA *et al.*, 2013).

The most recent advances in ultrasound technology are enabling the rapid development of 3D imaging in real-time allowing for volumetric visualization

and tracking the movements of imaged organs, like the motion of the human heart wall or valves, blood flows in various vessels and so on. Moreover, the real-time 3D ultrasound can be potentially integrated into different portable small-size devices suitable for diagnostic and therapeutic procedures (due to small probe size and safety) in the near future.

There are a number of constraints that should be considered when designing such devices, like the limited power consumption due to the limited capacity of the power supply battery or a huge amount of acoustic data that have to be acquired using a limited number of signal channels and processed on-the-fly during volumetric data acquisition with 2D matrix transducers consisting of thousands of elements and so on.

To mitigate this problem the sub-array architectures were considered in the literature based on the sub-aperture design (SAVORD, SOLOMON, 2003) or a separable beamforming design wherein a conventional 2D array beamforming is decomposed into a series of 1D beamforming problems at the cost of some reduction in image quality (YANG *et al.*, 2013). Another strategy to reduce the number of active elements is by using the sparse 2D arrays. For example, AUSTENG and HOLM (2002) proposed a method based on the principle of grating lobes suppression to form the optimal symmetric and non-symmetric regular sparse periodic and radially periodic designs. Sparsely sampled aperture patterns like the minimal-redundant arrays were proposed in (KARAMAN *et al.*, 2009). To reduce redundancy the authors developed a sparse array design procedure based on the spatial convolution of the transmit and receive patterns by using different combinations of linear sub-arrays of the 2D matrix transducer. Several non-rectangular 2D sparse array layouts have also been proposed, such as the concentric circular arrays (WANG *et al.*, 2002; ULLATE *et al.*, 2006) and spiral arrays (MARTÍNEZ-GRAULLERA *et al.*, 2010; YOON, SONG, 2019). A more detailed literature review on the 2D sparse arrays design can be found for example in (RAMALLI *et al.*, 2022).

Recently, the spectrum domain (SD) ultrasound imaging methods have been attracting growing attention due to their high computational speed. This is a significant advantage over the conventional time domain (TD) methods based on the classical delay-and-sum (DAS) technique (THOMENIUS, 1996). This makes them promising for the 3D ultrasound imaging in the real-time mode. Several SD methods have been reported in the literature (BUSSE, 1992; SKJELVAREID, 2012; CHENG, LU, 2006). In (CHENG, LU, 2006), theoretical development of the so-called phase migration method was presented. The data collected using 2D aperture were first transformed for each axial depth to the spectrum domain. Then the frequency-dependent propagator function was applied to each cross-sectional

spectrum followed by the frequency averaging within the considered frequency band. The magnitude of the inverse Fourier transform of the averaged spectra obtained for each axial depth independently, yielded the 3D ultrasound image. The numerical complexity of the phase migration method was comparable to the conventional 3D TD imaging methods at the same time this yielded the synthesized images of poor quality, therefore remaining a purely theoretical interest. In (SKJELVAREID, 2012), the well-known $\omega - k$ migration algorithm previously adopted for the 2D B-mode ultrasound (SKJELVAREID *et al.*, 2011) was generalized for the 3D imaging. The ultrasound data were first transformed to the spectrum domain. Next, the $\omega - k$ migration was applied to transform the temporal spectral variable ω to the spatial spectrum variable related to the axial spatial coordinate. Then the inverse 3D Fourier transform was computed to obtain the final 3D ultrasound image. In (CHENG, LU, 2006) yet another approach for 3D SD ultrasound image synthesis was proposed. It was based on the assumption of the plane acoustic wave insonification (MONTALDO *et al.*, 2009) by an infinite 2D aperture array. The acoustic signals detected by the same 2D array were represented as the superposition of harmonic waves reflected from the scatterers distribution in the examined volume. Each harmonic component within the limited frequency band was first transformed to the spectrum domain with respect to the lateral coordinates. Next, the mapping between the wave-vector components of the detected echoes and the back-scattered field related to the reflectivity function describing the scattering properties of the examined medium was applied in the spectrum domain. Finally, the inverse 3D Fourier transform yielded the final 3D ultrasound image.

The main objective of this research was to propose a new spectrum domain synthetic transmit aperture (SD-STTA) 3D image reconstruction method. It offers a promising solution to the aforementioned constraints, suitable for low-cost portable devices which should operate with a limited number of signal channels and limited power consumption. Specifically, the SD-STTA method is based on a novel approach which combines the non-overlapping sub-aperture data acquisition of the back-scattered ultrasound echoes by analogy with the TD-STTA methods (GAMMELMARK *et al.*, 2003; JENSEN *et al.*, 2006; NIKOLOV *et al.*, 2008; TROTS *et al.*, 2009; TASINKEVYCH *et al.*, 2012) and the ultrasound data processing in the Fourier spectrum domain. Using a limited number of elements in the transmit (TX) and receive (RX) modes allowed the amount of acoustic data collected and transferred during a single TX/RX event to be reduced by utilizing a limited number of signal channels (64 and 256 considered in this study). Moreover, the computational speed of the fast Fourier transform (FFT) algorithm used for the ultrasound image synthesis in the spectrum domain

makes the SD-STA method promising for the real-time ultrasound imaging.

The validation of the proposed method was carried out in two stages. First, the method was tested using numerical acoustic data simulated in MATLAB using Field II software (JENSEN, 1996; JENSEN, SVENDSEN, 1992). Next, the method was validated using experimental acoustic data acquired in a custom made 3D scattering phantom by means of the Verasonics Vantage 256™ research ultrasound system equipped with the dedicated 1024-element 2D array transducer operating at 3.47 MHz center frequency. The comparative analysis of the proposed SD-STA method with the conventional TD-STA method (TASINKEVYCH *et al.*, 2013) generalized for the case of 3D imaging (TASINKEVYCH, 2017), was conducted. It was evidenced both in simulations and measurements that the proposed SD-STA method provides high computational speed and imaging quality comparable to state-of-the-art TD-STA methods.

The rest of the paper is organized as follows. In the next section theoretical background of the proposed SD-STA method is given. Then, the method is described in Sec. 3. The results of 3D imaging using numerically simulated and experimentally obtained data are presented in Sec. 4. The discussion of the results obtained is given in Sec. 5. Finally, in Sec. 6 the summary of the work is presented.

2. Theory

Theoretical backgrounds of the SD-STA methods are briefly presented in what follows. Let one consider an $N \times N$ -element flat matrix transducer placed in the plane $z = 0$. The origin of the Cartesian coordinate system is in the center of the transducer aperture and its sides are parallel to the x - and y -axes. During a single TX/RX event the i -th $M \times M$ -element sub-aperture is excited with a short pulse (one sine cycle of the nominal frequency) and transmits an unfocused wave in the z -axis direction, where $i = 1, \dots, I$, $I = (N/M)^2$. Without loss of generality the back-scattered echoes can be assumed to be detected by the same $M \times M$ -element sub-aperture and the i -th LRI is then synthesized using the RF echoes detected during this single TX/RX event only (this case is referred to as the reduced matrix of $M \times M$ RF echoes in the Subsec. 3.1). A more general case of using several TX/RX events for the synthesis of a single LRI is discussed in the next section (this case is referred to as the full-size matrix of $N \times N$ RF echoes in Subsec. 3.1). The received echoes represent the spatially sampled back-scattered acoustic field $s(\mathbf{r}_\perp, t)$ in the plane $z = 0$ within the 2D sub-aperture; $\mathbf{r}_\perp \equiv (\mathbf{e}_x x + \mathbf{e}_y y + \mathbf{e}_z 0)$ is a position vector defining a location of individual element of the transducer in the plane $z = 0$; $s(\mathbf{r}, t)$ is the back-scattered acoustic

field in the volume of interest V ; $\mathbf{r} \equiv (\mathbf{e}_x x + \mathbf{e}_y y + \mathbf{e}_z z)$ is a position vector in V . The spatial spectrum of the back-scattered field detected by the i -th RX sub-aperture can be represented as a linear combination of harmonic components propagating from randomly distributed point scatterers in the volume V (CHENG, LU, 2006):

$$S(\mathbf{k}_\perp, t)_i = \int K(\omega) \left\{ \int_V f(\mathbf{r}) e^{i\mathbf{k}'\mathbf{r}} d\mathbf{r} \right\} e^{-j\omega t} d\omega, \quad i = 1, \dots, I, \quad I = (N/M)^2, \quad (1)$$

where $f(\mathbf{r})$ denotes an object function describing the scattering intensity of the random distribution of scatterers in the volume V . In Eq. (1) $\mathbf{k}' = \mathbf{k} + \mathbf{k}^\mathbf{I}$, $\mathbf{k}^\mathbf{I} = \mathbf{e}_x k_x^\mathbf{I} + \mathbf{e}_y k_y^\mathbf{I} + \mathbf{e}_z k_z^\mathbf{I}$ is the wave-vector of the transmitted acoustic wave. In the case of SD-STA considered in this paper $\mathbf{k}^\mathbf{I} = \mathbf{e}_z k_z^\mathbf{I}$; also, in Eq. (1) $\mathbf{k} = \mathbf{e}_x k_x + \mathbf{e}_y k_y + \mathbf{e}_z k_z$ is the wave-vector of the back-scattered wave; $\mathbf{k}_\perp = \mathbf{e}_x k_x + \mathbf{e}_y k_y$ and $K(\omega)$ is a transfer function that accounts for the influence of the transmit and receive circuitry. From Eq. (1) the relationship between the temporal-spatial spectrum of the back-scattered acoustic field $S(\mathbf{k}_\perp, \omega)$ and the spatial spectrum of the object function $F(\mathbf{k}')$ in V can be obtained:

$$S(\mathbf{k}_\perp, \omega)_i = K(\omega) F(\mathbf{k}') \cong F'(\mathbf{k}')_i, \quad (2)$$

where $F'(\mathbf{k}')_i$ is the so-called band-limited spatial spectrum of $f(\mathbf{r})$ obtained as a result of transmission and detection of the acoustic wave by i -th $M \times M$ -element sub-aperture. It defines the 3D spatial spectrum of the partial LRI reconstructed using the RF echoes detected by the i -th $M \times M$ -element sub-aperture:

$$F'(\mathbf{k}')_i \equiv I(\mathbf{k}')_i. \quad (3)$$

The spatial spectrum defined in Eq. (3) can be obtained from the temporal-spatial spectrum of the detected back-scattered echoes as:

$$I(\mathbf{k}'(\omega))_i = S(\mathbf{k}'(\omega))_i, \quad (4)$$

where the spatial spectrum $S(\mathbf{k}'(\omega))_i$ of the back-scattered signals is obtained from $S(\mathbf{k}_\perp, \omega)_i$ after the variable transform:

$$k'_x = k_x, \quad k'_y = k_y, \quad k'_z(\omega) = \frac{\omega}{c} + \sqrt{\left(\frac{\omega}{c}\right)^2 - k_x^2 - k_y^2}. \quad (5)$$

To obtain the final 3D HRI of the examined volume of interest its 3D spatial spectrum has to be synthesized first as a sum of the spatial spectra of all LRIs:

$$I(\mathbf{k}'(\omega)) = \sum_{i=1}^I I(\mathbf{k}'(\omega))_i, \quad (6)$$

followed by the inverse 3D Fourier transform applied to $I(\mathbf{k}'(\omega))$:

$$I(\mathbf{r}) = \frac{c}{4\pi^2} \iiint B(\mathbf{k}'(\omega)) I(\mathbf{k}'(\omega)) e^{j\mathbf{k}'(\omega)\mathbf{r}} d\mathbf{k}'(\omega). \quad (7)$$

In Eq. (7) the term $B(\mathbf{k}'(\omega))$ was introduced which is the Jacobian of the variable transformation in the spectrum domain defined in Eq. (5):

$$B(\mathbf{k}'(\omega)) \equiv \frac{(\sqrt{k'_z(\omega)^2 - k'_x(\omega)^2 - k'_y(\omega)^2})}{k'_z(\omega)}. \quad (8)$$

3. Methods

The SD-STA method proposed in this paper was tested using numerical data simulated in MATLAB using Field II software. Moreover, experimental measurements were conducted and acoustic data from the custom design 3D scattering phantom were collected using Verasonics Vantage™ research ultrasound system equipped with a 2D matrix transducer utilizing 1024 elements in a 32×32 grid and operating at 3.47 MHz center frequency.

3.1. Numerical simulation in Field II

First, the method was tested using numerical data simulated in Field II. For this purpose the 32×32 -element matrix array transducer operating at $f_0 = 3.47$ MHz frequency was modeled. The transducer element pitch was 0.3 mm and the element width was 0.275 mm. The sampling frequency was 13.87 MHz which corresponded to 4 time samples per acoustic wavelength of the recorded signal. There were $N_t = 1122$ time samples simulated in each RF echo (for the 60 mm depth assumed, see further discussion). The speed of sound $c = 1540$ m/s and the frequency dependent attenuation $\alpha = 0.5$ dB/[MHz · cm] around the center frequency f_0 (Jensen, 2021) were applied which is typical for the soft tissue (HILL *et al.*, 2004). The parameters applied in the numerical simulations were chosen to mimic the 2D matrix transducer used in the

experimental measurements (see discussion in the next section). The transducer was excited with a short pulse burst (one cycle of the nominal frequency). The sets of 5 anechoic spheres (cysts) and 5 scattering spheres located in the volume $z \times x \times y = 10 \times 10 \times 60$ mm filled with randomly distributed point-like scatters were simulated separately. The diameter of spheres was 5 mm. The spheres were spaced 10 mm axially and located on the z -axis normal to the 2D aperture. The number of point scatterers was 30 per mm^3 (in accordance with the Rayleigh scattering conditions), yielding the total number of $1.8e5$ point-like scatterers in the volume under consideration. In the case of cysts the uniform scattering amplitude was assumed for the scatterers distributed outside the cysts and the scattering amplitude for the scatterers inside the cysts was set to zero (anechoic spheres). In the case of scattering spheres the ratio of the scattering amplitudes for the inner and outer scatterers was assumed 10:1.

Numerical simulations were conducted for non-overlapping TX/RX sub-apertures arranged in 16×16 and 8×8 -element grids. Two different data acquisition schemes were examined. They differed in the number of RF echoes collected for a given TX sub-aperture which were then used for a single LRI synthesis.

First, to synthesize a single LRI corresponding to a given TX sub-aperture the RF echoes were simulated for all elements of the 2D matrix transducer, as illustrated in Fig. 1 for the particular case of 16×16 -element TX/RX sub-aperture.

Specifically, to synthesize the LRI #1 the interrogating pulse was transmitted four times by the TX sub-aperture #1 for each of the four RX sub-apertures used successively in the RX mode which yielded the full-size matrix of 32×32 RF signals denoted by $[RX1]$ in Fig. 1. This procedure was then repeated for each of the four TX sub-apertures. All the LRIs synthesized using the full-size matrices $[RX1]$ through $[RX4]$ of the RF signals collected this way were then summed in the spectrum domain yielding the final HRI. Therefore, to obtain the final image there were 16 TX/RX events required for the case of the 16×16 -element sub-aperture data acquisition and 64 TX/RX events for the case

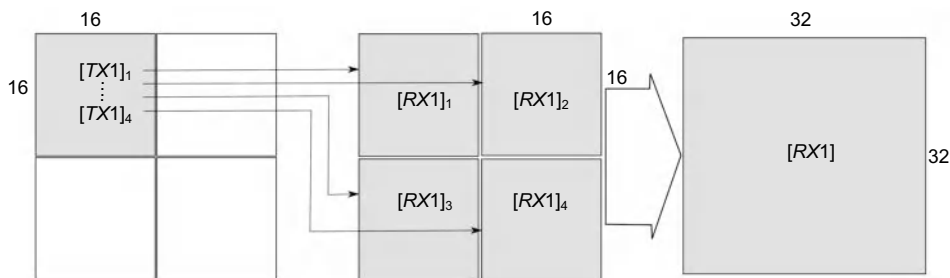


Fig. 1. Example of TX16/RX32 STA data acquisition utilizing 16×16 -element TX/RX sub-apertures and full-size matrix $[RX1]$ of 32×32 back-scattered RF echoes simulated during 4 TX/RX events. This matrix was then used to synthesize the LRI #1 corresponding the TX sub-aperture #1.

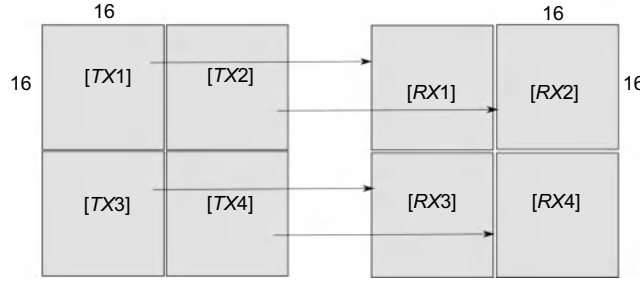


Fig. 2. Example of TX16/RX16 STA data acquisition utilizing 16×16 -element TX/RX sub-apertures and reduced matrices [RX1] through [RX4] of 16×16 back-scattered RF echoes simulated during 4 TX/RX events. This matrices were then used to synthesize the LRIs #1 through #4 corresponding the TX sub-aperture #1 through #4.

of the 8×8 -element one, respectively. These cases were denoted as TX16/RX32 and TX8/RX32 in Sec. 4, correspondingly.

Next, to obtain a single LRI corresponding to a given TX sub-aperture the so-called reduced matrices of the RF signals were simulated. In particular, for the case of 16×16 -element TX/RX sub-apertures to synthesize the LRI #1 corresponding to the TX sub-aperture #1 the interrogating pulse was transmitted only once and the RF echoes were then collected using the same grid of elements switched to the RX mode as depicted in Fig. 2. This yielded a reduced matrix [RX1] of 16×16 RF signals (see Fig. 2).

The rest of the full-size 32×32 matrix corresponding to inactive elements of the 2D array transducer was filled with zeros (as discussed later in this section) and the LRI #1 was synthesized then in the spectrum domain. This procedure was repeated for each of the

four TX sub-apertures and the final HRI was obtained in the same way as in the case of the full-size RF matrix data acquisition discussed earlier. Hence, to obtain the HRI in the case of the reduced RF matrix approach shown in Fig. 2 there were only 4 TX/RX events required for the 16×16 -element TX/RX sub-aperture data acquisition and 16 TX/RX events for the 8×8 -element one, respectively. These cases were denoted as TX16/RX16 and TX8/RX8 in Sec. 4, correspondingly.

Finally, for comparison the simulations were also conducted for the full-size 32×32 -element TX/RX aperture. In this case a single interrogating pulse was transmitted and the full-size matrix of 32×32 RF echoes was collected at once. These echoes were then used to synthesize the final HRI in the spectrum domain. This case was denoted as TX32/RX32 in Sec. 4.

The data-flow of a single LRI synthesis is sketched:

For j -th $M \times M$ -element TX sub-aperture, $j = 1, \dots, J$, $J = (N/M)^2$:

Reduced RF matrix

Full-size RF matrix

- | | |
|---|---|
| <ol style="list-style-type: none"> 1) Transmit interrogating pulse with j-th $M \times M$-element TX sub-aperture and acquire ultrasound echoes using the j-th $M \times M$-element RX sub-aperture. 2) Fill the rest of $N \times N$ RF matrix with zeros (empty RFs). 3) Compute the 3D temporal-spatial spectrum $S(\mathbf{k}_1, \omega)_j$ of the echoes with respect to the spatial variables x, y and the time t using the FFT algorithm. 4) Transform the variables $(k_x, k_y, \omega) \rightarrow (k'_x, k'_y, k'_z(\omega))$ (see Eqs. (4) and (5)) to obtain the spatial spectrum $I(\mathbf{k}')_j$ of the j-th LRI. 5) Accumulate the spatial spectrum of the HRI: $I(\mathbf{k}') = I(\mathbf{k}') + I(\mathbf{k}')_j$ (see Eq. (6)). | <ol style="list-style-type: none"> 1) Transmit interrogating pulse with j-th $M \times M$-element TX sub-aperture and acquire ultrasound echoes using the i-th $M \times M$-element RX sub-aperture, $i = 1, \dots, I$, $I = (N/M)^2$. 2) Fill full $N \times N$ RF matrix with acquired echoes. |
|---|---|

The ultrasound data needed to synthesize a single LRI were acquired first yielding the full-size or reduced matrix of RF echoes (step 1 and 2). Specifically, in the former case the data acquisition for the j -th $M \times M$ -element TX sub-aperture yielded a 3D matrix of $N \times N \times N_t$ time samples, where N_t is the number of time samples in a single RF echo ($N_t = 1122$), and $N \times N$ is the 2D matrix transducer size ($N = 32$). In the case of the reduced RF matrix approach only an $M \times M \times N_t$ sub-matrix of time samples was acquired during the j -th TX/RX event. The rest of the transducer elements remained inactive. To synthesize the partial LRI in this case the rest of the 3D matrix of $N \times N \times N_t$ time samples was filled with zeros which corresponded to empty RF echoes (N_t zero samples in each of them). This allowed the spectrum domain processing to be more versatile and suitable for different TX/RX sub-aperture size and position within the 2D transducer array which greatly simplified the HRI spatial spectrum synthesis (step 5). The 3D matrix of time samples was then used to compute the spatial-temporal spectrum $S(\mathbf{k}_{bot}, \omega)$ with respect to the lateral spatial variables x and y and the time variable t (step 3). For this purpose the *fft.m* routine from the MATLAB Signal Processing Toolbox was used. The variable transformation in the spectrum domain in the step 4 was implemented as a 1D interpolation procedure. Concretely, the temporal spectrum $S(:, \omega)_j$ was interpolated to the spatial spectrum $I(:, k_z(\omega))_j$ using Eq. (5). For this purpose the routine *interp1.m* from MATLAB was used. In the final step 5 the spatial spec-

trum $I(\mathbf{k}')_j$ of the j -th LRI was added (accumulated) to the spatial spectrum $I(\mathbf{k}')$ of the final HRI. Once all $I(\mathbf{k}')_j$ were synthesized the inverse 3D Fourier transform of $I(\mathbf{k}')$ yielded the final 3D ultrasound image $I(\mathbf{r})$ (see Eq. (7)).

Figure 3 depicts the comparison of ultrasound image formation for the SD and TD methods considered in this paper.

It should be noted that in the case of the TD-STA method the synthesized HRI is represented by the properly delayed and summed RF echoes collected during consecutive TX/RX events (TASINKEVYCH *et al.*, 2013). Therefore, the envelopes of the synthesized RFs must be computed first as shown in the diagram in Fig. 3. For this purpose the routine *envelope.m* from the MATLAB Signal Processing Toolbox was used. Furthermore, for consistency the images obtained using the TD-STA method were displayed as a function of spatial variables as in the case of the SD-STA one. For this purpose the relation between the axial spatial variable z and the time t was used: $z = ct/2$, c being the acoustic wave speed.

In the numerical simulations the 3D ultrasound images comprised of $N_x \times N_y \times N_z = 64 \times 64 \times 512$ spatial samples were synthesized using the SD-STA method proposed. Also, the same acoustic data were processed using the TD-STA method (TASINKEVYCH *et al.*, 2013; 2017) and the corresponding results were compared.

The cysts arrangement considered in the numerical simulations enabled the comparison of the image contrast and contrast-to-noise ratio (CNR) obtained

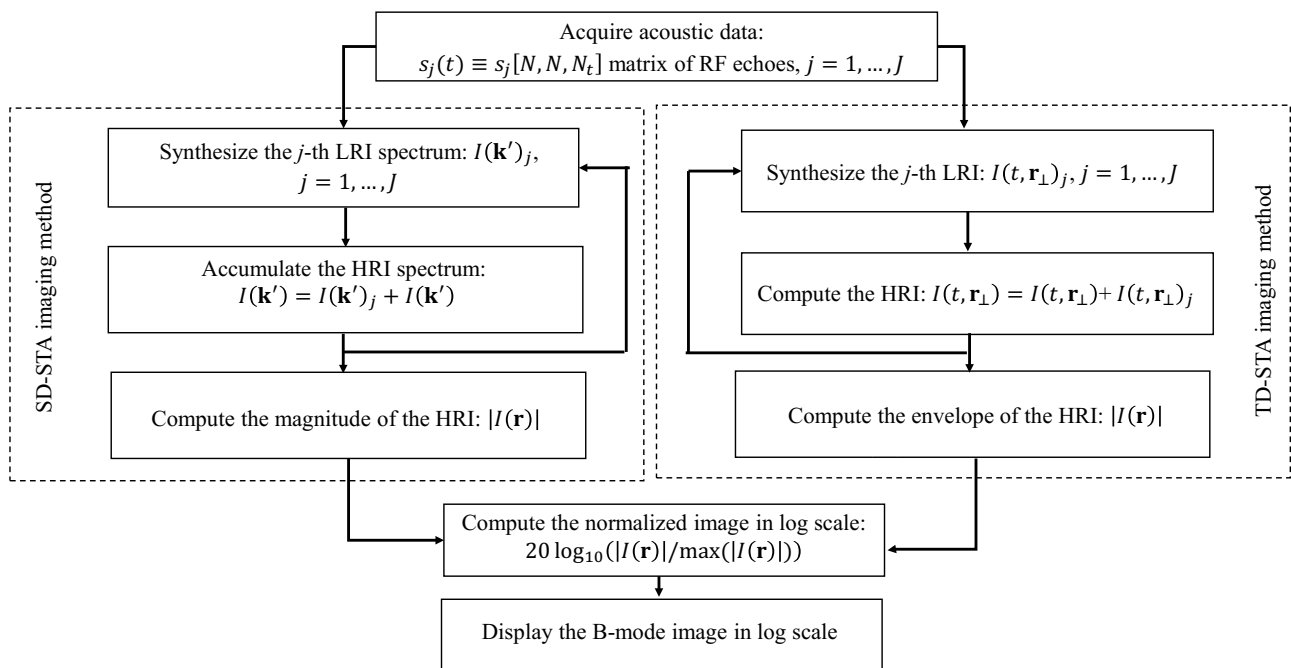


Fig. 3. Flow diagram showing the successive steps of the acoustic data processing in the considered SD-STA and TD-STA imaging methods.

for different data acquisition schemes considered. The contrast and CNR were defined as:

$$C = \frac{|\mu_c - \mu_r|}{\mu_r}, \quad \text{CNR} = \frac{|\mu_c - \mu_r|}{\sqrt{\sigma_c^2 + \sigma_r^2}} \quad (9)$$

where μ_c, μ_r are the mean intensities of cyst and reference regions; σ_c, σ_r are the standard deviations for the cyst and reference regions, respectively. The corresponding values of the contrast and CNR were assessed from the 2D B-mode images of the cross-sectional views of the cysts arrangement (the plane $Y = 0$). The cyst region in Eq. (9) was defined as a circle area of the diameter $D_c = 0.75D$ centered within the corresponding cross-section of the cyst, whereas the reference region was defined as an area between the circles of diameters $1.5D$ and $1.25D$ surrounding the cyst cross-section. Finally, the 3D imaging capability of the proposed method was demonstrated using acoustic data simulated for the set of scattering spheres arrangement discussed above. The isosurfaces at the fixed intensity level of the corresponding 3D reconstructed spheres were obtained using the *sliceomatic* visualization package for MATLAB.

3.2. Experimental measurements

Next, the SD-STA method was verified using measurement data. The experimental setup is shown schematically in Fig. 4.

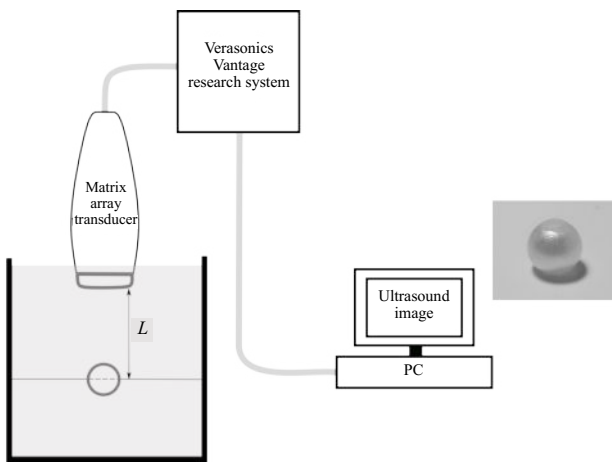


Fig. 4. Block diagram of the experimental set-up. Right panels show the real view of the scattering plastic sphere used in experimental measurements.

The ultrasound data for the scattering sphere with a diameter of 5 mm (shown on the right in Fig. 4) were acquired using the Verasonics Vantage 256™ research system (Kirkland, WA) equipped with the dedicated matrix transducer utilizing 1024 elements arranged in a 32×32 grid and operating at 3.47 MHz center frequency. The examined sphere had a through hole with a diameter of about 1 mm. It was suspended in

the water tank using a thin nylon wire with a diameter of 0.2 mm at a distance of 25 mm from the 2D array transducer face. The speed of sound $c = 1490$ m/s in water at the room temperature was applied in the image reconstruction (HILL *et al.*, 2004). The excitation voltage was 10 V with 12 dB amplification of the received signals. The scanner was preprogrammed to scan the phantom according to the 5 data acquisition schemes described in Subsec. 3.1. It should be noted that in the case of the full-size 32×32 -element TX/RX aperture the acoustic data were acquired using the dedicated software provided by the Verasonics Vantage 256™ research system manufacturer. It allowed a single flash transmit over all 1024 elements to be obtained, with each of the four 256-element RX sub-apertures used in the RX mode. Therefore, to collect the full-size matrix of 32×32 back-scattered RF echoes in this case four consecutive TX/RX events were required.

4. Results

4.1. Numerical simulations

The B-mode images of the numerical acoustics data simulated in Field II for the set of cysts (anechoic spheres) of 5 mm in diameter arranged axially in front of the 2D matrix transducer are shown in Figs. 5 and 6.

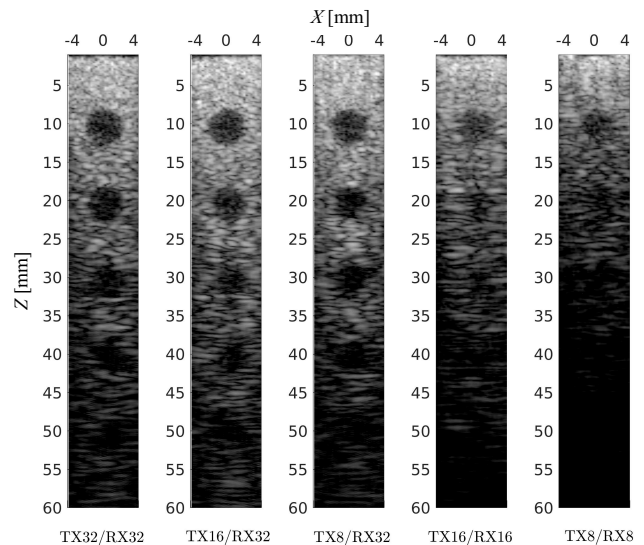


Fig. 5. B-mode images of the numerical data simulated in Field II for the set of anechoic cysts. The cross-sectional view (plane $Y = 0$) of the 3D reconstruction obtained using the FD-STA method for different data acquisition schemes is demonstrated. The images are plotted in logarithmic scale over 30 dB dynamic range.

The images in Figs. 5 and 6 present the cross-sectional views of the 3D reconstructed data obtained using the SD-STA method proposed in this work (Fig. 5) and the conventional TD-STA method generalized for 3D imaging (Fig. 6). All B-mode images were

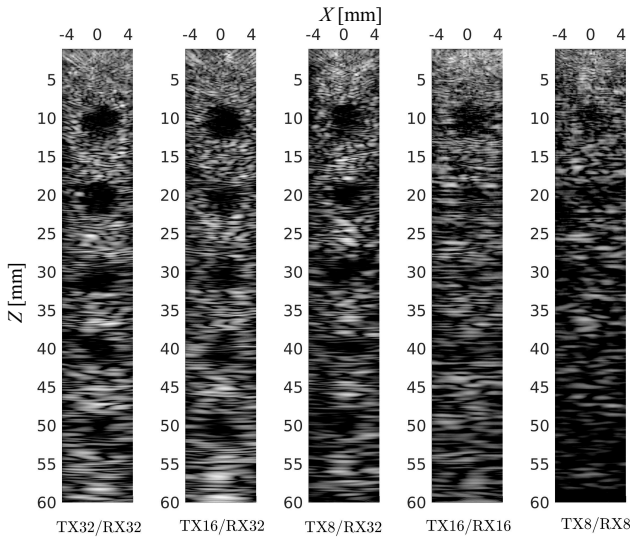


Fig. 6. B-mode images of the numerical data simulated in Field II for the set of anechoic cysts. The cross-sectional view (plane $Y = 0$) of the 3D reconstruction obtained using the time TD-STA method for different data acquisition schemes is demonstrated. The images are plotted in logarithmic scale over 30 dB dynamic range.

normalized with respect to their maximum value in the corresponding cross-sections and visualized in logarithmic scale over 30 dB dynamic range. The images in Figs. 5 and 6 correspond to different data acquisition schemes discussed in Subsec. 3.1. Specifically, the leftmost panel corresponds to the TX32/RX32 data acquisition when a single interrogating pulse was transmitted and the full-size matrix of 32×32 RF echoes was collected at once.

The images depicted in the panels TX16/RX32 and TX8/RX32 correspond to the 16×16 -element and 8×8 -element TX sub-apertures, respectively. The LRIs were synthesized from the full-size matrices of 32×32 RF echoes acquired for each TX sub-aperture as shown in Fig. 1 in the Subsec. 3.1. Finally, the images in the panels TX16/RX16 and TX8/RX8 correspond to the 16×16 -element and 8×8 -element TX sub-apertures, but in these cases the LRIs were synthesized from the reduced matrices of RF echoes, respectively.

In Figs. 7 and 8 the plots of the CNR and contrast assessed from the B-mode images depicted in Figs. 5 and 6, are shown, respectively.

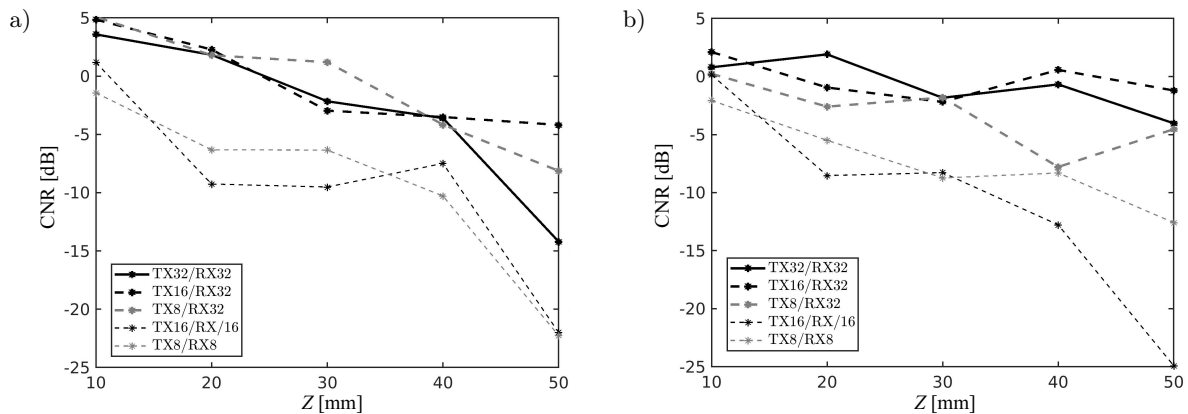


Fig. 7. Dependence of the CNR versus axial distance (z -coordinate) for the set of cysts assessed from the B-mode images shown in Figs. 5 and 6 and obtained using (a) SD-STA method and (b) TD-STA method (for both plane $Y = 0$). Different data acquisition schemes discussed in Subsec. 3.1 were considered.

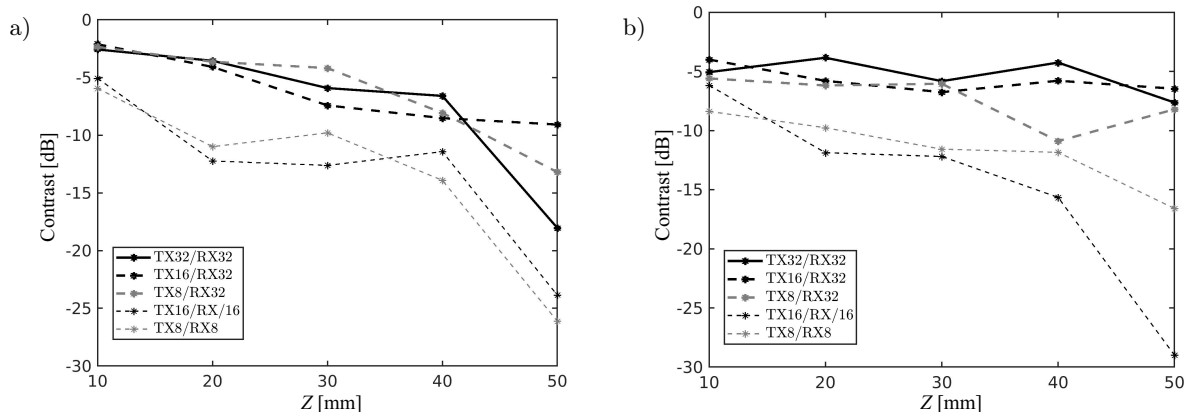


Fig. 8. Dependence of the contrast versus axial distance (z -coordinate) for the set of cysts assessed from the B-mode images shown in Figs. 5 and 6 and obtained using (a) SD-STA method and (b) TD-STA method (for both plane $Y = 0$). Different data acquisition schemes discussed in Subsec. 3.1 were considered

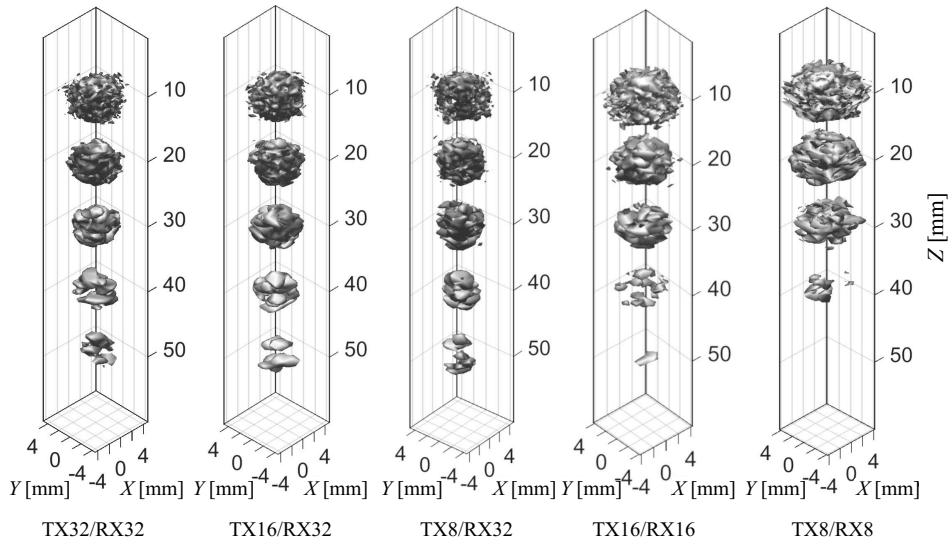


Fig. 9. 3D images of the set of 5 scattering spheres reconstructed using proposed SD-STA method for different TX/RX data acquisition schemes. The images are visualized using *sliceomatic* visualization package for MATLAB in logarithmic scale. Isosurfaces corresponding to the -30 dB level are shown.

In Fig. 9 the 3D images of the numerical acoustics data simulated in Field II for the set of scattering spheres arranged axially in front of 2D matrix transducer are shown (see Subsec. 3.1). The results were obtained using the SD-STA method for different data acquisition schemes. The images in Fig. 9 present the isosurfaces of the normalized 3D reconstructed data in logarithmic scale generated using *sliceomatic* visualization package for MATLAB and their arrangement is similar to that in Fig. 5.

4.2. Measurements

In Fig. 10 the 3D images of the experimental acoustics data acquired from the custom design scattering

phantom (see Subsec. 3.2) are shown. The results were obtained using the SD-STA method for different data acquisition schemes. The images present the isosurfaces of the normalized 3D reconstructed data in logarithmic scale generated using *sliceomatic* visualization package for Matlab. They are arranged in the same order as in Fig. 5.

The B-mode images of the cross-sectional views corresponding to the $X = 0$ and $Y = 0$ planes of the experimental acoustics data acquired from the custom design scattering phantom are presented in Figs. 11 and 12, respectively. All B-mode images were normalized with respect to their maximum value in the corresponding cross-sections and visualized in logarithmic scale over 30 dB dynamic range.

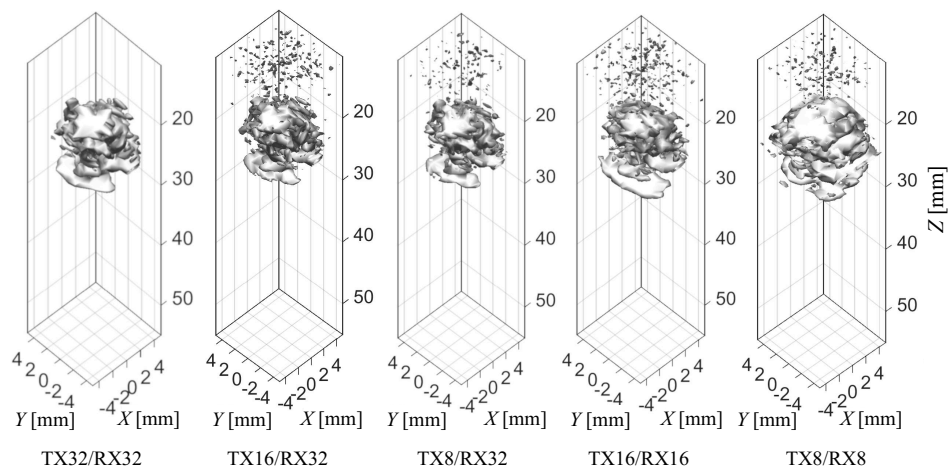


Fig. 10. 3D images of the experimental data acquired from the custom design scattering phantom reconstructed using proposed SD-STA method for different TX/RX data acquisition schemes. The images are visualized using *sliceomatic* visualization package for MATLAB in logarithmic scale. Isosurfaces corresponding to the -30 dB level are shown.

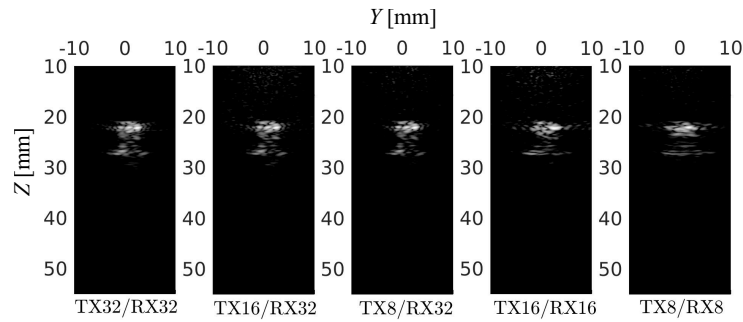


Fig. 11. B-mode images of the experimental acoustic data corresponding to the cross-sectional views (plane $X = 0$) of the 3D reconstruction obtained using the FD-STA method for different data acquisition schemes (see Fig. 10). The images are plotted in logarithmic scale over 30 dB dynamic range.

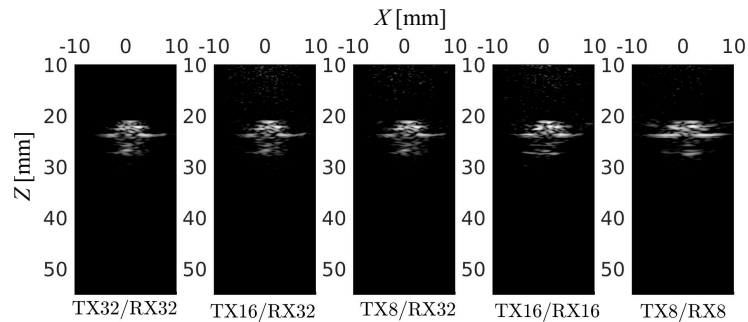


Fig. 12. B-mode images of the experimental acoustic data corresponding to the cross-sectional view (plane $Y = 0$) of the 3D reconstruction obtained using the FD-STA method for different data acquisition schemes (see Fig. 10). The images are plotted in logarithmic scale over 30 dB dynamic range.

5. Discussion

The results presented in this work confirmed effectiveness of the SD-STA 3D imaging method. Different data acquisition schemes based on the non-overlapping sub-apertures used in the TX/RX modes were studied and compared. For this purpose the numerical acoustic data simulated in Field II program and experimental data collected with the Verasonics Vantage 256™ research ultrasound system from the custom-design 3D scattering phantom were used. It was evidenced in this research both by numerical simulations and experimental data imaging that the trade-off exists between the frame-rate defined primarily by the number of acoustic data frames (volumes) acquired, and the imaging quality, assessed by the contrast and the CNR. Specifically, the B-mode cross-sectional views (see Fig. 5 in Subsec. 4.1) of the 3D numerical acoustic data simulated in Field II program for different data acquisition schemes and reconstructed using the SD-STA method were analyzed and compared. Only an insignificant change in the contrast and CNR for the depth below 40 mm was observed, provided the full-size matrices of 32×32 RF echoes was used for the synthesis of partial LRIs as evidenced further in this section. These cases were de-

noted as TX16/RX32, TX8/RX32, and TX32/RX32 in Figs. 7a and 8a, respectively. At the larger depths a slight increase in the contrast and CNR was observed for the TX16/RX32 and TX8/RX32 data acquisition schemes in comparison to the TX32/RX32 one. Specifically, about 9 dB and 5 dB increase in the contrast and 10 dB and 6 dB increase in the CNR was obtained for the TX16/RX32 and TX8/RX32 cases over the TX32/RX32 case, respectively. In the case of the TX16/RX32 data acquisition scheme, the final HRI was obtained by summing 4 LRIs which required 16 TX/RX events, while in the case of the TX8/RX32 one 16 LRIs and 64 TX/RX events were needed. Obviously, the time needed to acquire the acoustic data and synthesize the HRI determines the frame rate of the imaging method which is one of the most important parameters especially in the real-time 3D ultrasonography. Therefore, to reduce the number of TX/RX events required for the synthesis of the HRI the data acquisition schemes TX16/RX16 and TX8/RX8 were implemented and tested (see Subsec. 3.1). Specifically, a single TX/RX event was needed to acquire the reduced matrices of 16×16 and 8×8 RF signals with non-overlapping TX/RX sub-apertures comprised of 16×16 and 8×8 elements, respectively. These reduced matrices were then used for the LRIs synthesis. The

number of the LRIs needed to obtain the HRI did not change, but the data acquisition time was shortened 4 times for the TX16/RX16 and 16 times for the TX8/RX8 data acquisition schemes in comparison to the TX16/RX32 and TX8/RX32 ones, respectively. However, this increase in the data acquisition rate was achieved by the cost of the synthesized image quality deterioration, as evidenced by examples shown in Fig. 5, panels 4 and 5 denoted as the TX16/RX16 and TX8/RX8, respectively. This degradation of the image quality was quantified by the contrast and CNR, shown in Figs. 7a and 8a. Specifically, the decrease in the contrast was 3–5 dB at the depths below 40 mm up to 14 dB at the maximum simulation depth of 50 mm and the decrease in the CNR was 4–7 dB at the depths below 40 mm up to 18 dB at the 50 mm depth for the TX16/RX16 data acquisition scheme in comparison to the TX16/RX32 one, respectively. The corresponding values of the contrast and CNR decrease for the case of the TX8/RX8 data acquisition scheme in comparison to the TX8/RX32 one were 3–7 dB (contrast, Fig. 8a) and 6–8 dB (CNR, Fig. 7a) at the depths below 40 mm and up to 13 dB (contrast, Fig. 8a) and 14 dB (CNR, Fig. 7a) at the depth of 50 mm, respectively.

Similar dependence of the image quality on the number of TX/RX events based on the visual assessment was also observed in the case of the experimental data reconstruction. The corresponding examples are shown in Figs. 11 and 12, where the B-mode cross-sectional views in the planes $X = 0$ and $Y = 0$ of the 3D reconstructed data of the custom design scattering phantom (see Fig. 10) are depicted.

Furthermore, the performance of the SD-STA method was compared with the conventional TD-STA ultrasound imaging method. The same TX/RX data acquisition schemes were implemented and the image quality was assessed for both methods using the contrast and CNR parameters. In the case of the TD-STA method similar dependencies of the contrast and CNR parameters versus depth for different TX/RX data acquisition schemes were obtained as in the case of the SD-STA method. For instance, for the TX16/RX16 data acquisition scheme the decrease in the contrast was 2–8 dB at the depths below 40 mm up to 20 dB at the maximum simulation depth of 50 mm in comparison to the TX16/RX32 one, respectively (see Fig. 8b). The corresponding decrease in the CNR was 2–11 dB at the depths below 40 mm up to 22 dB at the 50 mm depth (see Fig. 7b). In the case of the TX8/RX8 data acquisition scheme the observed decrease in the contrast and CNR in comparison to the TX8/RX32 one were 1–5 dB (contrast, Fig. 8b) and 1–7 dB (CNR, Fig. 7b) at the depths below 40 mm and up to 11 dB (contrast, Fig. 9b) and 9 dB (CNR, Fig. 8b) at the depth of 50 mm, respectively.

Although the qualitative dependencies of the contrast and CNR vs. depth for the SD-STA and TD-STA

methods were similar, the quantitative changes in the values of corresponding parameters differed slightly for the data acquisition schemes considered. For example, comparison of the images reconstructed using both methods from the full-size matrices of 32×32 RF echoes confirmed that for the TX16/RX32 data acquisition scheme the contrast decreased approximately by 7 dB (from -2 to -9 dB, Fig. 8a) in the case of the SD-STA method and by approximately 4 dB (from -3 to -7 dB, Fig. 8b) in the case of the TD-STA method in the considered range of depths. For the TX8/RX32 data acquisition scheme the corresponding decrease in the contrast was approximately 11 dB (from -2 to -13 dB, Fig. 8a) in the case of the SD-STA method and approximately 5 dB (from -6 to -11 dB, Fig. 8b) in the case of the TD-STA, respectively. Also, slightly slower decrease of the CNR with growing depth was observed for images reconstructed using the conventional TD-STA as compared to the SD-STA. Specifically, the CNR decreased approximately by 9 dB (from 5 to -4 dB, Fig. 7a) in the case the SD-STA method and by approximately 3 dB (from 2 to -1 dB, Fig. 7b) in the case of the TD-STA method for the TX16/RX32 data acquisition scheme in the considered range of depths. The corresponding values for the TX8/RX32 data acquisition scheme were approximately 13 dB (from 5 to -8 dB, Fig. 7a) in the case of the SD-STA method and approximately 8 dB (from 0 to -8 dB, Fig. 7b) in the case of the TD-STA, respectively.

Comparing by visual assessment the B-mode cross-sectional views (see Figs. 5 and 6 in Subsec. 4.1) of the 3D numerical acoustic data simulated in Field II one can observe that the TD-STA method provided slightly better depth of visualization than the proposed SD-STA method especially for the cases of TX16/RX16 and TX8/RX8 data acquisition (see panels 4 and 5 in the Figs. 5 and 6). However, the SD-STA method provided better image resolution which can be visually assessed as image sharpness for the cysts over the entire range of depths considered.

Moreover, the proposed method allowed the time of the HRI synthesis to be reduced significantly due to the properties of the FFT algorithm (Brigham, 1988) utilized in the SD data processing. Specifically, the numerical complexity of the single LRI reconstruction was as large as $O(N_x N_y N_t \log(N_x N_y N_t))$ (TASINKEVYCH, 2017) for the case of the SD-STA method, where N_x and N_y are the number of samples in the synthesized image in the lateral plane and N_t – is the number of time samples recorded in a single RF acoustic echo. In the case of the conventional TD-STA method the corresponding value was $O(N_x N_y N_z N^2)$, where N_z is the number of samples in the synthesized image in the axial direction, and N^2 is the number of RF signals used for the LRI synthesis. The corresponding reduction of the LRI reconstruction time was therefore (TASINKEVYCH, 2017):

$$\frac{T_{\text{SD-STA}}}{T_{\text{TD-STA}}} = \frac{N_t \log(N_x N_y N_t)}{N_z N^2}.$$

In the case of the TX16/RX32 data acquisition scheme ($N = 32$) and for the reconstructed images of $64 \times 64 \times 512$ ($N_x \times N_y \times N_z$) samples where each RF had 1122 time samples (N_t) the corresponding value was: $T_{\text{SD-STA}}/T_{\text{TD-STA}} \sim 1/20$. This yielded about 80 times faster synthesis of the final HRI image comprised of 4 LRIs.

It is worth noting that to conduct a reliable comparative analysis of the results obtained using different methods (SD-STA and TD-STA) no data processing was applied to enhance the imaging quality, like dynamic apodization (GUENTHER, WALKER, 2007; MEHDIZADEH *et al.*, 2012; TASINKEVYCH *et al.*, 2013) or the time gain compensation taking into account the attenuation in the medium (SZABO, 2004), etc. This resulted among others in the relatively weak overall quality of the B-mode images obtained with the SD-STA and TD-STA methods, especially for the cases of TX16/RX16 and TX8/RX8 data acquisition schemes corresponding to the LRIs synthesis from the reduced matrices of RF echoes (see for instance Figs. 5 and 6 were the images obtained using the numerical data simulated for the set of anechoic cysts are shown). This examples clearly show the extent of final image quality deterioration due to acceleration of the acoustic data acquisition and processing. Therefore, further research is necessary in order to improve the quality of 3D ultrasound imaging with the use of the reduced RF matrices data acquisition schemes. Their development is especially important for the low-cost portable devices which should operate with a limited power consumption and will be the subject for future research.

6. Conclusions

In this work the SD-STA 3D image reconstruction method based on the non-overlapping TX/RX sub-aperture data acquisition combined with the spectrum domain data processing was proposed. For transmission of the interrogation signal and detection of the back-scattered echoes the limited number of signal channels (64 or 256) was used which determined the number of active elements utilized in the TX/RX events (8×8 and 16×16 -element non-overlapping TX/RX sub-apertures). Such a configuration of the ultrasound data acquisition schemes is consistent with the requirements of the low-cost portable devices usually operating within low power consumption limitation and using small number signal channels for transferring the acoustic data from the probe to the host.

The results obtained in this paper confirmed that a trade-off between the TX/RX sub-aperture size which determines the number of TX/RX events re-

quired for the synthesis of the final image and its quality exists. Specifically, in this research the optimal sub-aperture size was 16×16 -element one which required as much as 16 TX/RX events to reconstruct the HRI consisted of 4 LRIs, provided the full-size matrices of RF signals were used for their synthesis (TX16/RX32 data acquisition scheme). Applying the reduced RF matrix approach (TX16/RX16 data acquisition) the corresponding number of TX/RX events was reduced four times. However in the latter case the image quality deterioration was observed.

Moreover, the SD-STA method allowed a significant increase in the image reconstruction rate compared to the conventional TD-STA method. This acceleration was obtained at the cost of a slight deterioration in the image quality assessed by the contrast and CNR parameters which usually can be considered as tolerable in the case of the low-cost portable devices.

Further research will focus on improving the imaging quality. For this purpose the SD-STA method will be generalized for the case of overlapping sub-apertures. This however will inevitably lead to the frame rate decrease which is a crucial parameter in the real-time 3D ultrasonography. Therefore, optimization of the number and size of the TX/RX sub-apertures as well as their stride will be necessary to achieve the best possible quality maintaining the acceptable frame rate at the same time. Another possible way to improve the imaging quality is to generalize the SD-STA method for the case of the coherent compounding of ultrasound waves transmitted at different angles. In this case the numerical complexity of the SD data processing will increase significantly because one will have to deal with 3D interpolation of the spatial-temporal spectrum instead of the 1D interpolation which is required in the SD-STA method proposed in this paper.

References

1. AUSTENG A., HOLM S. (2002), Sparse 2-D arrays for 3-D phased array imaging – design methods, *IEEE Transactions on Ultrasonics, Ferroelectrics, and Frequency Control*, **49**(8): 1073–1086, doi: [10.1109/tuffc.2002.1026019](https://doi.org/10.1109/tuffc.2002.1026019).
2. BRIGHAM E.O. (1988), *The Fast Fourier Transform and Its Applications*, Prentice Hall, New Jersey.
3. BUSSE L.J. (1992), Three-dimensional imaging using a frequency-domain synthetic aperture focusing technique, *IEEE Transactions on Ultrasonics, Ferroelectrics, and Frequency Control*, **39**(2): 174–179, doi: [10.1109/58.139112](https://doi.org/10.1109/58.139112).
4. CAMPBELL S., LEES C., MOSCOSO G., HALL P. (2005), Ultrasound antenatal diagnosis of cleft palate by a new technique: the 3D reverse face view, *Ultrasound in Obstetrics and Gynecology*, **25**(1): 12–18, doi: [10.1002/uog.1819](https://doi.org/10.1002/uog.1819).

5. CHENG J., LU J. (2006), Extended high-frame rate imaging method with limited-diffraction beams, *IEEE Transactions on Ultrasonics, Ferroelectrics, and Frequency Control*, **53**(5): 880–899, doi: [10.1109/tuffc.2006.1632680](https://doi.org/10.1109/tuffc.2006.1632680).
6. FENSTER A., DOWNEY D.B., CARDINAL H.N. (2001), Three-dimensional ultrasound imaging, *Physics in Medicine & Biology*, **46**(5): 67–99, doi: [10.1088/0031-9155/46/5/201](https://doi.org/10.1088/0031-9155/46/5/201).
7. GAMMELMARK K.L., JENSEN J.A. (2003), Multielement synthetic transmit aperture imaging using temporal encoding, *IEEE Transactions on Medical Imaging*, **22**(4): 552–563, doi: [10.1109/TMI.2003.809088](https://doi.org/10.1109/TMI.2003.809088).
8. GUENTHER D.A., WALKER W.F. (2007), Optimal apodization design for medical ultrasound using constrained least squares part II simulation results, *IEEE Transactions on Ultrasonics, Ferroelectrics, and Frequency Control*, **54**(2): 343–358, doi: [10.1109/TUFFC.2007.248](https://doi.org/10.1109/TUFFC.2007.248).
9. HILL C.R., BAMBER J.C., TER HAAR G.R. [Eds.] (2004), *Physical Principles of Medical Ultrasonics*, 2nd ed., John Wiley & Sons, Ltd., New York, doi: [10.1002/0470093978](https://doi.org/10.1002/0470093978).
10. JENSEN J.A. (1996), Field: A program for simulating ultrasound systems, [in:] *Medical & Biological Engineering & Computing*, Proceedings of 10th Nordic-Baltic Conference on Biomedical Imaging, **34**(sup. 1): 351–353.
11. JENSEN J.A. (2021), *Users' guide for the Field II program*, Release 3.30, April 5, 2021, https://field-ii.dk/documents/users_guide.pdf (access: 5.04.2021).
12. JENSEN J.A., NIKOLOV S.V., GAMMELMARK K.L., PEDERSEN M.H. (2006), Synthetic aperture ultrasound imaging, *Ultrasonics*, **44**: e5–e15, doi: [10.1016/j.ultras.2006.07.017](https://doi.org/10.1016/j.ultras.2006.07.017).
13. JENSEN J.A., SVENDSEN N.B. (1992), Calculation of pressure fields from arbitrarily shaped, apodized, and excited ultrasound transducers, *IEEE Transactions on Ultrasonics, Ferroelectrics, and Frequency Control*, **39**(2): 262–267, doi: [10.1109/58.139123](https://doi.org/10.1109/58.139123).
14. JI S., ROBERTS D.W., HARTOV A., PAULSEN K.D. (2011), Real-time interpolation for true 3-dimensional ultrasound image volumes, *Journal of Ultrasound in Medicine*, **30**(2): 243–252, doi: [10.7863/jum.2011.30.2.243](https://doi.org/10.7863/jum.2011.30.2.243).
15. KARAMAN M., WYGANT I.O., ORALKAN Ö., KHURIYAKUB B.T. (2009), Minimally redundant 2-D array designs for 3-D medical ultrasound imaging, *IEEE Transactions on Medical Imaging*, **28**(7): 1051–1061, doi: [10.1109/TMI.2008.2010936](https://doi.org/10.1109/TMI.2008.2010936).
16. KOTSIANOS-HERMLE D., HILTAWSKY K.M., WIRTH S., FISCHER T., FRIESE K., REISER M. (2009), Analysis of 107 breast lesions with automated 3D ultrasound and comparison with mammography and manual ultrasound, *European Journal of Radiology*, **71**(1): 109–115, doi: [10.1016/j.ejrad.2008.04.001](https://doi.org/10.1016/j.ejrad.2008.04.001).
17. LANDRY A., SPENCE J.D., FENSTER A. (2005), Quantification of carotid plaque volume measurements using 3D ultrasound imaging, *Ultrasound in Medicine & Biology*, **31**(6): 751–762, doi: [10.1016/j.ultrasmedbio.2005.02.011](https://doi.org/10.1016/j.ultrasmedbio.2005.02.011).
18. MARTÍNEZ-GRAULLERA O., MARTÍN C.J., GODOY G., ULLATE L.G. (2010), 2D array design based on Fermat spiral for ultrasound imaging, *Ultrasonics*, **50**(2): 280–289, doi: [10.1016/j.ultras.2009.09.010](https://doi.org/10.1016/j.ultras.2009.09.010).
19. MEHDIZADEH S., AUSTENG A., JOHANSEN T.F., HOLM S. (2012), Minimum variance beamforming applied to ultrasound imaging with a partially shaded aperture, *IEEE Transactions on Ultrasonics, Ferroelectrics, and Frequency Control*, **59**(4): 683–693, doi: [10.1109/TUFFC.2012.2246](https://doi.org/10.1109/TUFFC.2012.2246).
20. MONTALDO G., TANTER M., BERCOFF J., BENECH N., FINK M. (2009), Coherent plane-wave compounding for very high frame rate ultrasonography and transient elastography, *IEEE Transactions on Ultrasonics, Ferroelectrics, and Frequency Control*, **56**(3): 489–506, doi: [10.1109/TUFFC.2009.1067](https://doi.org/10.1109/TUFFC.2009.1067).
21. NIKOLOV S.I., JENSEN J.A., TOMOV B.G. (2008), Fast parametric beamformer for synthetic aperture imaging, *IEEE Transactions on Ultrasonics, Ferroelectrics, and Frequency Control*, **55**(8): 1755–1767, doi: [10.1109/TUFFC.2008.860](https://doi.org/10.1109/TUFFC.2008.860).
22. PADILLA F. *et al.* (2013), Breast mass characterization using 3-dimensional automated ultrasound as an adjunct to digital breast tomosynthesis: a pilot study, *Journal of Ultrasound in Medicine*, **32**(1): 93–104, doi: [10.7863/jum.2013.32.1.93](https://doi.org/10.7863/jum.2013.32.1.93).
23. RAMALLI A., BONI E., ROUX E., LIEBGOTT H., TORTOLI P. (2022), Design, implementation, and medical applications of 2-D ultrasound sparse arrays, *IEEE Transactions on Ultrasonics, Ferroelectrics, and Frequency Control*, **69**(10): 2739–2755, doi: [10.1109/TUFFC.2022.3162419](https://doi.org/10.1109/TUFFC.2022.3162419).
24. SAVORD B., SOLOMON R. (2003), Fully sampled matrix transducer for real time 3D ultrasonic imaging, [in:] *IEEE Symposium on Ultrasonics*, pp. 945–953, doi: [10.1109/ULTSYM.2003.1293556](https://doi.org/10.1109/ULTSYM.2003.1293556).
25. SKJELVAREID M.H. (2012), Synthetic aperture ultrasound imaging with application to interior pipe inspection, Ph.D. Thesis, pp. 76–77, University of Tromsø, Norway.
26. SKJELVAREID M.H., OLOFSSON T., BIRKELUND Y., LARSEN Y. (2011), Synthetic aperture focusing of ultrasonic data from multilayered media using an omega-K algorithm, *IEEE Transactions on Ultrasonics, Ferroelectrics, and Frequency Control*, **58**(5): 1037–1048, doi: [10.1109/TUFFC.2011.1904](https://doi.org/10.1109/TUFFC.2011.1904).
27. SZABO T.L. (2004), Imaging systems and application, [in:] *Biomedical Engineering, Diagnostic Ultrasound Imaging*, pp. 297–336, Academic Press, doi: [10.1016/B978-012680145-3/50011-6](https://doi.org/10.1016/B978-012680145-3/50011-6).
28. TASINKEVYCH Y. (2017), 3D ultrasonography in real time: Image reconstruction methods, [in:] *Advances in*

- Medicine and Biology*, pp. 87–122, Nova Science Publishers, Inc., New York.
29. TASINKEVYCH Y., KLIMONDA Z., LEWANDOWSKI M., NOWICKI A., LEWIN P.A. (2013), Modified multi-element synthetic transmit aperture method for ultrasound imaging: A tissue phantom study, *Ultrasonics*, **53**(2): 570–579, doi: [10.1016/j.ultras.2012.10.001](https://doi.org/10.1016/j.ultras.2012.10.001).
 30. TASINKEVYCH Y., TROTS I., NOWICKI A., LEWANDOWSKI M. (2012), Optimization of the Multi-element Synthetic Transmit Aperture Method for Medical Ultrasound Imaging Applications, *Archives of Acoustics*, **37**(1): 47–55, doi: [10.2478/v10168-012-0007-6](https://doi.org/10.2478/v10168-012-0007-6).
 31. THOMENIUS K.E. (1996), Evolution of ultrasound beamformers, [in:] *Proceeding of IEEE Ultrasonics Symposium*, pp. 1615–1622, doi: [10.1109/ULTSYM.1996.584398](https://doi.org/10.1109/ULTSYM.1996.584398).
 32. TROTS I., NOWICKI A., LEWANDOWSKI M. (2009), Synthetic transmit aperture in ultrasound imaging, *Archives of Acoustics*, **34**(4): 685–695.
 33. ULLATE L.G., GODOY G., MARTINEZ O., SANCHEZ T. (2006), Beam steering with segmented annular arrays, *IEEE Transactions on Ultrasonics, Ferroelectrics, and Frequency Control*, **53**(10): 1944–1954, doi: [10.1109/TUFFC.2006.127](https://doi.org/10.1109/TUFFC.2006.127).
 34. WANG Y., STEPHENS D.N., O'DONNELL M. (2002), Optimizing the beam pattern of a forward-viewing ring-annular ultrasound array for intravascular imaging, *IEEE Transactions on Ultrasonics, Ferroelectrics, and Frequency Control*, **49**(12): 1652–1664, doi: [10.1109/TUFFC.2002.1159845](https://doi.org/10.1109/TUFFC.2002.1159845).
 35. YANG M., SAMPSON R., WENISCH T.F., CHAKRABARTI C. (2013), Separable beamforming for 3-D synthetic aperture ultrasound imaging, [in:] *Proceedings of SiPS 2013*, pp. 207–212, doi: [10.1109/SiPS.2013.6674506](https://doi.org/10.1109/SiPS.2013.6674506).
 36. YOON H., SONG T.K. (2019), Sparse rectangular and spiral array designs for 3D medical ultrasound imaging, *Sensors (Basel)*, **20**(1): 173, doi: [10.3390/s20010173](https://doi.org/10.3390/s20010173).

Research Paper

A Proposal Concerning Assessment of Alternative Cityscape Designs with Audiovisual Comfort and Health of Inhabitants

Agnieszka OZGA*, Jacek WIERZBICKI, Dominik MLECZKO

*Faculty of Mechanical Engineering and Robotics
Department of Mechanics and Vibroacoustics
AGH University of Krakow
Kraków, Poland*

*Corresponding Author e-mail: aozga@agh.edu.pl

(received December 10, 2022; accepted June 18, 2023)

The research concerning the future of sound in towns and cities is focused on two main issues: studies are conducted separately on the comfort, i.e., assessment of visual scenery and sound levels in a cityscape and separately, on the health protection issues. The policy of the acoustic environment control with regard to the health of its inhabitants is traditionally connected with measurements of noise levels presented with the help of the coefficients L_{den} and L_{night} noise indicators, while the models based on tranquillity rating (TR) with the help of the coefficients L_{Amax} , L_{Amin} , L_{Aeq} , L_{A10} . None of these coefficients refers to the soundscape. In this paper, we present a justification of the necessity to enter into discussion on the need to combine these research areas. The authorities managing towns and cities of the future should be provided with tools enabling them to assess modernisation projects from the point of view of both health and comfort of inhabitants. We present our ideas treating them as an invitation to a scientific discourse, in the form of analysis of actual projects concerning modification of existing cityscapes. The modifications are aimed at returning some unfavourably developed spaces to the inhabitants. When analysing the changes proposed in the projects, we take into account two models of the revitalised area quality assessment. The first model is used to assess the effect of noise on health. The second model, based on the indicator known as the TR, serves simultaneous assessment of an area from both visual and acoustical aspects. The models used contemporarily by scientists show multiple flaws, therefore, for the TR indicator we propose a modification taking the sound structure into account. The modification embodies the idea of masking unpleasant sounds with friendly ones. The changes to the model are presented, in this paper, in the context of two projects which were worked out in the framework of 12th edition of the intercollegiate workshop cycle The New Cityscapes. In the course of each workshop of the cycle, we combined art, science, and technology in order to seek solutions creating a better future. In view of the importance of this issue and the need to introduce a certain level of universalism, the authors offer an invitation to join a discussion on the future of sound in urban agglomerations.

Keywords: noise maps; tranquillity rating; enclaves of silence; alternative urban spaces; sound masking.



Copyright © 2023 The Author(s).
This work is licensed under the Creative Commons Attribution 4.0 International CC BY 4.0
(<https://creativecommons.org/licenses/by/4.0/>).

1. Introduction

Along with development of urban agglomerations, the effect of noise on health of residents becomes more and more noticeable. According to World Health Organization [WHO] (2018) document one European out of five is regularly exposed at night to sound levels posing a significant risk to health. For many years now, initiatives have been undertaken to enforce noise reduction through legislation. An example of such a legislative

initiative is Directive 2002/49/EC (Commission of the European Communities, 2002) in which main sources of noise were identified (road, railway, and air transport, industry), regular measurements of related noise levels were made obligatory together with the requirement to draw up noise maps and noise action plans for agglomerations with more than 100 000 inhabitants. The aforementioned WHO document contains a systematised survey of proofs evidencing relationship between exposure to noise, both in the daytime and at

night-time, and risk of adverse health effects in humans.

The mentioned documents are focused mainly on the issue of noise levels. In many cases, however, in view of necessary financial outlays (construction of screens, replacement of windows, road surface refurbishment) or time-scale (conversion to electric drive in vehicles), achieving required results is impracticable. It is, however, still possible, especially in cases of minor exceedances of the recommended levels, to reduce the discomfort of living in urban environments by modification of nature and contents of sounds (by sound masking) and provision of quiet places available, for instance, within public transport routes (bus/tram stops). Such activities exceed the scope of the acoustics alone and become an inherent part of interdisciplinary urban studies (KANG, 2006; RAIMBAULT, DUBOIS, 2005; CHOJNACKI *et al.*, 2018). This approach to the science, characterised by seeking universalism, represents an attempt to define the presence of a human both in a cityscape and in a specific location (OZGA, 2017), where the research work is joined by sociologists (BUKOWSKI *et al.*, 2018; GIDDENS, 1987), architects (KAPECKI, 2020), artists (GIBAŁA-KAPECKA, KAPECKI, 2014; 2016; KOOLHAS, MAU, 1998), acousticians (KUKULSKI *et al.*, 2018), and geographers (MURZYN-KUPISZ, DZIAŁEK, 2017; REDAELLI, 2019). This paper presents the point of view of acousticians hammered out after discussions held with artists, architects, and sociologists on the occasion of intercollegiate workshop Alternative Cityscapes which was held in Cracow in 2018 (GIBAŁA-KAPECKA *et al.*, 2019). Discussions with representatives of other disciplines of science have indicated clearly that the research concerning the future of sound in the cityscape was carried out in two different directions: separately on comfort of living among local residents and separately on health protection issues.

This paper presents two models allowing to assess urban space modernisation projects worked out in the course of the mentioned 2018' workshop. In the first model, sound levels only are taken into account (and therefore it concerns only the health of people present in the area of interest), while the second model is an extension of the first one with the sound structure analysis (and thus concerns the comfort of residents). The work on cityscape acoustic assessment models and cooperation of various disciplines of science was initiated in order to create cityscapes in which the visual scenery and the audio landscape scenery (soundscape) are fully adequate. On the acoustic side of the problem, we combine the two trends in research on the acoustics of urban agglomerations to make achieving the set goals more realistic.

The analysis carried out in the scope of the health protection issue was performed with the use of SoundPLAN software implementing unified measurement

and calculation methods known as CNOSSOS-EU (European Commission, 2012), the application of which became mandatory to all European Union Member States from January 1, 2019. The method includes algorithms used for predicting levels of road, railway, and air transport noise as well as the industry-generated sounds. In the present paper, the method is used to determine changes that would occur in the soundscape after implementing solutions proposed in cityscape modification projects. The second model defines the cityscape in terms of architecture, nature-related elements integrated into the architecture, and the soundscape. The model is a proposal concerning assessment of urban space designs based on the analysis of the visual scenery and the soundscape by means of the quantity known as the tranquillity rating (RT).

We are aware of difficulties involved in comparison of results obtained with the use of the above-presented models (based on L_{den} , L_{Aeq}) but we still hope that this paper will draw attention to the necessity to take into account not only the health but also the comfort of life in towns and cities and the need to work out new methods of assessing the latter.

2. Methods used to achieve acoustically alternative cityscapes

2.1. Health – protecting cityscape users from noise

Problems in contemporary urban agglomerations are growing much faster than our ability to solve them. Air pollution, ubiquitous noise, and climate warming require a change in our thinking about the cities and towns of the future. In our case, new ideas were first formulated in connection with a workshop named The New Cityscape. This intercollegiate event, combining art, science, and technology, was carried out from 26 to 29 November, 2018 in Cracow as the 12th subsequent edition of the workshop cycle known as Alternative Public Spaces. The challenge posed to the participants was to develop a proposal to modify a piece of urban space without taking into account the constraints of current legislations or economics. Students from four universities in Cracow were involved in the projects: Academy of Fine Arts (Faculty of Interior Design); Cracow University of Technology (Faculty of Architecture); Jagiellonian University (Institute of Sociology); and AGH University of Krakow (Faculty of Mechanical Engineering and Robotics, Field of Acoustic Engineering). The students were offered support from their lecturers and tutors as well as doctoral students and representatives of the Urban Greenery Management in Cracow.

In the urban area dealt with in the workshop framework, the main noise source is the sound generated by road traffic. There are also a tram route and a railway line running along the street; however, the noise

generated by them is definitely lower than the motor vehicle traffic. Additionally, the space is characterised by small share of green areas and very dense building development. Between buildings and the roadway, a footpath and tram routes are situated. The overall picture is typical of many cityscapes worldwide where people live and function.

The acceptable levels of noise in the environment, as applied in the long-term policy regarding protection from noise and while drawing acoustic maps, are determined by yearly indicators L_{den} and L_{night} . WHO recommends (2018) reducing noise levels produced by road traffic below 53 dB L_{den} , because noise above this level is associated with adverse health effects including ischemic heart disease (IHD), high annoyance (HA). For night noise exposure they recommend reducing the noise below 45 dB L_{night} , as night-time road traffic noise above this level is associated with adverse effects on sleep including high sleep disturbance (HSD). Below these levels, none of the listed negative effects will occur. However, the values set by the WHO are only recommendations, but in the case of road traffic noise they are strong recommendations, that according to WHO can be adopted as policy in most situations. Regardless, each European country has its own policies to control noise, including road traffic noise. This also involves self-determination of permissible environmental noise levels, which in each European country are higher than those recommended by the WHO. In Poland, since 2012 the acceptable noise levels have been determined by the Regulation of the Minister of Environment (2014). It has turned out, however, that the levels for “A” spa resorts and hospital areas beyond towns are the only ones that satisfy the WHO criteria. The acceptable noise level is higher in all the remaining areas referred to in the Regulation. In the case of the land considered in this work, the areas situated to the west of the Zakopianka motorway are subject to acoustic protection (as residential quarters), and the norms are respectively 68 dB (L_{den}) and 59 dB (L_{night}). The area east of the motorway is the home for workshops and stores for which no noise limits have been specified.

In the area of interest, measurements of noise levels were taken together with records concerning traffic intensity and structure. The obtained results were then used to develop and verify a calculation model in SoundPLAN 8.2 software environment. The model used to calculate noise levels in road traffic implemented in the software performs calculations according to the CNOSSOS-EU methodology.

Results of calculation for the current state are presented in Figs. 1 and 2.

Measurements taken in the current state indicate that thresholds recommended by WHO are exceeded both in the daytime and at night-time. The objective set for each of the projects developed in the workshop

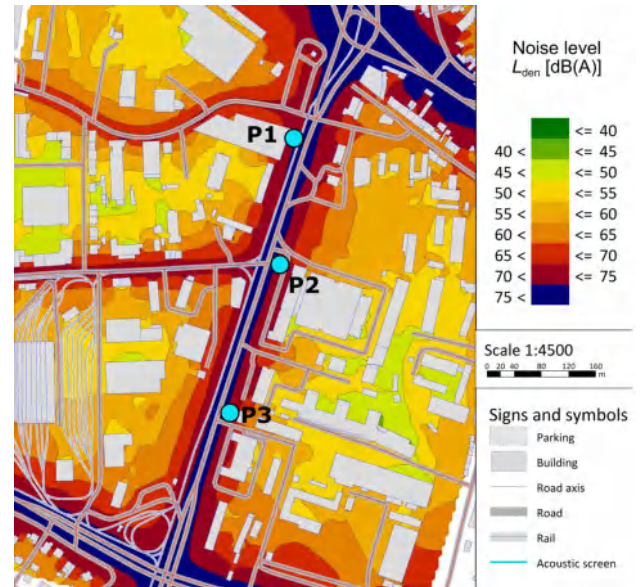


Fig. 1. Day-evening-night noise level (L_{den}) for the current state, calculated in the SoundPLAN 8.2 software.

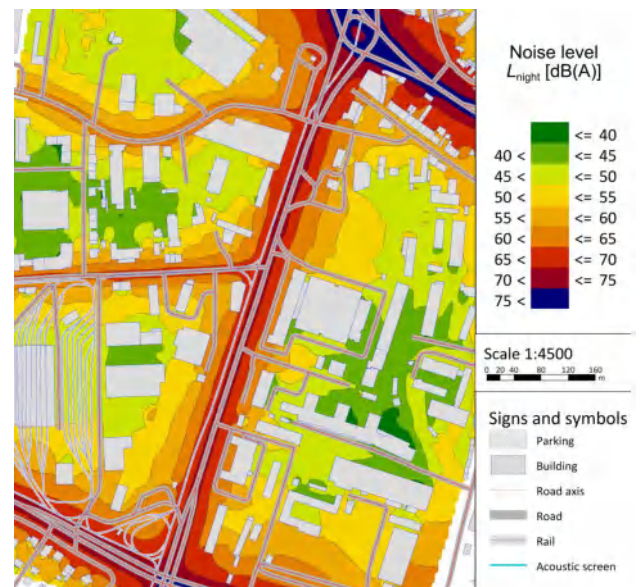


Fig. 2. Night noise level (L_{night}) for the current state, calculated in the SoundPLAN 8.2 software.

entitled Alternative Cityscapes was to reduce traffic noise along the examined road section down to the level L_{den} recommended by WHO. Several project teams decided to transfer the mainstream traffic to an underground tunnel – that was the first of innovative changes necessary to return the area to the residents. Results of sound level calculations indicate that with:

- reduction of the traffic on the road segment under consideration to 20 vehicles per hour guaranteeing the inhabitants the access to their property or apartments;
- reducing the permitted speed to 30 km/h;
- introduction of quiet means of public transport;

one obtains reduction of L_{den} down to the value of 55–62 dB and L_{night} to 50–55 dB (Figs. 3 and 4 – the day-evening-night noise level and the night noise level, respectively).

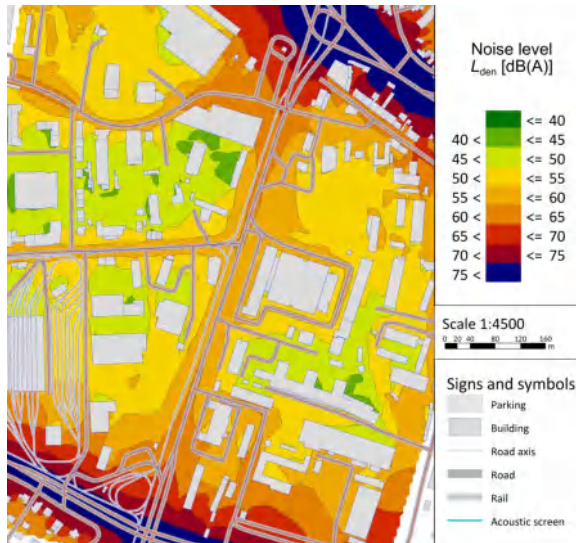


Fig. 3. Day-evening-night noise level (L_{den}) after traffic volume reduction to 20 passenger cars per hour, calculated in the SoundPLAN 8.2 software.

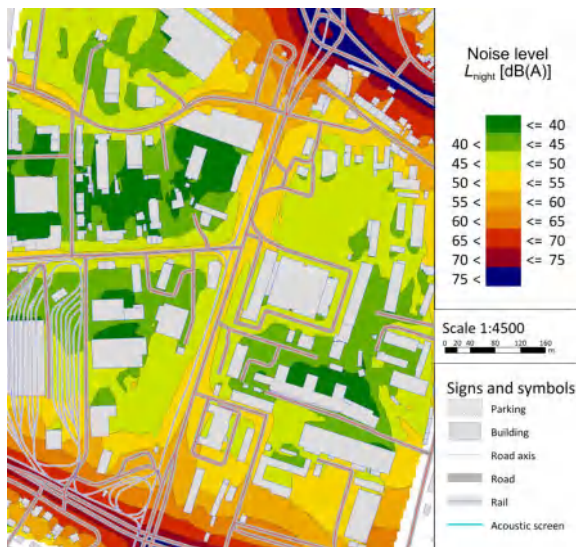


Fig. 4. Night noise level (L_{night}) after traffic volume reduction to 20 passenger cars per hour, calculated in the SoundPLAN 8.2 software.

Without using acoustic models of the space under consideration we would hardly know that the deployed measures were insufficient to solve the problem. To make such drastic limitations in vehicle traffic credible and possibly able to bring notable benefits in the form of noise level reduction over the whole street segment under consideration, it was necessary to introduce the means of acoustic protection aimed at reduction of the possibility of penetration of noise from neighbouring arterial traffic routes on which no such restrictions

will be introduced in the examined area. Therefore, 5-metres-high acoustic screens were provided in the project. Such a solution results in noise level reduction, especially in the direct vicinity of the screens. It should be indicated that the proposed acoustic screens are not situated directly in the area under consideration, but at its borders, in order to block the noise from reaching the main city roads. Moreover, the design includes the “green wall” type of screen, which is to be covered by climbing plants, thus becoming a biologically active element that will not decrease the aesthetic values of the surroundings. The results of noise level calculations are presented in Figs. 5 and 6, for the day-evening-night level and the night level, respectively.

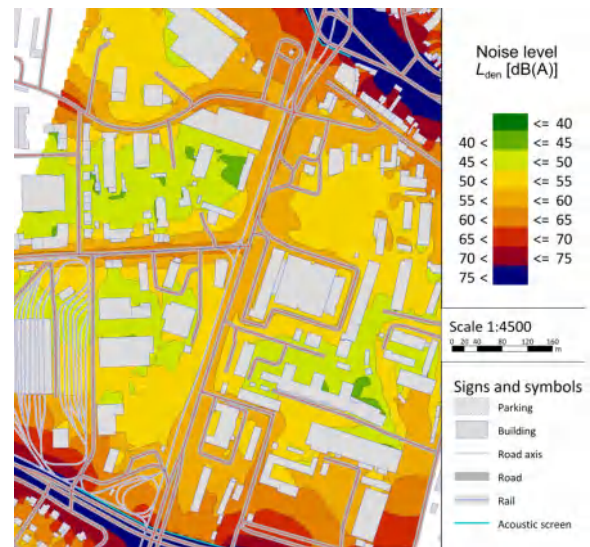


Fig. 5. Day-evening-night noise level (L_{den}) after traffic volume reduction to 20 passenger cars per hour and installing acoustic screens, calculated in the SoundPLAN 8.2 software.

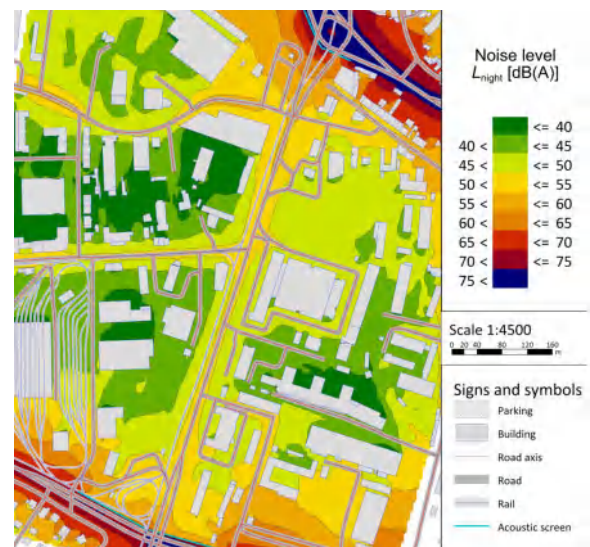


Fig. 6. Night noise level (L_{night}) after traffic volume reduction to 20 passenger cars per hour and installing acoustic screens, calculated in the SoundPLAN 8.2 software.

For the purpose of quantitative comparison of the effect induced by the introduced changes, sound level calculations were carried out for measurement points P1, P2, and P3. The situation of the points is shown in Fig. 1 and calculation results in Tables 1 and 2.

Table 1. Calculation results for the day-evening-night noise level (L_{den}).

| | Current state [dB] | Traffic volume reduction [dB] | Traffic volume reduction + acoustic screen [dB] |
|---------|--------------------|-------------------------------|---|
| Point 1 | 73.5 | 61.6 | 58.7 |
| Point 2 | 74.2 | 58.0 | 57.5 |
| Point 3 | 72.5 | 56.7 | 54.6 |

Table 2. Calculation results for the night noise level (L_{night}).

| | Current state [dB] | Traffic volume reduction [dB] | Traffic volume reduction + acoustic screen [dB] |
|---------|--------------------|-------------------------------|---|
| Point 1 | 66.8 | 54.7 | 51.8 |
| Point 2 | 67.5 | 51.2 | 50.6 |
| Point 3 | 65.8 | 50.0 | 47.9 |

The existing models for predicting noise levels in an environment may be used to determine changes which must be implemented in towns and cities to protect their inhabitants from harmful effects of noise. On the other hand, proper development of a cityscape aimed at “giving it back” to local residents involves further introduction of some changes in the visual sphere which can also be verified with the use of mathematical models. These noise reduction methods are applied in the so-called Action Plan when cities are modernised as a result of an analysis of noise maps.

2.2. Comfort – an application of the tranquillity rating to assessment of urban space modernisation projects

Studies carried out in various research centres show interdependence between tranquil urban areas and stress reduction (ULRICH *et al.*, 1991; TAKANO *et al.*, 2002). These works are focused only on the assessment of sound stimuli or the impact of visual and audial stimuli on a given space (PREIS *et al.*, 2015; NILSSON *et al.*, 2007). Several attempts have been made to describe the interdependence between the assessment of acoustic and visual quality of a space with the help of mathematical models. However, in the aspect of the evaluation of city space modernization projects, tranquillity rating seems the most promising tool to be used.

Assessment of usefulness of the area determined with the use of the tranquillity rating is defined by means of the equation:

$$TR = X \pm \alpha \cdot A_1 \pm \beta \cdot A_2 \pm \dots \pm \omega \cdot A_n, \quad (1)$$

where X is a constant which, like other quantities appearing in the formula, is determined based on psychoacoustic tests. To determine the actual form of the function, the regression analysis is used. A_1, A_2, \dots, A_n represent sociologically conditioned elements shaping the perception of tranquillity, whereas $\alpha, \beta, \dots, \omega$ are weights characterising the effect of each of the above elements.

The tranquillity rating may comprise a number of indicators, whereas positively perceived visual and sound elements increase, and negative ones decrease the parameter value.

A number of models for TR are discussed in the literature of the subject.

The tranquillity rating prediction tool (TRAPT) provides that the formula for TR value may take a number of forms determined with the use of the regression analysis, two of which are (PHEASANT *et al.*, 2009):

$$TR = 13.93 - 0.165 [L_{Amax}] + 0.024 NCF, \quad (2)$$

$$TR = 8.57 - 0.11 [L_{Aeq}] + 0.036 NCF, \quad (3)$$

where L_{Amax} is the maximum sound pressure level and L_{Aeq} is the equivalent continuous sound pressure level expressed in dB. The square brackets denote the numerical value of a given quantity, so for, e.g., $L_{Amax} = 50$ dB, $[L_{Amax}] = 50$. The quantity NCF (natural and contextual features) ranges from 0 to 100 and corresponds with the share p (expressed in percent) of natural features, i.e., flora, water, etc., in the environment, so $NCF = [p]$.

In each of the quoted forms, the TR can assume values from the minimum equalling 0 to the maximum of 10. If $TR > 10$ or $TR < 0$, its values of 10 and 0 are adopted, respectively. Assessment of the examined area is verbalised according to the scale: below 5 – unacceptable; [5, 6) – just acceptable; [6, 7) – fairly good; [7, 8) – good; 8 and above – excellent. The Eq. (3) was proposed for both urban and rural areas, which was a fundamental impediment to application of the model for the purposes of assessment of typically urban space modernisation projects. That gave rise to further research (WATTS, 2017; WATTS, MARAFA, 2017) as a result of which a new model was developed expressed by means of the equation:

$$TR = 10.55 - 0.146 [L_{Aeq}] + 0.041 NCF + MF, \quad (4)$$

where MF is a moderating factor offering the option of taking into account various factors having either positive or negative effect on perception of the space in question. Its effect is estimated to be ± 1 scale points. The approach in which researchers break down MF into factors characteristic for the location of interest and specific for users of the space in question, cannot be generalised to cover other spots. The research is of local nature. Additionally, impressions of subjects taking part in the research depend on such factors as

gender, age, or physical and mental state, therefore any change of one variable in the regression analysis (PHEASANT *et al.*, 2009) is explained by means of changes in the second variable at the determination level of $R^2 = 0.59$ (in the audio experimental conditions) and $R^2 = 0.5$ (for purely visual stimuli). Any psychoacoustic assessment obtained on the grounds of laboratory tests instead of on-site examination is also biased with a certain error resulting at least from the fact that the subjects are immersed in an environment illuminated with artificial lighting (and not the natural light). The sound reaching a user of a specific city spot and the view of the location make up a multi-dimensional spatial and sound scenery. In a laboratory, the perception is in a way reduced to two dimensions regardless of whether the subjects are presented a video or still photos of the location in question.

From the first portion of this paper we have learned that the sound level would fluctuate around 50 dB which means that for the model (3), the obtained TR value will be unacceptable, whereas for the model (4), it will be acceptable at 50% NCF. The research concerning the model (4) improves the presented situation significantly by reflecting perception of cityscapes more accurately, although it is far from solving all the involved problems. In urban conditions, it is difficult to obtain TR values better than the acceptable ones ($TR < 7$), which seems to be in contradiction with the reality. If a zone comfortable for people was characterised with TR values above 7, then according to the model (4), it would be necessary to introduce at least 92% of natural elements and nature-harmonised architectural features into the scene. In case of city modernisation projects taking into account the masking of unfriendly soundscape with sounds which can be considered friendly or neutral by the users of the space in question, none of the above-discussed models seems to be applicable. That is why in the next section, we propose a change to the TR model.

3. Modification of the tranquillity rating carried out for the purpose of assessing urban space modernisation projects

Cooperation with artists, sociologists, and architects in the framework of intercollegiate workshops has made us aware that there was a lack of tools for objective assessment of urban space modernisation projects. The problems have been identified:

- 1) Health (L_{den} and L_{night}) and tranquillity (PHEASANT *et al.*, 2008), as well as comfort or wildness, are described with the use of different acoustic indicators. The health is defined in terms of L_{den} , whereas the tranquillity is determined based on L_{Amax} , L_{Amin} , L_{Aeq} , and L_{A10} . In a method developed in England (KEPHALOPOULOS, PAVIOTTI, 2008; DEFRA, 2006) and used to determine the

road traffic noise, formulae for converting individual indicators into other ones obtained by estimation result in differences of the order of 2%, which gives an insignificant change for sound levels in the range 50–55 dB compared to the uncertainty taken into account when predicting sound levels in SoundPLAN software environment.

- 2) In case of modernising a cityscape, it is equally important what the appearance of the space in question is both in daytime and at night-time and what the related soundscape is at each time of the day.
- 3) The following can be noted about the TR in the currently used form:
 - the TR concerns perception of a space on a sunny day and only during the daytime;
 - the coefficients estimated in the course of the regression analysis suggest that any zone comfortable for people characterised with values of TR indicator above 7 is very difficult to obtain in city conditions, which seems to contradict the reality. Additionally, in the available literature, only point estimators of the regression line are used, suggesting that interval estimation analysis of the indicators is of no significance whatsoever. Such an approach to the topic seems to be erroneous;
 - the basic model is hardly universal – it applies to specific locations only and additionally, the coefficient of determination shows significant dispersion in reception of a given space by individual volunteers;
 - the model is designed for application to both urban and rural areas and is likely to upset perception of urban spaces in which the users seek tranquillity rather than silence which exists in the nature;
 - the structure of sound is not taken into account, so it is impossible to extend the research towards the use of sound masking.

We invite other scientific centres to join the work on putting forward and solving individual problems. Years of intensive work and discussion are still before us. In this article, we start with putting forward a proposal of changing the TR model through taking the structure of sound into account. We search for a solution universal enough to be suitable for application in different cultural environments on different continents.

3.1. Theory of complexity for the analysis of acoustic quality

Studies on soundscape indicate a far less dominating role of physical parameters of sound and a much more significant role of individuals and their perception (BROWN, 2010). It is not only the ability to identify sources of sounds that is important, but also the

proportion of time when the sound is perceptible. Designing of a coefficient model univocally describing the soundscape is still an open problem. We suggest that this model should include the SCF indicator (proposed by authors, first time introduced in this work, short for sound and contextual features) that represents a friendly soundscape taking into account the role of human perception included in the theory of complexity for the analysis of acoustic quality.

Now, let us refer to the theory of complexity for the analysis of acoustic quality (IPSEN, 2002; ELMQVIST, PONTÉN, 2013) based on differentiation of the soundscape. There is a relationship between the perception quality and complexity of the perceived sound. The interest in the soundscape decreases for a low level of sound complexity. The same occurs when complexity of a soundscape is very high as in such a case legibility of each sonic component making out the soundscape deteriorates. Low and high sound levels of complexity have never been clearly defined by the authors of the theory. As the authors of this paper understand it, a low sound level of complexity is a single acoustic event. The opposite of this phenomenon is the high level of complexity, that is, multiple events occurring frequently.

We propose that sound complexity is described using a second-order polynomial obtained by interpolation. Zeros of the function are assumed to fall at 30 and 70 dB. Bearing in mind that a normal conversation of two people corresponds to sounds with the level of 55–60 dB and thus not always contributes to friendly soundscape for other users of the same space, the maximum value of the function was assumed to be 50 dB. Masking the sounds with levels below 30 or exceeding 70 dB is pointless; the lower-limit values are possible to register only in parks late at night (WICIAK *et al.*, 2015), whereas upper limit levels are perceived as dis-

turbing in the context of seeking tranquillity, regardless of the sound structure:

$$\text{TR} = 10.55 - 0.146 [L_{\text{Aeq}} - L^*] + 0.041 \text{NCF}, \quad (5)$$

where L^* is the quantity corresponding to the theory of complexity for the analysis of acoustic quality expressed in the form of a second-degree polynomial and assumes values from 0 to 1.08 dB,

$$L^* = \text{SCF}(-0.000186 [L_{\text{Aeq}}]^2 + 0.018571 [L_{\text{Aeq}}] - 0.39) \text{ dB}, \quad (6)$$

where SCF is the indicator assuming values from the range (0, 100) corresponding to the percentage share of friendly sounds in the soundscape.

Referring to the theory of complexity for the analysis of acoustic quality we assume that for 30 dB the complexity of sounds in the soundscape is probably minor, and therefore the soundscape is dull. When the soundscape includes friendly sound sources (actual or disguising sounds of nature, like the sound of running or falling water), the complexity increasing the attraction of the soundscape will increase, reaching the maximum at 50 dB. At higher levels of noise, the attractiveness of the soundscape will slowly decrease. Taking into account that the soundscape might include unfriendly or neutral sound sources (a tram passing by or cyclists riding), the equation includes SCF index describing the proportion of friendly sounds in the soundscape. Since the model has been adjusted to urban space modification projects, SCF index is determined on the basis of a prognosis.

As for the proposed changes, the effect of friendly soundscape equalling approximately ± 1 scale point (Fig. 7) was assumed, which corresponds to the factor MF (4). In our model, the factor has been integrated

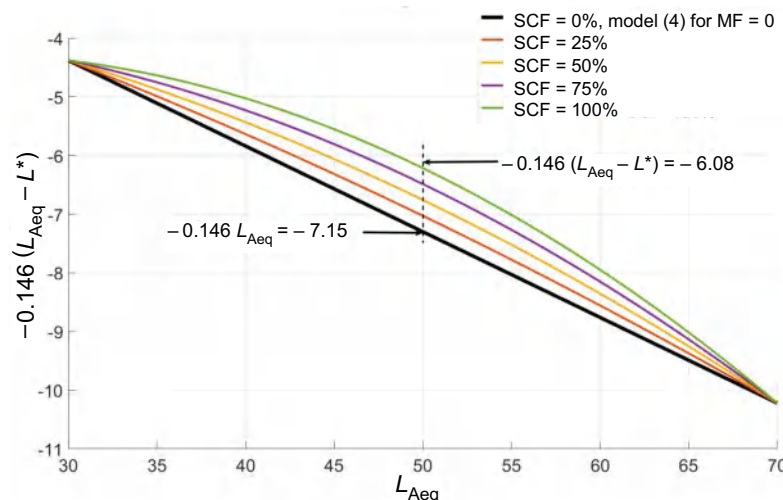


Fig. 7. Modification of tranquility rating proposed specifically for the purpose of assessment of cityscape modernisation projects. Equation (6), calculated with interpolation for the 100% favourable soundscape, between 45 and 55 dB does not increase the TR by more than 1 point, which is in accordance with the studies presented with the help of the model (4).

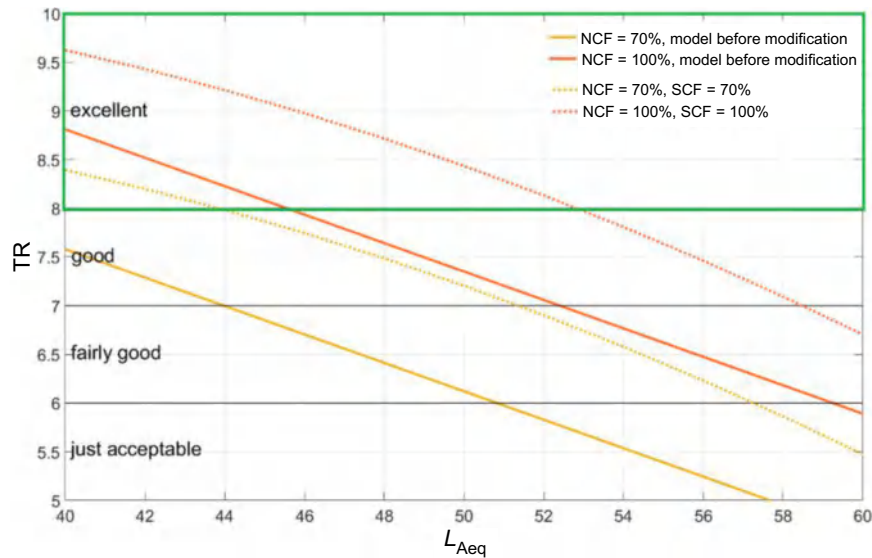


Fig. 8. TR before and after modification taking into account the sound structure and the theory of complexity for the analysis of acoustic quality.

into L_{Aeq} . The proposed change introduces some universalism to the model – there is no need to carry out any research on the issue which sounds and in what way contribute to increase of TR in a given location. This depends on the community members who use the space in question. We rely on a model assessing the comfort only provisionally, until new models based on the indicator L_{den} are developed taking into account the analysis of both point and interval estimators with a significantly higher coefficient of determination. At the moment, we would like to reliably assess the projects developed in the course of intercollegiate workshops. The proposed modification pertains only to city modernisation projects and does not affect conclusions drawn from the research carried out in other scientific centres.

By introducing the factor following from the acoustic theory of complexity for the analysis of acoustic quality (6), we have reproduced the perception of a cityscape more realistically – the concept of a comfort zone

now includes also provision of sound levels in the range of 55–58 dB which are normally observed in an office space or a coffee shop (Fig. 8) and which have no negative impact on human health.

3.2. Projects developed in the course of the workshop and their assessment with the use of the modified model

In the following, two projects out of the total number of nine which were worked out in the course of the Alternative Public Spaces workshop are presented and assessed. They are projects of modernization of the space presented in Sec. 2. The selected projects are those within the framework of which their authors predicted values of the indicators SCF and NCF. In the first project named the *Alsos Avenue* (where *Alsos* is a Greek word meaning *Grove*), bicycle lanes and pedestrian pavements were designed along the whole section of its route through the area (Fig. 9). Between



Fig. 9. The Alsos Avenue project. Authors: Karolina Motak, Paulina Habura, Marta Bil, Sanara Słojewska, Julia Idczak, Karol Piotrowski. Original pictures of the designs are accessible in (OZGA *et al.*, 2019).

these bicycle and pedestrian paths, green areas are planned to be created and – as a reference to the history of the location and the *Mateczny Spa* – construction of a ditch is being designed to form a channel for the creek. A ribbon-shaped metal structure filled up with a membrane was integrated into the cityscape. The function of the ribbon feature included the roofing of shelters, public transport stops or rest spots. An additional benefit of the ribbon was the possibility of using it as a mounting frame for sound shower type loudspeakers which enabled introduction of masking sounds to the soundscape. By assumption, the whole area was meant as a space encouraging inhabitants to arrange meetings in the open air and having a beneficial effect on physical and mental state of the people present. The NCF value predicted for the space is 70%, SCF is also forecasted to be on the level of 70%.

In the case of designs, it is impossible to calculate NCF – the percentage value of each natural element of the landscape in accordance with the rules given in (PHEASANT *et al.*, 2010). The authors of the project are obliged to create a space that is 70% biologically active, and on this basis NCF is accepted. It is far more difficult to forecast the SCF coefficient for the space in which quiet trams and car passage to the owner's property at the speed limit of 30 kmph have been allowed. Parking spaces for properties at Alsos Avenue were designed beyond the discussed area, pedestrian and bicycle lanes are lined up with specially designed pavements. A tram passage at the rush hour is forecasted at every ten minutes. The soundscape in such a space is like patchwork – filled with humans talking, sounds of water flowing in a stream and sounds of nature – which are either actual or meant to disguise something else. It cannot be precisely calculated since in spite of a finite number of sound sources that are forecasted, the number of combinations of acoustic events and their duration is infinite. The risk analysis shows that the most difficult situation will occur when the inhabitants commute to and from work. For these rush hours, the acoustic restrictions presented above allow a forecast of no less than 70% level. Most fre-

quently, a person staying at Alsos Avenue will hear the sounds of nature, water and conversations. The duration of unfriendly events will be short, like the passage of a quiet tram, departures or arrivals of individual cars at distant parking sites.

The function assumed for the second project named Zakopane Road Spa (Zakopianka Zdrój, Fig. 10) was the promotion of health. The project assumed creation of enclaves of silence. Revitalisation of the public space was aimed at reconstruction of identity of the existing location called Mateczny Roundabout, a site with some spa traditions. In 1898, drillings carried out by a town councillor Antoni Mateczny led to discovery of a source of sulphur mineral water with unusual healthful properties. The layout ended near the Shrine of the Divine Mercy, a religious cult centre, where water symbolises revival and exculpation. The curative water will be offered for tasting and purchase in the quiet areas. The NCF predicted for this space is 100%, with SCF also forecasted to be at the level of 100%. In the case of Zakopane Road Spa, space management and sound are 100% connected with water, which, according to the propagator of the concept of soundscape (SCHAFER, 1993) is the most beneficial of the attainable environments.

According to the model (4), for sound levels in the range 48–52 dB, the Alsos Avenue project would be assessed on the “fairly good/just acceptable” level (Fig. 8), whereas the presented solution after application of the proposed modification, was assessed as “good”. This makes assessment of perception of the space in question more realistic. The Zakopane Road Spa project, which was developed to protect health and promote a healthy way of life; without modification of the model, could be assessed as only “good”, whereas its perception and the modified indicator TR result in the assessment on the “excellent” level.

The presented alternative cityscape projects prove that it is possible to establish a reliable assessment system in which the visual scenery and soundscape are fully adequate both in the daytime and at nighttime.



Fig. 10. The Zakopianka Avenue project. Authors: Dominika Kuczera, Kinga Duda, Aleksandra Rogowiec, Janusz Rożdżyński.

4. Summary

The projects created in the framework of Alternative Public Spaces workshops cycle's 2018' edition were supposed to be free from either political or economic barriers which, in many cases, hinder the necessary changes. The students were made aware of the fact that although the information about the environment is perceived, first of all, via the sense of sight, and their projects would be assessed, as a rule, from the visual point of view in the first place, they should nevertheless draw their attention also to other stimuli. The existing strong interdependence between senses by which the environment is perceived (sight, hearing, smell, touch) is defined as the perception ecology.

The presented research results indicate that in many cases, it is virtually impracticable to achieve compliance with the required permissible sound levels in a cityscape. However, it is still possible to change the character of noise (by masking) which may result in an increase of the comfort of life. In view of the aforementioned, a modification of the TR indicator was proposed consisting in making it dependent on both sound nature and level. The proposal should be considered an idea aimed at extending the currently used environment status assessment coefficients rather than an alternative for the presently applied ones.

In view of conclusions from the research carried out by WHO, according to which one European out of five is regularly exposed at night-time to sound levels posing a significant risk to health, it is necessary to make out noise maps and use them for the purpose of noise reduction. In the daytime, on the other hand, despite technical impracticability to lower the sound level in large urban areas, attempts should be made to change the character of the sound and create acoustically alternative cityscapes, the so-called enclaves of silence or quiet areas. It is also necessary to work out methods and indicators for assessing their effect on people – the presently used set of sound-level-based indicators seems to be insufficient.

Acknowledgments

We owe our gratitude to the organisers of the workshop Alternative Public Spaces, who were Professor Beata Gibała-Kapecka and Professor Tomasz Kapecki, for inviting us to join the initiative and encouraging us to look into the related issues.

Furthermore, we direct our thankfulness to Professors Marta Smagacz-Poziemska and Marcjanna Nóżka from the Jagiellonian University, as well as the executives and employees of the Urban Greenery Management in Cracow for their kind cooperation. Our grateful thanks are also extended to students taking active part in the workshops for showing us alternative realities and putting forward their own ideas capable to

improve significantly the town's soundscape and visual values.

The article was financed by a research subsidy of the number: 16.16.130.942.

References

- BROWN A.L. (2010), Soundscapes and environmental noise management, *Noise Control Engineering Journal*, **58**(5): 493–500, doi: 10.3397/1.3484178.
- BUKOWSKI A., NÓŻKA M., SMAGACZ-POZIEMSKA M. (2018), How do parking practices structure urban territorial communities?, *Urban Development Issues*, **59**: 5–16, doi: 10.2478/udi-2018-0024.
- CHOJNACKI B., PIECHOWICZ J., MATYS M., PIOTROWSKI K. (2018), Noise control in urban parks in Cracow, [in:] *Euronoise 2018 – Conference Proceedings*, Greece.
- Commission of the European Communities (2002), *Directive 2002/49/EC of the European Parliament and of the Council relating to the assessment and management of environmental noise*, <https://eur-lex.europa.eu/legal-content/EN/TXT/?uri=celex%3A32002L0049> (access: 16.11.2022).
- DEFRA (2006), *Method for converting the UK road traffic noise index LA10,18h to the EU noise indices for road noise mapping*, Department for Environment Food and Rural Affairs, London, <https://webarchive.nationalarchives.gov.uk/ukgwa/20130822074033/http://www.defra.gov.uk/environment/noise/research/crtn/pdf/noise-crtn-update2006.pdf> (access: 16.11.2022).
- ELMQVIST T., PONTÉN E. (2013), Designing the urban soundscape, *Website The Nature of Cities*, <https://www.thenatureofcities.com/2013/08/25/designing-the-urban-soundscape/> (access: 16.11.2022).
- European Commission (2012), *Common noise assessment methods in Europe* (CNOSSOS-EU), Joint Research Centre, Institute for Health and Consumer Protection, <https://op.europa.eu/en/publication-detail/-/publication/80bca144-bd3a-46fb-8beb-47e16ab603db> (access: 16.11.2022).
- GIBAŁA-KAPECKA B., KAPECKI T., KAMISIŃSKI T. (2019), *On Sound, Acoustics, and Noise in the Cityscape* [in Polish: *O Dźwięku, Akustyce i Hałasie w Przestrzeni Miasta*], Wydawnictwo Akademii Sztuk Pięknych im. Jana Matejki, Kraków.
- GIBAŁA-KAPECKA B., KAPECKI T. (2014), *The New Cityscape 2013*, Wydawnictwo Akademii Sztuk Pięknych im. Jana Matejki, Kraków.
- GIBAŁA-KAPECKA B., KAPECKI T. (2016), The real city-the mental city, [in:] *Back to the Sense of the City: International Monograph Book*, Centre for Land Policy and Valuations.
- GIDDENS A. (1987), *Social Theory and Modern Sociology*, Stanford University Press, Stanford.
- IPSEN D. (2002), The Urban Nightingale – or some theoretical considerations about sound and noise, [in:] *Soundscape Studies and Methods*, pp. 185–197, Finnish Society for Ethnomusicology, Department of Art, Literature and Music, University of Turku.

13. KANG J. (2006), *Urban Sound Environment*, Taylor & Francis, London and New York.
14. KAPECKI T. (2020), Elements of sustainable development in the context of the environmental and financial crisis and the COVID-19 pandemic, *Sustainability*, **12**(15): 6188, doi: [10.3390/su12156188](https://doi.org/10.3390/su12156188).
15. KEPHALOPOULOS S., PAVIOTTI M. (2008), Differences among European noise mapping methods, *The Journal of the Acoustical Society of America*, **123**(5): 3032, doi: [10.1121/1.2932684](https://doi.org/10.1121/1.2932684).
16. KOOLHAS R., MAU B. (1998), *S, M, L, XL*, The Monacelli Press, New York.
17. KUKULSKI B., WSZOŁEK T., MLECZKO D. (2018), The impact of fireworks noise on the acoustic climate in urban areas, *Archives of Acoustics*, **43**(4): 697–705, doi: [10.24425/aoa.2018.125163](https://doi.org/10.24425/aoa.2018.125163).
18. MURZYN-KUPISZ M., DZIAŁEK J. (2017), Theorising artists as actors of urban change, [in:] *The Impact of Artists on Contemporary Urban Development in Europe*, MURZYN-KUPISZ M., DZIAŁEK J. [Eds.], doi: [10.1007/978-3-319-53217-2](https://doi.org/10.1007/978-3-319-53217-2).
19. NILSSON M.E., BOTTELDOOREN D., DE COENSEL B. (2007), Acoustic indicators of soundscape quality and noise annoyance in outdoor urban areas, [in:] *19th International Congress on Acoustics*, Madrid.
20. OZGA A. (2017), Scientific ideas included in the concepts of bioacoustics, acoustic ecology, ecoacoustics, soundscape ecology, and vibroacoustics, *Archives of Acoustics*, **42**(3): 415–421, doi: [10.1515/aoa-2017-0043](https://doi.org/10.1515/aoa-2017-0043).
21. OZGA A. et al. (2019), *Alternative Public Spaces: Mateczny-Borek Fałęcki. The Future of Sound in the City* [in Polish: *Alternatywne Przestrzenie Publiczne: Mateczny-Borek Fałęcki. Przyszłość Dźwięku w Mieście*], Wydawnictwo Akademii Sztuk Pięknych im. Jana Matejki, Kraków.
22. PHEASANT R.J., HOROSHENKOV K.V., WATTS G.R. (2010), Tranquillity rating prediction tool (TRAPT), *Acoustics Bulletin*, **35**(6): 18–24.
23. PHEASANT R., HOROSHENKOV K., WATTS G., BARRETT B. (2008), The acoustic and visual factors influencing the construction of tranquil space in urban and rural environments tranquil spaces-quiet places?, *The Journal of the Acoustical Society of America*, **123**(3): 1446–1457, doi: [10.1121/1.2831735](https://doi.org/10.1121/1.2831735).
24. PHEASANT R.J., WATTS G.R., HOROSHENKOV K.V. (2009), Validation of a tranquillity rating prediction tool, *Acta Acustica United with Acustica*, **95**(6): 1024–1031, doi: [10.3813/aaa.918234](https://doi.org/10.3813/aaa.918234).
25. PREIS A., KOCIŃSKI J., HAFKE-DYS H., WRZOSEK M. (2015), Audio-visual interactions in environmental assessment, *Science of the Total Environment*, **523**: 191–200, doi: [10.1016/j.scitotenv.2015.03.128](https://doi.org/10.1016/j.scitotenv.2015.03.128).
26. RAIMBAULT M., DUBOIS D. (2005), Urban soundscapes: Experiences and knowledge, *Cities*, **22**(5): 339–350, doi: [10.1016/j.cities.2005.05.003](https://doi.org/10.1016/j.cities.2005.05.003).
27. REDAELLI E. (2019), Creative placemaking: Leading social change with the arts, [in:] *Connecting Arts and Place: Cultural Policy and American Cities*, pp. 155–188, Springer, doi: [10.1007/978-3-030-05339-0_6](https://doi.org/10.1007/978-3-030-05339-0_6).
28. Regulation of the Minister of Environment (2014), *Regulation of the Minister of Environment of 15 October 2013 on permissible noise levels in the environment* [in Polish: *Obwieszczenie Ministra Środowiska z dnia 15 października 2013 r. w sprawie ogłoszenia jednolitego tekstu rozporządzenia Ministra Środowiska w sprawie dopuszczalnych poziomów hałasu w środowisku*], Journal of Laws of the Republic of Poland, item 112, <https://isap.sejm.gov.pl/isap.nsf/DocDetails.xsp?id=WDU20140000112> (access: 16.11.2022).
29. SCHAFER R.M. (1993), *The Soundscape: Our Sonic Environment and the Tuning of the World*, Destiny Books.
30. TAKANO T., NAKAMURA K., WATANABE M. (2002), Urban residential environments and senior citizens' longevity in megacity areas: The importance of walkable green spaces, *Journal of Epidemiology and Community Health*, **56**: 913–918, doi: [10.1136/jech.56.12.913](https://doi.org/10.1136/jech.56.12.913).
31. ULRICH R.S., SIMONS R.F., LOSITO B.D., FIORITO E., MILES M.A., ZELSON M. (1991), Stress recovery during exposure to natural and urban environments, *Journal of environmental psychology*, **11**: 201–230, doi: [10.1016/S0272-4944\(05\)80184-7](https://doi.org/10.1016/S0272-4944(05)80184-7).
32. WATTS G. (2017), The effects of “greening” urban areas on the perceptions of tranquillity, *Urban Forestry & Urban Greening*, **26**: 11–17, doi: [10.1016/j.ufug.2017.05.010](https://doi.org/10.1016/j.ufug.2017.05.010).
33. WATTS G., MARAFA L. (2017), Validation of the tranquillity rating prediction tool (TRAPT): Comparative studies in UK and Hong Kong, *Noise Mapping*, **4**(1): 67–74, doi: [10.1515/noise-2017-0005](https://doi.org/10.1515/noise-2017-0005).
34. WICIAK J. et al. (2015), Quietness in the soundscape of the Białowieża National Park, *Acta Physica Polonica A*, **128**(1A): 79–84, doi: [10.12693/aphyspola.128.a-79](https://doi.org/10.12693/aphyspola.128.a-79).
35. World Health Organization [WHO] (2018), *Environmental noise guidelines for the European region*, World Health Organization. Regional Office for Europe, <https://www.who.int/europe/publications/i/item/9789289053563> (access: 16.11.2022).

Research Paper

Quality Evaluation of Speech Transmission via Two-way BPL-PLC Voice Communication System in an Underground Mine

Przemysław FALKOWSKI-GILSKI^{(1)*}, Grzegorz DEBITA⁽²⁾

⁽¹⁾ *Faculty of Electronics, Telecommunications and Informatics
Gdańsk University of Technology
Gdańsk, Poland*

⁽²⁾ *General Tadeusz Kosciuszko Military University of Land Forces
Wrocław, Poland*

*Corresponding Author e-mail: przemyslaw.falkowski@eti.pg.edu.pl

(received June 21, 2022; accepted June 22, 2023)

In order to design a stable and reliable voice communication system, it is essential to know how many resources are necessary for conveying quality content. These parameters may include objective quality of service (QoS) metrics, such as: available bandwidth, bit error rate (BER), delay, latency as well as subjective quality of experience (QoE) related to user expectations. QoE is expressed as clarity of speech and the ability to interpret voice commands with adequate mean opinion score (MOS) grades. This paper describes a quality evaluation study of a two-way speech transmission system via bandwidth over power line – power line communication (BPL-PLC) technology in an operating underground mine. We investigate how different features of the available wired medium can affect end-user quality. The results of the described study include: two types of coupling (capacitive and inductive), two transmission modes (mode 1 and 11), and four language sets of speech samples (American English, British English, German, and Polish) encoded at three different bit rates (8, 16, and 24 kbps). Our findings can aid both researchers working on low-bit rate coding and compression, signal processing and speech perception, as well as professionals active in the mining and oil industry.

Keywords: coding; communication applications; compression; signal processing; speech processing; quality of service.



Copyright © 2023 The Author(s).
This work is licensed under the Creative Commons Attribution 4.0 International CC BY 4.0
(<https://creativecommons.org/licenses/by/4.0/>).

1. Introduction

The applicability of electric power networks for efficient data transmission has gained interest from both designers and users. This applies especially to all kinds of local area networks (LANs) employed in general plant communication systems. However, it should be emphasized that power line communication (PLC) technology does not provide such high-quality services as traditional wired and wireless transmission, including copper and optic fibers, or ZigBee. Nevertheless, in many applications, PLC technology is quite sufficient. Evidence of this fact may be found in the increasing development of the so-called smart grids and industrial

automation (MORELLO *et al.*, 2017; DING *et al.*, 2021; HAO, ZHANG, 2021).

One has to know that the main drawback of PLC transmission is its sensitivity to both conducted and induced electromagnetic interference (EMI) (BERNACKI *et al.*, 2019). This problem is of great importance, particularly in low-voltage networks. In this case, a bridging of the transmitted signals can occur due to impedances close in frequency to the range and values of PLC signals of randomly connected electrical receivers (HELD, 2016).

The main advantage of this technology is its ability of utilizing existing power grids, both low and high voltage. This approach does not incur additional in-

vestment costs or operator fees. Authors who are experienced with the challenges of creating secure and reliable communication systems, including mine operation, have identified the positive effects of using bandwidth over power line – power line communication (BPL-PLC) technology for data transmission. However, this requires a careful selection of many technical factors, including: signal frequency, type of coupling, and matching the characteristic impedance of the transmission medium (usually medium voltage cables).

The use of high frequency, in the range from 2 to 32 MHz, offers the opportunity to increase the speed of information transfer up to about 200 Mbps. This bit rate is about 1000 times faster compared to narrowband transmission (DEBITA *et al.*, 2019). Satisfactory field test results, under real-time mine operational conditions, encouraged the authors to utilize the BPL-PLC technology in middle voltage cable lines for voice transmission purposes.

It should be emphasized that safe working conditions, present in the mining and oil industry, particularly in underground environments, require an appropriate and reliable communication system. Such an exemplary environment is shown in Fig. 1.



Fig. 1. Exemplary underground mine environment.

Therefore, various wired and wireless loudspeaker and emergency communication systems are widely used. For example, a plant-wide telephone system can be connected to a radio communication system using the so-called radiating cable (MIŚKIEWICZ, WOJACZEK, 2016). The voice over Internet protocol (VoIP) telephony, which is becoming increasingly popular in mines, uses packet commutation network just like PLC.

The packet header contains data for both source and destination addresses. Thus, voice packets, in a digital form, are sent to the target device without using telephone exchanges with a switching field. It is obvious that the mine's technical environment significantly affects the efficiency of data transmission. Damage to

pavements during mine failures usually results in interruptions of any wired system and significant degradation of wireless communication (MIŚKIEWICZ, WOJACZEK, 2010).

In medium-voltage BPL-PLC technology, the transmission medium is the armored power cable itself. This theoretically makes it the most resistant to mechanical damage, ensuring continuity of transmission through both phase conductors as well as shields and armor. Therefore, in the case of pavement backfilling, BPL-PLC transmission, with battery powered modems, can serve as a last resort, significantly improving rescue operations. Considering the above, the authors conducted a series of simulations and field-test experiments. The obtained results enabled for both objective and subjective evaluation of a custom-build two-way voice transmission system via medium-voltage cable lines using BPL-PLC technology.

2. Related work

POČTA and BEERENDS (2015) investigated a set of audio codecs, including Ogg Vorbis, with bit rates ranging from 24 to 320 kbps. Their tests included subjective and objective metrics, with perceptual evaluation of audio quality (PEAQ) and perceptual objective listening quality assessment (POLQA) methods. Their paper is a valuable source of information concerning various commercial services available in terrestrial and online networks. Since modern-day users prefer mobile devices, particularly when consuming content via online streaming services (FALKOWSKI-GILSKI, 2020), with Spotify using the Ogg Vorbis format, Počta and Beerends' research becomes a major feedback for our upcoming studies.

Another study (FUCHS *et al.*, 2019) focused on improving the quality of speech coders by expanding the frequency range (from narrowband to wideband). The authors evaluated their model using both subjective and objective methods, on a set of signal samples including male and female speakers in three languages: French, German, and English. The speech samples were processed at 24 kbps, with sampling frequency set at 32 kHz. The subjective study, in a 100-step multiple stimuli with hidden reference and anchor (MUSHRA) scale, involved a group of 10 listeners. Whereas, the objective part was carried out utilizing the POLQA metric.

The topic of speech recognition, including end-to-end automatic solutions, as well as numerous simultaneous speakers, is discussed in (MENG *et al.*, 2019; DUBEY *et al.*, 2019; DELCROIX *et al.*, 2019). Whereas, more information on annotating speech data, including massive big data sets, may be found in (FALLGREN *et al.*, 2019; KOSTEK, 2019). Matters related to audio signal processing, including low bit rate and perceptual coding, is available in (HELMRICH *et al.*, 2014).

Similar solutions, together with noise classification and mapping applications (KOTUS *et al.*, 2012; SZCZODRAK *et al.*, 2014; MARCINIUK, KOSTEK, 2015), may be of great importance and aid for any voice communication system, particularly in the mining and oil industry.

It is evident that the topic of digital signal coding and compression, quality evaluation including both QoS and QoE aspects, as well as the design and maintenance of stable and reliable multimedia content distribution and communication services, continue to be extensively discussed topic (GIBSON *et al.*, 1998; MÖLLER, RAAKE, 2014; HOSSFELD *et al.*, 2014; BOZ *et al.*, 2019; FALKOWSKI-GILSKI, UHL, 2020).

3. Tested BPL-PLC system

In order to conduct research on the effectiveness of voice transmission via a BPL-PLC system, the authors selected a segment of a medium-voltage 6 kV cable line, about 300 m long, located in a tunnel in one of the operating mines in Southern Poland. The entire transmission channel was composed of a radial line (over 2 km long), connecting the switchgear at the top of the shaft with the switchgear at the bottom of the shaft.

Thanks to accessible busbars in the switchgears, it was possible to examine both inductive and capacitive coupling of modems with the cable. The digital transmitter and receiver, designed and developed by the authors, were first simulated in the Matlab-Octave environment. The block diagram of the evaluated system is shown in Fig. 2.

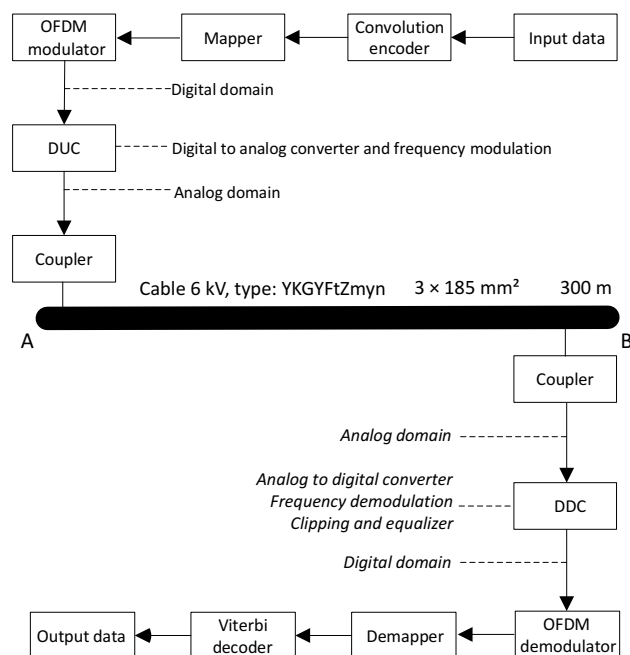


Fig. 2. Block diagram of the tested PLC-BPL speech communication system.

Next, the possibilities and limitations associated with the tested wired medium were examined in an objective QoS and subjective QoE studies.

4. QoS evaluation

According to the 3rd Generation Partnership Project (2011), digital communication services can be divided into two groups, namely: guaranteed bit rate (GBR) and non-guaranteed bit rate (Non-GBR), each with different QoS class identifier (QCI) requirements. Table 1 describes the main communication services with their requirements, including delay and error rate.

Table 1. Main communication services with their QoS requirements.

| QCI | Type | Delay [ms] | Error rate | Service |
|-----|---------|------------|------------|--|
| 1 | GBR | 100 | 10^{-2} | Conversational voice (real-time) |
| 2 | | 150 | 10^{-3} | Conversational video (live streaming) |
| 3 | | 50 | 10^{-3} | Online gaming (real-time) |
| 4 | | 300 | 10^{-6} | Non-conversational voice (buffered streaming) |
| 5 | Non-GBR | 100 | 10^{-6} | IMS signaling |
| 6 | | 300 | 10^{-6} | Video (buffered streaming), TCP-based (e-mail, chat) |
| 7 | | 100 | 10^{-3} | Voice, video (live streaming), Interactive gaming |
| 8–9 | | 300 | 10^{-6} | Video (buffered streaming), TCP-based (e-mail, chat) |

As shown, the GBR variant is linked with QCI from 1–4, whereas Non-GBR is related with QCI from 5–9. Our study focuses on voice (speech) communication. In the GBR variant, such services require delays ranging from approximately 100 ms (conversational voice) to 300 ms (non-conversational voice). For the Non-GBR variant, the required delay should be smaller than 100 ms. Regarding error rate, it should oscillate around 10^{-2} or 10^{-3} up to 10^{-6} . The results of our analysis, considering the tested wired medium, are shown in Fig. 3.

When examining obtained results for both transmission modes (mode 1: 3–7.5 MHz and mode 11: 2–7 MHz), IC refers to inductive coupling, whereas CC represents capacitive coupling. It was found that the error rate ranges from 10^{-2} to 10^{-3} , which is adequate for voice communication services. The results for jitter (time delay between packets) at various data packet sizes, during a 10 min interval, along with available

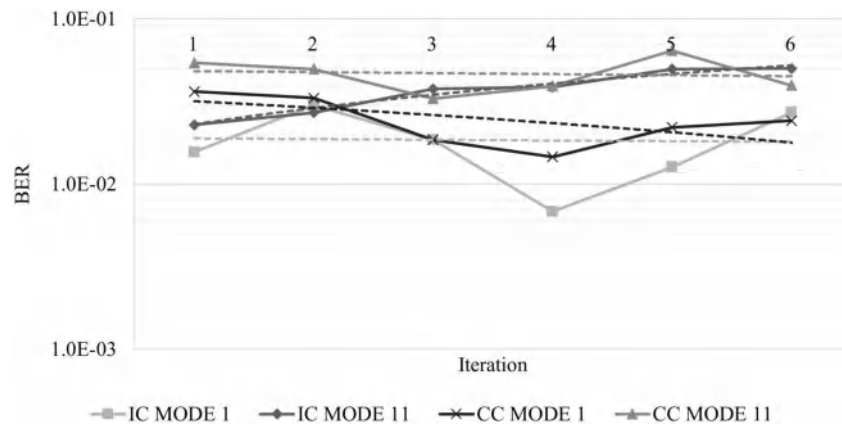


Fig. 3. Simulated BER for inductive coupling (IC) and capacitive coupling (CC) in both transmission modes (1 and 11).

bandwidth and as well as the number of retransmitted packets, are described in Table 2.

Table 2. Simulation results for both inductive and capacitive coupling.

| Data packet size [B] | Jitter [ms] | Bandwidth [Mbps] | No. of retransmitted packets |
|----------------------|-------------|------------------|------------------------------|
| 187 | 0.011 | 9.85 | 585 |
| 375 | 0.085 | 14.8 | 545 |
| 750 | 0.367 | 18.0 | 787 |
| 1500 | 0.857 | 18.9 | 1696 |

As observed, the jitter is very low, and less than 1 ms, regardless of the size of the utilized data packet, which proves it suitable for speech communication services. When it comes to available bandwidth, the range of approximately 10–19 Mbps is more than sufficient for implementing a simultaneous two-way voice transmission system. However, the number of retransmitted packets tends to increase with the larger data packet sizes. Based on obtained results and aiming for the best balance between factors such as size of a data packet, jitter, bandwidth and the number of retransmitted packets, the subjective QoE evaluation part, considering a fully-deployed custom-built system, was carried out for a data packet size of 375 B.

5. QoE evaluation

In order to evaluate QoE requirements for the designed solution, we transmitted a set of speech signal samples. These samples were sourced from ITU-T P.501 (International Telecommunication Union [ITU], 2017) and included sentences spoken by two female and two male individuals, in different languages. Bearing in mind the international profile of the oil and mining industry, four language sets were selected, namely: English in both American (AE) and British (EN) dialects, as well as German (GE) and Polish (PL).

The original samples were available in WAV format (16-bit PCM), with a sampling frequency of 32 kHz.

Next, each sample was processed using the Ogg Vorbis codec and was then transmitted through the BPL-PLC wired medium at different bit rates: 8, 16, and 24 kbps. A sampling frequency was set to 44.1 kHz. Previous studies (DEBITA *et al.*, 2020; FALKOWSKI-GILSKI *et al.* 2020; ZAMLYNSKA *et al.*, 2022) have shown that a bit rate of 24 kbps was sufficient to deliver quality voice commands using this codec.

The transmission system was established in both directions (from point A to B and vice versa) using a set of custom Linux-based modems designed for the purpose of this test. We selected the Ogg Vorbis format (KING *et al.*, 2012; KORYCKI, 2012) in order to have as much control as possible. This format offers full-compatibility with the Linux operating system, which powered both our transmitters and receivers. The transmitted signal samples were recorded at both ends for further processing purposes, namely for a subjective quality evaluation study.

The subjective study was carried out on a group of 16 participants, all of whom were native Polish speakers aged between 25–35 years old. As pointed out in a preliminary questionnaire, each person declared having advanced language skills in both English and German. This involved either possessing an appropriate certificate or being engaged in works with international client-related work. None of the participating individuals had hearing impairments. Each participant assessed the audio quality individually, following the ITU (2003) recommendation in turns (one by one), using Beyerdynamic Custom One headphones. Participants were asked to provide ratings on a 5-step mean opinion score (MOS) scale, with no reference signal available, with options ranging from 1 (poor quality) to 5 (excellent quality). The results of this test, averaged for both directions (from point A to point B and vice versa), including two transmission modes (mode 1 and 11), three bit rates (8, 16, and 24 kbps), as well as two types of coupling (inductive or capacitive), are shown in Figs. 4–9.

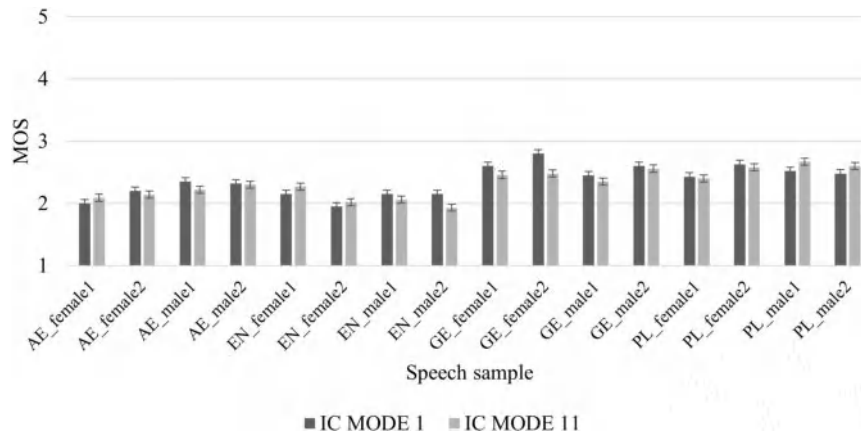


Fig. 4. IC – signal samples processed at 8 kbps.

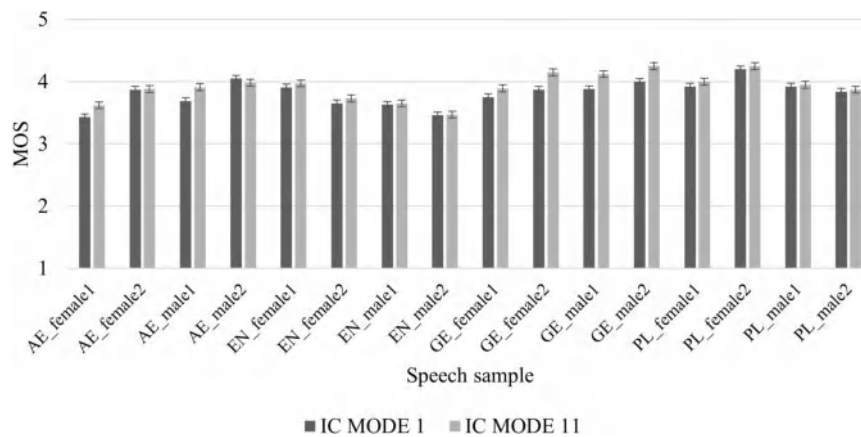


Fig. 5. IC – signal samples processed at 16 kbps.

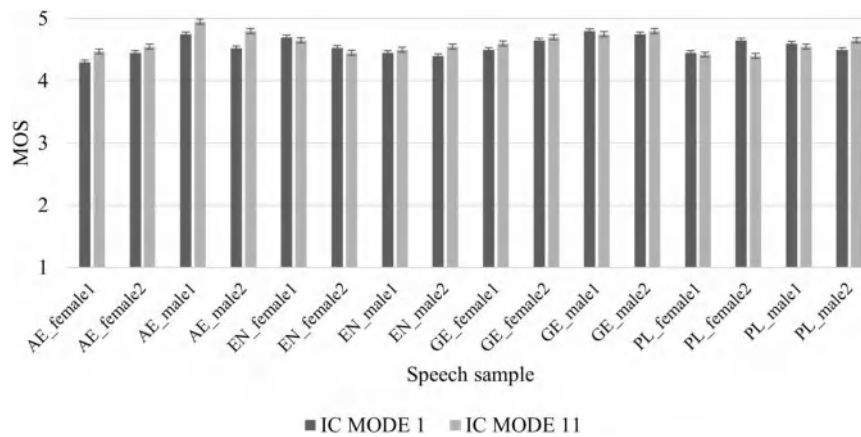


Fig. 6. IC – signal samples processed at 24 kbps.

All the obtained results were processed using the analysis of variance (ANOVA) statistical method, with confidence intervals set at 95% ($\alpha = 0.05$). The dispersion was less than 10%. Results related with inductive coupling (IC) are shown in Figs. 4–6, while those for capacitive coupling (CC) are presented in Figs. 7–9.

A single session took approximately 25 minutes, with a short break in the middle of the study. Before starting the main test, each person underwent a training phase to adjust the volume and become familiar

with the listening equipment. Further information on loudness and related topics may be found in (KOSTEK *et al.*, 2016; MAIJALA *et al.*, 2018; UNE, MIYAZAKI, 2020).

The obtained results have shown whether theoretical objective simulations, as well as field-test measurements, can be used to adequately predict and evaluate the subjective quality of this speech communication system during both the design and maintenance phases.

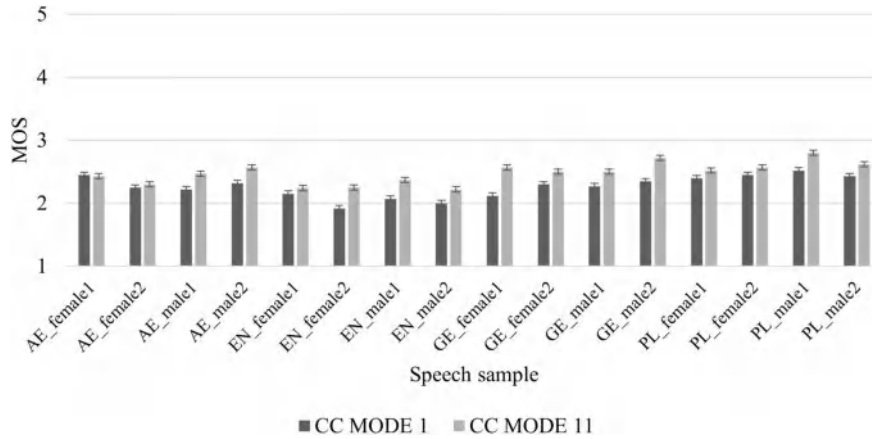


Fig. 7. CC – signal samples processed at 8 kbps.

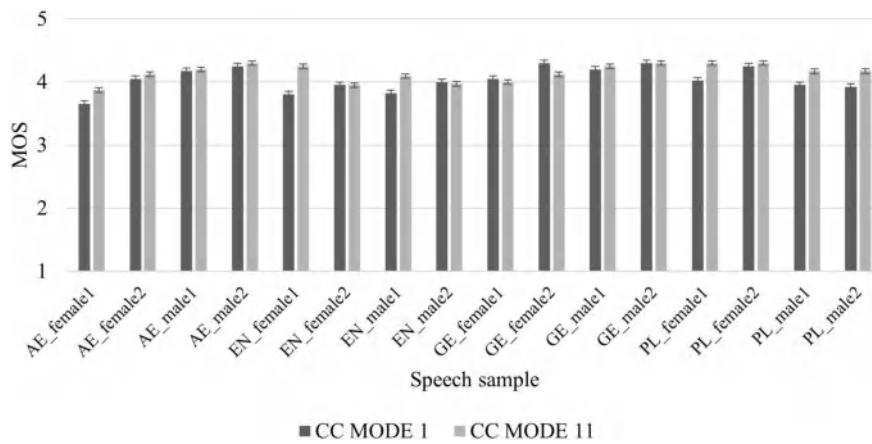


Fig. 8. CC – signal samples processed at 16 kbps.

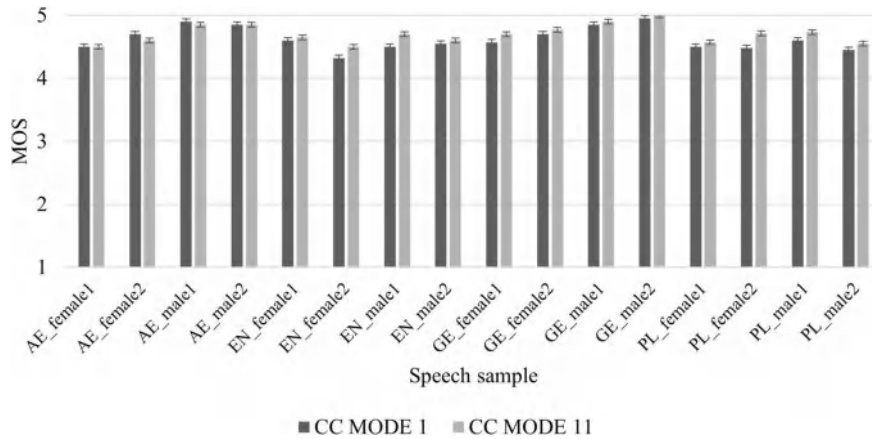


Fig. 9. CC – signal samples processed at 24 kbps.

As shown, the type of coupling, as well as transmission mode, has an observable effect on the end user quality. According to the obtained results, the lowest bit rate (8 kbps) proved to be insufficient to the extent that some individuals perceived these signals as simply annoying. On the other hand, the medium bit rate (16 kbps) was clearly ranked higher. However, not all samples were considered as acceptable. For the highest bit rate (24 kbps), all voice messages, regardless of

the speaker, delivered clear and easily understandable commands.

6. Conclusions

As shown, the BPL-PLC wired system can be effectively used for various data transmission purposes, especially additional and/or supplementary voice communication. This fact becomes crucial in case of emer-

gency situations, such as mine disasters. Since wired cable networks are very resistant to mechanical damage, the BPL-PLC technology, speech signal processing devices and voice communication terminals, together with battery-powered modems, could be implemented, regardless of electrical operating conditions.

This analysis has demonstrated that speech signals transmitted at 24 kbps are sufficient from a practical point of view. Lower bit rates, namely 8 and 16 kbps, did not provide clear and unambiguous statements. Generally speaking, regardless of the evaluated language and/or dialect (AE, EN, GE, PL) as well as the lector's gender (male or female), the level of 24 kbps may be considered as a break point necessary for conveying high-quality speech signal content. Similar results were obtained when changing the type of coupling and/or mode.

Furthermore, the displayed results clearly show the superiority of transmission mode 11 (2–7 MHz) over mode 1 (3–7.5 MHz). Additionally, CC most often provided higher MOS grades than IC. These remarks, observed regardless of the utilized bit rate, are particularly important for engineers responsible for designing and maintaining energy grids and related wired infrastructure.

The outcomes of this work provide practical insights for stakeholders in the mining and oil industry, not to mention researchers and professionals active in related fields. The obtained results may be of particular aid to researchers involved in the design and maintenance of a supplementary voice communication services in harsh environments, such as underground mines. They may be an interesting source of inspiration for engineers in other parts of the world as well. Future studies should consider, e.g., different types of dedicated wired media, a broader range of signal samples, and test scenarios involving listeners from various age groups and backgrounds.

Acknowledgments

The authors would like to thank KGHM Polska Miedź S.A. (Poland), as well as KOMAG Institute of Mining Technology (Poland), for their support and advice during this study.

References

1. 3rd Generation Partnership Project [3GPP] (2011), *Policy and charging control architecture*, Technical specification group services and system aspects, 3GPP Technical Specification 23.203, <https://portal.3gpp.org/desktopmodules/Specifications/SpecificationDetails.aspx?specificationId=810>, access: 21.06.2023.
2. BERNACKI K., WYBRAŃCZYK D., ZYGMANOWSKI M., LATKO A., MICHALAK J., RYMARSKI Z. (2019), Disturbance and signal filter for power line communication, *Electronics*, **8**(4): 378, doi: [10.3390/electronics8040378](https://doi.org/10.3390/electronics8040378).
3. BOZ E., FINLEY B., OULASVIRTA A., KILKKI K., MANNER J. (2019), Mobile QoE prediction in the field, *Pervasive and Mobile Computing*, **59**: 101039, doi: [10.1016/j.pmcj.2019.101039](https://doi.org/10.1016/j.pmcj.2019.101039).
4. DEBITA G. *et al.* (2020), Subjective and objective quality evaluation study of BPL-PLC wired medium, *Elektronika ir Elektrotechnika*, **26**(3): 13–19, doi: [10.5755/jol.eie.26.3.25794](https://doi.org/10.5755/jol.eie.26.3.25794).
5. DEBITA G., HABRYCH M., TOMCZYK A., MIEDZIŃSKI B., WANDZIO J. (2019), Implementing BPL transmission in MV cable network effectively, *Elektronika ir Elektrotechnika*, **25**(1): 59–65, doi: [10.5755/jol.eie.25.1.22737](https://doi.org/10.5755/jol.eie.25.1.22737).
6. DELCROIX M. *et al.* (2019), End-to-end SpeakerBeam for single channel target speech recognition, [in:] *INTERSPEECH 2019 – 21th Annual Conference of the International Speech Communication Association*, pp. 451–455, doi: [10.21437/Interspeech.2019-1856](https://doi.org/10.21437/Interspeech.2019-1856).
7. DING S.Y., LIU J.L., YUE M.H. (2021), The use of ZigBee wireless communication technology in industrial automation control, *Wireless Communications and Mobile Computing*, **2021**: 8317862, doi: [10.1155/2021/8317862](https://doi.org/10.1155/2021/8317862).
8. DUBEY H., SANGWAN A., HANSEN J.H.L. (2019), Toeplitz inverse covariance based robust speaker clustering for naturalistic audio streams, [in:] *INTERSPEECH 2019 – 21th Annual Conference of the International Speech Communication Association*, pp. 416–420, doi: [10.21437/Interspeech.2019-1102](https://doi.org/10.21437/Interspeech.2019-1102).
9. FALKOWSKI-GILSKI P. *et al.* (2020), Subjective quality evaluation of speech signals transmitted via BPL-PLC wired system, [in:] *INTERSPEECH 2020 – 22th Annual Conference of the International Speech Communication Association*, pp. 4601–4605, doi: [10.21437/Interspeech.2020-1077](https://doi.org/10.21437/Interspeech.2020-1077).
10. FALKOWSKI-GILSKI P., UHL T. (2020), Current trends in consumption of multimedia content using online streaming platforms: A user-centric survey, *Computer Science Review*, **37**(4): 100268, doi: [10.1016/j.cosrev.2020.100268](https://doi.org/10.1016/j.cosrev.2020.100268).
11. FALKOWSKI-GILSKI P. (2020), On the consumption of multimedia content using mobile devices: a year to year user case study, *Archives of Acoustics*, **45**(2): 321–328, doi: [10.24425/aoa.2020.133152](https://doi.org/10.24425/aoa.2020.133152).
12. FALLGREN P., MALISZ Z., EDLUND J. (2019), How to annotate 100 hours in 45 minutes, [in:] *INTERSPEECH 2019 – 21th Annual Conference of the International Speech Communication Association*, pp. 341–345, doi: [10.21437/Interspeech.2019-1648](https://doi.org/10.21437/Interspeech.2019-1648).
13. FUCHS G., ASHOUR C., BÄCKSTRÖM T. (2019), Superwideband spectral envelope modeling for speech coding, [in:] *INTERSPEECH 2019 – 21th Annual Conference of the International Speech Communication Association*, pp. 416–420, doi: [10.21437/Interspeech.2019-1620](https://doi.org/10.21437/Interspeech.2019-1620).

14. GIBSON J.D., BERGER T., LOOKABAUGH T., LINDBERGH D., BAKER R.L. (1998), *Digital Compression for Multimedia: Principles and Standards*, Morgan Kaufmann, San Francisco.
15. HAO S., ZHANG H.Y. (2021), A cross-layered theoretical model of IEEE 1901 power-line communication networks considering retransmission protocols, *IEEE Access*, **9**: 28805–28821, doi: [10.1109/ACCESS.2021.3059246](https://doi.org/10.1109/ACCESS.2021.3059246).
16. HELD G. (2016), *Understanding Broadband Over Power Line*, Auerbach Publications.
17. HELMRICH C.R., MARKOVIĆ G., EDLER B. (2014), Improved low-delay MDCT-based coding of both stationary and transient audio signals, [in:] *ICASSP 2014 – IEEE International Conference on Acoustic, Speech and Signal Processing*, pp. 6954–6958, doi: [10.1109/ICASSP.2014.6854948](https://doi.org/10.1109/ICASSP.2014.6854948).
18. HOŁFELD T. *et al.* (2014), Best practices for QoE crowdtesting: QoE assessment with crowdsourcing, *IEEE Transactions on Multimedia*, **16**(2): 541–558, doi: [10.1109/TMM.2013.2291663](https://doi.org/10.1109/TMM.2013.2291663).
19. International Telecommunication Union [ITU] (2003), *General methods for the subjective assessment of sound quality*, ITU Recommendation BS.1284, <https://www.itu.int/rec/R-REC-BS.1284/en>, access: 21.06.2023.
20. International Telecommunication Union [ITU] (2017), *Test signals for telecommunication systems*, ITU Recommendation P.501, <https://www.itu.int/ITU-T/recommendations/rec.aspx?id=14271>, access: 21.06.2023.
21. KING M., NIRAV D., ARVIND A. (2012), Automatic generation of hardware/software interfaces, [in:] *Association for Computing Machinery*, **47**(4): 325–336, doi: [10.1145/2248487.2151011](https://doi.org/10.1145/2248487.2151011).
22. KORYCKI R. (2012), Detection of tampering in lossy compressed digital audio recordings, [in:] *NTAV/SPA 2012 – New Trends in Audio and Video/Signal Processing: Algorithms, Architectures, Arrangements and Applications*, pp. 97–101.
23. KOSTEK B. (2019), Music information retrieval – The impact of technology, crowdsourcing, big data, and the cloud in art, *Journal of the Acoustical Society of America*, **146**(4): 2946, doi: [10.1121/1.5137234](https://doi.org/10.1121/1.5137234).
24. KOSTEK B., ODYA P., SUCHOMSKI P. (2016), Loudness scaling test based on categorical perception, *Archives of Acoustics*, **41**(4): 637–648, doi: [10.1515/aoa-2016-0061](https://doi.org/10.1515/aoa-2016-0061).
25. KOTUS J., SZCZODRAK M., CZYŻEWSKI A., KOSTEK B. (2012), Distributed system for noise threat evaluation based on psychoacoustic measurements, *Metrolgy and Measurement Systems*, **19**(2): 219–230, doi: [10.2478/v10178-012-0019-6](https://doi.org/10.2478/v10178-012-0019-6).
26. MAIJALA P., SHUYANG Z., HEITTOILA T., VIRTANEN T. (2018), Environmental noise monitoring using source classification in sensors, *Applied Acoustics*, **129**: 258–267, doi: [10.1016/j.apacoust.2017.08.006](https://doi.org/10.1016/j.apacoust.2017.08.006).
27. MARCINIUK K., KOSTEK B. (2015), Creating a numerical model of noise conditions based on the analysis of traffic volume changes in cities with low and medium structure, [in:] *Postępy Akustyki – Progress of Acoustics*, Opieliński K.J. [Ed.], pp. 347–358, Polskie Towarzystwo Akustyczne, Wrocław.
28. MENG Z., GAUR Y., LI J., GONG Y. (2019), Speaker adaptation for attention-based end-to-end speech recognition, [in:] *INTERSPEECH 2019 – 21th Annual Conference of the International Speech Communication Association*, pp. 241–245, doi: [10.21437/InterSpeech.2019-3135](https://doi.org/10.21437/InterSpeech.2019-3135).
29. MIŚKIEWICZ K., WOJACZEK A. (2010), *Radio Communication System Using Leaky Feeder in Mines Undergrounds* [in Polish: *Systemy radiokomunikacji z kablem promieniującym w kopalniach podziemnych*] Silesian University of Technology Publishing House, Gliwice.
30. MIŚKIEWICZ K., WOJACZEK A. (2016), How to assess and improve the quality of voice services in telephone communication and alarm systems in mines, *Mining – Informatics, Automation and Electrical Engineering*, **2**(526): 40–47.
31. MORELLO R., MUKHOPADHYAY S.C., LIU Z., SLOMOVITZ D., SAMANTARAY S.R. (2017), Advances on sensing technologies for smart cities and power grids: A review, *IEEE Sensors Journal*, **17**(23): 7596–7610, doi: [10.1109/JSEN.2017.2735539](https://doi.org/10.1109/JSEN.2017.2735539).
32. MÖLLER S., RAAKE A. (2014), *Quality of Experience. Advanced Concepts, Applications and Methods*, Springer Cham.
33. POĆTA P., BEERENDS J.G. (2015), Subjective and objective assessment of perceived audio quality of current digital audio broadcasting systems and web-casting applications, *IEEE Transactions on Broadcasting*, **61**(3): 407–415, doi: [10.1109/TBC.2015.2424373](https://doi.org/10.1109/TBC.2015.2424373).
34. SZCZODRAK M., CZYŻEWSKI A., KOTUS J., KOSTEK B. (2014), Frequently updated noise threat maps created with use of supercomputing grid, *Noise Mapping*, **1**(1): 32–39, doi: [10.2478/noise-2014-0004](https://doi.org/10.2478/noise-2014-0004).
35. UNE M., MIYAZAKI R. (2020), Musical-noise-free noise reduction by using biased harmonic regeneration and considering relationship between a priori SNR and sound quality, *Applied Acoustics*, **168**: 107410, doi: [10.1016/j.apacoust.2020.107410](https://doi.org/10.1016/j.apacoust.2020.107410).
36. ZAMLYNSKA M., DEBITA G., FALKOWSKI-GILSKI P. (2022), Quality analysis of audio-video transmission in an OFDM-based communication system, [in:] *Mobile and Ubiquitous Systems: Computing, Networking and Services. MobiQuitous 2021*, HARA T., YAMAGUCHI H. [Eds.], pp. 724–736, Springer Cham, doi: [10.1007/978-3-030-94822-1_47](https://doi.org/10.1007/978-3-030-94822-1_47).

Research Paper

Removal of Fouling from Steel Plate Surfaces Based on Multi-Frequency Eco-Friendly Ultrasonic Guided Wave Technology

Mingkun HUANG⁽¹⁾, Shuo JIN⁽²⁾, Gaoqian NIE⁽¹⁾, Xiaopeng WANG⁽¹⁾, Quanpeng ZHANG⁽¹⁾,
Yang AN^{(1),(3)}, Zhigang QU^{(1),(3)*}, Wuliang YIN⁽⁴⁾

⁽¹⁾ *College of Electronic Information and Automation
Tianjin University of Science and Technology
Tianjin, China*

⁽²⁾ *School of Electrical and Information Engineering, Tianjin University
Tianjin, China*

⁽³⁾ *Advanced Structural Integrity International Joint Research Centre
Tianjin University of Science and Technology
Tianjin, China*

⁽⁴⁾ *School of Electrical and Electronic Engineering, University of Manchester
Manchester, United Kingdom*

*Corresponding Author e-mail: zhigangqu@tust.edu.cn

(received September 15, 2022; accepted April 14, 2023)

Fouling is inevitable on the surfaces of industrial equipment, especially on heat-exchanging surfaces in contact with fluids, which causes water pollution and destroys the ecological environment. In this paper, a novel fouling-removal methodology for plate structure based on cavitation by multi-frequency ultrasonic guided waves is proposed, which can remove fouling on stainless steel plates. A numerical simulation method has been developed to study the acoustic pressure distribution on a steel plate. According to the simulation results, the distribution of sound pressure on the plate under triple-frequency excitation is denser and more prone to cavitation than in single-frequency cases and dual-frequency cases, which improves fouling removal rate. The stainless steel plate is immersed in water for the descaling experiment, and the results show that the fouling removal rates of three water-loaded stainless steel plates under different single-frequency excitation seem unsatisfactory. However, the multi-frequency excitation improves the descaling performance and the removal rate of fouling reaches 80%. This new method can be applied to the surface descaling of large equipment plates, which is of great significance for purifying water quality and protecting the ecological environment.

Keywords: fouling removal; cavitation; eco-friendly; ultrasonic guided waves; multi-frequency.



Copyright © 2023 The Author(s).
This work is licensed under the Creative Commons Attribution 4.0 International CC BY 4.0
(<https://creativecommons.org/licenses/by/4.0/>).

1. Introduction

Fouling is easy to deposit on the inner surfaces of industrial equipment due to long-term contact with the liquid medium. The industrial equipment includes boilers, chillers, and membrane filtration systems in which the heat exchanger part easily produces fouling, especially calcium carbonate (SOMERSCALES, 1990). Fouling reduces thermal conductivity leading to a decrease in production capacity and an increase in energy con-

sumption. Furthermore, some unexpected mechanical breakdowns may be incurred due to fouling, consequently causing financial loss and even severe industrial accidents (ABU-ZAID, 2000).

Traditional methods of descaling on the surface of industrial equipment mainly include a mechanical method, hydro-blasting method, chemical method, and ultrasonic method (KUDRYASHOVA *et al.*, 2019; GHOLIVAND *et al.*, 2010; KRZYZANOWSKI *et al.*, 2013; MASON, 2016). The ultrasonic method, dating from the

middle of the 20th century, has become a mainstream approach for cleaning, which is capable of removing surface fouling based on the acoustic cavitation effect (LEGAY *et al.*, 2013; DEPTUŁA *et al.*, 2016; MASON, 2016). In traditional ultrasonic cleaning methods, the transducers are attached to the bottom of the water tank with cleaning fluid, generating high-frequency mechanical vibrations to clean the objects immersed in the fluid through ultrasound cavitation (KIM *et al.*, 1999; WU, CHAO, 2011).

Ultrasonic guided waves (UGWs) technique has been widely used in structural health monitoring (SHM). In recent years, UGWs techniques have also been used to remove fouling on structures (HABIBI *et al.*, 2016). In our previous study, a new approach to pipeline descaling based on leaky-guided ultrasonic wave cavitation was proposed, and the experiment results showed that the new approach had high efficiency in removing fouling in the water-filled pipe (QU *et al.*, 2019). According to these findings, the UGWs have the potential for long-distance fouling removal because they can propagate a longer distance than traditional ultrasound. At the same time, this technique allows for non-stop operation, enabling continuous fouling removal. Additionally, the use of UGWs for fouling removal can significantly reduce maintenance costs.

Cavitation is an essential principle used in descaling. When UGWs propagate along a structure with a liquid load, a part of the energy will leak into the liquid through the solid-liquid boundary, which can cause liquid cavitation. The cavitation induced by ultrasonic waves can be used to clean solid surfaces and remove scale (PEČNIK *et al.*, 2016; SHCHUKIN *et al.*, 2011). In recent years, multi-frequency ultrasound has been reported to improve the ultrasonic cavitation effect (FENG *et al.*, 2002; SUO *et al.*, 2018; AVVARU, PANDIT, 2008). Twenty-kilohertz ultrasound was applied to a cross-flow ultrafiltration system with alumina membranes. The ultrasonic control of membrane fouling caused by silica particles was investigated under various solution conditions (CHEN *et al.*, 2006).

This paper mainly discusses the effect of the descaling on stainless steel plates using multi-frequency UGWs. The descaling effect on stainless steel plate under the same power and different frequency combination excitation is studied and analyzed. Mean-

while, a curve graph of the descaling rate with the corresponding descaling time is shown.

2. Theory

When the wave propagates in a bounded medium, solid boundaries can guide the propagation of waves in the form of reflection and refraction. The guided waves in the plate can be regarded as a superposition of waves led by bulk wave reflection and refraction at the upper and lower boundary of a plate (ZHU *et al.*, 2011). As the waves propagate along a plate with liquid loading, part of the energy leaks into liquid. A new descaling method based on UGWs for plates is proposed, as shown in Fig. 1.

For any isotropic medium, the displacement vector \mathbf{U} of UGW in the plate satisfies the Navier displacement equation of motion (RIZZO, SHIPPY, 1971; KOVARIK, 1995; MAZZOTTI *et al.*, 2014), which can be expressed as Eq. (1). Using Helmholtz decomposition, the displacement vector field can be expressed as the gradient of a scalar Φ and the curl of a vector ψ , as Eq. (2):

$$(\lambda + \mu)\nabla\nabla \cdot \mathbf{U} + \mu\nabla^2\mathbf{U} = \rho \cdot (\partial^2\mathbf{U}/\partial t^2), \quad (1)$$

$$\mathbf{U} = \nabla\Phi + \nabla \times \psi, \quad (2)$$

where λ and μ are Lamé's constants of an elastic isotropic solid, and ρ is the density.

When the plate surface is loaded with water, it provides a path for UGWs energy leakage. If the phase velocity of the UGWs in the plate is greater than in the fluid, energy will leak into the fluid (INOUE, HAYASHI, 2015). So the waves attenuate as they propagate in the plate, and the displacement is

$$\mathbf{U} = A_a e^{i(k_r x - \omega t)} e^{-\alpha x}, \quad (3)$$

where A_a is the amplitude of the wave in the plate, k is the wave number, and α is the decay factor.

Because shear stress cannot propagate in the liquid, vector potential is equal to zero. When longitudinal waves propagate in the water, the potential function Φ should be considered together with an additional displacement field equation (SATO *et al.*, 2007).

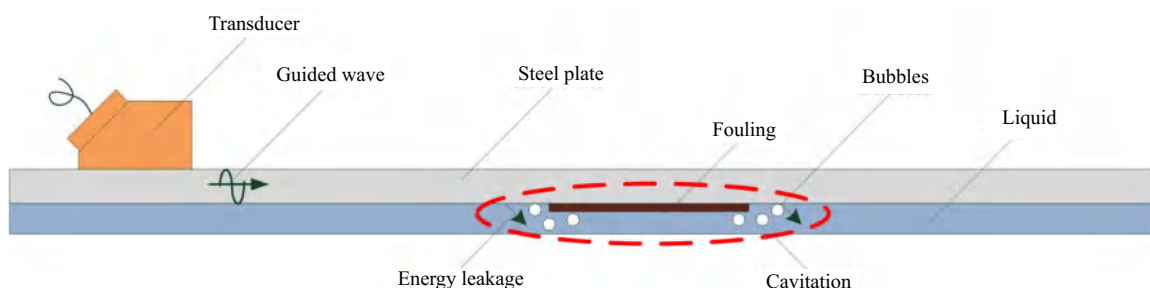


Fig. 1. Propagation direction of UGWs and the descaling principle of leakage UGWs on the steel plate.

The displacement \mathbf{U} in water by leaky UGWs can be expressed as the gradient of a scalar Φ :

$$\mathbf{U} = \nabla \Phi, \tag{4}$$

$$\Phi = A_l e^{-ik_l y} e^{i(kx - \omega t)}, \tag{5}$$

$$k_l = \sqrt{(\omega/c_l)^2 - k^2}, \tag{6}$$

where A_l is the amplitude of wave in the liquid, k is the wave number, and c_l is the longitudinal wave velocity in the liquid.

UGWs leaking into the liquid cause a cavitation effect. If the amplitude of acoustic pressure is higher than the cavitation threshold, the bubbles in liquid will expand under negative pressure and absorb a lot of energy from the sound field, compress and collapse sharply under positive pressure, resulting in high temperature and high pressure (SUSLICK *et al.*, 1999), which will effectively remove the fouling on the plate. The cavitation threshold is defined as the minimum amplitude of sound pressure required to initiate acoustic cavitation (NGUYEN *et al.*, 2017), which can be expressed as:

$$P_b = P_0 - P_V + \frac{2}{3\sqrt{3}} \left[\left(\frac{2\sigma}{R_0} \right)^3 / \left(P_0 - P_V + \frac{2\sigma}{R_0} \right) \right]^{1/2}, \tag{7}$$

where P_b is the cavitation threshold, P_0 is the hydrostatic pressure, P_V is the saturated vapor pressure, R_0 is the initial radius of a bubble, and σ is the tension coefficient of the liquid.

When the external driving sound pressure exceeds the cavitation threshold, not all bubbles will collapse. The cavitation effect occurs only when the ultrasonic frequency is less than the resonant frequency of the bubble or the initial radius of the bubble is smaller than the resonant radius. Otherwise, the cavitation bubble has nonlinear vibration. The resonant frequency of the bubble (SHIMA *et al.*, 1971) can be expressed as:

$$f_r = \frac{1}{2\pi R_0} \sqrt{\left[\frac{\gamma}{\rho} \left(p_0 + \frac{2\sigma}{R_0} \right) - \frac{2\sigma}{\rho R_0} \right]}, \tag{8}$$

where γ is the specific heat ratio, ρ is the liquid density, and f_r is the resonant frequency.

3. Simulation

Based on the theory presented in Sec. 2, leaky acoustic pressure is a critical factor in determining

whether cavitation occurs on the surface of the plate during the descaling process. To study the characteristics of the sound field at different frequencies, finite element simulation is used to understand the acoustic pressure distribution on the plate.

3.1. Model set-up

The model set-up is shown in Fig. 2a, wherein the plate is made of 304 steel material. The plate has a length of 500 mm, a width of 100 mm, and a thickness of 2 mm. On one side of the plate there is layer of CaCO_3 that spans a length of 180 mm. The plate is subjected to a water load. Most commonly used ultrasonic testing (UT) angle transducers use methyl polymethacrylate as the body wedge material. In this case and when emitting ultrasound waves to steel, it is possible to operate within the specified incidence angle range of 27.6–57.7° (KRAUTKRÄMER, KRAUTKRÄMER, 2013). The wedge-shaped transducer consists of PZT-5H piezoelectric material and a square aluminum base. The dimensions of the aluminum base are 85 × 48 × 50 mm, and the dimensions of the piezoelectric sheet are 50 mm outer diameter, 17 mm inner diameter, and 5 mm thickness.

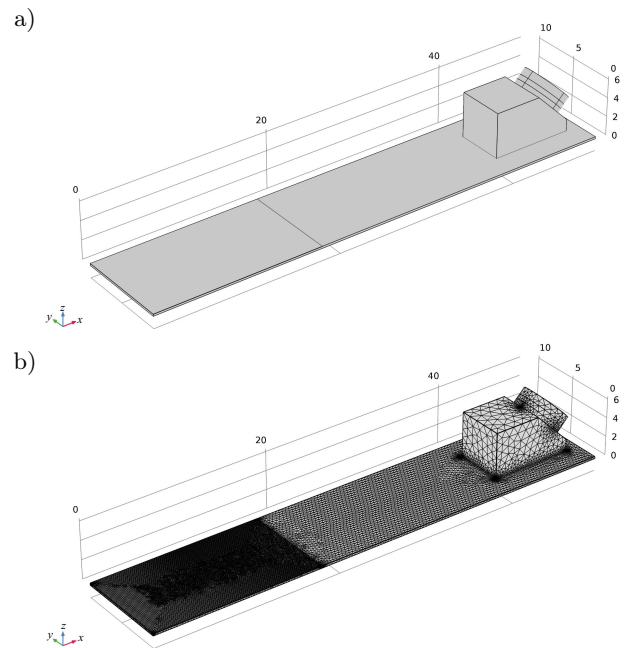


Fig. 2. a) FEM model; b) mesh of the model.

The performance parameters of the transducer-sensitive element PZT as shown in Table 1.

Table 1. PZT parameter of the transducer.

| Parameter | Radial resonant frequency (f_s) | Radial anti-resonant frequency (f_p) | Transverse electromechanical coupling coefficient (k) | Equivalent capacitance (C) | Elastic modulus (e) | Longitudinal wave velocity (V_l) | Transverse wave velocity (V_t) | Dielectric constant (ϵ) |
|-----------|-------------------------------------|--|---|--------------------------------|-------------------------|--------------------------------------|------------------------------------|------------------------------------|
| Parameter | 35 528 Hz | 38 200 Hz | 0.367 | 3050 pf | 61 Gpa | 4500 m/s | 2200 m/s | 380 |

The incident angle of the transducer is set at 45° , following the principle of oblique incidence and generating the UGW in the F mode. The transducer is coupled at one end of the plate to ensure that the UGWs energy excited by the transducer can be effectively transmitted. The mesh of the model is presented in Fig. 2b. The region covered with fouling on the plate is the main calculation domain, in which the largest cell size should be less than or equal to the $1/8$ minimum wavelength criterion. In Fig. 2b, the mesh of the main calculation domain (region covered with CaCO_3 fouling on the plate) is denser than the other parts to ensure calculation accuracy.

3.2. Simulation result

The absolute acoustic pressure results in the region covered with fouling under different frequencies are shown in Fig. 3. The three frequencies with peak acoustic pressure are 24.767, 35.144, and 42.498 kHz, under which the distribution of acoustic pressure on the plate is studied in the simulation.

The absolute acoustic pressure distribution results on the plate under different frequency combinations are shown in Fig. 4.

According to Fig. 4, under single-frequency excitation, the peak distribution of sound pressure on the

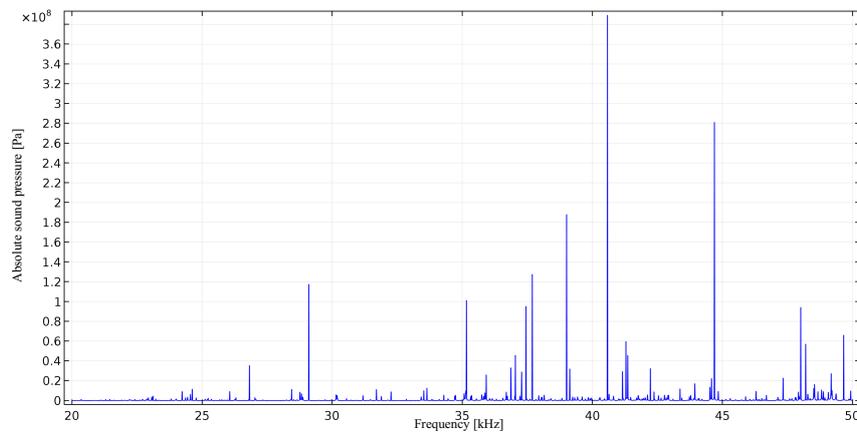


Fig. 3. Absolute acoustic pressure under different frequencies.

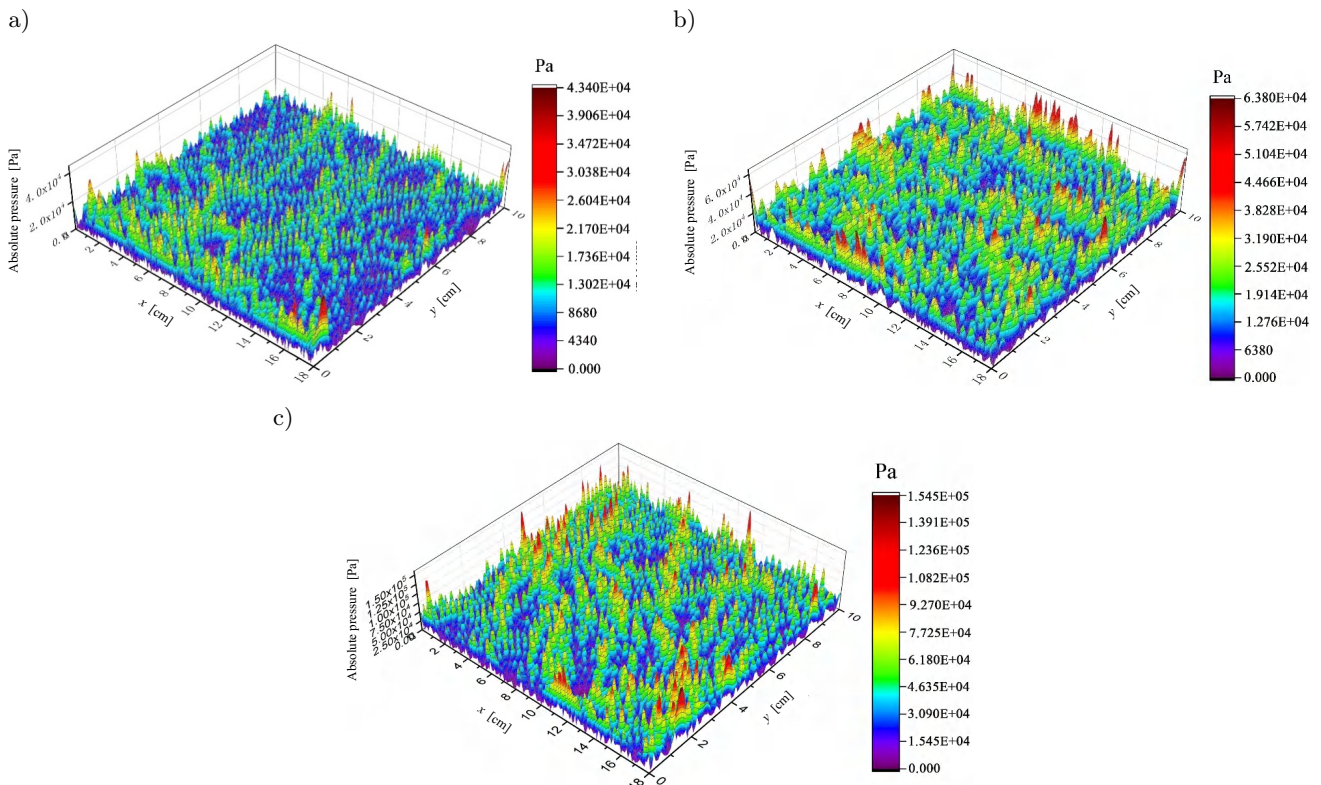


Fig. 4. Absolute sound pressure distribution under different frequency combinations: a) single-frequency 24.767 kHz; b) dual-frequency 24.767 and 35.144 kHz; c) triple-frequency 24.767, 35.144, and 42.498 kHz.

plate is scattered and the overall sound pressure value is relatively low. When the peak value reaches the cavitation threshold, cavitation for descaling occurs. In another way, cavitation for descaling cannot occur in areas where there are low acoustic pressure values. Hence the descaling on the plate under single-frequency excitation is not uniform. Compared with single-frequency excitation, the sound pressure on the plate under dual-frequency and triple-frequency excitation is more densely divided, and the sound pressure value increases. The uniformity of the sound pressure distribution in the triple-frequency mode is similar to that of the dual-frequency mode. However, the sound pressure values are an order of magnitude higher in the triple-frequency mode.

4. Experiments and results

4.1. Transducer testing

A single 45° beam angle transducer is used in this work, as shown in Fig. 5a, which consists of a square base and piezoelectric material. Electric energy is converted to mechanical vibration by a transducer based on the piezoelectric effect and generates UGWs propagation in the plate based on Snell's law.

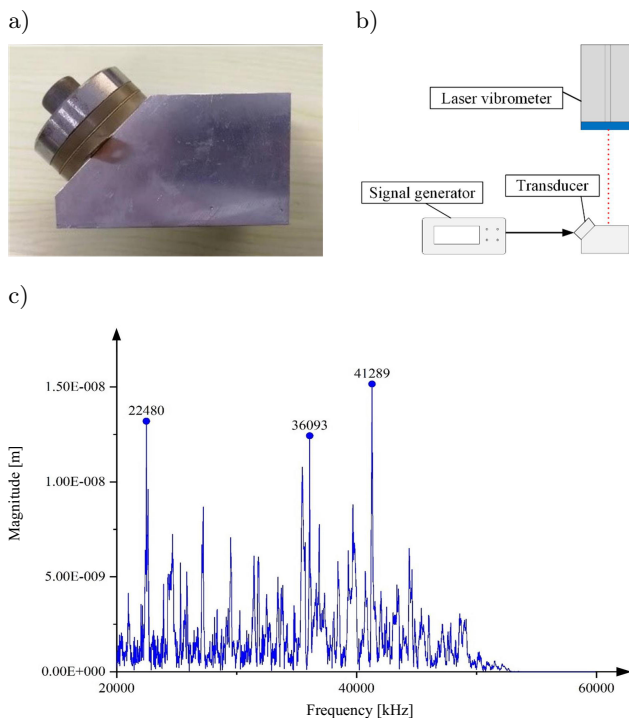


Fig. 5. a) Transducer used in this work; b) transducer testing set-up; c) displacement-frequency characteristic curve of the transducer.

To test the mechanical vibration performance of the transducer at each frequency, the transducer testing system is set up, as shown in Fig. 5b. A pulse signal is generated by the signal generator and input to the

transducer. The vibration characteristics of the transducer are obtained by using and reading a laser vibrometer, and the displacement-frequency characteristic curve of the transducer is shown in Fig. 5c.

The calibration results show that the displacement of the transducer reaches three peak values when the frequency is 22.480, 36.093, and 41.289 kHz, where the transducer has a good electrical-acoustic conversion efficiency. To improve the effect of cavitation for descaling, the above three frequencies are selected for the descaling experiments.

4.2. Electrochemical reaction

Calcium carbonate fouling is an intractable topic in industrial fields. Calcium carbonate fouling is easy to generate on the surface of heat-exchange equipment, boiler, and other industrial equipment (MACADAM, PARSONS, 2004), and this study mainly focuses on the removal of calcium carbonate fouling on plate surfaces. The system shown in Fig. 5a is designed to generate calcium carbonate fouling on the steel plate.

The output voltage of the power supply is 30 V. The experimental plate is set as the working electrode and connected to the negative electrode of the power supply. The other plate is set as a reference electrode and connected to the positive electrode. Two plates are both dipped in water-nanosized calcium carbonate colloid. The calcium carbonate fouling layer is formed by an electrochemical reaction on the working electrode plate.

Electrochemical reaction experiments are carried out on seven stainless steel plates of the same size: a length of 500 mm, a width of 100 mm, and a thickness of 2 mm. The electrochemical fouling preparation system is shown in Fig. 6. The reaction lasted 36 hours, and the steel plates were covered with a calcium carbonate fouling layer, as shown in Fig. 7.

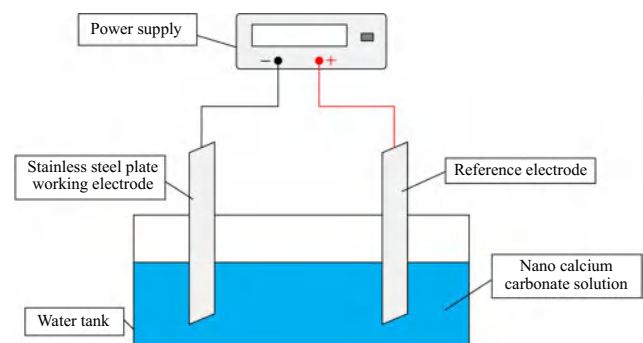


Fig. 6. Electrochemical fouling preparation system.

4.3. Descaling experiment

The descaling experiments are carried out on the steel plate covered with a fouling layer, and the system of the descaling experiment is presented in Fig. 8.

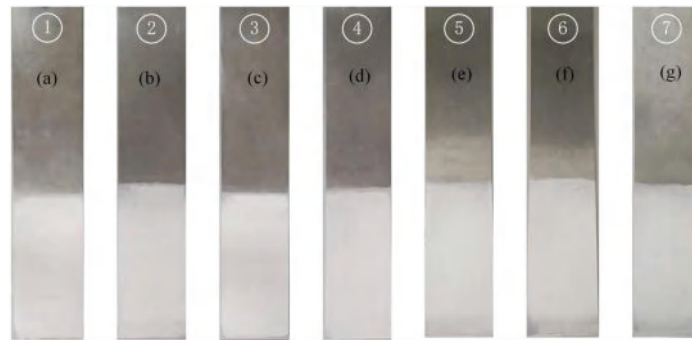


Fig. 7. Seven steel plates with calcium carbonate fouling before the descaling experiment.

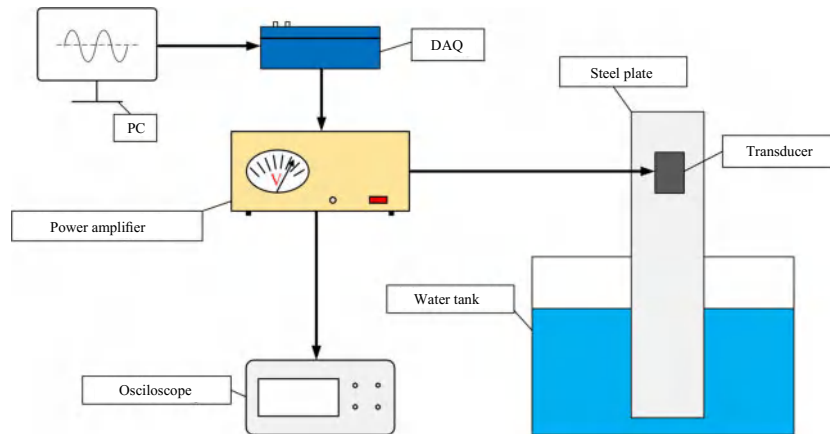


Fig. 8. System of the descaling experiment.

The digital signal is programmed by LabVIEW on a personal computer (PC) and converted into a voltage signal by a digital acquisition card (NI USB-6366). The amplitude of the voltage signal is increased to 400 V_{p-p} by the power amplifier (HFVP-83A) to drive the transducer, which converts an electrical signal into mechanical vibration based on the piezoelectric effect. In the water tank, one end of the plate covered with fouling is dipped into the water, and the transducer is attached to the other end of the plate. A single 45° beam angle transducer is used to generate UGWs in the plate.

Pressure waveforms at different frequency combinations are shown in Fig. 9. In the case of the same input amplitude, the output peak negative pressure of a dual-frequency signal is $\sqrt{2}$ times the single-frequency signal, and the output peak value of the tri-frequency signal is $\sqrt{3}$ times the single-frequency signal (SUO *et al.*, 2015).

In the following experiment, $A_0 = \sqrt{2}A_1 = \sqrt{3}A_2$ is used to ensure equal power generated between single-frequency, dual-frequency, and triple-frequency excitations. In the single-frequency descaling experiment, the input signal is a sinusoidal continuous signal:

$$s(t) = A_0 \sin(2\pi ft), \quad (9)$$

where f is the sinusoidal signal frequency: 22.480 or 36.093 or 4.437 kHz, and A_0 is the amplified amplitude of the voltage signal.

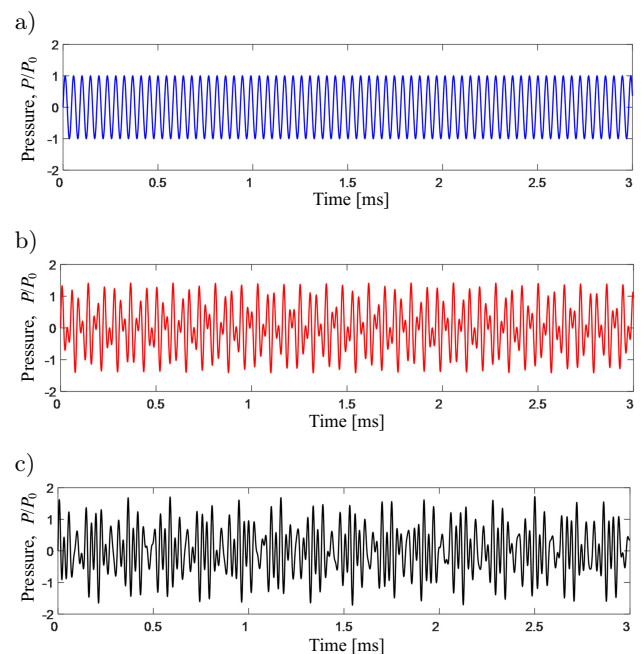


Fig. 9. Pressure waveforms at different frequency combinations: a) 22.480 kHz; b) 22.480 + 36.093 kHz; c) 22.480 + 36.093 + 41.289 kHz.

In the dual-frequency descaling experiment, the input signal is a sinusoidal dual-frequency continuous signal:

$$s(t) = A_1 \sin(2\pi f_1 t) + A_1 \sin(2\pi f_2 t), \quad (10)$$

where

$f_1 = 22.480$ kHz, $f_2 = 36.093$ kHz or $f_1 = 36.093$ kHz, $f_2 = 41.289$ kHz or $f_1 = 22.480$ kHz, $f_2 = 41.289$ kHz, and A_1 is the amplified amplitude of the voltage signal.

In the triple-frequency descaling experiment, the input signal is a sinusoidal triple-frequency continuous signal:

$$s(t) = A_2 \sin(2\pi f_1 t) + A_2 \sin(2\pi f_2 t) + A_2 \sin(2\pi f_3 t), \quad (11)$$

where

$f_1 = 22.480$ kHz, $f_2 = 36.093$ kHz, $f_3 = 41.289$ kHz, and A_2 is the amplified amplitude of the voltage signal.

There are seven different incentive modes in this experiment. To express the incentive modes of experiments more clearly and conveniently, different experiments are numbered, as shown in Table. 2.

Table 2. Corresponding number of different incentive modes.

| Frequency [kHz] | Serial number |
|----------------------------|---------------|
| 22.480 | S1 |
| 36.093 | S2 |
| 41.289 | S3 |
| 36.09, 41.289 | D1 |
| 22.48, 36.09 | D2 |
| 22.48, 41.289 | D3 |
| 22.480, 36.093, and 41.289 | T1 |

Seven descaling results after 40 minutes of the experiment are shown in Fig. 10. Among them, the stainless steel plates numbered 1–3 show the experimental results under the excitation modes S1–S3, and the plates 4–6 show the experimental results under the excitation modes D1–D3, the case numbered 7 shows the experimental result under the excitation mode T1.

It can be seen that descaling regions show different results. Under the single-frequency excitation mode, the removed fouling area is relatively low, which indicates that the descaling effect is poor. Compared

with the above single-frequency excitation mode, in the dual-frequency excitation mode, the removed fouling area accounted for a higher proportion, which shows that the descaling effect is improved. Under the three-frequency excitation mode, CaCO₃ fouling is eliminated, and the removed fouling area accounted for the highest proportion and the descaling effect was the best.

To quantitatively analyze the descaling result, the removal rate is introduced as:

$$\text{Removal rate} = \frac{W_r}{W_t}, \quad (12)$$

where W_r is the weight of fouling on a plate, which is removed in the descaling experiment, and W_t is the total weight of fouling in the plate before the descaling experiment.

The removal rate against time in seven descaling experiments is shown in Fig. 11.

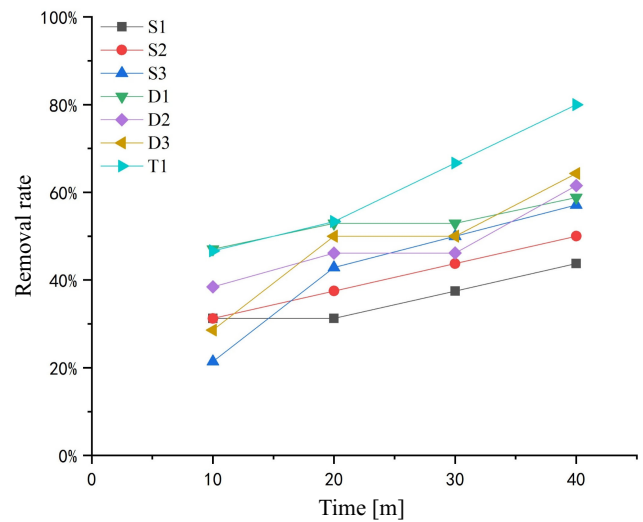


Fig. 11. Removal rate changes with time in the descaling experiment.

The removal rate in the seven experiments increased with time. However, the growth rates of descaling are different under different excitation conditions,

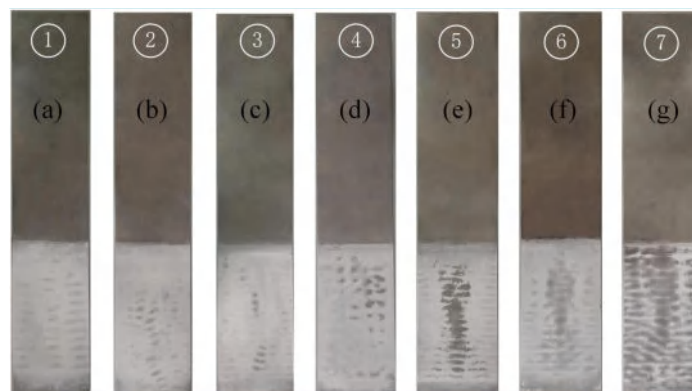


Fig. 10. Descaling results under different excitation modes: a)–c) single-frequency; d)–f) dual-frequency; g) triple-frequency.

resulting in the aliasing of the curves of the descaling rate. However, the final descaling rate showed an increasing trend from S1 to T1. Detailed data in the descaling experiments are listed in Table 3.

Table 3. Removal rate of descaling experiments.

| Excitation mode | W_t [g] | W_r [g] | Removal rate [%] |
|-----------------|--------------|--------------|---------------------|
| S1 | 1.6 | 0.7 | 43.75 |
| S2 | 1.6 | 0.8 | 50.00 |
| S3 | 1.4 | 0.8 | 57.14 |
| D1 | 1.7 | 1.0 | 58.82 |
| D2 | 1.3 | 0.8 | 61.54 |
| D3 | 1.4 | 0.9 | 64.29 |
| T1 | 1.5 | 1.2 | 80.00 |

According to Table 3, the final removal rate in the triple-frequency experiment is higher than that of dual-frequency and single-frequency modes. The descaling rate of dual-frequency is higher than that of single-frequency. It can be concluded that multi-frequency excitation may improve the efficiency of descaling.

5. Discussion

This paper focuses on plate descaling methodology under multi-frequency UGWs by simulation and experiments. A numerical simulation method was used to determine the distribution of acoustic pressure on the plate under different frequency combinations. According to the simulation results, the distribution of sound pressure on the plate under triple-frequency excitation is denser and more prone to cavitation than in single-frequency and dual-frequency cases, which is beneficial for the descaling process. In the descaling experiments, the stainless steel plate is immersed in water and the UGWs propagate along the surface of the stainless steel plate. The leakage energy causes the cavitation effect on the surface of the steel plate. The experimental results show that the descaling rate under triple-frequency UGWs excitation is higher than dual-frequency, and that under dual-frequency UGWs excitation is higher than that under single-frequency. With the increase in frequency number of UGWs, the fouling removal rate on stainless steel plates is gradually improved with 40 mins removal time, and the fouling removal is more uniform. Therefore, multi-frequency UGWs excitation can improve the descaling effect.

6. Conclusion

A new descaling methodology for plate structure based on UGWs was proposed in this paper. A 45° angle beam transducer was used for descaling, and the working frequencies of the transducer under three peak values were obtained by pulse calibration. They

are 22.480, 36.093, and 41.289 kHz. The descaling experiment using UGWs with single-frequency excitation showed a low descaling rate and uneven descaling. With the introduction of the second and third frequencies, the final descaling rate was higher than that of any single-frequency in the combination and the descaling rate of the triple-frequency was higher than that of the dual-frequency. Multi-frequency UGWs improve the descaling rate. This technology can be used to remove the surface dirt of steel plates in water, which is of great significance for industrial production and environmental protection.

Acknowledgments

This work was funded by the National Natural Science Foundation of China (grants no. 61873187, 62173246, and 61901299).

References

1. ABU-ZAID M. (2000), A fouling evaluation system for industrial heat transfer equipment subject to fouling, *International Communications in Heat and Mass Transfer*, **27**(6): 815–824, doi: [10.1016/S0735-1933\(00\)00162-7](https://doi.org/10.1016/S0735-1933(00)00162-7).
2. AVVARU B., PANDIT A.B. (2008), Experimental investigation of cavitation bubble dynamics under multi-frequency system, *Ultrasonics Sonochemistry*, **15**(4): 578–589, doi: [10.1016/j.ultsonch.2007.06.012](https://doi.org/10.1016/j.ultsonch.2007.06.012).
3. CHEN D., WEAVERS L.K., WALKER H.W., LENHART J.J. (2006), Ultrasonic control of ceramic membrane fouling caused by natural organic matter and silica particles, *Journal of Membrane Science*, **276**(1–2): 135–144, doi: [10.1016/j.memsci.2005.09.039](https://doi.org/10.1016/j.memsci.2005.09.039).
4. DEPTUŁA A., KUNDERMAN D., OSIŃSKI P., RADZIWAŃSKA U., WŁOSTOWSKI R. (2016), Acoustic diagnostics applications in the study of the technical condition of the combustion engine, *Archives of Acoustics*, **41**(2): 345–350, doi: [10.1515/aoa-2016-0036](https://doi.org/10.1515/aoa-2016-0036).
5. FENG R., ZHAO Y., ZHU C., MASON T.J. (2002), Enhancement of ultrasonic cavitation yield by multi-frequency sonication, *Ultrasonics Sonochemistry*, **9**(5): 231–236, doi: [10.1016/S1350-4177\(02\)00083-4](https://doi.org/10.1016/S1350-4177(02)00083-4).
6. GHOLIVAND Kh., KHOSRAVI M., HOSSEINI S.G., FATHOLLAHI M. (2010), A novel surface cleaning method for chemical removal of fouling lead layer from chromium surfaces, *Applied Surface Science*, **256**(24): 7457–7461, doi: [10.1016/j.apsusc.2010.05.090](https://doi.org/10.1016/j.apsusc.2010.05.090).
7. HABIBI H. *et al.* (2016), Modelling and empirical development of an anti/de-icing approach for wind turbine blades through superposition of different types of vibration, *Cold Regions Science and Technology*, **128**: 1–12, doi: [10.1016/j.coldregions.2016.04.012](https://doi.org/10.1016/j.coldregions.2016.04.012).
8. INOUE D., HAYASHI T. (2015), Transient analysis of leaky Lamb waves with a semi-analytical finite element method, *Ultrasonics*, **62**: 80–88, doi: [10.1016/j.ultras.2015.05.004](https://doi.org/10.1016/j.ultras.2015.05.004).

9. KIM J.O., KIM J.H., CHOI S. (1999), Vibroacoustic characteristics of ultrasonic cleaners, *Applied Acoustics*, **58**(2): 211–228, doi: [10.1016/S0003-682X\(98\)00039-5](https://doi.org/10.1016/S0003-682X(98)00039-5).
10. KOVARIK V. (1995), Distributional concept of the elastic-viscoelastic correspondence principle, *Journal of Applied Mechanics*, **62**(4): 847–852, doi: [10.1115/1.2896010](https://doi.org/10.1115/1.2896010).
11. KRAUTKRÄMER J., KRAUTKRÄMER H. (2013), *Ultrasonic Testing of Materials*, 4th ed., Springer Science & Business Media, Berlin, Heidelberg.
12. KRZYŻANOWSKI M., YANG W., SELLARS C.M., BEYNON J.H. (2013), Analysis of mechanical descaling: and modelling approach experimental, *Metal Science Journal*, **19**(1): 109–116, doi: [10.1179/026708303225008545](https://doi.org/10.1179/026708303225008545).
13. KUDRYASHOVA O.B., VOROZHTSOV A., DANILOV P. (2019), Deagglomeration and coagulation of particles in liquid metal under ultrasonic treatment, *Archives of Acoustics*, **44**(3): 543–549, doi: [10.24425/aoa.2019.129269](https://doi.org/10.24425/aoa.2019.129269).
14. LEGAY M., ALLIBERT Y., GONDREXON N., BOLDO P., LE PERSON S. (2013), Experimental investigations of fouling reduction in an ultrasonically-assisted heat exchanger, *Experimental Thermal and Fluid Science*, **46**: 111–119, doi: [10.1016/j.expthermflusci.2012.12.001](https://doi.org/10.1016/j.expthermflusci.2012.12.001).
15. MACADAM J., PARSONS S.A. (2004), Calcium carbonate scale formation and control, *Review in Environmental Science & Bio/Technology*, **3**: 159–169, doi: [10.1007/s11157-004-3849-1](https://doi.org/10.1007/s11157-004-3849-1).
16. MASON T.J. (2016), Ultrasonic cleaning: An historical perspective, *Ultrasonics Sonochemistry*, **29**: 519–523, doi: [10.1016/j.ultsonch.2015.05.004](https://doi.org/10.1016/j.ultsonch.2015.05.004).
17. MAZZOTTI M., MARZANI A., BARTOLI I. (2014), Dispersion analysis of leaky guided waves in fluid-loaded waveguides of generic shape, *Ultrasonics*, **54**(1): 408–418, doi: [10.1016/j.ultras.2013.06.011](https://doi.org/10.1016/j.ultras.2013.06.011).
18. NGUYEN T.T., ASAKURA Y., KODA S., YASUDA K. (2017), Dependence of cavitation, chemical effect, and mechanical effect thresholds on ultrasonic frequency, *Ultrasonics Sonochemistry*, **39**: 301–306, doi: [10.1016/j.ultsonch.2017.04.037](https://doi.org/10.1016/j.ultsonch.2017.04.037).
19. PEČNIK B., HOČEVAR M., ŠIROK B., BIZJAN B. (2016), Scale deposit removal by means of ultrasonic cavitation, *Wear*, **356**: 45–52, doi: [10.1016/j.wear.2016.03.012](https://doi.org/10.1016/j.wear.2016.03.012).
20. QU Z. et al. (2019), A descaling methodology for a water-filled pipe based on leaky guided ultrasonic waves cavitation, *Chemical Engineering Research and Design*, **146**: 470–477, doi: [10.1016/j.cherd.2019.04.027](https://doi.org/10.1016/j.cherd.2019.04.027).
21. RIZZO F.J., SHIPPY D.J. (1971), An application of the correspondence principle of linear viscoelasticity theory, *SIAM Journal on Applied Mathematics*, **21**(2): 321–330, doi: [10.1137/0121034](https://doi.org/10.1137/0121034).
22. SATO H., LEBEDEV M., AKEDO J. (2007), Theoretical investigation of guide wave flowmeter, *Japanese Journal of Applied Physics*, **46**(7S): 4521, doi: [10.1143/JJAP.46.4521](https://doi.org/10.1143/JJAP.46.4521).
23. SHCHUKIN D.G., SKORB E., BELOVA V., MOEHWALD H. (2011), Ultrasonic cavitation at solid surfaces, *Advanced Materials*, **23**: 1922–1934, doi: [10.1002/adma.201004494](https://doi.org/10.1002/adma.201004494).
24. SHIMA A. (1971), The natural frequencies of two spherical bubbles oscillating in water, *Journal of Fluids Engineering*, **93**(3): 426–431, doi: [10.1115/1.3425268](https://doi.org/10.1115/1.3425268).
25. SOMERSCALES E.F.C. (1990), Fouling of heat transfer surfaces: An historical review, *Heat Transfer Engineering*, **11**(1): 19–36, doi: [10.1080/01457639008939720](https://doi.org/10.1080/01457639008939720).
26. SUO D., GOVIND B., ZHANG S., JING Y. (2018), Numerical investigation of the inertial cavitation threshold under multi-frequency ultrasound, *Ultrasonics Sonochemistry*, **41**: 419–426, doi: [10.1016/j.ultsonch.2017.10.004](https://doi.org/10.1016/j.ultsonch.2017.10.004).
27. SUO D., GUO S., LIN W., JIANG X., JING Y. (2015), Thrombolysis using multi-frequency high intensity focused ultrasound at MHz range: An in vitro study, *Physics in Medicine & Biology*, **60**(18): 7403–7418, doi: [10.1088/0031-9155/60/18/7403](https://doi.org/10.1088/0031-9155/60/18/7403).
28. SUSLICK K.S. et al. (1999), Acoustic cavitation and its chemical consequences, *Philosophical Transactions of the Royal Society of London. Series A: Mathematical, Physical and Engineering Sciences*, **357**(1751): 335–353, doi: [10.1098/rsta.1999.0330](https://doi.org/10.1098/rsta.1999.0330).
29. WU J.-H., CHAO L. (2011), Effects of entrained air manner on cavitation damage, *Journal of Hydrodynamics*, **23**(3): 333–338, doi: [10.1016/S1001-6058\(10\)60120-5](https://doi.org/10.1016/S1001-6058(10)60120-5).
30. ZHU R., HUANG G.L., HUANG H.H., SUN C.T. (2011), Experimental and numerical study of guided wave propagation in a thin metamaterial plate, *Physics Letters A*, **375**(30–31): 2863–2867, doi: [10.1016/j.physleta.2011.06.006](https://doi.org/10.1016/j.physleta.2011.06.006).

Chronicle

LXIX Open Seminar on Acoustics Karpacz, Poland, September 25 – 29, 2023

On September 25–29, 2023, the LXIX Open Seminar on Acoustics OSA2023 was held in Karpacz. The conference was organized by the Wrocław Branch of the Polish Acoustical Society (PTA). Simultaneously with the OSA2023 conference two accompanying events were held: Signal Processing Symposium SPSympo23 and 5th Polish-German Structured Conference on Acoustics PGSCA2023. 240 specialists from Poland and abroad took part in the OSA2023, SPSympo23, and PGSCA23 conferences delivering 96 papers and 6 plenary presentations.

Abstracts

Acoustic insulation tests of a multi-layer composite modified with rubber recyclate

Norbert ABRAMCZYK¹ (n.abramczyk@wm.umg.edu.pl),
Daria ŻUK¹, Piotr PJ JAKUBOWSKI²

¹ Gdynia Maritime University
Gdynia, Poland

² Maritime Advanced Research Centre
Gdańsk, Poland

The paper presents acoustic studies of a multilayer composite made on the basis of Synolite 1967-G-1 polyester resin and glass fabric with a three-way arrangement of $\pm 45^\circ$, Triaxial type and a weight of 860 g/m^2 . As an addition, rubber recyclate created in the process of disposal of car tires was used. The material was made using the vacuum infusion method. By vacuum lamination, composite materials were produced in the form of plates with the addition of rubber recyclate in four variants of the amount of recyclate used in the produced composite – 20%, 30%, 40% and 50%. Each variant contained 6 layers of fabric and five layers of rubber recyclate. The samples were tested in the vibroacoustic laboratory on a dedicated measuring station of the reverberation chamber assembly without lateral transmission, in which the specific acoustic insulation R was determined in accordance with PN-EN ISO 10140-2 and related standards, i.e. PN-EN ISO 10140-1, PN-EN ISO 10140-4, PN-EN ISO 10140-5 and PN-EN ISO 717-1. All manufactured variants of the composite material with the addition of rubber recyclate were characterized by acoustic insulation in the range of $R_w = (32.5 \div 39.5) \text{ dB}$. High sound insulation parameters

for tested panels up to 12 mm thick constitute a barrier to counteracting the spread of unwanted airborne noise. Combined with good mechanical properties such as tensile strength, toughness and hardness, they form the basis for the easy design of all shields in many industries. The use of rubber recyclate obtained in the process of disposal of car tires has a positive impact on improving environmental protection.

* * *

Sound propagation experiments in the western baltic sea

Jan ABSHAGEN (janabshagen@bundeswehr.org),
Christian HAAK

Bundeswehr Technical Center for Ships and Naval Weapons
Maritime Technology and Research (WTD 71)
Schleswig-Holstein, Deutschland

Sound propagation in the Baltic Sea exhibits special characteristics due to complex oceanographic conditions in this area. In the last two decades experiments on sound propagation in the Baltic sea have been predominately performed east of the Darss Sill. Compared to the central Baltic Sea, the coastal areas of the western Baltic Sea, like the Kiel bay, are much shallower and display differing oceanographic conditions, mainly due to the salinity distribution. The oceanography of the western Baltic Sea gives rise to specific sound propagation conditions. Experiments on the transmission loss, as well as on spatial and temporal variability in the shallow water area of the Kiel bay are presented. In order to examine the sound field properties within the water column, distributed receiver buoys and a vertical hydrophone array were utilized. A stationary, as well as a towed sound source were employed as sound projectors. The sound propagation experiments were conducted with RV ELISABETH MANN BORGESE (Institute for Baltic Sea Research, IOW).

* * *

Diagnosis of acoustic hazards of the environment and its identification problems

Wojciech Michał BATKO (batko@agh.edu.pl)
Academy of Applied Sciences in Krosno
Krosno, Poland

The problems of control and control of the state of acoustic hazards of the environment have a certain unrecognized scientific and application potential. This is because its

identification research dimension has a number of specific properties. They shape the performance peculiarities of the model process, describing the recognized mechanisms: noise generation and propagation, classification of noise hazard states and their forecasts.

Failure to comply with the methodological requirements inherent in identification tasks aimed at: the genesis classification and prognosis of the state of environmental noise hazards – in a manner consistent with their perception by humans – is currently the source of a number of paradoxes and related errors of interpretation.

The speech will review them. The correctness of the decibel algebra will be analyzed, and its corrections will be proposed, opening up new fields of research for the diagnosis of the state of acoustic hazards. The role of proper selection of metrics for decibel comparisons of measurement results, in the process of classifying the state of noise hazards, is outlined. It was found that the currently used Euclidean distance measures in such a process can raise significant objections. Related: methodological, interpretive and application implications are outlined.

The need for new measures for the analysis of comparisons and exceedances of permissible sound levels, free from the limitations of current control practice, was pointed out.

The issues analyzed in the paper were supplemented by an analysis of the problems present in the estimation of the uncertainty of research diagnoses, present in the practice of controlling the state of acoustic hazards of the environment, and the presentation of paths leading to their solution.

* * *

A new, bio-inspired microphone design

Daniel BEER¹ (daniel.beer@idmt.fraunhofer.de),
 Andreas MÄNNCHEN¹, Claudia LENK²,
 Martin ZIEGLER², Tzvetan IVANOV²

¹ Fraunhofer IDMT
 Ilmenau, Germany

² TU Ilmenau

Ilmenau, Germany

Diverse trending technologies such as the voice control of machines or automatic acoustic condition monitoring are creating an ever-increasing demand for a microphone technology that is well-suited to as many different sound situations as possible. This article presents a novel bio-inspired microphone and uses measurements to estimate its potential, compared to conventional microphones, as an acoustic sensor in future applications.

* * *

The potential of liquid marbles and Pickering droplets as templates for colloidal capsules

Rafał BIELAS (rafal.bielas@amu.edu.pl),
 Tomasz KUBIAK, Arkadiusz JÓZEFCAK

Adam Mickiewicz University
 Poznań, Poland

One of the challenges in biomedical applications is the efficient protection of active substances (e.g., drug molecules) and precise delivery to the site of interest when a patient is under treatment or medical diagnostics. Capsules of rigid and dense shells can efficiently preserve the

active substances. They can be fabricated from droplets coated with solid particles suspended in a carrier liquid (known as Pickering droplets). Another potential strategy is using so-called liquid marbles, which are droplets covered with particles but suspended in the air.

In the presentation, I will discuss the production of Pickering droplets and liquid marbles based on magnetic fluids. When exposed to a high-frequency alternating magnetic field, these droplets provide the basis for capsule formation. In the tested systems, polymer micro-particles constituting a shell around the droplets change their properties when influenced by generated heat in magnetic hyperthermia. Then, droplets formed in this way can be manipulated using a constant (DC) magnetic field and filled with an active substance, such as an antibiotic suspension. The results from our research will be supplemented with examples from the literature demonstrating the potential of droplets in the transport and release of active substances triggered by, among others, high-intensity ultrasound.

The presentation will also provide further possibilities in this area, including the control of droplet manipulation processes using ultrasound techniques and the active substance release from the droplets by ultrasound and controlled by electron paramagnetic resonance (EPR) techniques.

* * *

Comparison of the acoustic parameters of the commercial ceiling swirl diffusers with the prototype model

Grzegorz BOGUSŁAWSKI (grzegorz.boguslawski@p.lodz.pl),
 Joanna Maria KOPANIA, Patryk GAJ, Kamil WÓJCIAK

¹ Lodz University of Technology
 Lodz, Poland

² Instytut Energetyki
 Łódź, Poland

Understanding the behaviour of the airflow in ventilated rooms is essential for architects in order to provide the most efficient ventilation system and also for users of the rooms. In mechanical ventilation, it is necessary to control air quality in the human-occupied zone and this can be achieved by air diffusers of different kinds also called ATD's (air terminal devices) – a general term used to describe supply, exhaust or transfer diffusers and grilles. These units in ventilation systems are important because they create a swirl to supply air to rooms where people are and allow mixing flow ventilation in the comfort zone. But inside buildings fitted with air-conditioning systems, the majority of the noise comes from the air, i.e. caused by the movement and distribution of air between ducts and from the ducts into different areas through vents, diffusers and return grilles. In this work, an aeroacoustic study of four commercial adjustable-blade ceiling swirl diffusers and compare with prototype one was performed. Two positions of adjustable-blade, fully opened and by 45 angles, were performed. The objects were installed on the standard plenum box with a side entry without the regulation damper. The prototype blade was printed by the 3D printer. The aeroacoustics parameters were set out according to ISO 5135 in the reverberation room.

* * *

Evaluation of the impact of a leak on the sound transmission loss of a building partition using sound intensity measurements

Romuald BOLEJKO (romuald.bolejko@pwr.edu.pl),
Wrocław University of Technology
Wrocław, Poland

Leaks in building partitions, e.g. at the point of their connection or in the form of poorly filled joints, can significantly affect the resultant sound transmission loss. For partitions in existing buildings with potential leaks, a leak identification method and, above all, a way of assessing the impact of such a leak on their parameters are needed. In this paper, a new method of evaluating the impact of leakage on the resultant sound transmission loss of the partition based on sound intensity distribution measurements was proposed. The tested building element is represented by two-element partition: a tight element and a leak of a certain area and sound insulation. The relationship between the sound transmission loss of a tight partition and the leak is determined on the basis of the measurement of the sound intensity distribution on the surface of the tested element with a leak. Once the relationship is defined, it is possible to predict the recovery of sound transmission loss of the partition as a result of removing the leak.

The paper presents the developed methodology and the results of its verification based on the measurement of sound insulation of a homogeneous partition, with and without leak, using the sound pressure method and the sound intensity method. Measurements were carried out in downscaled reverberation chambers with scale 1:4. A homogeneous MDF board was used with the leakage in the form of holes of a specific diameter. The measurement results were also compared to the values obtained by calculation using well-known Gomperts model of sound transmission loss of the partition with a leak. The measurements and calculations confirmed the possibility of determining the impact of leakage on the resultant sound insulation based only on the measurement of the sound intensity distribution on the surface of the tested partition.

* * *

Objective assessment of the speech signal quality broadcasted by local digital radio in selected locations in Wrocław

Stefan BRACHMAŃSKI¹ (stefan.brachmanski@pwr.edu.pl),
Maurycy J. KIN¹, Natalia RURZYŃSKA²

¹ Wrocław University of Science and Technology
Wrocław, Poland

² KFB Acoustics
Wrocław, Poland

The development of digital radio, observed in recent years, and the advantages offered by this medium are resulting in the expansion of the audience. In order to ensure the proper quality of broadcasting, it is necessary to monitor this quality. The assessment based on listening tests is very expensive and organizationally inconvenient. The development of methods for objective evaluation of signals makes it possible to monitor the quality of transmitted content, without the need for troublesome procedures associated with subjective evaluation. The good correla-

tion of subjective evaluation results and objective measurements in the transmission of perceptually encoded signals, reported in the literature, may allow for random quality monitoring. The authors decided to test the feasibility of using two objective evaluation methods to assess the quality of the speech signal transmitted on digital radio by comparing the results obtained with the result of subjective evaluation. The paper presents the results of objective measurements of speech quality transmitted via Digital Audio Broadcasting+ in Wrocław agglomeration. Measurements have been done in various city sites in order to determine the influence of the location on speech quality. The obtained results of the assessment performed by the use of two methods of testing: PESQ and POLQA, allowed to find a correlation between the objective and subjective results of quality evaluations. The method of objective testing may be used for monitoring the quality of signals in Digital Audio Broadcasting networks especially spoken broadcasts.

* * *

Residual convolutional neural network for continuous identification of aircraft noise

Michał J. BUKAŁA¹ (michal.bukala@polsl.pl),
Artur NOWOŚWIAT¹, Andrzej CHYLA²

¹ Silesian University of Technology
Gliwice, Poland

² SVANTEK
Warsaw, Poland

Continuous aircraft noise monitoring systems are the key to a strategic approach to noise management in the vicinity of airports and helipads. They support shaping the spatial distribution of the emitted noise, e.g. by providing data to optimize the use of approach and departure paths, the distribution of aircraft types during the day etc. in the annual perspective, taking into account alterations in the airport operating patterns and the fleet served.

In the single-operation scope noise monitoring systems allow for indicating anomalous aircraft movements which often become an issue from the perspective of a local community, and thus are of interest to airport authorities.

The latter class of problems requires a system to quickly, automatically and accurately identify whether the limit-exceeding noise event is caused by the aircraft operation. Due to the often delayed access to airport operation logs, the system should operate with minimal or no non-acoustic data. The paper proposes the architecture of a noise detection method, meeting the above requirements and attempts to assess its effectiveness.

Proposed approach involves using the residual convolutional neural network for solving the task. The network operates on 1/3 octave noise input data, returning the similarity of the input sound to the aircraft noise.

The accuracy of the proposed method determined for a single data frame using mixture of real-life measurements exceeds 95% for a frame length of at least 30 seconds.

The proposed method gives promising enough results that it can be implemented in a test environment on a larger scale. In parallel, further work is progressing, focusing mainly on improving the quality of training data and fine-tuning the hyperparameters of the network.

* * *

Research in the use of metamaterial sound-absorbing structures in electroacoustics

Bartłomiej CHOJNACKI (bchojnacki@agh.edu.pl),
Aleksandra CHOJAK, Jan PAWLIK,
Wojciech BINEK, Julia IDCZAK

AGH University of Krakow
Kraków, Poland

The metamaterial structures in sound absorbers' role have increased in popularity in many acoustic applications. However, electroacoustics's most popular absorber type is still porous material such as polyester fibers or acoustic foam. This paper will present the recent finding on the possibility of application for metamaterial acoustic absorbers dedicated to selected features in loudspeaker enclosures, such as standing wave attenuation or absorption of diaphragm backpropagation. The selected applications of metamaterial optimized structure will be demonstrated through numerical simulation and experimental measurements. The optimized structures for the selected application were modeled using COMSOL Multiphysics FEM modeling and Transfer Matrix Method calculation. The selected aspects of sample preparation produced in the 3D printing technique with different technologies of printing will be discussed, as well as the required postprocessing for this type of prototyping technique. We have used the most common rapid prototyping methods, such as FDM, DLP, and SLS, with different mechanical modifications and post-processing to best match the modeling results in measurements on the impedance tube. The summary will provide feedback on the current stage of metamaterial structures applications in electroacoustics and difficulties in this research topic.

The project was funded and supported by the Polish Government, National Centre of Research and Development, agreement no. LIDER/11/0065/L-12/20/NCBR/2021.

* * *

The simulation of the influence of the Doppler effect on wideband hydroacoustic signals

Zuzanna CYMERMAN (zuzannacymerman1@gmail.com),
Iwona KOCHAŃSKA

Gdańsk University of Technology
Gdańsk, Poland

In Underwater Acoustic Communications (UAC) the Doppler effect, that results from the mutual motion of the system's transmitter and receiver, as well as the signal's reflection from the waves forming on the water surface, causes significant distortions of the signal reaching the receiver and reduces the achievable Bit Error Rate (BER) of the data transmission.

The article presents the design and implementation of the simulator of the Doppler effect influence on wideband hydroacoustic signals. The simulator implements two methods of modeling the influence of the Doppler effect. First of which consists of shifting the spectral components of the signal, the second – the compression or expansion of the signal in the time domain. Differences in simulation results obtained with both methods for wideband signals used in UAC systems are presented.

* * *

Sound power level as a means of effectiveness of distributed mode loudspeakers

Karol CZESAK (charles35.41@gmail.com),
Piotr KLECZKOWSKI

AGH University of Krakow
Kraków, Poland

Distributed Mode Loudspeakers (DMLs) are characterized by properties, which make them significantly different from – commonly used – conventional electrodynamic loudspeaker with a piston diaphragm. Such differences occur due to the design assumptions of the DML, which are totally differing from design principles of conventional loudspeakers. The vibrations of DML consist of bending waves traveling across the rectangular surface of the loudspeaker. That is the cause, why transducers of this type present frequency characteristics with sharp local minima occurring at various frequencies, depending on the angle between the loudspeaker's surface and a measurement microphone. Because of such a property DML produce an acoustic field which is diffusive in the proximity of the loudspeaker. Also, the directivity characteristics of the DML are differing from those related to piston loudspeakers. The previous works of these authors have shown that the strongest radiation did not occur at the axis of the transducer, which leads to a conclusion that the Sound Pressure Level measured on the axis of the loudspeaker ought not be conceived as the reference level when normalizing measurement results and calculating directivity specifications.

In this work, a series of sound pressure level measurements of DML in a reverberation chamber has been carried out, which were compared with analogous ones, carried out for a conventional electrodynamic loudspeaker. In further steps – sound power level, according to ISO 3741:2010 standard was determined from the results of conducted measurements for both types of transducers. The sound power level was calculated in 1/3 octave bands, for the filtered pink noise excitation of constant amplitude. It may be concluded, that the sound power level obtained with these two different types of loudspeakers is not significantly differing between each other, despite of various operating principles of transducers.

* * *

Molecular structure and thermophysical properties of ionanofluids

Marzena H. Dzida (marzena.dzida@us.edu.pl)

University of Silesia in Katowice
Katowice, Poland

Investigated ionanofluids are hybrid systems composed of multi-walled carbon nanotubes dispersed in ionic liquids by ultrasonication method. They exhibit a range of desirable properties, including improved thermal conductivity, nonflammability as well as high chemical and thermal stability, making them efficient and safe heat transfer media. In particular, a remarkable increase in thermal conductivity was observed for ionanofluids based on C-sp² rich, long, crystalline multi-walled carbon nanotubes. The structural, cryo-transmission electron microscopic studies revealed the existence of subzipping effect of long multi-walled carbon nanotube networks in ionic liquids as a result of interactions

between two neighboring nanotubes which fragmentarily coalescent by the ionic liquid nanolayers, i.e. intertube zipping together with locally unzipped individual pairs of nanotubes and/or longitudinally unzipped nanotubes. The energy of interactions between the carbon nanotube walls and ionic liquids, obtained from the molecular dynamics simulations, indicated that the formation of carbon nanotube networks, separated by a layer of ions, was thermodynamically favorable. Additionally, the correlation between the ID/IG and ID/I2D integrated intensity ratios in the Raman spectra suggested the formation of new covalent bonds between the ultrasonically induced broken nanotubes and the most likely cation. Consequently, the molecular perfection of the multi-walled carbon nanotube structure, along with its supramolecular arrangement and interactions with ionic liquid, significantly contribute to the extraordinary enhancement in thermal conductivity and optimal rheological characteristics.

This work was financially supported by the National Science Centre (Poland) Grant No. 2017/27/B/ST4/02748.

* * *

Crowd noise spectra for the calculation of the speech transmission index for public address systems

Paweł DZIECHCIŃSKI (pawel.dziechcinski@pwr.edu.pl)

Wrocław University of Science and Technology
Wrocław, Poland

Knowledge about interfering noise in the area of coverage is necessary for the correct design of a public address system. Acquiring this knowledge for existing buildings is possible, for example, by measurements. In the case of a non-existing or non-operating building, it is possible to obtain data on the basis of similar buildings. In practice, knowledge about interfering noise for design purposes is obtained from the literature, calculated, or using in-house experience. The sound levels of interfering noise can be obtained, for example, from BS 5389-1. It is more difficult to acquire knowledge of the interfering noise spectra, and as presented in the paper, the spectrum is also important for speech intelligibility. For example, for interfering noise with a sound level of 60 dB, in the free field, for large distances from the source, the value of the Speech Transmission Index for Public Address Systems (STIPA) for noise with a male speech spectrum can be as much as 0.15 greater than for noise with a pink noise spectrum. The paper attempts to systematise interference spectra occurring in public buildings where public address systems are most commonly used. As shown in the paper, the error in determining STIPA for appropriately selected normalised interfering noise spectra (speech for adequate vocal effort and white, pink and brown noise), relative to STIPA values for measurement-acquired noise spectra is relatively small. The main focus was on crowd noise, in buildings such as sports arenas and stadiums, waiting rooms, offices, restaurants, stores, airport terminals, etc., and interference on railway platforms. In the study, these analyses were performed by computer simulations using the STIPA statistical model.

* * *

Influence of the laboratory measurement method of the reduction of transmitted impact noise by covering floors on a heavyweight standard floor on the result

Leszek DULAK (leszek.dulak@polsl.pl),
Rafał ŻUCHOWSKI

Silesian University of Technology
Gliwice, Poland

The article presents the results of laboratory measurements of the reduction of transmitted impact noise ΔL by floor coverings on a heavyweight standard floor. The tests were carried out for a floating floor with EPS T insulation in two thicknesses: 43/40 mm and 22/20 mm. Each test was carried out for two types of screed: cement and anhydrite. The tests were repeated for an additional screed load simulating furniture load and without load. An attempt was made to determine the impact of the lack of load on the test result and to check whether a small difference in the weight of the screed significantly affects the result.

* * *

Reconstruction of source components from hydroacoustic time series

Andreas GALKA (andreasgalka@bundeswehr.org)

Bundeswehr Technical Center for Ships and Naval Weapons
Maritime Technology and Research (WTD 71)
Schleswig-Holstein, Deutschland

Hydroacoustic time series may contain mixtures of source components originating from natural or artificial sources. We demonstrate that reconstruction of these components can be accomplished by employing the methodology of parametric time series analysis. The core element of the proposed approach is the estimation of models for the prediction of the given time series, such as autoregressive moving-average models or state space models. These models can be generalised for non-stationary situations, such as gradual fading of sources or time-dependent frequencies, e.g., due to Doppler effects. Estimation of states and model parameters is implemented by Kalman filtering and numerical maximisation of the innovation likelihood. As a result of the proposed approach, source components can be detected and reconstructed, also in presence of strong background noise; this is important for the analysis of the hydroacoustic signature of ships. In some cases, additional information regarding the sources can be obtained, such as velocity and distance, or rotation rate of the propeller. As an additional benefit, parametric estimates of the power spectrum can be computed, which have attractive properties, as compared to classical methods for spectral analysis.

* * *

Comparison of the transitional states of singing voice registers depending on the presence of the singer's formant

Mateusz GAWLIK (mateogawel@gmail.com)

AGH University of Krakow
Kraków, Poland

This paper provides an in-depth comparison of the transitional states of singing voice registers, specifically focusing

on the influence of the singer's formant. The singer's formant, a spectral characteristic usually found in professionally trained singers, is considered crucial in the projection and resonance of the singing voice. This study examines how the presence or absence of this formant affects the transitions between vocal registers, a critical aspect of vocal performance. By presenting a comprehensive analysis, the paper seeks to broaden understanding of vocal mechanics, potentially informing better training and performance strategies for singers.

* * *

Reducing the impact of fundamental frequency on the HFCC parameters of the speech signal

Stanislaw GMYREK (stanislaw.gmyrek@pwr.edu.pl),
Robert HOSSA, Ryszard MAKOWSKI

Wrocław University of Science and Technology
Wrocław, Poland

The voiced parts of the speech signal are shaped by glottal pulse excitation, the vocal tract, and the speaker's lips. Semantic information contained in speech is shaped mainly by the vocal tract. Unfortunately, the quasiperiodicity of the glottal excitation, in the case of HFCC parameterization, is one of the factors affecting the significant scatter of the feature vector values by introducing ripples into the amplitude spectrum. This paper proposes a method to reduce the effect of the quasiperiodicity of the excitation on the feature vector. For this purpose, blind deconvolution was used to determine the vocal tract transfer function estimator and the corrective function of the amplitude spectrum. Then, based on the obtained HFCC parameters, statistical models of individual Polish speech phonemes were developed in the form of mixtures of Gaussian distributions, and the influence of the correction on the quality of classification of speech frames containing Polish vowels was investigated.

* * *

Investigation of tribological interactions influence on dynamics of optimal surgical robot with DC motor and PID controller taking into account inputs from in vitro experiments on cardiovascular tissue

Grzegorz ILEWICZ (grzegorz.ilewicz@pw.edu.pl)

Warsaw University of Technology
Warsaw, Poland

Tribological interactions are one of the basic reactions affecting the course of the drive torque in surgical robot joints. It is interesting to test out what is the impact of friction on its dynamics because it gives the possibility to effective control. Inputs from two in vitro experiments on cardiovascular tissue were added to optimization model which include such important physical phenomena as: natural vibrations, linear buckling and history of the deformation. It was assumed that the accuracy of positioning and repeatability of a surgical robot with a serial chain is influenced by such criteria as: first natural frequency, buckling coefficient, mass, dynamic safety factor during transient states and displacement of an end of the effector under the impact of emerging loads. A vector objective function for these

four criteria was determined and its optimum with the usage of finite element method, Pareto fronts and the genetic algorithm NSGA-II was specified too. For the optimal obtained geometry, a model of dynamics of driving torques was constructed by using the block diagram method, taking into the account the inertia tensors and the locations of masses centers. The electromechanical DC motor model was added to each joint. PID regulator models were also added to them and step responses with optimal indicators of the regulation quality was received using gradient descent method. For a specific mechatronic system of the surgical robot, dynamic friction model was formulated based on the Lund-Grenoble model equation including the deformation of the cooperating plastic and elastic surfaces, and including the Stribeck effect.

* * *

Magnetic Pickering emulsions characterization by ultrasound attenuation spectroscopy

Bassam M. JAMEEL (bassam.mufeed.jameel@gmail.com),
Rafał BIELAS, Arkadiusz JÓZEF CZAK

Adam Mickiewicz University in Poznań
Poznań, Poland

A magnetic Pickering emulsion is an emulsion stabilized by magnetic nanoparticles, that accumulate at the droplet interface. However, it is crucial to characterize the stability of Pickering droplets and determine the shell thickness from an application perspective. In this research, the ultrasound attenuation was measured experimentally, and an ultrasound scattering theory based on core-shell model was implemented to analyze the measurement data. The implemented model takes into account the contribution of the shell on the droplet's core during ultrasound wave propagation.

The first part of the results focused on the theoretical calculation of ultrasound attenuation for core-shell model. The change in the ultrasound attenuation values was observed for different core radii, shell sizes, concentrations, and ultrasound frequencies. In the second part of the results, the core-shell model was used to analyze ultrasound attenuation spectra to determine the size of Pickering droplets and shell sizes. We found that the shell thickness varied with various volume concentrations of magnetic particles in the system. Additionally, we investigated the formation of Pickering emulsion under the application of an electric field. The data showed that the thickness of the shell increased compared to samples before electric field treatment.

This work was supported by project no. 2019/35/O/ST3/00503 (PRELUDIUM BIS) of the Polish National Science Centre.

* * *

Contrast-enhanced magneto-motive ultrasound imaging of sentinel lymph nodes

Katarzyna KACZMAREK¹ (katarzyna.kaczmarek@us.edu.pl),
Sandra SJÖSTRAND², Marion BACOU³, Adrian THOMSON⁴,
Tomas JANSEN⁵, Susan MOUG⁶, Susan M. FARRINGTON³,
Carmel M. MORAN⁴, Helen MULVANA²

¹ Institute of Chemistry, University of Silesia in Katowice
Katowice, Poland

² Department of Biomedical Engineering,
University of Strathclyde
Glasgow, UK

³ Institute of Genetics and Cancer, University of Edinburgh
Edinburgh, UK

⁴ Centre for Cardiovascular Science, University of Edinburgh
Edinburgh, UK

⁵ Department of Clinical Sciences Biomedical Engineering,
Lund University
Lund, Sweden

⁶ Department of Surgery, Royal Alexandra Hospital
Scotland, UK

A very crucial step in cancer staging is the process of identification of cancerous lymph nodes. The absence of metastases in the sentinel node determines the lower probability of metastasis in other draining nodes and distant organs. Commonly used in clinical practice methods, such as blue dye-, isotope-, and green fluorescence-staining, are lacking accuracy.

As an alternative to generally used sentinel lymph node identification methods, Contrast-Enhanced Magneto-Motive Ultrasound (CE-MMUS) has been proposed. CE-MMUS uses magnetic microbubbles (microbubbles with attached magnetic nanoparticles) as contrast agents. Subsequently, a low-frequency alternating magnetic field induces oscillations of magnetic microbubbles to generate tissue-laden movement. The tissue-laden movement caused by magnetic microbubbles is tracked and recorded with a phase and frequency tracking algorithm.

Results showed that the functionalization of microbubbles with magnetic nanoparticles does not negatively affect their applicability as contrast agents, and their presence in the sentinel lymph node visibly increased its echogenicity. Derived with the tracking algorithm tissue displacement increased after the addition of magnetic microbubbles compared to displacement caused by magnetic nanoparticles only. Therefore, the CE-MMUS improved lymph node identification. Experiments were conducted on mice models *in vivo*.

This work was supported by CRUK-grant numbers A23333/24730.

* * *

The impact of infrasound on the level of activation

Cezary KASPRZAK (cekasp@agh.edu.pl)

AGH University of Krakow
Kraków, Poland

The present study provides a comprehensive analysis of research data elucidating the impact of infrasound on human activation levels. The levels of activation were quantified using the Activation-Deactivation Adjective Check List a widely recognized self-assessment questionnaire. Experimental studies were conducted in two independent research scenarios: the experimental study and the control study. The research procedures were uniform, differing only in the acoustic stimulus applied. In the experimental study, an acoustic stimulus with a frequency of $f = 13$ Hz and a sound pressure level of SPL = 105 dB (Lin) was employed. Statistically significant changes in activation level were obtained.

* * *

Acoustic aspects of the modernization project of the Pomeranian Philharmonic in Bydgoszcz

Tadeusz KAMISIŃSKI (kamisins@agh.edu.pl)

AGH University of Krakow
Kraków, Poland

The comprehensive modernization of the Pomeranian Philharmonic, planned by the city of Bydgoszcz Ignacy Jan Paderewski will cover the existing part of the building with the well-known concert hall with recognized acoustics and the extension of the building with new rooms. The paper discusses selected acoustic and functional aspects of rooms in the context of acoustic parameters of interiors, construction and testing of acoustic structures and noise protection of rooms. These solutions fit into a very interesting and bold architectural design.

* * *

Acoustic metamaterial design for levelling the impact of double-wall resonance on sound insulation

Aleksandra KLIMEK (aleksandra.klimek@pwr.edu.pl),
Andrzej B. DOBRUCKI

Wrocław University of Science and Technology
Wrocław, Poland

This paper presents two solutions employing locally resonant metamaterial to level the mass-air-mass resonance impact on the sound insulation. The first operates on the cantilever beam resonance, and the second uses masses vibrating in flexural mode cut out from the additional panel. Both structures are mounted between two lightweight, honeycomb cardboard panels with a double-wall resonance of 420 Hz. Solutions were analysed numerically for their vibration and acoustic properties and measured in the reverberation chamber, resulting in information about the dispersion curve, effective dynamic mass, and sound insulation. The analytical results of Sound Transmission Loss (STL) and the experimental measurements of diffused-field Sound Reduction Index (SRI) proved the existence of sound-insulation enhancement. The local rise in SRI resulted in an increase of broadband Weighted SRI up to 5 dB.

* * *

Prediction of effects of impact pile driving noise on marine fauna in the PEEZ: A comparison of different scenarios

Zygmunt KLUSEK (klusek@iopan.gda.pl)

¹ IO PAN Sopot
Sopot, Poland

The construction of wind power plants in offshore areas is usually associated with the generation of high energy and high sound pressure.

In the Polish Exclusive Economic Zone (PEEZ), the construction of a complete network of wind power generator fields is planned, which will result in an increase in the level of underwater acoustic field both during the construction phase and during the operation of the generators.

The negative and sometimes destructive impact of high amplitude and high energy sounds on marine organisms is

relatively well recognised, at least for some types of animals such as mammals and some fish species.

Hence, the estimation of the values and extent ranges of basic metrics of underwater sound associated with piling is undergoing constant attention from administrative bodies and is an interesting research topic.

This paper presents the results of modelling studies carried out to predict the ranges of impact of sound associated with piling on marine organisms.

Numerical modelling of acoustic wave propagation was carried out using an approximation of the wave equation in the form of the parabolic equation of acoustics.

The sound sources were located in several planned wind power plant areas, mainly located north of Słupsk Bank.

Various scenarios were considered to simulate the range of noise impacts, such as seasonal variations in sound propagation in the basin, pile diameter and/or application of different sound mitigation methods.

* * *

The nature of the variability of the underwater noise field on the Słupsk Bank

Zygmunt KLUSEK¹ (klusek@iopan.gda.pl),
Aliaksandr LISIMENKA

¹ IO PAN Sopot
Sopot, Poland

² Gdynia Maritime University
Gdynia, Poland

Analysis of underwater noise long term measurements was performed in shallow waters of the Southern Baltic Sea. Measurements were conducted in the course of seasonal changes of sound propagation conditions from typical for winter to early summer (from February to beginning of July). Investigation of similarity between basic noise metrics at two points was aimed to establish proper inference about noise levels in the area. At both sites, broadband (31.5–16 000 Hz) noise spectra and noise level revealed their dependency on ship traffic.

The analysis of the dependence of noise level on wind speed indicated different forms of this dependence in the two frequency ranges. For frequencies above 800 Hz, the spectrum level increases with wind speed, while in the lower frequency range it decreases.

Despite of relatively shallow site of observations occurrence of seasonal trends in the level noise in both anthropogenic and natural sources was established, what confirm and extend earlier reports regarding seasonal changes of the wind driven noise in the Baltic Sea Deeps.

Thought-provoking short-term periodicities in the noise level independent of meteorological conditions, but hypothetically dependent on vertical diel fish migrations, has been identified in some frequency bands.

* * *

Analysis of asthma patients' auscultatory sounds

Jędrzej KOCIŃSKI¹ (jedrzej.kocinski@amu.edu.pl),
Honorata HAFKE-DYS^{1,2}, Tomasz GRZYWAŁSKI^{3,2},
Anna PASTUSIAK^{1,2}, Adam BINIAKOWSKI²,
Krzysztof SZARZYŃSKI²

¹ Department of Acoustics, Faculty of Physics
Adam Mickiewicz University

Poznań, Poland

² StethoMe Sp. z o.o.

Poznań, Poland

³ WAVES Research Group

Department of Information Technology

Ghent University

Ghent, Belgium

Asthma is a global chronic disease that poses a significant burden on public health. The World Health Organization estimates that approximately 300 million people worldwide suffer from asthma, and this number is projected to increase by 100 million by 2025. Childhood asthma is the most prevalent chronic disease, affecting 10–12% of children worldwide and accounting for a significant portion of the childhood health burden. Despite its high prevalence, the current treatment outcomes for childhood asthma remain inadequate, and preventable deaths occur each year. Furthermore, diagnostic challenges contribute to both overdiagnosis and underdiagnosis of childhood asthma.

The current asthma diagnosis is primarily based on the subjective measurement of respiratory symptoms, which are reported by patients or their caregivers during routine clinical visits over an extended period of up to one year. However, this subjective measurement approach introduces a high degree of uncertainty into the input data, making accurate diagnosis challenging.

Objective analysis of respiratory sounds presents a solution for obtaining more precise and reliable diagnostic data. This study proposes an approach for the objective analysis of auscultatory signals in asthma patients. By implementing this approach, physicians can obtain more objective data for asthma diagnosis and improve treatment outcomes, ultimately reducing the burden of asthma on public health.

* * *

The use of psychoacoustic tests and objective methods of hearing examination in the study of Alzheimer's disease patients

Jędrzej KOCIŃSKI¹ (jedrzej.kocinski@amu.edu.pl),
Andrzej WIECHER¹, Anna PASTUSIAK¹,
Magdalena PUCHAŁSKA¹, Natalia SUDAJ¹,
Marcin GÓRNIAK²

¹ Adam Mickiewicz University
Poznań, Poland

² Specialist Medical Practice
Poznań, Poland

Background: The prodromal phase of Alzheimer's disease (AD) is characterized by the emergence of mild cognitive impairment that falls short of the diagnostic criteria for dementia. During this phase, individuals commonly exhibit subtle memory deficits, word-finding difficulties, challenges in problem-solving, and overall cognitive decline, which often progress to the development of full-blown Alzheimer's dementia. Early identification and intervention during the prodromal phase are crucial for implementing appropriate treatment and support strategies that may potentially slow down disease progression.

Materials and methods: This study employed a comprehensive set of psychoacoustic and objective methods of hearing examination, i.e.: temporal gap detection, amplitude modulation detection, interaural time/level difference discrimination thresholds, speech reception threshold in noise, distortion product otoacoustic emissions (DPOAEs), auditory brainstem responses (ABRs), and auditory evoked potentials (P300). A small group of patients in different stages of AD were tested and compared to individuals with normal hearing.

Results: Considering the fact that only a small group of patients have been tested so far, case study analyzes were performed. Overall, when compared to the reference values, the majority of individuals with AD showed elevated speech reception thresholds. Moreover, there were notable elevations observed in temporal gap detection thresholds and binaural parameters, concomitant with a significant prolongation of the P300 wave latency, as indicated by objective measurements.

Conclusions: Although the data collected in this study did not yield conclusive statistical findings regarding changes in the measured psychoacoustical parameters in AD patients, the results are promising. Further research, incorporating speech, visual, and memory tests, will be conducted to deepen our understanding of the auditory perception changes associated with AD.

* * *

Aeroacoustic parameters of the ceiling swirl diffuser with prototype adjustable-blades

Joanna Maria KOPANIA¹ (joanna.kopania@p.lodz.pl),
Grzegorz BOGUSŁAWSKI¹, Patryk GAJ², Kamil WÓJCIAK²

¹ Lodz University of Technology

Łódź, Poland

² Instytut Energetyki

Łódź, Poland

For the major part of our lives we are in the indoor air spend time in artificial climates such as work/home environments and transport vehicles. So, clean air in a room is an essential component for a healthy indoor environment. Ventilation systems are responsible for exchanging air in rooms. Devices controlling the room ventilation are called ATD's (air terminal devices) – a general term used to describe supply, exhaust or transfer diffusers and grilles. The ceiling swirl air diffusers are mechanical devices designed to control the characteristics of fluid at the entrance to a thermodynamic open system. These units in HVAC systems are important because they create a swirl to supply air to rooms where people are and allow mixing flow ventilation in the comfort zone, but also they are the source of the noise. In this work, an aeroacoustic study of ceiling swirl diffusers with prototype manually adjustable air control blades in two positions, fully opened and by 45 angles, was performed. The objects were installed on the plenum box with a side entry without the damper. The prototype blades using the 3D printer were used to find the one with lower noise parameters which are set out by measuring according to ISO 5135.

* * *

Design and practical realization of an amplifier constructed on the basis of Nuvistors used in the preamplifier circuit

Tomasz KOPCIŃSKI (253179@student.pwr.edu.pl),
Maurycy J. KIN

Wrocław University of Science and Technology
Wrocław, Poland

The work aims to show the method of designing, practical realization and measurement of an electroacoustic amplifier constructed on the basis of electron tubes, especially Nuvistors used in the preamplifier circuit. Nuvistor tubes 6N52S were used in the input stage and phase inverter system in the self-symmetry system. The single channel of power amplifier uses a pair of EL84 power pentodes working in a Push-Pull system. The amplifier also uses a passive tone control system in the Baxhandall system.

The paper presents the complete stages of designing, construction and measurements. The realized device and the measurements as well as the subjective tests confirmed the possibility of using Nuvistor lamps in devices working with an acoustic signal. The use of Nuvistors allowed to reduce the anode voltages compared to the traditionally used ECC83 triodes. Also, the reduction of the dimensions of the device and achieving a frequency bandwidth of -2.6 dB/+0.0 dB from 20 Hz to 20 kHz, are available.

* * *

Test stand for study of reverberating plates with adjustable features

Adam KORYTOWSKI (adamkor@agh.edu.pl),
Wojciech WRONKA

AGH University of Krakow
Kraków, Poland

Vibrations of plates can be used for synthesis of artificial reverberation, which is one of the most important signal processors in audio engineering. This paper describes a process of creating a test stand for measurements of reverberating plates. The stand was assumed to have possibilities to modify the output reverberation signal in perceptually significant way by affecting the plate vibrations. The paper contains description of mechanical and signal parts of the stand and their way of working as well as how they can be used in order to achieve differences in the output reverberation signal. The test stand will allow to examine how exactly affecting the vibrating plate will affect features of the reverberation signal.

* * *

Sound insulation performance of cube-shaped enclosures

Krzysztof KOSAŁA (kosala@agh.edu.pl)

AGH University of Krakow
Kraków, Poland

The subject of the research described in the article are the sound insulating properties of a cube-shaped enclosures, the walls of which are made of plates of homogeneous materials and double-layer baffles. As an enclosure for an omnidirectional sound source imitating a noisy machine or device, a prototype test stand for testing the acoustic

properties of materials and enclosures was used. The three tested variants were enclosures with walls made of plastic plates, such as polyethylene, solid polycarbonate, and plates in the form of rigid polyethylene foam. The fourth variant was an enclosure with walls made of sandwich baffles in the form of a steel plate with a rubber layer glued on. Calculations of the effectiveness of the enclosure were carried out using the previously developed theoretical calculation model for Insertion loss (IL). The obtained results were related to the IL obtained in the course of experimental tests. The research showed slight discrepancies between the calculations and the measurement results for almost all tested materials in the entire frequency range (100–5000 Hz), with the exception of rigid polyethylene foam, for which the discrepancies were relatively the largest in the lower frequency range, i.e. below 400 Hz.

* * *

Lossy coding and bitrate effects on changes in formant frequencies in Japanese and English speech signals

Mateusz A. KUCHARSKI
(mateusz.kucharski@pwr.edu.pl)

Wrocław University of Science and Technology
Wrocław, Poland

Since speaker recognition and verification became heavily used technology, both in professional applications like forensics and more everyday ones, the question arose: what factors can impact results of those processes? One thing that may be important with respect to this subject is lossy coding, as some of the information contained in an original file is lost in the coding process. In the era of globalization, not only native languages or languages of neighboring countries are of interest to researchers, but also those quite far, especially from Asia – the biggest exporter of goods and services to Europe. Those economic relationships are usually connected with the interchange of personnel, which further shortens geographical distance. The article presents the results that are a continuation of research on the behavior of Japanese language formants. Earlier research looked at changes to the trajectories of the first and second formants. This article presents the results of research on the third and fourth formants. The knowledge of these changes is indicated in the process of speaker identification in forensics using the spectrographic method. At the Department of Acoustics and Multimedia, Wrocław University of Science and Technology and in many centers around the world, the auditory-spectrographic method is used, which is a combination of the aural and spectrographic methods. In the spectrographic part, a person is identified on the basis of a comparison of the formants' trajectory.

* * *

Experimental validation of the asymmetric PZT optimal shape in the active vibration reduction of triangular plates

Romuald KURAS (r.kuras@prz.edu.pl),
Sebastian HAJDER

Rzeszów University of Technology
Rzeszów, Poland

In the active vibration reduction of two-dimensional structures, piezoelectric actuators of regular shapes, e.g. rectangular, circular, are commonly used. However, the shape of the transducers can be irregular, asymmetric (a-PZT), and its geometry can be an object for optimization. The paper presents an experimental validation of the application of optimal shaped a-PZT in the active reduction of triangular plate vibrations. Optimization was based on the criterion of the maximum bending moment. This means that the center of a-PZT is located at the point where the bending moment of the plate has reached its absolute maximum. The isosceles right triangular plate with simply supported edges was chosen as the research object. The research confirms the validity of the criterion used for optimization and may be an introduction to considering the use of optimal a-PZT in the active reduction of vibrations for more complex structures.

* * *

Contextual localization bias for a wide range of azimuth and frequency conditions

Bernhard LABACK (Bernhard.Laback@oeaw.ac.at)

Austrian Academy of Sciences
Vienna, Austria

The perceived azimuth of a sound source is biased by a preceding source (precursor), typically, towards midline (medial) by a lateral and towards the side (lateral) by a central precursor. Little is known about effects of intermediate precursor azimuths and the contribution of low and high frequency regions. We tested the hypothesis that for a certain intermediate precursor azimuth, lateral and central biases cancel each other out. Ten normal-hearing listeners localized 300-ms targets following 600-ms precursors using a head-pointing task in a virtual audio-visual environment. Both target and precursor azimuths were systematically varied across the azimuth range from left (-90°) to right ($+90^\circ$). Stimuli were white noises, filtered with listener-specific head-related transfer functions. Low-pass (0.5–2 kHz), high-pass (2.8–16 kHz), and broadband (0.5–16 kHz) conditions were tested to investigate the role of frequency regions dominated by different localization cues: interaural time differences in low-pass, interaural level differences and spectral shape in high-pass, and all three cues in broadband stimuli. Precursor effects were overall strongest for target azimuths of $\pm 70^\circ$. Cancellation of lateral and central biases was found only for $\pm 70^\circ$ -targets, for a mean precursor azimuth of 58.3° . Importantly, the data showed selective spatial contrast enhancement for targets preceded by azimuthally matched Ps. Patterns of precursor effects were relatively similar across frequency regions.

* * *

Infinitesimal volume area of physical space-time in acoustics and electromagnetics

Henryk LASOTA (henlasot@pg.edu.pl)

Gdańsk University of Technology
Gdańsk, Poland

In practical communication engineering, the mathematics of waves, both acoustic and electromagnetic, deals

usually with vast areas of physical space. The author experience in time-domain analysis of two-aspect fields in amorphous media – fluids and dielectrics has shown a far-reaching affinity of transients in acoustics, on the one hand, and wideband signals in UWB wireless communications, on the other hand.

It is worth noting that the wave relationships and equations themselves are derived by means of formal transformations relating to local interactions taking place “here and now” – in an infinitely small volume, in an infinitely small period of time. In this infinitesimal “space-time” there is an immediate interaction between phenomena. At the same time, the mechanism of this interaction can be very different depending on the physical scale of the space and time involved.

Analysis of phenomena performed in infinitesimal areas of fluids and dielectrics leads to significant results of general importance: A – it indicates the existence in both cases of a space-time with two-aspect physical dynamic properties, B – it gives a practical, engineering insight into the philosophical-practical problem of the “reality” of time/space, C – it gives a tool for determining time (frequency) ranges and linear sizes for the main classes of medium models and phenomena occurring in it – classic (continuous), statistic (granular), and quantum mechanic.

The current physics of the universe struggles with the imbalance of matter and energy. The mass-energy gap problem still needs to be addressed. A return to Lorentz’s concept of ether seems potentially useful, perhaps modified by adding a trace energy-mechanical mass content to the space otherwise “endowed with only electric and magnetic properties” (original Lorentz’s definition of ether accepted in 1922 by Einstein).

* * *

Selected problems of active plate vibration suppression

Lucyna LENIOWSKA (lzeniowska@ur.edu.pl)

University of Rzeszów
Rzeszów, Poland

The main aim of the control systems designed for planar flexible structures is to cancel their vibrations and related acoustic radiation as much as possible. This problem is often solved by the application of active methods. This paper presents the derivation of the models for planar structures with surface mounted piezoelectric actuators. The first approach consists in modelling the structural dynamics in the form of the partial differential equations (PDE) derived from physical principles such as the balance of forces and moments. In the second approach, a parametric system identification procedure is employed to establish a mathematical model of the considered system on a basis of the data collected from the measurements. The main objective is to estimate the control-oriented models that are suitable for designing controllers. On the basis of the models derived, the adaptive control algorithms based on solution of Diophantine equation are used to suppress circular plate vibrations. The results of performed simulations and tests are included and discussed.

* * *

First-order ambisonics microphone with MEMS and condenser capsules

Marcin LEWANDOWSKI (marcin.lewandowski@pw.edu.pl),
Aleksander AUGUSTYNIAK

Warsaw University of Technology
Warsaw, Poland

Technologies that produce and deliver immersive VR content are still growing. Ambisonic microphones are available in various types, from the FOA (first-order ambisonics, e.g., Sennheiser AMBEO VR Mic) to HOA (up to fourth-order ambisonics, e.g., MH Acoustics Eigenmike). They are designed with different capsules, from low-cost electret transducers, MEMS (Zylia ZM-1) to high-grade condenser capsules (NEVATON VR). This paper presents two designs of a low-cost FOA microphone based on low-noise MEMS (Infineon IM69D130) and electret capsules (JLI-2590A) in an identical tetrahedral arrangement. This paper details the design, fabrication, and testing of two FOA microphones, including their frequency and directivity response and subjective evaluation compared to commercially available solutions. This study aims to indicate whether the microphone capsule’s type affects the recorded sound field’s quality and its significance.

* * *

A design of an acoustic coupler for calibration of pressure sensors at ultra low frequencies

Karol Jakub LISTEWNIAK (k.listewnik@we.umg.edu.pl)

Gdynia Maritime University
Gdynia, Poland

The article aims to present a coupler developed for the calibration of alternating pressure of the pressure sensors at ultra-low frequencies up to 0.1 Hz for the Central Office of Measures (GUM). This study is part of the project “Concept for the construction of metrological infrastructure in the area of underwater acoustics at GUM”, which is part of the Polish Metrology program. The growing demand for research of marine objects in the field of infrasound underwater noise and research of the hydrodynamic field of ships requires ensuring the reliability and repeatability of recorded data and it starts with reliable calibration of pressure sensors. The choice of calibration method was based on a detailed and extensive analysis of calibration methods and similar solutions. The proposed solution is based on an eccentric mechanism driven by a stepper motor. The article contains an analysis of the literature of similar solutions and presents the theoretical basis, describes the designed coupler structure, configuration of the measurement system and a summary.

* * *

Experimental aeroacoustic studies of selected three types of helicoidal resonators

Wojciech ŁAPKA¹,
Piotr P JAKUBOWSKI² (piotr.jakubowski@cto.gda.pl)

¹ Poznań University of Technology
Poznań, Poland

² Maritime Advanced Research Centre
Gdańsk, Poland

The paper presents experimental studies of selected three types of helicoidal resonators carried out on an aeroacoustic laboratory stand with the use of pink noise and a duct terminated with a reverberation chamber. The same ratio $s/d = 1.976$ is considered for three numbers of helicoidal turns $n = 0.671$, $n = 0.695$ and $n = 1.0$. The results of the acoustic attenuation performance depending on the air flow velocity were compared in relation to the numerical test carried out, with resulted in a decrease in resonance frequencies with an increase in the air flow velocity. The measurements were carried out with a high resolution of the FFT spectrum in order to illustrate the changes in the acoustic attenuation performance as accurately as possible. One-third octave bands of flow noise studies were also carried out.

* * *

Investigation of flow features and acoustic radiation of a set of rectangular cavities in a channel

Paweł ŁOJEK (lojek@agh.edu.pl),
Katarzyna SUDER-DEBSKA

AGH University of Krakow
Kraków, Poland

Due to the widespread use of ventilation and air-conditioning systems in modern buildings, the issue of the generation and propagation of noise generated during the operation of these systems is becoming very important. The source of undesirable sounds have various origins – both directly related to the devices used and related to the flow of the air through the devices, ducts and other elements that are part of these systems.

This article focuses on noise of aerodynamic origin. The paper presents the results of numerical simulations of the air flow in a channel with a set of rectangular cavities. Then, the aeroacoustic wave equation was used to determine the acoustic pressure generated by the flow. Various configurations of the cavities made it possible to study the influence of their reciprocal location on the generated sound.

* * *

Preliminary study: Mobile phone as a phonocardiographic signal recorder

Michał ŁUCZYŃSKI (michal.luczynski@pwr.edu.pl)

Wrocław University of Science and Technology
Wrocław, Poland

The aim of this work is to analyze the possibility of using a mobile phone with a voice recorder function as a phonocardiographic signal recorder. Test measurements were carried out by placing the phone at various points on the chest. For one selected point, measurements were carried out for a group of about 100 people, using different models of mobile phones. Data on weight, height and age were collected through a survey. Participants of the study were also asked about potential problems related to the measurement.

Signal quality was assessed using qualitative parameters. It was checked how the selected methods of signal pre-processing (editing of recordings, filtering, noise reduc-

tion) affect the values of quality parameters. The obtained recordings were subjected to automatic signal classification.

The result of this work is an extended analysis of the use of mobile phones as electronic stethoscopes and an analysis of the usefulness of signals obtained using this measurement method.

The results of these studies are important for the field of medical diagnostics, especially in situations where access to traditional stethoscopes is limited. If mobile phones prove to be effective recorders of phonocardiographic signals, it will open new possibilities in the field of remote heart monitoring and telemedicine.

However, it should be noted that further research, including validation and comparison of results obtained with mobile phones with those obtained with traditional stethoscopes, is needed before this technology is introduced into clinical practice.

* * *

Modeling human sound-source localization: Current state and future directions

Piotr MAJDAK (piotr.majdak@oeaw.ac.at)

Austrian Academy of Sciences
Vienna, Austria

Spatial hearing allows us to orient ourselves and navigate in a 3D environment. The acoustic basis for 3D spatial hearing is described by the listener-specific head-related transfer functions (HRTFs). While much attention has been put on the aspects along the left/right dimension, spatial hearing goes beyond the lateral dimension, and such investigations often require novel modeling approaches. In this talk, we will focus on the dimensions of sound localization that are particularly sensitive to listener-specific HRTFs, that are, near distances (sound externalization/internalization) and sagittal planes (top/down, front/back). We will discuss recent psychoacoustic findings and computational models aiming at simulating mechanisms underlying the process of sound localization. Further, we will explore the possibility of employing Bayesian inference as a quantitative method to predict 3D human sound localization in dynamic auditory scenes and including self-motion. As outlook, we will describe a unified probabilistic framework potentially able to integrate outcomes from various perceptual experiments to develop functional models of space perception, discussing its advantages and its limits and future directions.

* * *

Infrasound and well-being: A study of wind turbine impact

Paweł MAŁECKI¹ (pawel.malecki@agh.edu.pl),
Małgorzata PAWLACZYK-ŁUSZCZYŃSKA²,
Tadeusz WSZOŁEK¹, Bohdan DRZYMAŁA³

¹ AGH University of Krakow
Kraków, Poland

² Instytut Medycyny Pracy im. prof. J. Nofera
Łódź, Poland

³ SourceTech Business Process Outsourcing
Przemysław, Poland

Wind turbines serve as a distinctive source of noise, possessing unique attributes such as amplitude modulation,

tonality, and components of infrasound and low frequency. This study explored how these sounds affect human well-being. A total of 129 subjects participated in the study, carrying out attention-focused tests and filling out surveys under three different conditions: normal background noise, artificially created low-frequency noise, and wind turbine-originated infrasound. The test results and the number of discomforts reported post-experiment did not significantly differ among the various conditions for both males and females. However, it was noted that the well-being before the study had a bearing on the complaints reported after the study.

* * *

Analysis of dynamic mechanical properties of composite materials for electric guitar construction

Paweł MAŁECKI^{1,2,3} (pawel.malecki2.dokt@pw.edu.pl),
Paula PIETRZAK¹, Rafał PERZ^{1,2,3},
Filip ZAKRZEWSKI^{1,2,3}, Marek MATYJEWSKI¹

¹ Warsaw University of Technology
Warsaw, Poland

² Sieć Badawcza Rafał Perz
Mysiadło, Poland

³ RUF Guitars
Mysiadło, Poland

In recent years, composites have been presented widely as an alternative to traditional materials in many technological applications. Composite materials can be used for manufacturing musical instruments. In the case of an electric guitar, the guitars body, neck and fretboard can be made out of the composite structures. The mechanical properties of composite and epoxy-based materials may determine the final timbre of the instrument. Therefore, analysis of the dynamic response of those materials should be made, to ensure the optimal structural composition. In this paper, three different composite and epoxy-based materials were examined in terms of their dynamic mechanical properties. Firstly, samples of different composite materials were prepared and measured to obtain accurate geometry and mass data. Next, the samples underwent experimental modal impact hammer testing and then obtained output data was analyzed. As preliminary state of research storage modulus was calculated to observe differences in dynamic properties of the evaluated variants of composite materials. Obtained results indicate the possibility of differentiating the variants of composite materials to obtain the best fit for manufacturing the body of an electric guitar.

* * *

Analytical modeling of the harmonic distortion caused by squeeze film damping in MEMS-based acoustic transducers

Anton MELNIKOV¹ (anton.melnikov@bosch-sensortec.com),
Hermann A.G. SCHENK¹, Franziska WALL²

¹ Bosch Sensortec
Reutlingen, Germany

² Fraunhofer IPMS
Dresden, Germany

Miniaturized microelectromechanical system (MEMS) microspeakers are currently trending in the development

of acoustic transducers. When a transducer is scaled down to fit on a microelectronic chip, its physics differ from the macroscopic world, and some common modeling assumptions become invalid. One of the effects observed in MEMS microspeakers is nonlinear squeeze film damping. Understanding this effect is crucial as non-linearities in the speaker can result in harmonic distortion, which is highly regulated in audio applications. In this study, we analyze the influence of squeeze film damping on harmonic distortion using a lumped parameter model of a MEMS microspeaker. This leads to a non-linear ordinary differential equation, and an approximate analytical solution for moderate non-linearities is obtained using homotopy. We present our solution strategy, including the resulting closed-form expression, and verify our findings against numerical solutions.

* * *

The influence of diffusing elements arrangement in a reverberation room on the results of airborne sound insulation measurements

Dominik MLECZKO (dmleczko@agh.edu.pl)

AGH University of Krakow
Kraków, Poland

The primary issue in evaluating airborne sound insulation lies in quantifying the sound energy emitted by the barrier. This is typically accomplished by measuring sound pressure levels and acoustic absorption within the receiving chamber. When significant fluctuations in sound pressure levels occur within a reverberation room, it indicates the presence of standing waves, necessitating the incorporation of diffusing elements. ISO 10140 has established specific thresholds that dictate the inclusion of reverberation time for frequencies equal to or surpassing 100 Hz. Nevertheless, there are instances, particularly in spacious rooms, where acquiring the requisite parameters becomes arduous and, at times, unfeasible. Under such circumstances, it becomes imperative to ascertain whether the measured sound insulation is contingent upon the reverberation time.

The presentation presents the measurement results of various diffusing elements configurations in a reverberation room. These diffusers aim to improve the uniformity of the acoustic field in terms of acoustic pressure and reverberation time. Therefore, the focus was on these two parameters. The ultimate goal was to assess the impact of changes in the arrangement of diffusers on the results of sound insulation measurements.

* * *

Investigating the restorative properties of natural soundscapes

Dorota MŁYNARCZYK (dorotam@agh.edu.pl)

AGH University of Krakow
Kraków, Poland

With the increasing levels of stress and the challenges associated with psychological restoration, natural soundscapes have gained attention for their therapeutic qualities. However, there is a need for an objective classification system to facilitate psychoacoustical research in this area. This paper focuses on analyzing the restorative properties

of diverse natural soundscapes. By examining acoustic, eco-acoustic, and psychoacoustic parameters, as well as conducting psychoacoustic tests utilizing virtual reality tools, this study aims to provide a comprehensive understanding of the factors that contribute to the restorative effects of these soundscapes. The research results and their analysis have led to the creation of a classification of soundscape parameters that significantly affect the ratings of their restorative properties. In the future, further analyses will allow for the development of a guide that describes which soundscape parameters and their values are crucial for their positive restorative evaluation.

* * *

Acoustic classification with the descriptor of the weighted standardized level difference $D_{nT,w}$ and of the weighted apparent sound reduction index R'_w . Are the classes the same?

Reinhard O. NEUBAUER (dr.neubauer@ibn.de)

IBN Bauphysik GmbH & Co. KG
Ingolstadt, Germany

Building regulations specifies technical requirements to sound insulation performance. This will be often done by using a single number rating like the weighted apparent sound reduction index R'_w or the weighted standardized level difference $D_{nT,w}$. A better description of the quality of sound insulation would be the formation of classes. If acoustic classes are provided, the question arises to what extent are R'_w and $D_{nT,w}$ the same. Can a sound insulation class be equal with both descriptors R'_w and $D_{nT,w}$? This paper compares the two parameters and presents the class formation of both descriptors.

* * *

Micro-perforated stretched ceilings for acoustic, lighting and climate design

Christian NOCKE (nocke@akustikbuero-oldenburg.de)

Akustikbüro Oldenburg
Oldenburg, Germany

Stretched foils used as ceilings, wall coverings and other set-ups have been applied for more than 30 years. By introducing a nearly invisible micro-perforation into the stretched material the foil becomes highly sound absorptive. The classical set-up of a micro-perforated sound absorber consists of a micro-perforated panel in front of an air cavity. The sound absorption coefficient of these set-ups can easily be calculated with a high accuracy according to the well-known approximation of D.-Y. Maa if all defining geometrical parameters (diameter of microperforation, distance between orifices, panel thickness and air cavity depth) are known. Measurements in the reverberation chamber are presented for several set-ups.

These materials are applied in architectural design. Here the combination of acoustic absorption, lighting design and climatization is most interesting – three functions in one ceiling set-up. Furthermore optically transparent sound absorbers are available to cover glass surfaces.

Different applications in rooms will be presented from various projects.

* * *

New draft DEGA guideline 103-1 in sound protection classes

Christian NOCKE (nocke@akustikbuero-oldenburg.de)

Akustikbüro Oldenburg
Oldenburg, Germany

The DEGA recommendation 103 (DEGA-Empfehlung – Schallschutz im Wohnungsbau und Schallschutzausweis) has been introduced in the year 2009 and includes a classification scheme for dwellings. Seven classes are defined. The classification is based on different criteria for air borne noise, impact noise and other quantities. In 2018 a revised version has been published. Both versions relied on classical quantities such as air born sound insulation R'_w and impact sound insulation $L'_{n,w}$.

A new version has recently been published as a draft DEGA guideline 103-1 (Entwurf zur DEGA-Richtlinie 103-1 “Schallschutz im Wohnungsbau, Teil 1”). In this new draft the idea of seven classes has been taken over. The classification is based on traditional values such as R'_w and $L'_{n,w}$ but also offers the use of the weighted sound level differences $D_{nT,w}$ and weighted standardized impact sound pressure level $L'_{nT,w}$. It is suggested to use the latter quantities. This dual track approach allows a better design and will lead to a higher acceptance among acousticians and other users.

The new draft is presented and will be discussed in relation to other approaches for sound protection in dwellings.

* * *

Simulation of acoustic lens influence on wavefront shaping

Tomasz NOWAK (t.nowak@pwr.edu.pl),

Andrzej B. DOBRUCKI

Wrocław University of Science and Technology
Wrocław, Poland

The main objective of the presented study is to examine the influence of an acoustic lens on the shape of the wavefront. To conveniently illustrate the difference between acoustic pressure wave propagation with and without the lens, an isodynamic transducer was chosen as a source. This kind of loudspeaker generates a flat wavefront as a result of an approximately uniform distribution of speed and phase on the entire diaphragm. The designed lens consisted of a matrix of individual waveguides. Manipulation of size and position of the output matrix in relation to the input matrix allowed for achieving the desired waveguide length distribution. Differences in lengths of the lens's channels resulted in wavefront delay distribution at the output matrix. A numerical model of the transducer and waveguide matrix was created to evaluate the behaviour of acoustic pressure wave propagation through the designed lens. With a stationary study, a spatial pressure distribution was calculated, in the near field and far field, in a hemisphere in front of the lens as well as in a hemisphere in front of just the transducer. The differences in wavefront shapes between the two cases were clearly visible in comparisons, confirming the expected pressure wave delay distribution of the lens. The resulting wavefront curvature was compared to the assumed one in theoretical design. Results of those comparisons proved the possibility of influencing the wavefront shape, by manipulating the output matrix.

with some caveats discussed in the paper. The data from numerical calculation of pressure propagation allowed for visualizing calculated sound pressure level distribution, adding the directivity evaluation to the comparisons.

* * *

Assessment of acoustic quality of residential buildings in Poland – case study

Elżbieta NOWICKA (e.nowicka@itb.pl)

Institut Techniki Budowlanej
Warsaw, Poland

The requirements of people in relation acoustic comfort are very diverse. They depend on many factors. With regard to residential buildings notion of “satisfactory acoustic conditions” must take into account the need to provide a sense of intimacy, peace and security. Taking care of the appropriate acoustic quality of buildings, should result from compliance with applicable laws and be the responsibility of all participants in the construction process.

The article discusses the acoustic classification of residential buildings with a better acoustic quality, introduced in Poland in 2017. Also the overall legislative problem will be discussed.

* * *

Acoustic adaptation of ventilation system prototypes dedicated to individual classrooms

Artur NOWOŚWIAT (artur.nowoswiat@polsl.pl),

Rafał ŻUCHOWSKI, Michał MARCHACZ,

Marcelina OLECHOWSKA

Silesian University of Technology
Gliwice, Poland

The prototypes of innovative ventilation systems dedicated to individual classrooms are designed to solve the problem of poor air quality in schools while reducing the need for the energy necessary for heating. At the same time, the working ventilation system must meet the acoustic requirements. These requirements specify the permissible value of the L_{Aeq} of the sound level = 40 dB as the average value of six measurement points. For this purpose, several studies have been carried out. First, a room was prepared that mimics a real-scale classroom with equipment and models of students. Calibration of such a room model was carried out by means of reverberation time measurements in octave bands of the frequencies 125 Hz, 250 Hz, 500 Hz, 1000 Hz, 2000 Hz, 4000 Hz. In the calibrated room, The prototypes of innovative ventilation prototypes were successively installed and the noise level in the room was tested. In the event of failure to meet the requirements, acoustic adaptations were made, and measurements were made again. The task was successful when the sound level at each measurement point and the average sound level did not exceed 40 dB.

* * *

Estimation of the improvement of the impact sound insulation of a carpet floor covering on a wooden floor based on the results of tests carried out on a massive floor

Łukasz NOWOTNY (l.nowotny@itb.pl), Jacek NURZYŃSKI

Institut Techniki Budowlanej
Warsaw, Poland

This paper presents the relationship between the sound insulation properties of carpet floor coverings on the massive and lightweight reference floor structures. Most floor covering impact sound insulation tests are performed on a massive reference floor. There is actually no data on lightweight floor, which means that the possibilities of damping the impact sounds of floors on such structures are unknown. It turns out that it is achievable to estimate the parameters of impact sound insulation of carpet coverings installed on a wooden floor on the basis of tests performed on a massive reference floor. The proposed method uses the mobility parameters of the elements involved in the acoustic test. The use of this method allows to reduce the number of tests necessary to select the appropriate solution for damping the impact sound energy in the lightweight floor structures.

* * *

Validation of Adaptive Categorical Listening Effort Scaling (ACALES) for Polish language

Anna PASTUSIAK¹ (anna.pastusiak@amu.edu.pl),

Jędrzej KOCIŃSKI¹, Anna WARZYBOK-OETJEN²

¹ Adam Mickiewicz University
Poznań, Poland

² Carl von Ossietzky Universität Oldenburg
Oldenburg, Germany

Introduction: Considering the complexity of perceiving and properly processing speech signals, it is important in audiological diagnostics to assess not only intelligibility itself but also the so-called auditory effort, understood as a mental load needed to understand acoustic information in speech signals.

Purpose: The aim of the study was to prepare and validate in terms of the accuracy and repeatability of results (test-retest) the Polish version of the Adaptive Categorical Listening Effort Scaling (ACALES) test. The speech material used was the Polish Matrix Sentence Test. 60 listeners participated in the measurements – 20 younger and 20 older individuals with normal hearing, as well as 20 individuals with sensorineural or mixed hearing loss of varying degrees. Using the Oldenburg Measurement Application (OMA) software listening effort was assessed using a 13-point scale in various acoustic conditions including stationary, modulated, and cafeteria noises. In addition, speech recognition thresholds (SRT) and slope were determined adaptively under the same masking conditions.

Results: Similar to speech intelligibility, the influence of the masker type on the measured listening effort was observed – it was usually greater in the case of stationary noise compared to modulated signals. Listening effort decreased as the signal-to-noise ratio (SNR) value increased. At unfavourable SNR values, listening effort ratings depended on measured intelligibility to a greater extent than at higher SNR values. Older, normal-hearing listeners and people with hearing loss rated their listening effort higher compared to young, normal-hearing listeners.

Conclusion: It has been shown that the Polish version of the ACALES is a reliable, repeatable, and simple tool characterized by a small variability between test/re-test values

and can provide complementary information to the value of speech intelligibility, supporting the multi-faceted assessment of the patient's ability to effectively hear in the context of communication situations.

* * *

Identification of errors in the digital transmission paths of radio stations

Marcin PATER (marcin.pater000@gmail.com),
Marcin A. GROCHOWINA

University of Rzeszów
Rzeszów, Poland

Radio stations currently use a hybrid method of broadcasting. The transmission between the studio and the transmitter is digital. In the transmitter, the digital signal is converted to analog form and transmitted using AM or FM modulation.

The identified problem are transmission errors in the digital path. Single cases of transmission errors are not uncommon and happen in most systems. However, repeated errors occurring in clusters are usually a sign of damage to the transmission path and require intervention.

The article presents an exemplary solution that allows automatic detection of some errors that manifest themselves in the identified way. In order to identify transmission errors, basic statistical methods were used that allowed the creation of a reference data set on the basis of which it is possible to identify the fact of an error based on patterns and algorithms from the machine learning area.

People associated with the radio industry are keenly interested in studying this phenomenon because there are currently no reliable solutions that would allow automatic detection and identification of such problems.

* * *

Practical aspects of diffuse reflection and sound diffraction modeling in room acoustics simulations

Piotr PEKALA^{1,2} (p.pekala@akustix.pl)

¹ AkustiX

Przeźmierowo, Poland

² Adam Mickiewicz University
Poznań, Poland

Most modern programs for modeling room acoustics contain implementations of algorithms that enable modeling of diffuse reflection and diffraction of sound inside rooms. However, these algorithms are often based on different mathematical models, require different sets of input data, and also differ significantly in computational complexity and precision of the calculation results. The use of these capabilities of simulation programs is possible provided access to data on the characteristics of the sound scattering coefficients of the materials used. The most commonly used coefficients are these obtained in a diffuse field.

The presented paper discusses the implementation of diffuse reflection and sound diffraction modeling algorithms in the most popular simulation programs.

In addition, the influence of modeling these phenomena on the accuracy of the obtained results was analyzed on exemplary room models.

* * *

Acoustic screen as a practical anti-noise protection

Janusz PIECHOWICZ (piechowi@agh.edu.pl)

AGH University of Krakow
Kraków, Poland

Acoustic screens are commonly used in Poland and in many countries as the only protection of noise-prone areas. They are used both in the outdoor environment and in the working environment in industrial rooms and offices. The history of the use of acoustic screens dates back to the second half of the 20th century. Since then, they have been used to reduce noise from roads, railways, airports, manufacturing plants, and municipal noise, as well as for many other noise sources. The effectiveness of an acoustic screen is a function of many factors that must be considered in the design process. The article presents the multi-variant application of acoustic screens, discusses the methods of testing acoustic parameters of screens in laboratory and in situ conditions.

* * *

Azimuth and elevation errors in binaural reproduction of ambisonic sound

Agnieszka Pietrzak (A.Pietrzak@ire.pw.edu.pl)

Warsaw University of Technology
Warsaw, Poland

Binaural decoding of an ambisonic sound is reproducing the information about a soundfield over headphones. It is done based on the spherical harmonics representation of the spatial sound and on the use of Head Related Transfer Function (HRTF). Inaccuracies in the decoding process, which can be caused for example by using non-personalized HRTF, may lead to difficulties in localizing the sound source by the listener. Especially in the elevation plane, localization errors can be significant. In this study, listening tests were conducted in order compare azimuth and elevation errors for different binaural decoders. It is discussed how azimuth and elevation errors vary depending on the type of the binaural decoder used, for 1st and 3rd order ambisonic recordings of pink noise bursts.

* * *

Optimisation of the model for the numerical determination of the HRTF

Przemysław PŁASKOTA (przemyslaw.plaskota@pwr.edu.pl)

Wrocław University of Science and Technology
Wrocław, Poland

Recently, the issue of numerically determining the Head Related Transfer Function has been still considered. The HRFT is the basis for creating individualised sound experiences in metaverse solutions.

This paper presents an analysis of different variants of the numerical model of an artificial head. Optimisation was carried out considering the upper limit frequency of the model, the size of the elements and their size distribution, the size and the enclosure properties of the head model.

The numerical model obtained as a result of the work is characterised by a short computation time with a sufficiently high upper limit frequency. The results obtained were compared with measurements of the real object, which confirmed the correctness of the designed model.

* * *

Control of spectral components in additive resynthesis as a means to alter sensation of consonance in chords

Marek Janusz PLUTA (pluta@agh.edu.pl)

AGH University of Krakow
Kraków, Poland

A prior study presented a possibility to impact the sensation of consonance by controlling spectral components of simultaneous pitches consisting a chord in sound synthesis using the additive method. It involves considering spectral components in all simultaneously sounding pitches consisting a chord. Components within the range of beating and roughness are modified to gradually strengthen or weaken both phenomena. So far, the idea and method had been implemented in a basic additive synthesizer producing simple, abstract, time-invariant timbres. The current study carries out the research further, and discusses problems of implementing aforementioned consonance-altering mechanism in a more complex additive synthesizer, applied to resynthesize sound of selected acoustic instruments. The study deals with natural independent evolution of spectral components, where consonance gradually varies with time. Moreover, it presents a solution to mitigate impact of the mechanism on a total signal level, caused by attenuation of selected components.

* * *

Acoustic model for the classification of Polish vowels

Karolina Maria PONDEL-SYCZ
(karolina.pondel.dokt@pw.edu.pl)

Warsaw University of Technology
Warsaw, Poland

The study explored the performance of vowel recognition using an acoustic model built on Audio Fingerprint techniques. The research compares the performance of Support Vector Machines (SVMs), Hidden Markov Models (HMMs), Artificial Neural Networks (ANNs) and K-Nearest Neighbors (k-NN) classifiers in the recognition of isolated and within-word vowels and investigates the importance of different types of acoustic speech features in this process. Temporal, spectral, cepstral, formant, LPC and perceptual features of speech were examined. Importance of features was tested using a random forest classifier. Vowel classification was tested at three confidence levels for feature importance: 90%, 95% and 99%. Two author databases consisting of a total of 1,200 samples from 20 speakers, recorded under household conditions, were used. The classifiers were evaluated by confusion matrix, accuracy, precision, sensitivity and F1 score. A segmentation of words into speech sounds was carried out using a tool based on BiLSTM recurrent neural networks and the BIC criterion. Three most important features were determined: power spectral density, spectral cut-off and Power-Normalised Cepstral Coefficients. In the isolated vowel recognition task, the SVM classifier was the most effective with a feature significance confidence level of 95% obtaining accuracy = 81%, precision = 81%, sensitivity = 81%, F1 score = 80%. In the task of recognising a vowel within a word, it was verified if the algorithm detected the presence of vowels in the correct segment and if it recognised

the correct vowel within it. The best results were obtained by the k-NN classifier (statistical confidence level of feature importance of 99.9%). However, these results were low, correct recognition of the vowel in the word: A, E, U: 20%, I, O: 7%, Y: 23%. This indicates strong influence of the neighbourhood of other speech sounds in speech on the acoustic model of vowels and their recognition.

* * *

The effect of ultrasonic noise on a worker's ability to perform their basic tasks

Jan RADOSZ (jarad@ciop.pl)

Central Institute for Labour Protection
– National Research Institute
Warsaw, Poland

Noise, defined as the presence of undesirable sound, has been extensively documented in the context of its impact on human health. Exposure to elevated levels of acoustic pressure can result in adverse health outcomes such as hearing impairment, the perception of tinnitus, and various other health-related issues. In recent times, there has been a growing concern surrounding the potential health ramifications of exposure to ultrasonic noise. A number of countries have officially recognized ultrasonic noise as a health hazard within occupational settings. Despite ongoing investigations into the frequency range above 20 kHz, there remains a deficiency in comprehensive data pertaining to its effects on the human organism. Furthermore, there is a notable absence of internationally accepted standards for the assessment of ultrasonic noise within workplace environments. While recent research endeavors have contributed to the expansion of our understanding in this domain, there remains a substantial gap in knowledge. This deficiency encompasses inquiries into potential health consequences and the development of enhanced dosimetry methods. Moreover, this knowledge gap is particularly significant within the context of workplaces and the welfare of employees, underscoring the critical need to establish comprehensive measures that safeguard them against potential adverse health effects.

* * *

Electrodynamic pick-up for electric string instruments

Edward R. RESZKE¹ (ertec@wp.pl),
Andrzej B. DOBRUCKI²

¹ Ertec-Poland Edward Reszke
Wrocław, Poland

² Wrocław University of Science and Technology
Wrocław, Poland

The most important elements in electric musical string instruments are pick-ups. They convert vibration of strings into electric signal. Usually, two types of pick-ups are used: electromagnetic and piezoelectric. Electromagnetic pick-up, called also a pick-up with moving armature, converts vibration of string into an electric signal using change of magnetic flux in the magnetic circuit by the vibration of the string made of magnetic material. Vibrating string causes change of the air gap between the string (which is a moving armature) and rest of magnetic circuit. A variable electromotive force is generated in the stationary winding. In order for it to be proportional to the speed of vibration,

polarization is needed, which is achieved by using a permanent magnet in the magnetic circuit. In a piezoelectric transducer, an electric current is generated due to the deformation of the piezoelectric material under the influence of a vibrating string. The subject of this paper is a stringed instrument with a electrodynamic transducer, which converts mechanical vibration of strings into an electromotive force which is produced between the ends of moving wire placed in the permanent magnetic field. This transducer is also called a transducer with moving wire. A wire (string) is made of a conductive material, but not necessarily a magnetic material. The principle of operation is similar to that of a ribbon microphone. The electromotive force induced at the ends of the string is very small and must be strongly amplified. It's a novel technique which is applicable in electric stringed instruments such as guitar, violin, viola, cello, double bass, and others. It has already been described in form of the patent application registered by Polish Patent Office and it is now designated to the further patent actions abroad based upon this priority document.

* * *

A tool for designing water tanks for measuring hydroacoustic transducers

Roman SALAMON,
Jacek MARSZAL (jacek.marszal@eti.pg.edu.pl),
Iwona KOCHAŃSKA

Faculty of Electronics, Telecommunications
and Informatics
Department of Sonar Systems
Gdańsk University of Technology
Gdańsk, Poland

Special water tanks are commonly used to measure the parameters of underwater acoustic systems. They must meet specific requirements, the fulfilment of which ensures very small but acceptable measurement errors. These requirements define the size of the tank and its shape as well as the strong damping of reflected waves. At the design stage, it is necessary to determine the impact of the tank structure on the measurement errors and to adapt it to the expected measurement methodology. The article presents a mathematical tool for designing such water tanks using the impulse response method. Contrary to the use of this method in architectural design, the presented method is here used to determine the measurement signals emitted by ultrasonic transmitting transducers and received by receiving transducers (hydrophones). The relationships are given between the parameters of the pulse response and the design parameters of the tank and the measurement system, as well as its transfer functions and sample measurement signals.

* * *

Thermodynamic properties of 1-allyl-3-methylimidazolium dicyanamide and 1-vinyl-3-methylimidazolium bis(trifluoromethylsulfonyl)imide

Lukasz SCHELLER (lukasz.scheller@us.edu.pl),
Krzysztof CWCYNAR, Marzena H. DZIDA

University of Silesia in Katowice
Katowice, Poland

Ionic liquids (ILs) have emerged as promising alternatives to traditional organic solvents due to their unique properties, such as low volatility, high thermal stability, and remarkable tunability. Understanding the thermodynamic properties of ILs is crucial for their application in various fields, including energy storage, separation processes, and catalysis. In this study, we experimentally investigate the thermodynamic properties of two ILs, namely 1-allyl-3-methylimidazolium dicyanamide ([AMim][DCA]) and 1-vinyl-3-methylimidazolium bis(trifluoromethylsulfonyl)imide ([VMim][NTf2]), which have not been previously studied.

The speed of sound and isobaric heat capacity were measured in the temperature range from 293.15 to 323.15 K at atmospheric pressure. The density was measured in the temperature range from 278.15 to 363.15 K at ambient pressure. From the experimental data the related thermodynamic properties were calculated, i.e. isentropic and isothermal compressibility coefficients as well as the isobaric thermal expansion coefficients.

The results reveal that [AMim][DCA] exhibits higher values of speed of sound and isobaric heat capacity compared to [VMim][NTf2]. On the other hand, [VMim][NTf2] demonstrates higher density values and calculated coefficients compared to [AMim][DCA]. It was found that for that for [AMim][DCA] the temperature dependence of the isobaric coefficient of thermal expansion is stronger and negative – contrary to [VMim][NTf2], where this dependence is smaller and positive.

The data obtained in this study contribute to the development of reliable thermodynamic databases for ILs and a comprehensive understanding of their thermodynamic properties. The acquired knowledge enhances our understanding of IL behavior and facilitates the advancement of IL-based technologies.

This work was financially supported by the National Science Centre (Poland) Grant No. 2021/41/B/ST5/00892 in the framework of OPUS program.

* * *

Experimental tests of selected sound-absorbing materials dedicated for a hydroacoustic measuring basin

Aleksander M. SCHMIDT (aleksander.schmidt@pg.edu.pl),
Lech KILIAN, Jacek MARSZAL

Faculty of Electronics, Telecommunications
and Informatics
Department of Sonar Systems
Gdańsk University of Technology
Gdańsk, Poland

Several scientific institutions from the Gdańsk community participate in the implementation of the grant from the Ministry of Education and Science “Concept of building metrological infrastructure in the area of underwater acoustics at the Central Office of Measures”. In practice, the concept includes, among other things, the design of two measurement basins: a large-size one for measurements in the range of possibly low ultrasound frequencies (from several dozen kHz) and a small-size one (from several hundred kHz). One of the basic conditions for the proper implementation of measurements is to obtain minimum sound reflec-

tions from the water surface, walls and bottom in basins. This is possible by covering these surfaces with sound-dispersing materials or so-called acoustic absorbers. The frequency characteristics of these properties are decisive here, but also the price, ease of assembly, cleaning and slow aging. The article presents the results of the measurements of the signal attenuation after passing through the tested materials, the values of the levels of attenuated echoes and the calculated of the absorption coefficients of currently available and promising layers of “synthetic grass” with different lengths of blades, plates made of various plastics and, for comparison, curtains made of dispersing brushes, damping the measuring basin of the Department of Sonar Systems for several decades. The obtained characteristics were compared with those presented by the manufacturer of commercial absorbent panels.

* * *

Low-power underwater modem for shallow water communications

Jan H. SCHMIDT,
Iwona KOCHAŃSKA (iwona.kochanska@pg.edu.pl),
Aleksander M. SCHMIDT

Faculty of Electronics, Telecommunications
and Informatics
Department of Sonar Systems
Gdańsk University of Technology
Gdańsk, Poland

The low-power underwater acoustic modem is usually an important component of the Underwater Wireless Sensor Network (UWSN). Network nodes have predetermined energy resources that will not be replenished during the life of the node. In shallow waters, multipath propagation is constantly occurring and for the modem to work effectively, solutions to overcome them must be used, which will also meet the important criterion of energy efficiency. The article presents the concept of a low-power underwater modem using BFSK modulation and the fast frequency-hopping spread spectrum (FFHSS) technique. The results of simulation and experimental tests, which were carried out to determine the performance of the modem, are included. Simulation tests were performed using a Watermark simulator, and experimental tests in a model pool.

* * *

Experimental setup design to evaluate acoustical privacy protection in small enclosed compartments

Alois SONTACCHI¹ (sontacchi@iem.at),
Christian BLÖCHER¹, Thomas HATHEIER²

¹ Institute of Electronic Music and Acoustics
Graz, Austria

² AUDIO MOBIL Elektronik GmbH
Ranshofen, Austria

Privacy protection is an upcoming topic in our society caused by increased individual mobility and forced availability by telephone. Acoustic communication in small, closed compartments exhibits a challenge to establish a private sphere for a single user without heavily affecting the acoustical surrounding, e.g. in a quiet environment, for

other persons. For a specific use-case in car compartments a recently developed approach will be examined within a listening test. To ensure control over several conditions of the experimental setting while still providing the listeners a comfortable situation mimicking real conditions a specific real-time capable setup in an anechoic room is used.

Within the experiment different positions for both speaker and would-be listener are examined under multiple driving conditions. Psychoacoustic principles like spectral and spatial auditory masking of signal-dependent broadband noise as well as signal-dependent temporal distractors are evident and adjustable components of the evaluated approach. Therefore, in the proposed experimental setup the listening subjects initially have to adjust the level of the broadband component individually to the point of perfect masking of presented speech signals. However, while these levels should guarantee complete unintelligibility, they will cause the most affecting loudness increase in the car cabin potentially causing increased passenger annoyance. Therefore, these levels will provide the anchors to start an individual adaptive adjustment procedure. Subjects presented with masked spoken sentences will echo the recognized parts immediately. Their responses will be evaluated by an automatic speech recognition system in real-time to guarantee sufficient masking. Within this procedure the broadband noise levels will be readjusted by additionally applying temporal compact distractors. Thus, the overall loudness will be reduced while preventing listening in.

* * *

Validation of the measurement data for different heights of a microphone position in outdoor environment

Andrzej C. STANIEK (astaniek@gig.eu)

National Research Institute
Katowice, Poland

One of the major problems when performing measurements of noise generated in outdoor environment is assessment of the influence of the microphone position (height). For measurement of noise generated by wind turbines it is important as in EN 61400 standard the measurement technique specifies mounting of the microphone on a mounting board on the ground level. So for the other microphone positions, practically demanded especially for long term monitoring, it should be carefully analysed and transfer function should be evaluated. Other problem which is under investigations is the influence of wind and the correction due to wind speed ought to be estimated.

* * *

Subjective tests of speaker recognition for selected voice disguise techniques

Piotr STARONIEWICZ (piotr.staroniewicz@pwr.edu.pl)

Wrocław University of Science and Technology
Wrocław, Poland

Research work on the effectiveness of voice disguise techniques is important for the development of biometric systems (surveillance) as well as phonoscopic research (forensics). A speaker recognition system or a listener can be deliberately or non-deliberately misled by technical or

natural methods. It is important to determine the impact of these techniques on both automatic systems and live listeners. This paper presents the results of listening tests conducted on a group of 40 people. The effectiveness of speaker recognition was investigated using selected natural (chosen from four groups of deliberate natural techniques: phonation, phonemic, prosodic and deformation) and technical (pitch shifting, GSM coding) voice disguise techniques. The results were related to the previously obtained outcomes for the automatic method of verification carried out using a classical speaker recognition system based on MFCC (Mel Frequency Cepstral Coefficients) parameterisation and GMM (Gaussian Mixture Models) classification.

* * *

Acoustic aspects of the Goseck Circle area

Katarzyna SUDER-DĘBSKA (suder@agh.edu.pl)

AGH University of Krakow
Kraków, Poland

Goseck Circle is an example of monumental buildings from the Neolithic period called rondels. The object was discovered in the 1990s, then archaeologically reconstructed and opened to the public in 2005. Currently, it is considered to be the oldest known object of this type, and its creation is estimated at around 4900 BC. The object is roughly circular in shape. It has one ditch and two palisade rings. There are three entrances leading to the interior of these structure, two of which are located on the south side and coincide with the places of sunrise and sunset during the winter solstice. Therefore, the Goseck Circle is considered as the oldest solar observatory, as a worship or ritual place.

A number of studies on both contemporary and archaeological objects indicate that the objects display the characteristic features depending on their intended use. Therefore, it can be assumed that if the Goseck Circle structure was to be a place of worship, then in terms of acoustics it should be characterized by such values of acoustic parameters that will also prove this. This concept was the reason for carrying out a series of numerical calculations that allowed for the determining of the selected parameters characterizing the acoustic field inside the analyzed object. The article presents and discusses the results of these numerical analyses.

* * *

Cloning the voice and speech of Piotr Fronczewski for Polish speech synthesis

Krzysztof SZKLANNY (kszklnny@pjwstk.edu.pl)

Polish-Japanese Academy of Information Technology
Warsaw, Poland

The quality of synthetically generated speech has improved significantly in recent years, largely due to the technological development of speech synthesis systems, in particular those based on deep neural networks (DNN). However, the problem of emotion in speech synthesis still remains a challenge. Most of the existing speech synthesis systems do not convey the pervasive emotional contexts in human-human interaction. The lack of expression limits the emotional intelligence of current speech synthesis systems.

This work aimed to develop a recording method for preparing a balanced corpus of emotional recordings in the Polish language for use in speech synthesis based on artificial intelligence (AI) algorithms. An essential aspect of the work was the selection of a voice-over artist who would allow the recording of the spectrum of an actor's voice, emphasizing the actor's interpretations and emotions derived from the content. Outstanding actor Piotr Fronczewski was chosen for the role.

* * *

Wind turbine noise annoyance prediction in the low-frequency range

Bartłomiej STEPIEŃ (Bartlomiej.Stepien@agh.edu.pl),
Tadeusz WSZOŁEK, Dominik MLECZKO, Paweł MAŁECKI,
Paweł PAWLIK, Maciej KŁACZYŃSKI, Marcjanna CZAPLA

AGH University of Krakow
Kraków, Poland

Currently, wind turbine noise is modelled using commonly used calculation methods such as ISO 9613-2, CNOSSOS-EU, and NORD 2000. The ISO 9613-2 and CNOSSOS-EU methods allow calculations in octave bands from 63 Hz to 8 kHz, while NORD 2000 allows calculations in one-third octave bands from 25 Hz to 10 kHz. Neither of these computational models takes into account the additional physical phenomena occurring in the low-frequency range (tonality, frequency modulation) that increase the annoyance of the noise generated by these devices. This paper presents the results of calculations using the aforementioned computational methods for modelling low-frequency noise generated by wind turbines, taking into account tonality and signal modulation determined experimentally. The suitability of the presented approach was verified by comparing the obtained calculation results with measurements taken around the wind farm.

This research has been funded by the National Centre for Research and Development – project No. NOR/POL NOR/Hetman/0073/2019.

* * *

Effect on imaging quality of ultrasound probe parameters in Doppler tomography method

Tomasz ŚWIETLIK (tomasz.swietlik@pwr.edu.pl)

Faculty of Electronics, Department of Acoustics,
Multimedia and Signal Processing
Wrocław University of Science and Technology
Wrocław, Poland

Doppler tomography (DT) is a method that allows the reconstruction of 2D or 3D images of the interior of the examined object. For this purpose, a two-transducer ultrasound probe is used. In this method, the Doppler phenomenon and the so-called Doppler signal are used to obtain an image. Therefore, the probe is one of the most important components of the measurement system of this method.

It should be noted that Doppler tomography differs significantly from the well-known Doppler method of measuring blood flow in blood vessels. In the DT method, stationary cross-sectional images of the object under examination are obtained. In order to produce the Doppler effect in this

case, the probe can move around or along the object being imaged.

This paper will present a simulation of the effect of the frequency of the ultrasound probe on the imaging quality of a single inclusion.

* * *

Selected acoustic structures for effective sound absorption at low frequencies

Patrycja ŚWIRK (pswirk@ur.edu.pl),
Lucyna LENIOWSKA

University of Rzeszów
Rzeszów, Poland

The article presents a summary of the results of absorption tests for selected sound-absorbing-insulating materials: commonly used acoustical systems and composite materials of specially composed composition. In addition, we propose a new type of metamaterial in the form of a multi-layered acoustic system, which consists of an insulating material and a core in the form of a profiled steel plate loaded with a point mass, vibrating in an air gap environment. The research aims to evaluate the sound absorption performance of selected materials in the low frequency range. The results confirmed the very good absorption properties of the developed composite materials. In addition, promising absorption coefficient values were also obtained for the acoustic metamaterial in the case of matching the point mass to the local resonance.

* * *

Impact of changes in the shape of sensor part of sensor-actuator hybrid on its effectiveness in plates' vibroacoustic reduction

Roman TROJANOWSKI, Jerzy WICIAK (wiciak@agh.edu.pl)
AGH University of Kraków
Kraków, Poland

This work is a continuation of authors previous works on modelling a piezo electric sensor-actuator hybrid. For these models a change in sensor shape will be introduced to determine how it impacts the results. In order to preserve continuity with previous and future work a steel plate with 2 piezo elements and a half sphere of air was modelled using ANSYS software. One was used to excite plate's vibration, the other one for the purpose of vibration reduction. The first piezo element is a standard square based piezoactuator which will be used to excite the plates' vibrations. The second one can be either a standard square based piezoactuator or a sensor-actuator hybrid with a square based actuator part and either disc or square based sensor part with different sizes. Harmonic analyses were performed for the 1st, 2nd, 4th and 5th mode shapes using internal ANSYS optimization functions with the goal function being the minimization of displacement vector sum of a number of nodes with 3 possible cases. 1st case – all nodes making the back of the plate used as sensor, 2nd case – “virtual” sensor placed on diagonal of the plate, 3rd case – sensor placed where the sensor part of a hybrid is placed. Results presented obtained reduction for the plate and the differences between standard actuators and proposed sensor-actuator hybrids.

* * *

Annoyance of noise penetrating partitions in multi-family and multi-function buildings

Hanna TURKOWSKA (h.turkowska@itb.pl)

Instytut Techniki Budowlanej
Warsaw, Poland

Multi-family residential buildings often combine residential and commercial functions. At the same time, the amount of time spent in the home is increasing, partly due to the increasing prevalence of remote working. In such a situation, the problem of providing suitable acoustic conditions for work and rest becomes particularly important. Many works indicate that standard – single – number methods for assessing the acoustics of partitions are insufficient to determine whether occupants are adequately protected from noise. The main purpose of this study is to assess the annoyance of noise penetrating different types of partitions. The spectral waveforms of exemplary noises penetrating into living spaces were analysed, and the results obtained were related to indices for assessing noise annoyance. This indicates the need for further work on methods for assessing the building envelope in residential and commercial buildings.

* * *

Sound insulation – comparison of standard vs. real world situations

Michael VORLAENDER (mvo@akustik.rwth-aachen.de)

RWTH Aachen University
Aachen, Germany

Standardized sound insulation metrics are essential for testing of building elements and for field measurements in order to ensure comparability of data. When it comes to a real-world situation, however, the source and receiver positions and the source directivities might differ from those in the standard setting. An auralization framework based on ISO 12354-1 is briefly described. In an application of the framework, a study on the impact of specific source positions and orientations on the effective sound level difference is discussed in a few examples.

* * *

The influence of the use of a system of resonators in the structure of a sonic crystal on its effectiveness

Julia WESOŁOWSKA (julia.wesolowska@silencions.com)

Silencions
Wrocław, Poland

This paper concerns the topic of layered structures of sonic crystals. Sonic crystals are periodic systems of acoustic scatterers placed in a homogeneous medium. They achieve effectiveness through the impedance difference between the medium and the scatterer. These structures are characterized by the ability to tune the system to the selected frequency band, as well as the possibility of free air flow. The paper discusses the impact of replacing the scatterers in the sonic crystal structure with a system of resonators (by making holes in the cylinders) on their effectiveness in the selected frequency band. The transmission drop was calculated analytically and then verified by measurements performed in free field conditions. The analysis

of the effectiveness of the solution was confirmed by measurements using a directional loudspeaker as a sound source and two configurations of sonic crystals. The first one, made of scatterers, and the second one, made of Helmholtz resonators, obtained by making holes in the cylinders building the crystal.

* * *

Comparative analysis of selected voice parameters of patients with obstructive pulmonary disease and dysphonia

Karolina WĘGLARZ¹ (karolinaw.roz@gmail.com),
Wiesław WSZOLEK², Elżbieta SZCZYGIEL³,
Daria HEMMERLING²

¹ Andrzej Frycz Modrzewski Krakow University
Kraków, Poland

² AGH University of Krakow
Kraków, Poland

³ Akademia Wychowania Fizycznego
im. Bronisława Czecha w Krakowie
Kraków, Poland

A quality of voice is an important matter in communication, and can determine self-esteem and relationship quality. Speech pathologies can be a serious disability of the accusation, leading in extreme cases to social exclusion. Voice problems are similar both among people working with professional voice and patients with respiratory disease, including chronic obstructive pulmonary disease.

The purpose of the work was a comparative analysis of selected voice parameters of patients with obstructive pulmonary disease and dysphonia.

Research material: Research tests were taken on a group of 61 people: 30 healthy people (mean age 25.1 years), 16 patients with COPD (mean age 67.4 years) and 15 patients with dysphonia (56.4 years).

In order to obtain changes in the acoustic signal, characteristic for dysphonia and obstructive pulmonary disease, it was necessary to verify according to: body position and selected voice parameters.

Body position was assessed using the photogrammetric method. The three-plane position of the body in space was established. In order to study the acoustic signal of speech, an analysis was carried out in the time and frequency domain of the collected voice recordings. In contrast to the “classical” methods of speech signal assessment and analysis, the directions of research mentioned and conducted by many authors bring little when it comes to speech pathologies. The acoustic signal of pathological speech should be justified from the three-point source of this signal: the process of articulation – the process of origin – the stage of deformation of one and the other process by determination.

As a result of the research, the parameters of the speech acoustic signal were obtained, which provide additional information about changes in the sound source, which manifest themselves in the form of deformation of the sound signal.

The research method presented in the article will provide the patient with comprehensive and necessary diagnostics, as well as the process of treatment and rehabilitation.

* * *

Questionnaires and acoustic measurements in Longyearbyen Area, Svalbard

Jerzy WICIAK (wiciak@agh.edu.pl), Dorota MŁYNARCZYK,
Paweł MAŁECKI, Janusz PIECHOWICZ

AGH University of Krakow
Kraków, Poland

Svalbard is a Norwegian province in the Arctic, covering the Svalbard archipelago and islands within 71°–81°N and 10°–35°E. The largest town on the island of Spitsbergen is Longyearbyen, with a population of around 2100. It is the main centre of administration with the governor’s office, and there are many public buildings, a housing estate, a harbour and an airport. This paper presents selected results from a survey on the quality of environment and soundscape of Spitsbergen. The results of acoustic measurements of selected sites near Longyearbyen are also presented. Based on the responses, three groups of tourist activity were identified: (1) Longyearbyen activity: a round trip of town, visit to the museum, mine no. 3 and UNIS visits, (2) Snowmobile trips: to Barenstburg, East Cost and Elveneset, (3) Nature hikes: trips to the summits of the Sarkofagen and Trollsteinen peak, hiking on the Larsbreen, Longyearbreen and Tellbreen glaciers and visits to glacier caves. Of these sites, acoustic analyses (SPL – time and frequency characteristics) were conducted at the following locations: Longyeardalen: Unis area and city centre, Adventalen: dog sleds and snowmobiles rides, Nature hike: to Sarkofagen peak and caves in Larsbreen and Longyearbreen glaciers.

* * *

Beamforming in nearfield – metaheuristic approach and speech intelligibility tests

Agnieszka WIELGUS (agnieszka.wielgus@pwr.edu.pl),
Bogusław SZLACHETKO, Michał ŁUCZYŃSKI

Wrocław University of Science and Technology
Wrocław, Poland

A set of microphones spatially arranged in space in a array pattern is called a microphone array. Such an array has many applications, inter alia: sonars, radars, or speech processing. It can be used to extract and enhance the signal of interest from its observation corrupted by other interfering signals, such as noise or to estimate the direction of arrival of a source. Since the microphones are in different places in space, the phase of the signal components that arrive to each of the microphone can be different and some frequencies can be attenuated. Therefore, the array can be perceived as a spatial filter that consolidates the acoustic signals received by individual microphones to form a beam. Such process is called beamforming.

In this paper we focus on a problem in which the desired signal (speech signal) is interfered by other signal with partially overlapping band but with different localization. Our goal is to attenuate the interfering signal. We experimentally study the method in which microphones do not have to be equally spaced and all information regarding signal phase is hidden in a transfer function of the microphone. We focus on determining the microphones positions to minimize and FIR filter coefficients so that the actual output the beamformer is as close as possible to the desired one in the sense of l_2 norm. To solve this problem, we

use a metaheuristic algorithm. Since the interfering signals, i.e. background noise reduce speech intelligibility (SI), we study how the proposed microphone matrix influences this parameter (SI) – a variable, being an index of the comprehensibility of speech signals. SI is defined as the average percentage of words or phonetic units that human listeners can recognize.

* * *

Noise testing of multi-disc fan

Kamil WÓJCIAK (kamil.wojciak@itc.edu.pl),
 Patryk GAJ, Joanna KOPANIA

Instytut Energetyki
 Łódź, Poland

The impeller of a multi-disc fan was made of rotating smooth discs spaced close together. The concept of such machine came from Nikola Tesla in 1909. The fluid, based on the principle of friction against the rotating surfaces of the discs, flows outwards from the disc pack into an outlet. According to the literature, such a design is characterized by low noise emissions. Based on calculations, a prototype of a multi-disc fan was designed and then manufactured. Tests were carried out for the sound power level emitted from the fan's outlet. The examination was performed in a reverberation chamber according to ISO 3741:2010 standard. The noise source was visualized using an acoustic camera. The aerodynamic characteristics were also determined experimentally according to ISO 5801:2017 standard. The acoustic and aerodynamic characteristics of the multi-disc fan were determined.

* * *

Algorithm for detection of wave packets in a circular waveguide

Piotr WRZECIONO¹ (piotr_wrzeciono@sggw.edu.pl),
 Michał SZYMAŃSKI¹, Hydayatullah BAYAT²

¹ Institute of Information Technology
 Warsaw University of Life Sciences
 Warsaw, Poland

² Institute of Civil Engineering
 Warsaw University of Life Sciences
 Warsaw, Poland

This paper presents an algorithm for detecting wave packets in a circular waveguide. The waveguide terminated with a concrete plug was used to test the method. The concrete was made in accordance with the Eurocode standard. During the tests, a significant difference was observed between the behavior of the speaker and the concrete plug. The pulse reflected from the plug maintained its shape regardless of the sound level. The reflection of the pulse from the speaker's diaphragm resulted in a significant change in the form and duration of the wave packet. These changes were dependent on the sound level of the wave packet. As a result of these modifications was a significant difference between the measurement uncertainty of detecting a pulse reflected from the concrete and the speaker. In the case of reflection from the concrete plug, an uncertainty of 0.036% was obtained. The smallest measurement error value for the pulse reflected from the speaker was 2.5%.

* * *

Measurement verification of model calculations results of noise distribution around large industrial plants

Tadeusz WSZOŁEK (twszolek@agh.edu.pl)

AGH University of Krakow
 Kraków, Poland

Noise mapping of large industrial plants is typically carried out in preparing Integrated Pollution Prevention and Control (IPPC), environmental impact assessments and as part of strategic noise mapping. The construction of an acoustic model of a large plant at the development stage is similar to the modelling of other facilities. Essential differences arise at the calibration and verification stage of such a model. In an industrial plant, noise sources are distributed over a large area and noise emissions are usually measured at the plant boundary, at varying distances from the noise sources. Noise sources in large cities are distributed over an even larger area, but the calculations can be verified directly in their surroundings (e.g. next to a road), with the influence from other sources eliminated. In addition, the layout of the sources is repeatable (roads, railways, etc.). These are features that increase the accuracy of the modelling. In the case of an industrial plant, which is often seen as a black box, the points for calibrating the model are outside. Then the calibrated (measured) level is not the emission from an individual source but the summed emission level from all sources on the site. The noise emission from noise sources at the measurement point strongly depends on the attenuation along the propagation path. The magnitude of this attenuation for each source is different, as it depends on the location of the source relative to the measurement point and the obstacles between the source and the measurement point. As the EU recommended computational models (ISO 9613-2 and CNOSSOS) allow calculations to be performed under specific weather conditions, the problem of measurement verification of the model becomes even more important.

The paper focuses on the consistency of weather conditions and measurement verification and their influence on the result of noise prediction in the surroundings of a large industrial plant. The results of control point calculations using ISO 9613-2, CNOSSOS algorithms and the Nord 2000 model, which allows calculations under practically any weather conditions, are shown. The results of the analyses were compared with the measured results at the control points under “real” weather conditions.

* * *

Tests of windshields for wind turbines noise measurements

Tadeusz WSZOŁEK,
 Maciej KLACZYŃSKI (maciej.klaczynski@agh.edu.pl),
 Paweł PAWLIK, Bartłomiej STĘPIEŃ,
 Paweł MAŁECKI, Dominik MLECZKO

AGH University of Krakow
 Kraków, Poland

Measuring noise from wind turbines is a problematic metrological task due to the significant interference caused by the wind, especially in the low-frequency range. In the

audible band, especially A-weighted, the impact of interference from wind is significantly less than in the low-frequency and infrasound bands. For this reason, methods are still being sought to reduce interference from wind in the lowest frequency bands effectively. Experimental tests within the scope of the work were carried out using several windshields: with a single standard spherical windscreen (90 mm diameter) at 1.5 m and 4 m height above ground level; with an additional microphone's shield (tent); with a set of the double-shell type consisting of a standard spherical windscreen made of polyurethane foam and a second shield covered with a double thin fabric (included 90% nylon with 10% admixture of polyurethane/cotton, which is often used in pop-filters) with high flexibility and a 300 mm diameter placed at the height of 1.5 m above ground level; on the board with a double windscreen at a ground level according to IEC 61400-11. An effectiveness analysis of the proposed measurement methods was carried out on the wind farm in various wind condition. Performed research indicates that the best of the tested variants, when measuring wind turbine noise especially in the low-frequency range, is to place the microphone on the board with a double windscreen according to IEC 61400-11. It is also acceptable to use a double spherical cover.

* * *

Effect of phase modification of sound components on spatial impression in 2 and 3-component signals

Kamil ZIMNY (kzimny@agh.edu.pl)

AGH University of Krakow
Kraków, Poland

Spatial perception of sounds is one of the fundamental properties of the auditory system, allowing for the localization of sound sources in space or the evaluation of room size. However, the mechanisms responsible for this phenomenon have not been fully understood and described yet. Research in this area indicates the existence of mechanisms in the higher levels of the auditory system that are responsible for creating the impression of spatiality. On the other hand, other studies have shown that the auditory system is sensitive to phase coherence between the components of complex signals, suggesting a relationship between these phenomena. Preliminary informal listening tests suggested that continuous phase shifts introduced into components of complex sounds evoke an impression of spatiality of these sounds.

The subject of this paper is the investigation of the influence of phase modifications on the perception of sound spatiality and the presentation of its results. Harmonic signals composed of 2 or 3 pure tones at specific fundamental frequencies were used in the study. The signal components were then phase-modified using specially designed algorithms and various parameters of phase change. The listening test involved a dozen participants, mostly students without specialized listening training, who were asked to compare the spatial impressions of sounds with phase modifications to those without them. The research was conducted in an audiometric cabin using headphones.

* * *

Evaluation of hydroacoustic channel stationarity for reciprocal movement of transmitter and receiver

Andrzej ŻAK¹ (a.zak@amw.gdynia.pl),
Ryszard STUDAŃSKI², Agnieszka CZAPIEWSKA³,
Łukasz WOJEWÓDKA², Andrzej ŁUKSZA²

¹ Polish Naval Academy
Gdynia, Poland

² Gdynia Maritime University
Gdynia, Poland

³ Gdańsk University of Technology
Gdańsk, Poland

For shallow water areas, the hydroacoustic channel is characterized by strong multipath and at the same time long memory times. In the case of reciprocal movement of the transmitter relative to the receiver, coherence times should be expected to be extremely short. Classical methods of assessing the stationarity of a channel, for example, proposed on the recommendations of ITU-R P.1407-7, in the case of hydroacoustic channels do not allow the determination of coherence times primarily due to the long memory time of the channel. In view of this, the paper proposes a method for assessing channel stationarity based on simultaneously transmitted chirp signals of increasing and decreasing frequency. The study was carried out in a laboratory pool for different rates of movement of the transmitter relative to the receiver. In the pool there was strong multipath i.e. very difficult propagation conditions for data transmission. The paper evaluates the stationarity of the channel as a function of the speed of movement of the transmitter, the bandwidth occupied by the measurement signal and its duration. The study shows that the hydroacoustic channel is not always stationary for the duration of the symbol and this assumption is often made in simulation studies of data transmission in the hydroacoustic channel.

* * *

Profile analysis: A framework for the study of auditory sound spectrum analysis

Jan ŻERA (jan.zera@pw.edu.pl)

Warsaw University of Technology
Warsaw, Poland

Profile Analysis (PA) is a research approach in measuring the listeners' ability to discern the changes in the spectral envelope shape of complex tones. PA is based on a specific experimental design in which the listener is forced to perform across-frequency spectral comparisons. This is achieved by using a procedure of signal level roving to prevent the subjects from responding on the basis of their ability of detecting the change of level in a single frequency channel. The studies, initiated by D.M. Green and his co-workers in 1980s, explored the topic of PA in a thorough, systematic way. The experiments concerned the detection of amplitude increment (or decrement) of a single component in a multicomponent logarithmic complex, detection of multicomponent spectral changes, tilted spectra, or using a pedestal. The use of logarithmically spaced components accounted for the auditory filter bandwidths (ERBs) as in such spectra the same number of components fall in each and every auditory filter along a wide frequency range.

Later experiments included harmonic spectra more typical of music. A novel approach in PA was to separate across-frequency spectral envelope shape comparisons in a complex tone and across-time level comparisons in given particular frequency channel. This procedure has brought new insight into timbre perception explorations in real-life conditions of sound perception, such as differentiating timbre changes in musical sounds during which both across frequency and along time comparisons are made. PA offered a new approach to the study of auditory sound spectrum analysis but was followed by only few researchers. The paper recalls results of the PA studies and provides discussion of some links between the PA and the results of listening tests conducted during a course aimed at the development of timbre evaluation skills among the students at the Chopin University of Music in Warsaw.

* * *

**Assessment of the impact
of road traffic noise based
on post-realization analysis of a project**

Rafał ŻUCHOWSKI (rafal.zuchowski@polsl.pl),
Artur NOWOŚWIAT

Silesian University of Technology
Gliwice, Poland

The article presents the issue of post-implementation analysis of the road in terms of noise generated by road traffic, which affects the quality of life of residents and requires effective remedial actions. The post-implementation analysis allows for the assessment of the actual effects of road noise, the identification of areas requiring protection against noise and the monitoring of the effectiveness of the applied noise solutions based on field studies. It presents factors influencing the acoustic climate, such as traffic intensity, type of vehicles, road surface and applied acoustic protection. Presented is the current land development, such as the location of the road, its infrastructure and surroundings in the form of data obtained on the basis of the conducted terrain scanning. The conducted analysis of the measurement results was the basis for additional tests of the acoustic parameters of the existing acoustic screens. In addition, computer simulations were carried out, which allowed the assessment of the current acoustic

climate along the entire length of the road and were the basis for developing a repair program to the extent required.

* * *

**The influence of composite material manufacturing
technology on the change of insulation
from impact sounds**

Daria ŻUK¹ (d.zuk@wm.umg.edu.pl),
Norbert ABRAMCZYK¹, Piotr P.J. JAKUBOWSKI²

¹ Gdynia Maritime University
Gdynia, Poland

² Maritime Advanced Research Centre
Gdańsk, Poland

The paper shows the influence of the composite material manufacturing technology on the change of the insulation parameter from impact sounds and the ability to dampen structural vibrations by modifying the structure of the composite material with the addition of rubber recycle. Tests of acoustic insulation from impact sounds were carried out on a sandwich composite made on the basis of Synolite 1967-G-1 polyester resin and glass mat with a random arrangement of fibers and a weight of 350 g/m². As an additive modifying improving damping efficiency, rubber recycle created in the process of disposal of car tires was used. The material was made using the vacuum infusion method. Composite materials were tested in three variants of the arrangement of recycle in the produced composite in the form of 1, 2 and 3 sandwich layers. In the field of “in-situ” field tests, the reduction of the impact sound level by the ceiling with the tested plate made of composite material in relation to the ceiling without $\Delta L'$ plate was determined in accordance with PN-EN ISO 16283-2 and PN-EN ISO 717-2. The best insulation from impact sounds was obtained for a board made of material with 3 sandwich layers, which is $\Delta L' = 20.6$ dB. A decrease in the impact sound level of the board with 3 sandwich layers in relation to the composite board without the addition of recycle was also determined, demonstrating the effect of rubber recycle additives on the attenuation of structural sounds in the tested material. The use of rubber recycle obtained in the process of disposal of car tires has an impact on improving environmental protection.

* * *

FROM THE EDITORIAL BOARD

The Editorial Committee wishes to express many thanks and appreciation to all the reviewers, listed below, for their valuable opinions concerning papers submitted to the Archives of Acoustics in 2023:

| | | | |
|-----------------|-------------------------|--------------------|-----------------------|
| Ajish K. | ABRAHAM | Debasish Ray | MOHAPATRA |
| Szymon | BANASZAK | Leszek | MORZYŃSKI |
| Nicolas | BENECH | Maciej | NIEDŹWIECKI |
| Stefan | BRACHMAŃSKI | Mats | NILSSON |
| Teresa | BRAVO | Artur | NOWOŚWIAT |
| Rafał | BURDZIK | Jacek | NURZYŃSKI |
| Abdelmajid | BYBI | Lu-Ean | OOI |
| Agnieszka | BETKOWSKA CAVALCANTE | Krzysztof J. | OPIELIŃSKI |
| Joyraj | CHAKRABORTY | Hanna | PAMUŁA |
| Marcos | CHIMENO | Małgorzata | PAWLACZYK-ŁUSZCZYŃSKA |
| Zbigniew | CZECH | Paweł | PAWLIK |
| Zbigniew | DĄBROWSKI | Anna | PERELOMOVA |
| Andrzej Bogdan | DOBRUCKI | Janusz Piotr | PIECHOWICZ |
| Szymon | DRGAS | Adam | PILCH |
| Marzena | DZIDA | Przemysław | PLASKOTA |
| Paweł | DZIECHCIŃSKI | Marek | PLUTA |
| Ilia | CHINIFOROOSHAN ESFAHANI | Peter | POCTA |
| Sahar Ali | FAWZI | Michiel | POSTEMA |
| Jan | FELCYN | Prasant Kumar | PRADHAN |
| Fatma Nafaa | GAAFER | Anna | PREIS |
| Luis | GOMEZ-AGUSTINA | Rafał | RADECKI |
| Natalia | GORSKA | Zbigniew | RANACHOWSKI |
| Piotr | GRALL | Wojciech P. | RDZANEK |
| Tadeusz | GUDRA | Mohd Hafiz Abdul | SATAR |
| Zühre Sü | GÜL | Christine | SHADLE |
| Zhicheng | HE | Ewa Barbara | SKRODZKA |
| Denny | HERMAWANTO | Bartłomiej | STĘPIEŃ |
| Ireneusz | JABŁOŃSKI | Paweł | STRUMIŁŁO |
| Wiesław | JAKUBIK | Tong-jing | SUN |
| Guo | JIANZHONG | Krzysztof | SZCZUROWSKI |
| Arkadiusz | JÓZEF CZAK | Krzysztof | SZEMELA |
| Katarzyna | KACZMAREK | Malina | SZYCHOWSKA |
| Tadeusz Marek | KAMISIŃSKI | Venkatesan | THIRUMAL |
| Jonathan Andrew | KEMP | Piotr | TADZIK |
| Robin | KERSTENS | Ayşe | TIRYAKIOĞLU |
| Michał | KLICHOWSKI | Fabián C. | TOMMASINI |
| Zygmunt | KLUSEK | Jesus Alejandro | TORRES |
| Maciej | KŁACZYŃSKI | Piero | TORTOLI |
| Jędrzej | KOCINSKI | Zbigniew | TRAWIŃSKI |
| Peter | KOPCANSKY | Geoffroy | VANDERREYDT |
| Krzysztof | KOSAŁA | Jan | WARCZEK |
| Bożena | KOSTEK | Stefan | WEYNA |
| Henryk | LASOTA | Andrzej | WICHER |
| Urszula | LIBAL | Alicja | WIECZORKOWSKA |
| Bogumił | LINDE | Stanisław | WRONA |
| Jerzy | LITNIEWSKI | Yang | YANG |
| Yuxi | LUO | Kenji | YOSHIDA |
| Ewa | ŁUKASIK | Adam | ZAGUBIEŃ |
| Omid | MAHPEYKAR | Oleksandr I. | ZAPOROZHETS |
| Paweł | MALINOWSKI | Maciej | ZAWISZA |
| Paweł | MAŁECKI | Sławomir Krzysztof | ZIELIŃSKI |
| Marzena | MIĘSIKOWSKA | Norbert | ZOLEK |
| Dominik | MLECZKO | Edward | ZOREBSKI |

AIMS AND SCOPE

Archives of Acoustics was founded in 1976 and since then publishes original research papers from all areas of acoustics including:

- acoustical measurements and instrumentation,
- musical acoustics,
- acousto-optics,
- architectural, building, and environmental acoustics,
- bioacoustics,
- electroacoustics,
- linear and nonlinear acoustics,
- noise and vibration,
- psychoacoustics,
- physical and chemical effects of sound,
- physiological acoustics,
- speech processing and communication systems,
- speech production and perception,
- sonochemistry,
- transducers,
- ultrasonics,
- underwater acoustics,
- quantum acoustics.

INFORMATION FOR AUTHORS

- Manuscripts intended for publication in *Archives of Acoustics* should be submitted in pdf format by an on-line procedure using **New Submission** link in **User Home** menu.
- Manuscript should be original and should not be submitted either previously or simultaneously elsewhere, neither in whole, nor in part.
- Submitted papers must be written in good English and proofread by a native speaker.
- In principle the papers should not exceed 40 000 typographic signs (about 20 typewritten pages).
- A brief abstract must be included. The keywords and subject classification for the article are required.
- Postal addresses, affiliations and email addresses for each author are required.
- The submitted manuscript should be accompanied by a cover letter containing the following information:
 - why the paper is submitted to *Archives of Acoustics*,
 - suggestion on the field of acoustics related to the topic of the submitted paper,
 - the statement that the manuscript is original, the submission has not been previously published, nor was it sent to another journal for consideration,
 - 3–5 names of suggested reviewers together with their affiliations, full postal and e-mail addresses; at least 3 suggested reviewers should be affiliated with other scientific institutions than the affiliations of the authors,
 - author's suggestion to classification of the paper as the research paper, review paper or technical note.
- Information regarding the preparation of manuscripts is provided on the journal's website <https://acoustics.ippt.pan.pl>.
- Reviews of manuscript is available online.
- Full information about the journal are available at <https://acoustics.ippt.pan.pl>.

Each manuscript is initially evaluated by the Editor and then allocated to an Section Editor according to specific subject area. Upon receiving the Section Editor sends it to reviewers. The Editor and the Section Editors make the final recommendation. Their opinions are crucial for the Editorial Committee to decide whether the paper can be accepted for publication or not.

The Word or L^AT_EX source and pdf files of the final version of articles will be requested after acceptance for publication. High-quality illustrations (format bitmap (gif, jpg) or PostScript, with resolution no lower than 300 dpi) should be sent along with the manuscript.

Editorial Board
Archives of Acoustics